Development of a Cessna Skymaster mathematical model

A Two Step method aerodynamic and engine model identification from flight test data

Jan Wiącek

Delft University of Technology

TU Delft

Development of a Cessna Skymaster mathematical model

A Two Step method aerodynamic and engine model identification from flight test data

by

Jan Wiącek

to obtain the degree of Master of Science
at the Delft University of Technology,
Faculty of Aerospace Engineering,
to be defended publicly on Thursday November 6, 2025 at 09:30.

Student number:	5215102	
Project duration:	March 3, 2025 - November 6, 2025	
Thesis committee:	Prof. dr. ir. L. L. M. Veldhuis,	TU Delft, Chair
	Ir. J. A. Melkert,	TU Delft, Supervisor
	Dr. ir. C. C. de Visser,	TU Delft, Examiner

TU Delft

Preface

This thesis concludes the master's degree program of Aerospace Engineering at TU Delft, but is also the last part of my invaluable five years studies at this faculty. I consider myself very fortunate to have had the opportunity to work on the challenging, yet rewarding project of early-stage flight test system identification of one of the faculty research aircraft. It has been the quintessence of what I believe is key to engineering - being able to find one's way between the idealised picture on the drawing board or computer screen and an effective application in the physical world, all within the topic of my personal interest - flight testing.

In this report, it is assumed that the reader is familiar with aerospace engineering topics at the level of master's degree. For an elaborate derivation of equations of motion of the aircraft, Appendix A is referenced. Readers particularly interested in the development of the numerical application of the Two Step method are referred to [80].

I would like to thank a number of people who have contributed to this project. Primarily, my thanks go to my supervisor ir. Joris Melkert for his valuable time, advice and support, the mechanics Fred den Toom, Menno Klaassen and Brent van den Berk as well as test pilots dr. ir. Alexander in't Veld and ir. Hans Mulder for making my experiments possible. In addition, I would like to thank prof. dr. ir. Leo Veldhuis, dr. ir. Coen de Visser, dr. ir. Daan Pool, dr. ir. Rene van Paassen and ir. Ferdinand Postema for answering my multiple questions as well as ir. Rowenna Wijlens for sharing the IMU sensors.

Finally, a very special thanks to my parents for their indisputable support, far beyond the last five years of my university education.

Jan Wiącek
Delft, October 2025

Summary

In early 2025, the fleet of TU Delft research aircraft is joined by a Cessna Skymaster, a twin propeller aircraft aiming to serve as a flying test bed for novel propulsion systems. As a result, a need for an aircraft model has emerged as an initial step of reaching the long-term goal of implementing a digital twin into the Aerospace Engineering Faculty Simona simulator. Therefore, the aim of this study is to identify a mathematical model of the aircraft, quantifying its airframe dynamics and engine behaviour.

The aerodynamic model is determined with the Two Step method of system identification applied on flight test data collected throughout 19 decoupled doublet and 3211 manoeuvres. As the first step, the flight path within each manoeuvre is reconstructed with an Iterated Extended Kalman Filter employing the aircraft kinematic equations with the aim of smoothing the measurements and filtering out noise. In the second step, the reconstructed flight path is fed into an Ordinary Least Squares estimator, which determines the aerodynamic and control derivatives of the aerodynamic model of a predetermined structure. The engine model is built as a digitised version of the engine performance and propeller efficiency maps, coupled together to provide the temperature and altitude corrected engine horsepower, thrust and total pressure gain across the propeller as outputs.

In order to include the contribution of the aircraft change in geometry to its dynamic behaviour, a method is developed to measure the control surface deflection in the absence of existing dedicated instrumentation. This is done by measuring the displacement of the control column and pedals, whose translational motion is translated into rotation by a spring-loaded pulley. The pulley rotation is measured with attached IMU sensors recording its attitude. The measured steering column and pedals displacement is correlated to the control surface deflection. The proposed method compromises the time constraint, costs, and safety requirement of being non-invasive while providing high-frequency and low-noise measurements. However, it ignores slack or extension of the control cables and should not be used in coupled manoeuvres in which the aircraft rotational rate interferes with the one recorded by the IMU.

Required for dynamic analysis, the 3D centre of gravity and inertia matrix of the aircraft are determined. The former is found experimentally by measuring the reaction forces of the stationary aircraft at ground contact points for different pitch attitudes. A model including fuel, crew and cargo load as variables predicts the COG for an aircraft at MTOW as [3.56, 0.0, 1.68] [m]. The inertial properties of the aircraft are computed with the help of a CAD surface model. Percentages of aircraft mass are attributed to aircraft structural components based on empirical statistics and applied to the CAD model using an empty shell mass distribution. For the aforementioned COG at MTOW, the moment of inertia [I_{xx}, I_{yy}, I_{zz}] is modelled as [5,776, 5,438, 9,960] [kg m^2] and the product of inertia I_{xz} as 296 [kg m^2].

The aerodynamic model demonstrates a robust performance for symmetrical forces C_X, C_Z and yawing moment C_n. The C_l estimation is rather weak, as several of its parameters have been determined with a high variance, likely caused by the strong correlation of δa and p, particularity excited in aileron-induced rolling manoeuvre. A sensitivity analysis suggests little dependence of the model parameter on potential errors in COG, inertia, fuel mass or control deflection determination. The modelled engine power shows a high correlation with its counterpart estimated by the engine monitor, yet the estimation difference, ΔP, varies in time. A trend is observed relating ΔP with engine horsepower and manifold pressure, suggesting a potential dependence of the ΔP on flight conditions. A sensitivity analysis indicates an uncertainty of around 6 [N] in thrust and 0.5 [hp] in power, in cruise conditions.

The scope of the aerodynamic model is limited by the envelope of its identification flight tests, which have been performed at around 90 [kt] and 4,000 [ft]. The model structure specifies the terms contributing to the modelled aircraft dynamics and includes the incidence angles, rotational rates and control surface deflections, but excludes the engine dynamics, wing and cowl flaps or landing gear. The scope of the engine model is limited by the range of applicability of the engine performance and propeller efficiency maps. Extending the scope of the aerodynamic and engine models can therefore be given as the main recommendation for future studies.

Contents

List of Figures

List of Tables

Nomenclature

Abbreviations

Abbreviation	Definition
ADS-B	Automatic Dependent Surveillance - Broadcasting
AHRS	Altitude and Heading Reference System
AOA	Angle of Attack
AOI	Angle of Incidence
AR	Aspect Ratio
AVGAS	Aviation Gasoline
BHP	Brake Horsepower
BOM	Broadcasting Outer Module
CAD	Computer Aided Design
CFD	Computational Fluid Dynamics
COG	Centre of Gravity
CSU	Constant Speed Unit
CHT	Cylinder Head Temperature
DEAC	Dutch Electric Aviation Centre
DoF	Degrees of Freedom
DUT	Delft University of Technology
ECI	Earth-Centered Inertial coordinate frame
EDC	Engine Data Converter
EGT	Exhaust Gas Temperature
EHRD	Rotterdam The Hague Airport ICAO location indicator
EKF	Extended Kalman Filter
FL	Flight Level
FMU	Fuel Metering Unit
FTI	Flight Test Instrumentation
GLS	Generalised Least Squares
GS	Ground Speed
GPS	Global Positioning System
IAS	Indicated Air Speed
IEKF	Iterated Extended Kalman Filter
IMU	Inertial Measurement Unit
IRM	International Reference Meridian
ISA	International Standard Atmosphere
KF	Kalman Filter
LEW	Licenced Empty Weight
MC	Minimum Controllable (speed)
ML	Maximum Likelihood
MLW	Maximum Landing Weight
MOI	Moment of Inertia
MSL	Main Sea Level
MTOW	Maximum Take-Off Weight
NACA	National Advisory Committee for Aeronautics
NASA	National Aeronautics and Space Administration
NATO	North Atlantic Treaty Organisation
OEI	One Engine Inoperative
OEW	Operating Empty Weight
OGE	Out of Ground Effect
OLS	Ordinary Least Squares

Abbreviation	Definition
PFD	Primary Flight Display
POH	Pilot Operating Handbook
ROC	Rate of Climb
SI	Système Internationale (d'Unités) / International (Unit) System
S/N	Serial Number
TAS	True Air Speed
TO	Take-Off
UKF	Unscented Kalman Filter
UTC	Universal Time Coordinated
USAF	United States Air Force
WAAS	Wide Area Augmentation System
WGS	World Geodetic System
WLS	Weighted Least Squares

Symbols

Greek

Symbol	Definition
α	Angle of attack
β, β_p	Sideslip angle, propeller blade pitch angle
Γ	Dihedral angle
γ	Flight path angle
Δ, ∂	Change, partial derivative
$\delta_{()}$	Control surface deflection angle
ε	Error, residual
η	Efficiency
θ	Pitch angle, identified parameter
Λ	Sweep angle
λ	Taper ratio, constant bias
ρ	Density
σ	Standard deviation
ϕ	Roll angle
ψ	Yaw angle
Ω	Body rotational rate vector

Latin

Symbol	Definition
$\mathbf{A}$	Regression matrix, body acceleration vector
A	Surface area
$\mathbf{B}$	Input matrix
b	Wing span
C_L	Lift coefficient
C_l	Nondimentional moment around X body axis
C_m	Nondimentional moment around Y body axis
C_n	Nondimentional moment around Z body axis
C_P	Power coefficient
C_T	Thrust coefficient
C_X	Nondimentional force in the X body axis
C_Y	Nondimentional force in the Y body axis
C_Z	Nondimentional force in the Z body axis

Symbol	Definition
c	Wing chord
D	Diameter
e	Quaternion
$\mathbf{F}$	System matrix
F	Frame of reference
$\mathbf{f}$	Nonlinear state transition function
$f(x)$	Function f of x
g	Gravitational acceleration
$\mathbf{H}$	Observation matrix
$\mathbf{h}$	Nonlinear measurement function
h	Altitude, time step, height
$\mathbf{I}$	Identity matrix
I	Moment or product of inertia
J	Advance ratio, cost function
K	Kalman gain
k	Step indicator
L	Lie derivative, likelihood function
l	Length
m	Mass
N	Engine rotational speed
n	Load factor, number of given item
$\mathbf{O}$	Observability matrix
O	Order of magnitude
P	Engine power, error covariance
p	Rotational rate about X body axis, pressure
$\mathbf{Q}$	Process noise covariance matrix
Q	Torque
q	Rotational rate about Y body axis, dynamic pressure
$\mathbf{R}$	Measurement noise covariance matrix
$\mathbf{r}$	Position vector
r	Rotational rate about Z body axis
S	Wing surface area
T	Temperature, Thrust force
t	Time, thickness
u	Longitudinal body velocity
$\mathbf{u}$	Input vector
V	Airspeed
v	Lateral body velocity
$\mathbf{v}$	Output noise vector
W	Wind velocity
w	Normal body velocity, width
$\mathbf{w}$	Input noise vector
$\mathbf{x}$	State vectors
$\mathbf{y}$	Measurement vector (OLS)
$\mathbf{z}$	Measurement vector (KF)
$\dot{(.)}$	Time derivative
$\hat{(.)}$	Prediction, estimated parameter
$\bar{(.)}$	Mean value
$(.)^\intercal$	Matrix transpose

1 Introduction

As a global leader in research on sustainable aviation, the Faculty of Aerospace Engineering at Delft University of Technology works on innovations in aerospace propulsion systems allowing for a reduction of their footprint on the environment. In January 2025, a twin propeller engine Cessna Skymaster was welcomed into the existing fleet of university research aircraft. With its configuration of engines placed along the longitudinal axis and counter-rotating propellers, the platform facilitates in-flight practical testing of researched concepts of novel propulsion systems, hydrogen as sustainable fuel or propeller noise [8]. Prior to the introduction the Skymaster as an adjustable flying test bed, it is desired to study its flight dynamics in its nominal configuration, representing the control behaviour of the aircraft in any future comparative experiments. The quantification of the aircraft dynamic motion and engine response to control inputs is also the first step of creating the aircraft digital twin which can be implemented in a flight simulator, thus allowing to mitigate pilot risk and avoid the combustion of hydrocarbons. Therefore, the need for a mathematical model of the Skymaster emerges at this early stage of research on the acquired aircraft.

In this study, the realisation of the long-term goal of implementation of the Skymaster digital twin into the TU Delft Simona research simulator is initiated with the objective of determining the aircraft mathematical model. The latter is composed of two separate parts: an aerodynamic model and an engine model. The aerodynamic model consists of aerodynamic and control derivatives composing the longitudinal and lateral dimensionless forces and moments and is identified from flight testing with the Two Step method. The scope of the model is limited by the envelope of the flown manoeuvres. The engine model is based on the digitised version of the integrated engine performance and propeller efficiency maps. It provides the engine thrust and power output corrected for altitude and temperature and is limited by the range of the performance charts. In order to reach the objective of model identification, efforts have been made to overcome the limited available data on the aircraft and currently available instrumentation. As a result, the three dimensional centre of gravity model is determined from experimental ground testing, whereas the inertia matrix model is computed by decomposing the aircraft mass into individual inertial contributors. To address the lack of control surface deflection measurement instrumentation, a method of measuring the steering column and pedal deflection is proposed, allowing to subsequently correlate the output to actual aileron, elevator and rudder deflection.

The report begins with chapter 2 in which an overview of the aircraft technical parameters is given, together with a literature study. A formulation of the research objective and question is presented in section 2.2. The methodology behind the Two Step method of system identification is elaborated upon in chapter 3. In section 3.1, the first part of the approach is explained by describing the flight path reconstruction process done with an Iterated Extended Kalman Filter and includes a verification of the tool performance. Subsequently, the aerodynamic model parameter identification with the Ordinary Least Squares approach follows in section 3.2, together with the description of the working principle of the engine model. chapter 4 addresses the experimental part of the study, describing, among others, the development of the control surface deflection measurement method, flight testing procedures and data analysis. chapter 5 presents the experimental determination of the location of the centre of gravity and the analytical identification of the inertia matrix of the aircraft. The research question is answered quantitatively in chapter 6, in which the results of the aerodynamic model identification and engine model performance estimation are presented. A qualitative assessment of the results is performed in chapter 7, which includes a validation, sensitivity analysis and discussion of outcomes. Lastly, the study is concluded in chapter 8, including recommendations for further studies.

2
Literature Review

This chapter aims to set the background of the research topic and review the literature treating on available methodologies of approaching the research question. First, the analysed aircraft is briefly introduced in section 2.1. Next, the research objective is formulated together with the research question in section 2.2. The mathematical framework of the aircraft model is presented in section 2.3, methods of determining the inertial characteristics are explored in section 2.4, while different approaches to aircraft system identification are decomposed into steps and described in section 2.5.

2.1. Cessna 337F Super Skymaster

Recently taken over from the Dutch Electric Aviation Centre Teuge (DEAC), the Cessna 337F Super Skymaster (reg. N4207X, S/N 337-0050, see Figure 2.1) has become the new TU Delft Aerospace Engineering Faculty flying research platform. Given its distinct push-pull engine configuration, the aircraft has been acquired to facilitate testing of innovative concepts for aviation sustainability advancements such as hydrogen or electrical propulsion [8].

The Cessna 337 is a personal and utility aircraft in the two tones Maximum Take-Off Weight (MTOW) class, with several variants being developed throughout its production between 1963 and 1982, including a military observation version (the O-2 Skymaster) [52], a pressurised version, or a turbocharged version. The serial number S/N 337-0050 unit is the F337F variant, produced in Reims, France in 1972, with an increased gross weight, refined instrument panel and retractable landing gear, as opposed to original design [62] [71].

Figure 2.1: Cessna 337F Super Skymaster, registration N4207X, S/N 337-0050 at EHRD [8]

In its design phase, the Skymaster was addressed to those who are "not primarily airplane pilots but rather executives of a company, engineers, salesmen, doctors, farmers, or individuals just flying for fun and recreation" [2, p. 1]. With its first flight completed in 1961, the Cessna Skymaster aircraft design

aimed to provide a twin-engine platform without the handling drawbacks of one engine inoperative operation (OEI) but also avoid the legal requirement of the pilot to maintaining OEI proficiency - in essence, having "the advantages of a twin engine airplane with the simplicity of a single engine machine" [2]. This resulted in a push-pull configuration with both counter-rotating engines placed in the symmetry plane of the aircraft, generating centreline thrust and cancelling each other's torque, while decreasing the criticality of the one-engine-out minimum control speed (V_{MC}) [30].

Cruising at 5,500 [ft], the aircraft can cover a range of 1,700 [km] at 165 [kt], with both engines at 75% of their Maximum Continuous Power (MCP) being 210 [hp] each. With an empty weight of 1,222 [kg], the C337 can be loaded with 878 [kg] of useful load to reach a Maximum Take-Off Weight (MTOW) of 2,100 [kg]. Made primarily of aluminum 2024, the airframe spans 11.7 [m] and is 9.1 [m] long. The high wing of 18.7 [m^2] has an inner rectangular and outer trapezoidal planform with no sweep, positive dihedral and a taper of 0.67. Further details regarding the performance characteristics, airframe dimensions and propulsion system of the aircraft are listed in section F.1, section F.2 and section F.3 of Appendix F.

2.2. Research Objective and Question

Given the need for a preliminary analysis of the TU Delft Aerospace Engineering faculty Cessna 337F Super Skymaster research aircraft's dynamic behaviour, the research objective of this thesis is formulated as:

> **To identify, verify, and validate a mathematical model of the Cessna 337F Super Skymaster faculty research aircraft, including both its longitudinal and lateral dynamics, based on flight test data.**

This leads to the formulation of the main research question:

> **How can a flight test data based mathematical model of the Cessna 337F Super Skymaster faculty research aircraft, including both longitudinal and lateral dynamics, be identified, verified, and validated?**

To facilitate answering the main research question, the following guiding sub-questions are formulated:

RQ1 What are the longitudinal and lateral aerodynamic derivatives of the C337 aircraft?

RQ2 What are the elevator, aileron and rudder control derivatives of the C337 aircraft?

RQ3 How do the aerodynamic and control derivatives change with altitude and airspeed for the C337 aircraft?

RQ4 How can the propulsion system of the C337 aircraft be modelled?

RQ5 What is the scope of applicability of the developed mathematical model of the C337 aircraft?

RQ6 What is the validity of the derived mathematical model of the C337 aircraft?

2.3. Aircraft mathematical model

In order to quantify the behaviour of a flying aircraft, a formulation of an appropriate mathematical expressions describing the physical flight behaviour is necessary. There exists several options to fulfil this goal, the most popular include non-linear differential equations, state space models or transfer functions [40, p. 93]. The scope and applicability of the model depend on the degree of simplification of reality, which is usually defined by stating the assumptions made. The motion described by the equations of motion (see Appendix A) is also to be anchored to an applicable frame of reference. This section therefore aims to address the aforementioned topics and present the available methods of formulation of the aircraft mathematical model together with identifying their applicability.

2.3.1. Assumptions

The assumptions made in the creation of the mathematical model define its scope of validity, limiting the accuracy of description of reality by the model. Addressing the following simplifications is considered applicable.

1. In a three dimensional frame of reference, the aircraft is assumed to have six degrees of freedom (DoF), which allow for translation and rotation in all of the three axes of three dimensional space [15, p. 67] [20, p. 10] [5, p. 40] [38, p. 32]. The frame of reference itself can be defined in various ways, as elaborated in subsection 2.3.2.
2. The aircraft can be assumed a rigid body [40, p. 94] [5, p. 41] [24, p. 2] which neglects any airframe deformation and thus ignores aeroelastic effects. This assumption allows to neglect any changes in position of points within the aircraft body with respect to the body itself [15, p. 67], structural distortion or sloshing of fuel [24, p. 2]. The latter can be further extended into assuming a constant mass of the aircraft during the brief time interval of motion studied [5, p. 41]. This should not be confused with the assumption of constant mass throughout flight, here inapplicable.
3. The gravitational acceleration g field can be considered uniform and invariant with altitude. This allows to superimpose the centre of mass and centre of gravity of the aircraft [24, p. 2].
4. There are no other forces acting on the aircraft other than aerodynamic, propulsion and gravity forces [24, p. 2].
5. The Earth rotation is ignored and its surface is assumed to be flat, i.e. the local surface curvature is assumed to be negligible. This allows to fix the Earth in the inertial space [38, p. 29] [24, p. 2] [5, p. 41].
6. The airframe and mass distribution are assumed symmetrical in the XZ plane. This allows to approximate the products of inertia as null, namely $I_{xy} = I_{yz} = 0$. Cook [15] states that a further simplification can be made, if it is assumed that the aircraft body axes are aligned to be principal inertia axes. In this case I_{xz} is also null. However, this simplification is not often used because of the difficulty of precisely determining the principal inertia axes. Nevertheless, the symmetry of the aircraft implies that $I_{xz} << I_{xx}, I_{yy}, I_{zz}$ [15, p. 72].
7. Given the maximum airspeed attainable at Maximum Continous Power (MCP) $V_H = 90$ [m/s] and service ceiling $h_{max} = 5,900$ [m] from Table F.2, the maximum Mach number can be calculated as $Ma = 0.28$. This allows to ignore the compressibility affects in aerodynamic analysis of the aircraft, as the Mach number is inferior to 0.3 [4, p. 203]. A Mach number of 0.32 is achieved at V_{NE} and h_{max}, yet these conditions are not expected to be reached in normal operation of the aircraft. The propeller efficiency is assumed to account for all compressibility effects acting on the propeller.

2.3.2. Frame of reference

In order to quantify the position and motion of the aircraft, a reference frame is needed. From the numerous frames of reference used in aerospace, the following are described [20, p. 6] [67, p. 5] [38, pp. 29–31] [15, pp. 2–22] [45, p. 12]. Their convenience depends on the circumstances and application.

The **Earth-fixed reference frame** F_E [21] also called navigation frame, the Earth axes [65] [54] is fixed in space (inertial), with the X_E axis pointing north, Y_E axis pointing east and Z_E axis pointing down. The vehicle position (x, y) and altitude h are measured from its origin, which is placed on an arbitrary point

on the Earth's surface.

Another **Earth-fixed reference frame** F_I is the J2000, which is Earth-centered inertial (ECI). By definition, its origin is coincident with the centre of mass of Earth, the X_I points to the mean vernal equinox, Z_I points north, while Y_I completes the right-hand rule system. The World Geodetic System of reference F_{WGS} is another ECI, different from the F_I by the direction of X_{WBS}, going through the International Reference Meridian (IRM) intersection with the equator, while $Z_{WBS} = Z_I$.

The **aircraft body-fixed reference frame** F_b has its origin at the centre of gravity of the aircraft. The X_b axis is directed along the fuselage towards the nose, lying in the symmetry plane of the aircraft. The Y_b is directed along the right wing towards its tip and Z_b down, also lying in the symmetry plane. The body reference frame is particularly useful when experimental measurements are taken in flight, as the measurement equipment installed on the airframe takes data in the F_b frame.

The **Xsens sensor body-fixed reference frame** F_X is applicable to the Xsens sensor only. Its origin is defined at the centre of gravity of the sensor, as defined on Figure C.1. The axes of the F_X frame are defined on Figure 4.1, with the X_X directed along the longer side of the sensor, Y_X along the shorter side of the sensor and Z_X normal to its surface.

The local **Earth-fixed reference frame** F_L is defined as a right-handed Cartesian coordinate system with positive X_L pointing East, positive Y_L pointing North, positive Z_L pointing up [81]. It is used to express the Xsens sensor attitude.

The **aircraft fuselage stations with respect to datum frame** F_D has its origin on the horizontal Earth ground level, 65 [in] in front of the firewall, in the plane of symmetry of the aircraft. It is used to define the position of the aircraft structural components with respect to each other, defining the location of centre of gravity and in the moment of inertia determination. Figure 2.2 defines the datum of the F_D frame and some of the fuselage stations [61]. The X_D is horizontal and points backwards, Y_D points along the right wing of the aircraft, whereas Z_D points up. It should be noticed, that the fuselage, wing and tail boom stations have individual definitions, but can be oriented with respect to each other.

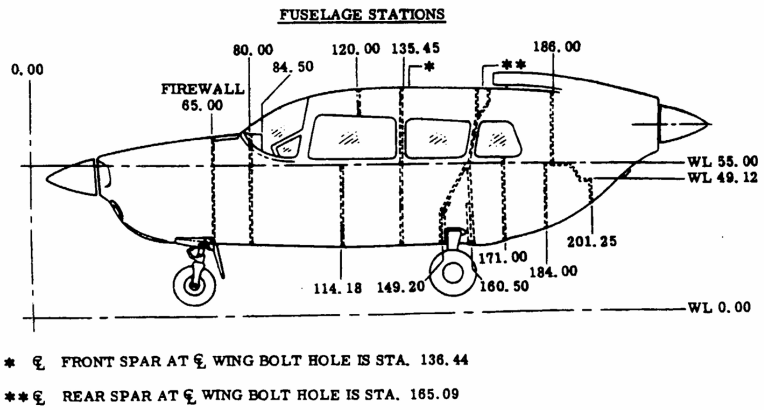

Figure 2.2: Definition of the F_D origin and fuselage stations [61]

The **vehicle-carried vertical reference frame** F_v [21] takes the centre of gravity of the aircraft as its origin and its axes parallel to the F_E system. The transformation between the F_E and F_v systems is therefore purely translational. The aircraft attitude (pitch θ, roll ϕ and yaw ψ Euler angles) is defined as the orientation of the aircraft body system F_b and vehicle carried F_v vertical axes [20, p. 6].

2.3.3. Equations of Motion

The aircraft Equations of Motion in six degrees of freedom can be derived from Newton's second law, as presented in detail in the dedicated Appendix A. The use of Newton's second law as starting point in the derivation of equations of motion is the common initial step in most aircraft mathematical models. Subsequently, forces in the X, Y Z and moments L, M, N acting in the six degrees of freedom can

expressed. The next paragraphs introduce the kinematic, aerodynamic and observation mathematical models of the aircraft employed in the system identification process.

Kinematic model
A kinematic model of rigid body aircraft motion consists of ordinary differential equations expressing the first time derivatives of the aircraft state variables as function the aircraft recorded linear accelerations, body rotational rates, velocities, attitude and constants. The state variables can include the aircraft position in F_E (GPS coordinates), velocities in F_b (u, v, w) and attitude of F_b with respect to F_E (Euler angles).

The model is used to describe the history of the aircraft motion in time in the flight path reconstruction process and excludes the aerodynamic forces and moments. The latter makes it particularly useful in determining and quantifying the behaviour of an aircraft, the aerodynamic characteristics of which are yet unknown. Together with the observation model and measurement error model, the kinematic model is used in the flight path reconstruction problem (see section 2.5) [45, p. 24].

The derivation of the equations constituting the aircraft kinematic model is presented in section A.4 of Appendix A, whereas its application in the flight path reconstruction problem is elaborated upon in subsection 3.1.4, together with the definition of the state, input and observation vectors.

Observation model
Observation models describe the relation between on-board measured variables such as the aircraft position, body velocity components, attitudes, which essentially constitute the aircraft state vector, but also the air data such as airspeed, angle of attack or angle of sideslip. Observation models model the expected true value of what cannot be directly measured or is believed to be inaccurate. For a significant part of the state vector variables, the model expresses the measured variable as exactly the state variable, populated with some measurement noise.

Depending on the exact definition of the measurement and state vectors however, the observation models can take different forms. The exact definition of the observation models for the measurement and input vectors used in this study is stated in the dedicated subsection 3.1.4.

Measurement error model
Although the measurement always aims to be as accurate as possible, it is convenient to model the measurement error. A simple, yet commonly used example of measurement error model for a measurement y_m can be expressed by Equation 2.1.

$$y(i)_m = y(i) + \lambda + w(i) \tag{2.1}$$

in which λ represents a constant bias error correction and w an additive stochastic error, such as the process input noise, at discrete time i. As specified in subsection 2.5.2, a requirement might be imposed on the measurement errors so that they are uncorrelated and have a zero mean [45, p. 43]. The measurement error model is defined in subsection 3.1.4.

2.3.4. Aerodynamic model

The aerodynamic model expresses the forces X, Y, Z and moments L, M, N acting on the aircraft in the body frame F_b as function of the nondimensionalised force and moments coefficients, dynamic pressure and characteristic length, as defined on Equation 2.2 [33, p. 36] [45, pp. 30–36]. The forces in the negative directions of the X_b and Z_b axes are closely related to the lift and drag via the orientation of the F_b with respect to the undistributed free stream. Performance parameters such as C_{D_0}, C_{D_α}, $C_{D_{\alpha^2}}$, C_{L_0}, C_{L_α} can therefore be determined from the identified aerodynamic derivatives.

$$\begin{aligned} X &= \frac{1}{2}\rho V^2 S C_X & Y &= \frac{1}{2}\rho V^2 S C_Y & Z &= \frac{1}{2}\rho V^2 S C_Z \\ L &= \frac{1}{2}\rho V^2 S b C_l & M &= \frac{1}{2}\rho V^2 S \bar{c} C_m & N &= \frac{1}{2}\rho V^2 S b C_n \end{aligned} \tag{2.2}$$

C_X, C_Y, C_Z and C_l, C_m, C_n are nondimensional force and moment coefficients, respectively. The nondimensional coefficients of the model can be dependent on a variety of effects, which is only limited by the scope of the model. A typical coefficient dependence can be expressed as $C_i = f\left(C_{i_a}, C_{i_p}, C_{i_t}\right)$ where the aerodynamic a, propulsive p and atmospheric turbulence t effects are included in the coefficient of degree of freedom i [5, p. 45]. The dependences of coefficient effects are further elaborated upon in Equation 2.3.4 and subsection 2.3.5. The complete definition of the aerodynamic model is presented in subsection 3.2.3.

Aerodynamic model structure

The dimensionless coefficients described in subsection 2.3.3 can be approximated with different types of functions of the measured independent variables characterising the flight conditions. The functional relationship should be decided upon when choosing the model structure, depending on the anticipated manoeuvres and measured variables. Options commonly used in aerospace parameter estimation problems (see section 2.5) are Taylor's series, univariate and multivariate splines, feed forward or radial basis function neural networks [75]. In most cases however, particularly during a first estimate of the coefficient derivatives, Taylor's series expansion about the independent variables guarantees a sufficient level of approximation [36, p. 52].

A dependence on first order of the independent variables only can be chosen, as done by [29, p. 102] [26] [51]. This results in an expression of the nondimensional coefficient as presented on the example of C_Z on Equation 2.3. This can be considered as a standard base model, in which the forces and moments are assumed to depend on the flow incidence angles α and β, dimensionless rotational rates variables $pb/2V$, $q\bar{c}/V$ and $rb/2V$ representing the effective curvature of the free stream flow field, and the control surface deflections δa, δe and δr, representing the variable part of the aircraft geometry [36, p. 52].

$$C_Z = C_{Z_0} + C_{Z_\alpha}\alpha + C_{Z_q}\frac{q\bar{c}}{V} + C_{Z_{\delta_e}}\delta_e \tag{2.3}$$

A quadratic dependence on selected state variables (usually only angle of attack α and sideslip β) can be chosen, as done by [40, p. 145] [25, pp. 5–6] [7, p. 9]. This results in an expression of the nondimensional coefficient as presented on the example of C_Z on Equation 2.4. The inclusion of the second power of the angle of attack can become useful for high amplitude manoeuvres, where the induced drag term, captured mostly by $C_{X_{\alpha^2}}$, becomes important [36]. Gerlach [25] argues that a polynomial estimation of degree two can be comparable to a polynomial including the first derivative of state variables.

$$C_Z = C_{Z_0} + C_{Z_\alpha}\alpha + C_{Z_{\alpha^2}}\alpha^2 + C_{Z_q}\frac{q\bar{c}}{V} + C_{Z_{\delta_e}}\delta_e \tag{2.4}$$

A dependence on first time derivatives of independent variables (usually only angle of attack α and sideslip β, other time derivatives are generally disregarded [21]) can be chosen, as done by [20, p. 31] [33, p. 50] [45, p. 31]. This results in an expression of the nondimensional coefficient as presented on the example of C_Z on Equation 2.5. Lombaerts [40] argues that using time derivative regressors (particularly $\dot{\alpha}$), although not used for modelling large civil airliners performing "benign manoeuvres with relatively small flight path angles", can be applicable for agile aircraft, such as the C337. First time derivatives of α and β tend to represent the time histories of the flow incidence angles [36].

$$C_Z = C_{Z_0} + C_{Z_\alpha}\alpha + C_{Z_{\dot{\alpha}}}\dot{\alpha} + C_{Z_q}\frac{q\bar{c}}{V} + C_{Z_{\delta_e}}\delta_e \tag{2.5}$$

An expression of the coefficient can be formulated as multivariate polynomial, cross coupling different state variables, as done by [24, p. 30]. This results in an expression of the nondimensional coefficient as presented on the example of C_Z on Equation 2.6.

$$C_Z = C_{Z_0} + C_{Z_\alpha}\alpha + C_{Z_\beta}\beta + C_{Z_q}\frac{q\bar{c}}{V} + C_{Z_{\delta_e}}\delta_e + C_{Z_{\alpha\beta}}\alpha\beta \tag{2.6}$$

A multivariate cubic dependence on selected state variables (again, usually angle of attack α and sideslip β, but also nondimensional dynamic pressure change due to propeller $\frac{\Delta p_t}{\frac{1}{2}\rho V^2}$) can be chosen, as done by [46] [5, p. 48] [67] [27]. This results in an expression of the nondimensional coefficient as presented on the example of C_Z on Equation 2.7.

$$C_Z = C_{Z_0} + C_{Z_{\Delta p_t}} \frac{\Delta p_t}{\frac{1}{2}\rho V^2} + C_{Z_\alpha}\alpha + C_{Z_{\alpha^2}}\alpha^2 + C_{Z_{\alpha^3}}\alpha^3 + \\ C_{Z_q}\frac{q\bar{c}}{V} + C_{Z_{\delta_e}}\delta_e + C_{Z_{\delta_e\beta^2}}\delta_e\beta^2 + C_{Z_{\delta_f}}\delta_f + C_{Z_{\alpha\delta_f}}\alpha\delta_f \tag{2.7}$$

V − h dependence
In order to increase the validity of determined aerodynamic and control derivatives on the full flight envelope, the effect of airspeed V and altitude h on their value can be studied. Adding C_{i_V} and C_{i_h} terms in the C_i equation can allow to address this problem, yet it adds onto the computational complexity of the parameter estimation process and is rarely done. Because of the expected limited nonlinearity of the coefficients dependence on he $V - h$ state-plane, the coefficients determined with the parameter estimation process can be regressed with respect to the airspeed and altitude [29].

2.3.5. Engine model

The necessity of estimating engine performance originates from the aircraft force and moment balance equations (see Equation A.5 and Equation A.13), as the engine is the main contributor in generating forces in the X_b body axis.

Mulder et al. [45, p. 30] proposes an integration of the propulsion effect at the level of aerodynamic model, where it is represented by a nondimensionalised contributor to dimensionless symmetrical forces C_X, C_Z and moment C_m under the form of nondimensionalised total pressure change across the propeller $\Delta p_t / \frac{1}{2}\rho V^2$, assuming that the propeller obeys the actuator disk theory. Further derivation allows to express the nondimensionalised change in total pressure over the propeller as $\eta_p P / \frac{1}{2} A_{eff} \rho V^3$, with A_{eff} being the effective propeller area and is further elaborated in subsection 3.2.4. Other authors [33, p. 36] tend to separate the thrust force contribution from the force balance along X_b, resulting in excluding it from the aerodynamic model. In this case, the thrust force is kept in the dimensional form.

2.4. Aircraft inertial characteristics

The moment of inertia characterises the aircraft resistance to change in orientation, whereas the centre of gravity defines its pivot point. The knowledge of both variables is key in a dynamical behaviour analysis and methods of their determination are addressed in this section.

2.4.1. Centre of gravity model

The longitudinal centre of gravity of the aircraft can be determined from the last Mass and Balance supplement (17.05.2022, FAA A&P 3289471) stating a $x_{c.g.,OEW}$ of 3.57 [m] (140.47 [in], given a datum defined 65 [in] in front of the firewall) for an OEW of 1,382 [kg] (3,047 [lbs]). The travel of $x_{c.g.}$ with loading configuration can be determined by summing the additional moments caused by fuel, passengers and cargo, determined from from the loading graph provided by the manufacturer [12], adding it to the moment around the datum point for an empty aircraft and subsequently dividing the total moment by total aircraft weight.

The vertical centre of gravity of the aircraft $z_{c.g.}$ can be determined by measuring the reaction force from each of the wheels at different aircraft pitching attitudes [57, p. 5]. The higher the difference in attitudes between the measurements, the more accurate the vertical centre of gravity determination. This measurement can also be used to confirm the expected longitudinal and lateral centre of gravity location $x_{c.g.}$ and $y_{c.g.}$, respectively. The determination of centre of gravity of the aircraft is presented in detail in the dedicated section 5.1.

2.4.2. Moment of inertia model

The knowledge of the inertial properties of the aircraft is necessary to describe its dynamic behaviour in flight, given that the inertia terms are present in the equations defining the forces and moments acting on the aircraft (see Equation 3.23 and Equation 3.24 of chapter 3). In a symmetrical aircraft, the I_{xy} and I_{yz} products of inertia terms are expected to be close to zero (see subsection 2.3.1), therefore, what is desired to be determined are the moments of inertia terms I_{xx}, I_{yy}, I_{zz} around the three body axes of the aircraft as well as product of inertia term I_{xz}. Attempts to obtain the inertial properties of the Cessna Skymaster from the manufacturer or maintenance service providers have been unsuccessful. However, several methods are available to estimate the moment of inertia of an aircraft, for which the accuracy of the moment of inertia usually increases with the time and effort spent. The choice and details of the approach chosen are described in the dedicated section 5.2 of chapter 5.

As a preliminary approach, the moments of inertia can be estimated empirically based on collected data of aircraft of similar mission and configuration [56]. The Roskam's Class I method for aircraft inertia estimation [59, pp. 17–21] relies on the assumption that "it is possible to identify a radius of gyration $R_{x,y,z}$ within each airplane category". $R_{x,y,z}$ is nondimenionalised by scaling it with aircraft length L, wingspan b or the combination thereof, which provides a better statistical match with aircraft weight. The method is unable to predict the product of inertia and remains a preliminary estimation of low accuracy. The non traditional configuration of the C337 can also make the use of empirical relations less applicable.

One way of determining the inertial properties of the aircraft is to measure it experimentally. This involves oscillating the aircraft and can be done by swinging it while suspended on a test rig [45, p. 157], as done for the TU Delft DHC-2 Beaver (see Figure 2.3) or spring loading on a fixed fulcrum [79], as done for the F-106A, or a combination of those [57], about the longitudinal, lateral and vertical axes.

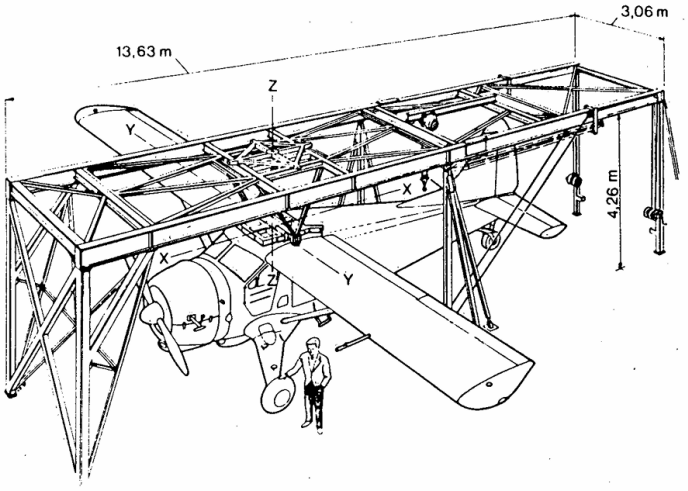

Figure 2.3: Rig for measurement the DHC-2 Beaver aircraft moments and products of inertia [45]

By measuring the oscillation frequency and knowing the moment arm between the aircraft centre of mass and axes of rotation as well as the spring stiffness (if used), the moment of inertia can be calculated. The product of inertia I_{xz} can be estimated by oscillating the aircraft in yaw at different pitch attitudes. At a roll to yaw ratio of zero, I_{xz} is zero, therefore the axis of oscillation must be a principal axis. The pitch angle at which the roll to yaw ratio vanishes is the inclination of the principal axis, from which an analytical expression for the I_{xz} can be determined [69, p. 10]. Although providing accurate results, the experimental method is time consuming and has been estimated to cost around 7,400 man hours in the case of the F-106A [79], while introducing the risk of damaging the aircraft. The presence of fuel in the tanks and its sloshing during oscillation can also affect the validity of the measurement [57].

The inertial properties of the aircraft can be determined from flight test, as described by [42]. The process follows the same logic as in the case for determining the control and aerodynamic derivatives. This can seem to yield this approach inapplicable as the control and aerodynamic derivatives themselves

are necessary to identify the inertial constants, while inertial constants are necessary in the coefficient identification process. However, the DATCOM tool (see subsection 2.5.2, [53]) could be used to determine preliminary aerodynamic and control derivatives [6]. With the DATCOM estimated derivatives, flight tests can be performed, inducing small deviations from trimmed conditions to allow linearisation of the equations of motion, yet with large amplitude changes in roll rate and analyse the data using the pitch and roll equation only [42, p. 6]. Once the inertial properties are determined, the accuracy of coefficient estimation can be improved by performing dedicated flight tests and parameter estimation. Given the mutual dependency of aerodynamic and control derivatives and inertial characteristics of the aircraft in the equations of motion, this approach can lead to inaccurate results, particularly given that the applicability of the DATCOM tool to the C337 is not certain.

The aircraft inertia can also be computed analytically from available knowledge of its geometry and mass distribution. One approach of doing this is the lumped masses approach, which involves representing the aircraft by a series of distributed point masses that can be evaluated with respect to the aircraft centre of mass. A CAD software can support this approach as described by [56], at the cost of requiring a detailed weight and centre of gravity breakdown of the aircraft. Laham [37] simplifies this approach by allocating fractions of total weight of the aircraft to individual subsystems based on statistics derived from empirical data and calculating their centroids assuming their simplified geometry. Moutlon's method is similar [43] - the aircraft is decomposed into large sections approximated as ideal geometrical figures with readily available solutions for piece wise moments of inertia. [22] adds in an empirical scaling factor to each of the major systems moment of inertia to account for the difference between idealised and real system shape. Within this group of methods, depending on the assumptions made, the error can reach 20% for a constant density wing assumption, or 1-2% for neglecting airfoil camber [43, p. 28].

2.5. Aircraft system identification

The aircraft system identification process is the subsequent step after the choice of the mathematical model, as shown on the block diagram on Figure 2.4 [33, p. 21] [75]. The key phases of the identification process are elaborated upon in this section.

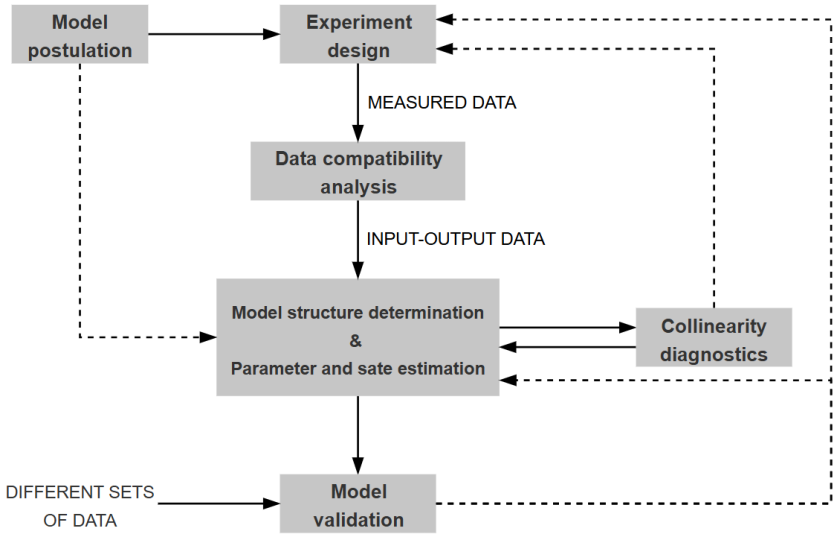

Figure 2.4: Block diagram of aircraft system identification, based on [33, p. 20]

2.5.1. Experiment design

The experiment design follows a postulation of the mathematical model, which is based on an a priori knowledge of the aircraft. Naturally, at this stage the model is incomplete, as the parameter estimation has not been completed yet. The postulated model helps to define the data to be collected, and therefore the form of the experiment itself.

The experiment design phase includes the flight test design and execution, data logging and pre-processing. Before the flight test, the input and output variables should be decided upon. The input variables are usually sources of aircraft excitation - the powerplant controls as well as control surface deflection controls. The output variables are what is being measured with the Flight Testing Intrumentation (FTI) or standard aircraft instruments and usually include the magnitude and direction of air-relative velocity, body rotational rates and translational accelerations, Euler attitude angles and any variables defining the flight conditions [33].

Flight test data acquisition
The flight test data acquisition of the N4207X aircraft can be realised from three main monitoring systems:

- The Garmin avionics including the GTN750 with G500 TXi display, from which measured parameters can be extracted via the arinc. Parameters recorded and used in this study are listed on Table 4.13 of chapter 4.
- The Levil Aviation Broadcasting Outer Module (BOM), an autonomous, wireless aerodynamic pod mounted under the aircraft wing powered by its integrated air flow turbine. Its avionics include WAAS GPS, ADS-B and AHRS, but also air data, dimensionless angle of attack and temperature measurements thanks to integrated pitot tube and static ports [16]. Pictures of the BOM installed under the aircraft wing can be found in Appendix C.
- The Electronics International MVP-50P engine monitor, which is a system comprising of measuring probes connected to an Engine Data Converter (EDC). The EDC processes raw data and computes additional parameters (such as engine power or differential pressure, depending on available measurement), which are sent to a display in the cockpit [50]. The used parameters measured by the engine monitor are listed in Table 4.13.

Control surface deflection
The aforementioned flight test intrumentation does not provide data on the pilot aerodynamic input control - the control surface deflections. In order to fill this measurement gap, a simple, yet reliable and safe method has to be proposed.

Several methods can be considered in order to record the control surface deflections of the aircraft. The most common ones include the use of servo-mechanical sensors on the control mechanism, such as in the case of the Cessna Citation faculty research aircraft, or an electro-hydraulic control system recording the input of an actuator induced signal, as in the case of the DHC-2 Beaver faculty research aircraft [45]. Although the installation of servo-mechanical sensors is anticipated on the Skymaster in future, it is not available at the time of the study. Table 2.1 lists other considered methods of control surface deflection and presents their major advantages and disadvantages.

Table 2.1: Pros and cons of considered control surface deflection measurement methods

Method	Advantages	Disadvantages
Mechanical protractors, rulers	Inexpensive, simple	Inaccurate, not recorded
Digital protractors, inclinometers	Repetitive, simple	Alignment errors, intrusive, not recorded
Laser tracking	High accuracy	Expensive, high setup time, potentially intrusive
Optical motion capture	Nonintrusive, multiple control surface recorded simultaneously	Expensive in time and calibration efforts
String potentiometers	Simple, accurate, recorded	Intrusive, prone to wear
Inertial Measurement Units	Nonintrusive, self contained, recorded	Prone to drift, if uncorrected

From the methods listed on Table 2.1, a combination of string potentiometers, IMU and mechanical indications is chosen and used in this study. This choice is made as compromise between simplicity,

accuracy, intrusivity, time expense and availability of equipment. The method is said to be a combination of three, as it includes elements inspired from multiple of the approaches presented.

In order to obtain the control surface deflection input signal in time, IMU sensors can be coupled with a pulley, inducing the rotational motion of the IMU with the help of a spring loaded string attached to the steering column and pedals as they change position. This approach is a combination of the IMU and string potentiometer method and allows to reduce the IMU drift by translating the translational motion of the steering column and pedals into a rotation of the sensor. The details of the developed method are presented in the dedicated chapter 4 and illustrations can be found in Appendix C.

Flight testing
The flight testing envelope should be designed in a way to cover the anticipated flight envelope of the aircraft model. Although estimated correlations can be extrapolated or interpolated, the measured data remains valid only at the specific flight conditions at which it has been acquired. In order to isolate the influence of, for example, airspeed V or altitude h on the measured aircraft state, it is common practice to vary only one of these parameters at a time [67] [29]. As an example, this would imply testing for airspeeds V_1, V_2, V_3, ... at altitude h_1, subsequently climbing to altitude h_2 and testing for the same range of airspeeds V_1, V_2, V_3, ... and so on.

Commonly used control surface signals used to excite the aircraft include [45, pp. 210–211] [47, pp. 104–110] [23]:

The **doublet input signal** consists of two consecutive step-like inputs of length $2\Delta t$, switching between signal amplitude $+\Delta a$ and $-\Delta a$ at time Δt and back to zero at $2\Delta t$. It is one of the most widely used signals for lateral and longitudinal excitations via all primary control surfaces (elevator, ailerons and rudder). It excites the short period motion appropriately while suppressing the phugoid motion.

The **pulse input signal** consists of a smooth, but fairly rapid surface deflection (step-like) followed by a return to trim position, which can also be defined as half of the doublet input. The pulse input can also be used to excite the short period, yet it tends to induce a phugoid mode. The attitude post signal is expected to be different from trim and return to it original state only after the phugoid motion is fully damped.

The **3211 input signal** consists of a series of oscillating control surface deflections, with usually two peaks at either deflection side. Given a signal length of $7\Delta t$, the switching times are $t = 3\Delta t$, $t = 5\Delta t$ and $t = 6\Delta t$, giving the name of 3211.

The **Mehra, Shulz and DUT input signals** can be described by a set of weighted sine functions and are results of optimising the input signal in order to maximise the parameter estimation accuracy.

In a TU Delft DHC-2 Beaver flight test campaign, the lateral doublet and longitudinal 3211 manoeuvres have been found to result in higher parameter estimation accuracies compared to DUT manoeuvres [33, p. 234].

Once the flight test data has been collected, it shall be pre-processed to facilitate further post-processing. This can include choosing a common sampling frequency, which should be high enough to distinguish the dynamic aircraft behaviour, but also consider the computational limitation of processing hardware. Clear outliers, glitches or noise should be eliminated, yet the available methodology for this process is further described in subsection 2.5.2. Flight testing and data pre-processing is described in the dictated section 4.4 of chapter 4.

2.5.2. State and parameter estimation

Before the state estimation, a data compatibility analysis can be applied to measured aircraft responses to verify data accuracy, which could be affected by instrumentation errors. The procedure includes comparing measured aircraft responses to responses reconstructed with estimation based on known rigid-body kinematics with the aim to estimate the systematic instrumentation errors [33, p. 22] [40, p. 98]. In this study, no dedicated data compatibility analysis is performed, rather a Kalman filter is used to reconstruct the flight path.

The data compatibility can be followed by a model structure determination , which is nothing else but selecting an appropriate form of the mathematical model, as addressed in Equation 2.3.4. While the

model should address the principle of parsimony in order to retain appropriate prediction capability, it should still adequately represent the physical phenomena [42, p. 22].

The parameter and state estimation are the main part of the aircraft system identification process. Most of the methods used can be classified as the equation error or output error methods. The equation error approach uses the ordinary least-squares principle based on linear regression. The desired aerodynamic and control derivatives are estimated by minimising the sum of squared differences between measured and simulated aerodynamic forces and moments. Linear regression constitutes a linear estimation problem, meaning that the model output is linearly dependent on the model parameters. On the other hand, in the output error method, the desired coefficients are obtained by minimising the sum of weighted square differences between measured and modelled outputs. The problem becomes nonlinear as the unknown coefficients appear in the equations of motion, integrated to compute the aircraft state. Outputs are computed from the states, controls and parameters using the output equations, thus making it an iterative nonlinear estimation problem [33, p. 22].

Kalman filters

Any random external disturbances acting on the aircraft during measurements, such as turbulence, make the model stochastic (cause model noise), in addition to the sensor noise, imposing the need to estimate the state before estimating the parameters. Another motivation of state reconstruction includes the impossibility to directly measure a state or improvement of its accuracy by combining different sensors (sensor fusion) [75]. The Kalman filters can be used for this purpose and a full description of the their application in this study is presented in the dedicated section 3.1 of chapter 3.

The Kalman Filter (KF) working principle is based on the calculation of a weighted average between measured and predicted state, where the weight, called Kalman gain, defines which value, between the measurement and prediction, has a higher influence on the estimated state. In the simplest, linear form, the KF consists of five steps, in which the first two are a prediction of the state measurement and its error covariance based on previous step. A more detailed mathematical formulation of Kalman filters is presented in subsection 3.1.1.

The Kalman Filter, although simple and with low computational cost, is valid for linear systems only. The system model has to be known and fully observable, so have to be the noise statistics, under the assumption of Gaussian noise distribution. In order to lift the linearity assumption, the Kalman Filter can be Extended (EKF), allowing for estimation of the state vector of nonlinear systems. An additional step is introduced after the state measurement prediction, namely the calculation of Jacobians of state transition and observation equation, at the cost of increased the computational cost. The nonlinear state observation equations are also linearised about their nominal values using a first order Taylor expansion, which limits the EKF application to functions that can be linearised locally. Due to this first order approximation, the EKF also does not guarantee a global convergence to optimal solution [75]. Its mathematical formulation is elaborated upon in subsection 3.1.2.

In order to increase the accuracy of the EKF, an Iterated EKF (IEKF) can be chosen, which introduces a three step iterative algorithm after computing the error covariance prediction. The iterative loop recalculates the Jacobian of the measurement equation and the Kalman gain and updates the measurement and state estimation. The IEKF is more computationally expensive compared to the EKF, while still locally linearises the state observation equations. It is semi-optimal for nonlinear systems [75] and described in more detail in subsection 3.1.3.

The Unscented Kalman Filter (UKF) [31], aims at eliminating the drawbacks of IEKF and EKF by proposing a solution applicable to nonlinear systems. Instead of locally linearising the state observation equations, the UKF approximate the probability distribution. This is done by selecting a set of sample points (so called sigma points) such that their mean and covariance are the same as the probability distribution. The sigma points are then propagated through the nonlinear system model to calculate the statistical characteristics of the Gaussian distribution, subsequently used to compute the updated state estimate [41] [29].

The EKF and IEKF remain the most widely used method for state estimation of nonlinear aircraft models [9], despite their local linearisation, and have successfully been implemented, as exemplified by

[60]. Some argue for a slight superiority of UKF over IEKF in terms of computational efficiency and theoretical prospects of both classes [29], even though the accuracy is comparable.

The parameter estimation is a subsequent problem of finding values of unknown system parameters, given a known state measurement. In aerospace applications, the least squares [29] [63] and maximum likelihood approaches [39] [13] [35] are among the most popular. The former aims at minimising the cost function, which relates to finding values of parameters such that the difference between measured data and data derived from the model solution is minimum. The latter method attempts to chose model parameters such that the model output matches the most likely output values measured [75].

Least Squares estimator
The ordinary least squares approach (OLS) assumes that the dependent variable signal is a linear combination of independent variable signals, which allows the so called linear in parameter function to be expressed as $\mathbf{A}(\mathbf{x}) \cdot \theta$, with the regression matrix $\mathbf{A}$ and parameter vector θ. In order to guarantee a global minimum of the linear regression residual, a convex quadratic cost function can be formulated, the minimum of which provides the solution to the optimisation problem becomes. The full description of the OLS used in this study is presented in the dedicated subsection 3.2.1.

The OLS estimator is limited to linear in parameter model functions, for which it is true that $\frac{\partial p(x,\theta)}{\partial \theta} = f(x)$, and assumes that the regression residual has a constant variance for all measurements, is uncorrelated and has zero mean. With different distribution of noise for different measurements, the parameters can vary from one identification data sample to another, which is a drawback of the method [40][75].

If the noise covariance matrix is not constant in time, the accuracy of the OLS can be greatly improved with a weighted least squares approach (WLS) or generalised least squares (GLS), which remove the time varying noise dependency of the parameters by implementing weights. The challenge remains to determine the covariance matrix which is often unknown [32] [29].

Maximum Likelihood
In the presence of non uncorrelated zero mean noise and state noise, the maximum likelihood (ML) approach offers a solution. The method only assumes that the measurement depends in some way on an unknown parameter θ. θ is estimated based on what measurements $\mathbf{y}$ are most likely to occur, which is translated into maximising a likelihood function - a probability density function f_0 of the measurement $\mathbf{y}$, given the parameter θ: $f_0(\mathbf{y}|\theta_0)$. If all the measurements are of the same distribution class, the Bayes rule allows to formulate the likelihood function $L(\mathbf{y}|\theta)$ as shown on Equation 2.8.

$$f(y(1), y(2), ..., y(N)|\theta) = f(y(1)|\theta) \cdot f(y(2)|\theta) \cdot ... \cdot f(y(N)|\theta) = \prod_{i=1}^{N} f(y(i)|\theta) = L(y|\theta) \tag{2.8}$$

The solution to the optimisation problem becomes $\hat{\theta} = \arg\max L(\mathbf{y}|\theta)$. It can be further derived [75] [32] that $\hat{\theta}_{ML} = \arg\max \left(\ln (2\pi)^{N/2} |\Sigma(\theta)|^{0.5} + 0.5(\mathbf{y} - \mathbf{A}(\mathbf{x}) \cdot \theta)^T \Sigma(\theta)^{-1} (\mathbf{y} - \mathbf{A}(\mathbf{x}) \cdot \theta) \right)$, where $\Sigma(\theta)$ is the residual covariance matrix that needs to be known a priori. The ML parameter estimates are characterised by being asymptotically unbiased (for dynamic system), consistent, asymptotically efficient and normal [33, pp. 190–191].

Two Step method
The Two Step method structures the system identification in two separate steps. First, the state is estimated in the flight path reconstruction process which consists of the application of a Kalman filter onto the noisy flight test data measurements in combination with kinematic aircraft relations with the aim to reconstruct the actual trajectory and filter out measurement noise. Subsequently, a least squares method is employed in the parameter estimation process to determine the aircraft aerodynamic coefficients [49].

The Two Step method does not suffer from the single step methods convergence problems caused by a large number of unknown parameters. This constitutes a significant advantage of the Two Step method, which has been implemented in many system identification problems, as given by the examples [60] [40] [29] [55]. The Two Step method in the context of the present study is further elaborated upon in the dedicated chapter 3.

Alternative approaches
As elaborated upon in [78], neural networks offer an alternative for aerodynamic model identification, having the advantage of not defining the internal structure of the model and allowing for an unconstrained learning of dependencies between input and output. The main outlined disadvantage is the recency effect, which can be described as forgetting the knowledge based on past input - output dependencies, if that relation is not shown in recent input - output pairs [40, p. 125].

The use of splines can be an alternative to the usual polynomial structure widely used in aerodynamic models. Polynomials have a limiting approximation capability, proportional to their degree and, according to Runge's phenomenon, a polynomial approximating a function on fixed domain, oscillates towards its high end [75]. This requires an adaptation of the flight test excitation signals with the aim of reducing the dimensional couplings. It is in contrast with the goal of the aerodynamic model, which would gain in scope by performing long and large amplitude manoeuvrers that cover larger portions of the flight envelope [40, pp. 126–127]. Splines allow to divide the domain into subdomains, in which a fit of lower degree is performed, allowing to circumvent Runge's phenomenon. Multiple variations of the spline method, including multivariate, simplex or adaptive splines [76] [74] [73] have been developed and successfully implemented in aircraft parameter estimation problems.

DATCOM
As an alternative to system identification based on flight test data as addressed before, the aerodynamic derivatives can be calculated with analytical methods proposed by the U.S. Air Force (USAF) DATCOM. Its numerical implementation into a Fortran program in 1976 resulted in the creation of Digital DATCOM providing static stability, high-lift and control device, and dynamic-derivative characteristics of aircraft and aimed to reduce workload and costs at preliminary aircraft design stage. The aircraft is modelled by individual modules that define the body, wing, vertical, and horizontal tail. The effects of propulsion, high lift and control surfaces can be included as well as a twin vertical tail or fins. Although remaining a powerful tool, the Digital DATCOM applicability for the C337 is limited due to the unconventional configuration of the aircraft. Limitations of the program specific to the C337 are listed below, while the full documentation is provided in [53].

1. The model structure is limited to basic derivatives, excluding some of the cross coupling dynamic and control terms.
2. The body is defined as an array of fuselage cross sectional area and circumference values along the longitudinal axis. Due to internal program memory restrictions, the array length is limited to 20, whereas a single line entry to 80 characters, which negatively affects the precision of fuselage definition. Moreover, the method does not provide means of differentiating between the C337 fuselage and tail booms.
3. A single airfoil definition can be attributed to each lifting surface, which does not allow to accurately represent the C337 wing.
4. The vertical tail module is located in the XZ_b plane by default. It is therefore replaced by the twin vertical panel module, the airfoil of which however, cannot be specified. As a result, the asymmetrical rolling and yawing derivatives are not computed.
5. The contribution of two propellers can only be specified assuming their common location along the X_b axis and different location along the Y_b axis. This is not the case for the C337, thus the propeller contribution is not defined. The program models the propulsion to only affect the longitudinal stability derivatives.

The aforementioned limitations are considered to be too significant to treat the Digital DATCOM results as meaningful comparison to the ones obtained from flight test system identification. Nevertheless, an input file assuming a tail-boom-less fuselage, no propeller contribution, constant NACA2412 wing

airfoil and flat twin vertical tail panel is generated (see section E.2) and run at flight conditions recorded during flight testing. Applicable results are shown in section E.1 of Appendix E together with the full Digital DATCOM output file in section E.3.

2.5.3. Model validation

Given an available flight test data set, a part of it can be used for the aircraft system identification, yet some should be kept for model validation. Since validation should not be performed with data used in the parameter identification, available flight test data should be split into identification and validation datasets, with the validation dataset size not exceeding the identification dataset size, as presented in section 4.4. The validation dataset should be similar to the identification one and contain sufficient dynamics to uncover potential model limitations [75]. The complete model can be fed with flight test data measured inputs and compared with measured outputs. This is done in the dedicated section 7.1 of chapter 7. The statistical characteristics of estimated parameters such as mean, minimum and maximum of the parameter and its variance should be reported as done by [29], while the assumptions of the employed methods should be confirmed.

3

System Identification

System identification is the process of creating a mathematical model of a physical system from the relation of its input to output. In this report, the system identification is performed with the Two Step method which separates the process into two independent steps: flight path reconstruction, introduced in section 3.1, and parameter identification, elaborated upon in section 3.2. The structure of the Two Step method is shown in form of a block diagram on Figure 3.1.

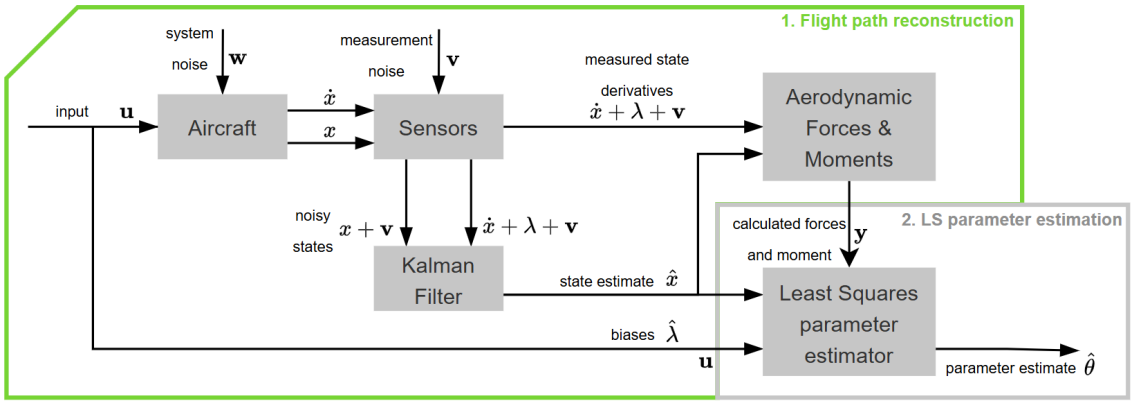

Figure 3.1: Block diagram illustrating the Two Step Method process, based on [75]

3.1. Flight path reconstruction

The flight path reconstruction is the first part of the Two Step method and aims at eliminating any noise and bias from the measurements, later used in the parameter identification phase. The significance of this step lies in assuring that the developed mathematical model describes the actual physical system, rather that its noisy or biased version of it. The flight path reconstruction therefore consists of reconstructing the original sequence of noiseless and unbiased states as function of time, given a series of measurements which, in the case of this study, are taken in flight.

A Kalman filter is developed and used for the flight path reconstruction of this Cessna Skymster system identification. Given the nonlinearlity of the navigation model implemented in the filer, the extended (EKF) and iterated extended (IEKF) versions of the Kalman filter are developed and their performance compared. The following section elaborates on the principles of the Kalman filter, starting with the concept of linear filters (KF, subsection 3.1.1) and expanding onto the working principle of EKF (subsection 3.1.2) and IEKF (subsection 3.1.3). The structure of the applied filters is explained stating the state, input and measurement vectors, as well as the navigation model equations. Finally the state observability is discussed to assess the Kalman filter convergence, given the available measurements.

The numerical implementation of the flight path reconstruction is done in files `part2_EKF.m` and `part2_IEKF.m`, as described in Appendix D.

3.1.1. Basic Kalman Filter (KF)

The basic linear Kalman filter is based on a set of linear, stochastic differential equations describing a time varying state-space model [75] [29]:

$$\begin{aligned} \mathbf{x}(t) &= \mathbf{F}(t)\mathbf{x}(t) + \mathbf{B}(t)\mathbf{u}(t) + \mathbf{G}(t)\mathbf{w}(t), \quad \mathbf{x}(t_0) = \mathbf{x_0} \\ \mathbf{z}(t) &= \mathbf{H}(t)\mathbf{x}(t) + \mathbf{D}(t)\mathbf{u}(t) + \mathbf{v}(t) \\ \mathbf{z_m}(t_k) &= \mathbf{z}(t_k) + \mathbf{v}(t_k), \qquad k = 1, 2, ... \end{aligned} \tag{3.1}$$

Where $\mathbf{x}(t)$ is the state vector, $\mathbf{u}(t)$ is the input vector, $\mathbf{z}(t)$ is the measurement or observation vector, $\mathbf{w}(t)$ is the system noise (or process noise due to, for example, turbulence) and $\mathbf{v}(t)$ is the measurement noise (or output noise due to, for example, sensor imperfections). The vector dependencies are governed by the system matrix $\mathbf{F}(t)$, input matrix $\mathbf{B}(t)$, system noise input matrix $\mathbf{G}(t)$, observation matrix $\mathbf{H}(t)$ and feed forward matrix $\mathbf{D}(t)$. The initial state of the state space model in Equation 3.1 is given by $\mathbf{x}(t_0) = \mathbf{x_0}$ and has a known mean value $\mu_0 = \mathbb{E}\{\mathbf{x}_0\}$ and covariance matrix $\mathbf{P}_0 = \mathbb{E}\{(\mathbf{x}_0 - \mu_0)(\mathbf{x}_0 - \mu_0)^\intercal\}$. Even though the initial state $\mathbf{x}_0$ and covariance matrix $\mathbf{P}_0$ should be provided, they can be chosen arbitrarily, with the latter being chosen sufficiently large for initial estimation. For numerical application, the system matrix $\mathbf{F}(t)$, input matrix $\mathbf{B}(t)$ and noise input matrix $\mathbf{G}(t)$ can be discretised into matrices $\mathbf{\Phi}(t_k)$, $\mathbf{\Psi}(t_k)$ and $\mathbf{\Gamma}(t_k)$, respectively.

The linear time varying state-space model defined by Equation 3.1 can be generalised to the expression of Equation 3.2, applicable to nonlinear cases, such as the one in this study. Equation 3.1 also assumes a purely additive system noise, while in reality it can be propagated through the system dynamics. The set of nonlinear, stochastic differential equations describing a time varying state-space model is therefore stated as [75] [29]:

$$\begin{aligned} \mathbf{x}(t) &= \mathbf{f}[\mathbf{x}(t), \mathbf{u}(t), t] + \mathbf{G}(\mathbf{x}(t), t)\mathbf{w}(t) \\ \mathbf{z}(t) &= \mathbf{h}[\mathbf{x}(t), \mathbf{u}(t), t] \\ \mathbf{z_m}(t_k) &= \mathbf{z}(t_k) + \mathbf{v}(t_k) \qquad k = 1, 2, ... \end{aligned} \tag{3.2}$$

Where $\mathbf{f}[\cdot]$ is the nonlinear state transition function and $\mathbf{h}[\cdot]$ the nonlinear measurement function, both assumed continuous and differentiable with respect to all elements of $\mathbf{x}$ and $\mathbf{u}$. In addition, the system noise $\mathbf{w}$ and measurement noise $\mathbf{v}$ are both assumed to be zero mean white ($\mathbb{E}\{\mathbf{w}(t)\} = \mathbb{E}\{\mathbf{v}(t)\} = 0$) and uncorrelated ($\mathbb{E}\{\mathbf{w}\mathbf{v}^\intercal\} = 0$). Their covariances are defined as follows:

$$\mathbb{E}\{\mathbf{w}\mathbf{w}^\intercal\} = \mathbf{R} \qquad\qquad \mathbb{E}\{\mathbf{v}\mathbf{v}^\intercal\} = \mathbf{Q} \tag{3.3}$$

Where $\mathbf{Q}$ and $\mathbf{R}$ are defined as diagonal matrices filled with system and measurement noise squared standard deviations σ^2, respectively. These noise statistics have to be known and can be determined from sensor calibration or stationary measurements.

The purpose of a Kalman filter is to determine a value of a parameter that cannot be measured directly, given a noise or biased measurement and an a priori known model predicting the measurement value. Figure 3.2 gives an overview of the working principle of a general Kalman filter, which can be decomposed into five steps:

1.0. The one-step-ahead prediction of the state $\hat{\mathbf{x}}_{k+1,k}$ is computed with the internal model:

$$\hat{\mathbf{x}}_{k+1,k} = \Phi_{k+1,k}\mathbf{x}_{k,k} + \Psi_{k+1,k}\mathbf{u}_k, \qquad \hat{\mathbf{x}}_{0,0} = \hat{\mathbf{x}}_0$$

2.0. The covariance matrix of state prediction error $\mathbf{P}_{k+1,k}$ is computed by comparing the prediction with the actual measurement:

$$\mathbf{P}_{k+1,k} = \Phi_{k+1,k}\mathbf{P}_{k,k}\Phi_{k+1,k}^\intercal + \mathbf{\Gamma}_{k+1,k}\mathbf{Q}_{k,k}\mathbf{\Gamma}_{k+1,k}^\intercal \qquad \mathbf{P}_{0,0} = \mathbf{P}_0$$

3.0. The Kalman gain one step ahead K_{k+1} is computed:

$$K_{k+1} = \mathbf{P}_{k+1,k}\mathbf{H}_{k+1}^\intercal(\mathbf{H_{k+1}}\mathbf{P_{k+1,k}}\mathbf{H_{k+1}^\intercal} + \mathbf{R})^{-1}$$

4.0. The one-step-ahead optimal state estimation $\hat{\mathbf{x}}_{k+1,k+1}$ is computed, also allowing to update the measurement:

$$\hat{\mathbf{x}}_{k+1,k+1} = \hat{\mathbf{x}}_{k+1,k} + K_{k+1}(\mathbf{z}_{k+1} - \mathbf{H}_{k+1}\hat{\mathbf{x}}_{k+1,k})$$

5.0. The covariance matrix of state estimation error $\mathbf{P}_{k+1,k+1}$ is computed:

$$\mathbf{P}_{k+1,k+1} = (\mathbf{I} - K_{k+1}\mathbf{H}_{k+1})\mathbf{P}_{k+1,k}$$

As the filter advances along the measurements in time t_k, the steps are repeated for each step k.

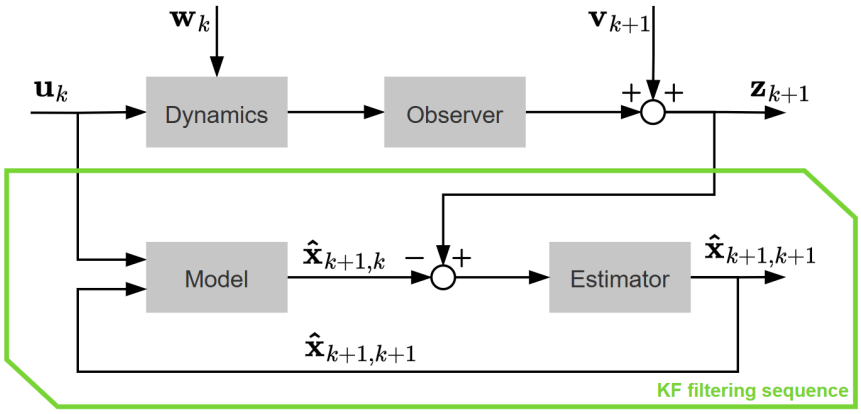

Figure 3.2: Overview of the general Kalman filter sequence, based on [29]

3.1.2. Extended Kalman Filter (EKF)

The Extended Kalman Filter allows for treating nonlinear state space models, however it does not guarantee convergence to optimal solution [75]. This is due to the linearisation around nominal values $\mathbf{x}^*(t)$ and $\mathbf{u}^*(t)$ performed inside the EKF and use of first order approximation only, limiting performance to small perturbations of the state vector. The extension of the EKF, compared to the linear KF, involves two additional steps performed after the one-step-ahead prediction, here defined for nonlinear systems:

1.0. The one-step-ahead prediction of the state $\hat{\mathbf{x}}_{k+1,k}$ is computed with the internal model:

$$\hat{\mathbf{x}}_{k+1,k} = \hat{\mathbf{x}}_{k,k} + \int_{t_k}^{t_{k+1}} \mathbf{f}(\hat{\mathbf{x}}_{k,k}, \mathbf{u}_k^*, t)dt$$

1.1. The linearisation is performed by computing the Jacobians of $\mathbf{f}$ and $\mathbf{h}$ to obtain $\mathbf{F_x}$ and $\mathbf{H_x}$, respectively:

$$\mathbf{F_x}(\mathbf{x}^*(t), \mathbf{u}^*(t), t) = \frac{\partial}{\partial \mathbf{x}}\mathbf{f}\left(\mathbf{x}(t), \mathbf{u}(t), t\right), \quad \mathbf{H_x}(\mathbf{x}^*(t), \mathbf{u}^*(t), t) = \frac{\partial}{\partial \mathbf{x}}\mathbf{h}\left(\mathbf{x}(t), \mathbf{u}(t), t\right)$$

1.2. The discretisation of state transition and input matrices into $\mathbf{\Phi}_{k+1,k}(\mathbf{x}^*(t), \mathbf{u}^*(t), t)$ and $\mathbf{\Gamma}_{k+1,k}(\mathbf{x}^*(t), \mathbf{u}^*(t), t)$, respectively.

Steps from 2.0 to 5.0 are common to both filters.

3.1.3. Iterated Extended Kalman Filter (IEKF)

The Iterated Extended Kalman Filter attempts to improve the convergence of the EKF using local iterations through measurement update steps [75]. The use of local iterations ensures improved accuracy of linearisation using updated states. Steps 1.0 to 2.0 are common to EKF and IEKF. The local iteration loop is performed after step 2.0 and before step 5.0, replacing 3.0 and 4.0:

3.0. The measurement equation Jacobian is recalculated:

$$\mathbf{H}_{\mathbf{x}}(\eta_i) = \frac{\partial}{\partial \mathbf{x}} \mathbf{h}(\eta_i, \mathbf{u}(t), t)$$

3.1. The Kalman gain $K_{k+1}(\eta_i)$ is recalculated:

$$K_{k+1}\left(\eta_i\right) = \mathbf{P}_{k+1,k}(\mathbf{x}^*(t), \mathbf{u}^*(t), t)\mathbf{H}_{\mathbf{x}}{}^{\intercal}\left(\eta_i\right)\left[\mathbf{H}_{\mathbf{x}}\left(\eta_i\right)\mathbf{P}_{k+1,k}(\mathbf{x}^*(t), \mathbf{u}^*(t), t)\mathbf{H}_x^{\intercal}\left(\eta_i\right) + \mathbf{R}_{k+1}\right]^{-1}$$

3.2. The measurement and state estimate are updated:

$$\eta_{i+1} = \hat{\mathbf{x}}_{k+1,k} + K_{k+1}(\eta_i)\left(\mathbf{z}_{k+1} - \mathbf{h}(\eta_i, \mathbf{u}_{k+1}) - \mathbf{H}_{\mathbf{x}}(\eta_i)(\hat{\mathbf{x}}_{k+1,k} - \eta_i)\right), \quad \hat{\mathbf{x}}_{k+1,k+1} = \eta_1$$

where η_i is defined as an iterator equal to the perturbed nominal state $\mathbf{x}^*_{k+1}$.

3.1.4. Kinematic and navigation models

The described EKF and IEKF are integrated into a kinematic model and navigation (or observation) model which together allow to reconstruct the aircraft flight path. The models assume a state vector $\mathbf{x}$ comprising of the aircraft position in the flat earth navigation frame F_E, body velocity components expressed in the frame F_b and the attitude expressed as Euler angles. The state vector is augmented by a bias vector λ comprised of the bias terms of the linear body accelerations and rotational rates measured by the IMU as well as the wind velocity in F_E, all of which are to be estimated by in the flight path reconstruction process. Together, the state and bias vector form an augmented state vector $\mathbf{x_{aug}}$, as defined by Equation 3.4.

$$\begin{gathered}\mathbf{x} = \begin{bmatrix} x_E & y_E & z_E & u & v & w & \phi & \theta & \psi \end{bmatrix} \qquad \lambda = \begin{bmatrix} W_{x_E} & W_{y_E} & W_{z_E} & \lambda_x & \lambda_y & \lambda_z & \lambda_p & \lambda_q & \lambda_r \end{bmatrix} \\ \mathbf{x_{aug}} = \begin{bmatrix} \mathbf{x} & \lambda \end{bmatrix}^{\intercal}\end{gathered} \tag{3.4}$$

The input vector is defined on Equation 3.5 and comprises of linear accelerations and rotational rates measured in the body frame F_b by the onboard IMU. It is assumed that the measured accelerations and rotational rates are biased and have white measurement noise w, the former of which is estimated in the augmented part of the state vector and the noise statistics for the latter are known.

$$\begin{gathered}\mathbf{u_m} = \begin{bmatrix} A_{x_m} & A_{y_m} & A_{z_m} & p_m & q_m & r_m \end{bmatrix}^{\intercal} \\ A_{x_m} = A_x + \lambda_x + w_x \\ A_{y_m} = A_y + \lambda_y + w_y \\ A_{z_m} = A_z + \lambda_z + w_z \\ p_m = p + \lambda_p + w_p \\ q_m = q + \lambda_q + w_q \\ r_m = r + \lambda_r + w_r\end{gathered} \tag{3.5}$$

The measurement vector comprises of the aircraft position and velocity components in the F_E frame as measured by the GPS, the attitude expressed as Euler angles as well as air data, namely the measured true airspeed V_m, angle of attack α_m and angle of sideslip β_m, as given by Equation 3.6.

$$\mathbf{z_m} = \begin{bmatrix} x_{GPS_m} & y_{GPS_m} & z_{GPS_m} & u_{GPS_m} & v_{GPS_m} & w_{GPS_m} & \phi_{GPS_m} & \theta_{GPS_m} & \psi_{GPS_m} & V_m \\ \alpha_m & \beta_m \end{bmatrix}^{\intercal} \tag{3.6}$$

The kinematic model expressing the first derivative of the state vector $\mathbf{x_{aug}}$ variables with respect to time is expressed by Equation 3.7, the derivation of which is presented in section A.3 and section A.4 of Appendix A. The kinematic model constitutes the heart of the state transition function $\mathbf{f}[\cdot]$. Given that the augmented part of state vector is composed of constant bias terms, the time derivative of λ is zero. The integration of the kinematic model with respect to time is performed with Runge-Kutta scheme of order four, as defined by Equation D.4 in section D.1 of Appendix D.

$$
\begin{aligned}
\dot{x}_E &= \left[u\cos\theta + \left(v\sin\phi + w\cos\phi\right)\sin\theta\right]\cos\psi - \left(v\cos\phi - w\sin\phi\right)\sin\psi + W_{x_E} \\
\dot{y}_E &= \left[u\cos\theta + \left(v\sin\phi + w\cos\phi\right)\sin\theta\right]\sin\psi + \left(v\cos\phi - w\sin\phi\right)\cos\psi + W_{y_E} \\
\dot{z}_E &= -u\sin\theta + \left(v\sin\phi + w\cos\phi\right)\cos\theta + W_{z_E} \\
\dot{u} &= A_x - g\sin\theta - qw + rv \\
\dot{v} &= A_y + g\cos\theta\sin\phi + pw - ru \\
\dot{w} &= A_z + g\cos\theta\cos\phi - pv + qu \\
\dot{\phi} &= p + q\sin\phi\tan\theta + r\cos\phi\tan\theta \\
\dot{\theta} &= q\cos\phi - r\sin\phi \\
\dot{\psi} &= q\frac{\sin\phi}{\cos\theta} + r\frac{\cos\phi}{\cos\theta}
\end{aligned}
\tag{3.7}
$$

The navigation (or observation) model defines the measurement vector as function of the state and input vectors, however, in this case the input vector contribution is null (equivalent to $\mathbf{D} = 0$ for linear system). In this flight path reconstruction problem, the navigation model is the heart of the measurement function $\mathbf{h}[\cdot]$. Equation 3.8 defines the complete set of observation equations. Each observation variable i is polluted with measurement noise $\mathbf{v_i}$ to form the measured observation variable i_m.

$$
\begin{aligned}
x_{GPS_m} &= x + v_x \\
y_{GPS_m} &= y + v_y \\
z_{GPS_m} &= z + v_z \\
u_{GPS_m} &= \left[u\cos\theta + \left(v\sin\phi + w\cos\phi\right)\sin\theta\right]\cos\psi - \left(v\cos\phi - w\sin\phi\right)\sin\psi + W_{x_E} + v_u \\
v_{GPS_m} &= \left[u\cos\theta + \left(v\sin\phi + w\cos\phi\right)\sin\theta\right]\sin\psi + \left(v\cos\phi - w\sin\phi\right)\cos\psi + W_{y_E} + v_v \\
w_{GPS_m} &= -u\sin\theta + \left(v\sin\phi + w\cos\phi\right)\cos\theta + W_{z_E} + v_w \\
\phi_{GPS_m} &= \phi + v_\phi \\
\theta_{GPS_m} &= \theta + v_\theta \\
\psi_{GPS_m} &= \psi + v_\psi \\
V_{TAS_m} &= \sqrt{u^2 + v^2 + w^2} + v_{V_{TAS}} \\
\alpha_m &= \tan^{-1}\tfrac{w}{u} + v_\alpha \\
\beta_m &= \tan^{-1}\frac{v}{\sqrt{u^2+w^2}} + v_\beta
\end{aligned}
\tag{3.8}
$$

3.1.5. State observability

The observability analysis is a measure to indicate the ability to observe the internal state of a dynamic system from a series of external measurements [75] [29], essentially verifying whether the augmented vector $\mathbf{x_{aug}}$ can be reconstructed given the available measurements $\mathbf{z}$. The observability condition requires that the rank of the observability matrix $\mathbf{O}$ is not smaller than n, the state vector dimensionality.

For linear systems, the observability matrix $\mathbf{O}$ can be constructed as a $n \times 1$ in which the observation matrix $\mathbf{H_{k+1,k}}$ is multiplied by the discretised state transition matrix $\mathbf{\Phi}_{k+1,k}$ raised to the power equivalent to the row number minus one. For nonlinear systems, the observability matrix $\mathbf{O}$ can be defined by consequently applying the Lie derivative to the observation equations, as stated by Equation 3.9 [75]:

$$
\mathbf{O}(x) = \begin{bmatrix} \partial_x(L_f^0\mathbf{h}) \\ \partial_x(L_f^1\mathbf{h}) \\ \partial_x(L_f^2\mathbf{h}) \\ \vdots \\ \partial_x(L_f^{n-1}\mathbf{h}) \end{bmatrix}
\tag{3.9}
$$

Where the Lie derivative is defined as:

$$\begin{aligned} L_f^0\mathbf{h} &= \partial_x \mathbf{h} \\ L_f^1\mathbf{h} &= \partial_x \mathbf{h} \cdot \mathbf{f} \\ L_f^2\mathbf{h} &= \partial_x (L_f^1\mathbf{h}) \cdot \mathbf{f} \\ &\vdots \\ L_f^{n-1}\mathbf{h} &= \partial_x \mathbf{h} (L_f^{n-2}\mathbf{h}) \cdot \mathbf{f} \end{aligned} \tag{3.10}$$

Applying the given arithmetic iteratively allows to estimate the nonlinear state observability. If the observability matrix $\mathbf{O}$ reaches full rank within the first $n-1$ Lie derivatives, nonlinear observability is guaranteed. If full rank is achieved within the first iteration, the system can also be considered as locally observable. Any additional iterations deteriorate the local nonlinear observability [29]. Given the stated measurement and state vectors, the system built for this study is locally observable, with the rank of $\mathbf{O}$ of 18, reached within the first iteration.

3.1.6. Kalman Filter verification

In order to verify the correct functioning of the Kalman filter, it can be fed with flight data for which the flight path is known exactly. This is done given the availability of simulated flight data of the Cessna Citation 550 aircraft performing uncoupled and laterally coupled 3211 and doublet manoeuvres, as provided by [75].

Data of the simulated aircraft motion are artificially populated with noise of known distribution and bias to mimic real measured flight test data. The noisy and biased data are subsequently fed to the Kalman filter and the reconstructed flight path is compared to the clean and unbiased simulated one. This subsection thus aims to briefly present the performance of the developed tool by graphically showing the reconstructed state vector $\mathbf{x}$ and filtered measurement vector $\mathbf{z}$, compared to the true state and measurement. Further tool performance analysis applied to the simulated data is described in [80].

Figure 3.3 compares the EKF and IEKF estimation of the unaugmented state vector $\mathbf{x}$ to the true state, whereas Figure 3.4 compares the estimated augmented part of the state λ to the actual wind and biases.

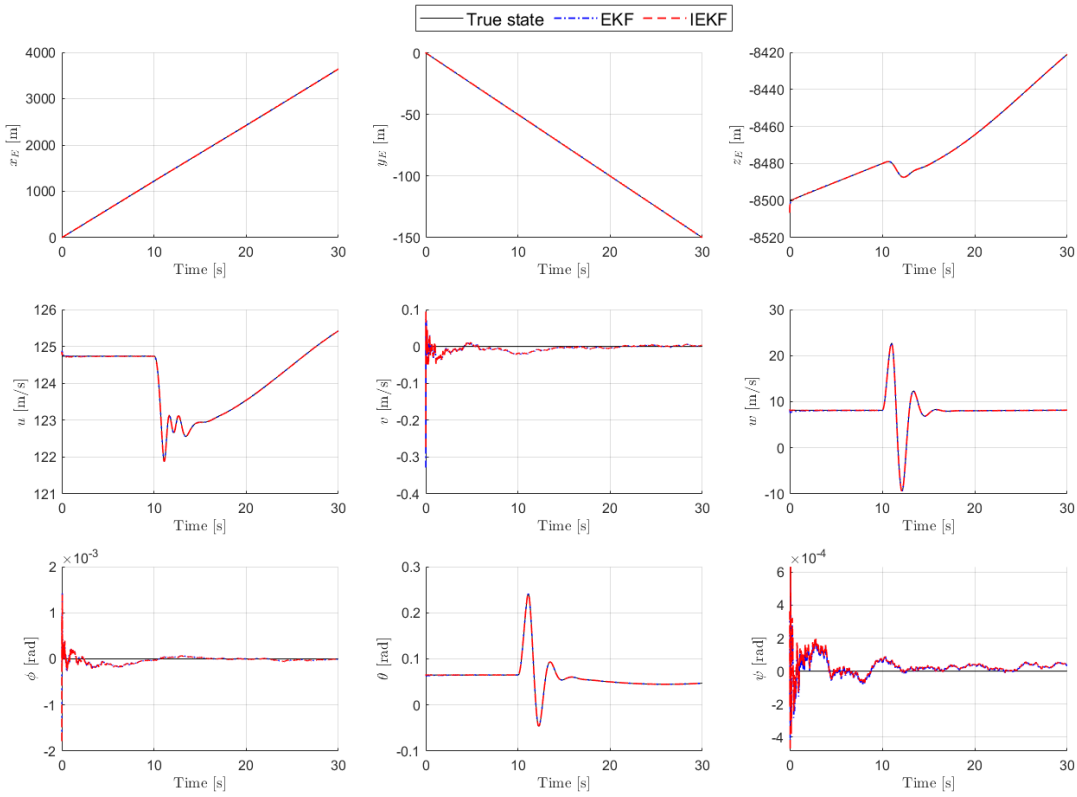

Figure 3.3: EKF and IEKF estimated unaugmented part of the state compared to true state for a simulated elevator doublet

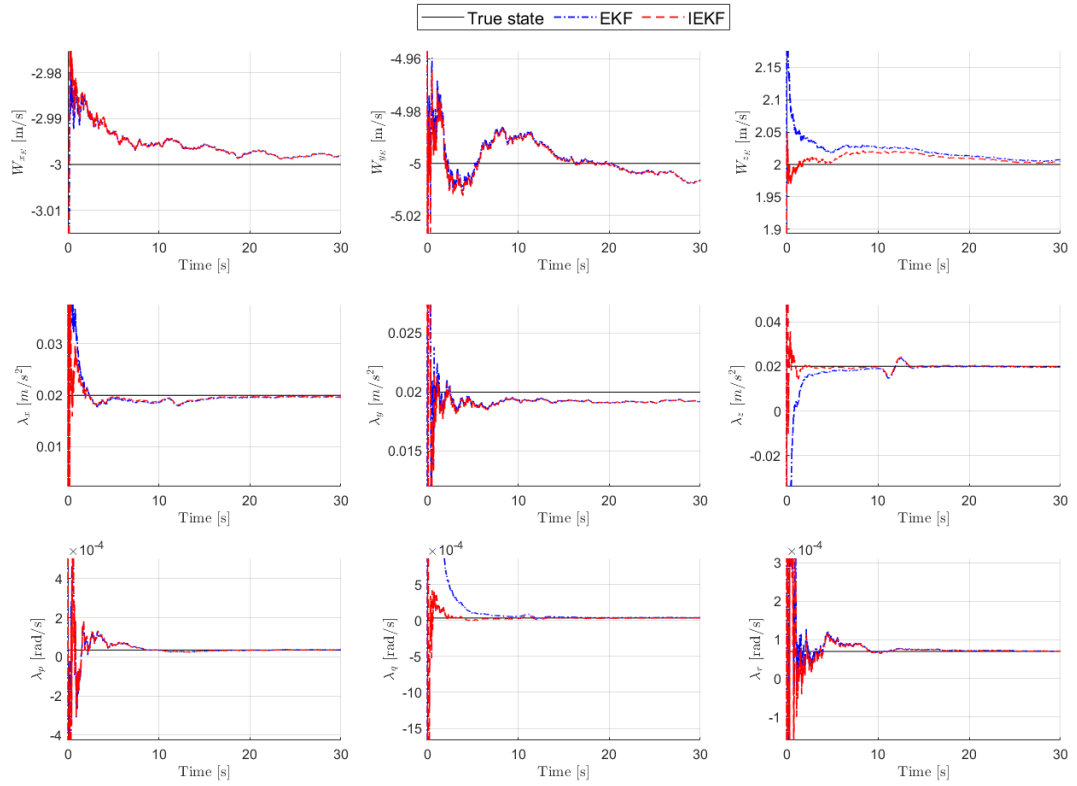

Figure 3.4: EKF and IEKF estimated augmented part of the state compared to true state for a simulated elevator doublet

Figure 3.5 compares the EKF and IEKF filtered GPS position and velocity components to the raw measurements, whereas Figure 3.6 shows the same for the attitude and air data part of the measurements vector **z**.

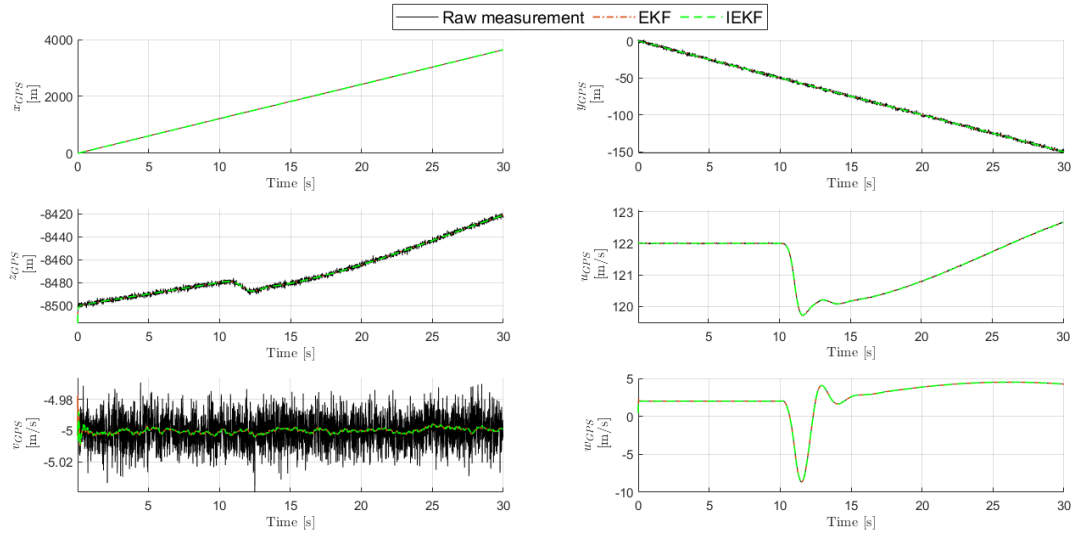

Figure 3.5: EKF and IEKF filtered GPS measurements compared to raw measurements for an elevator doublet

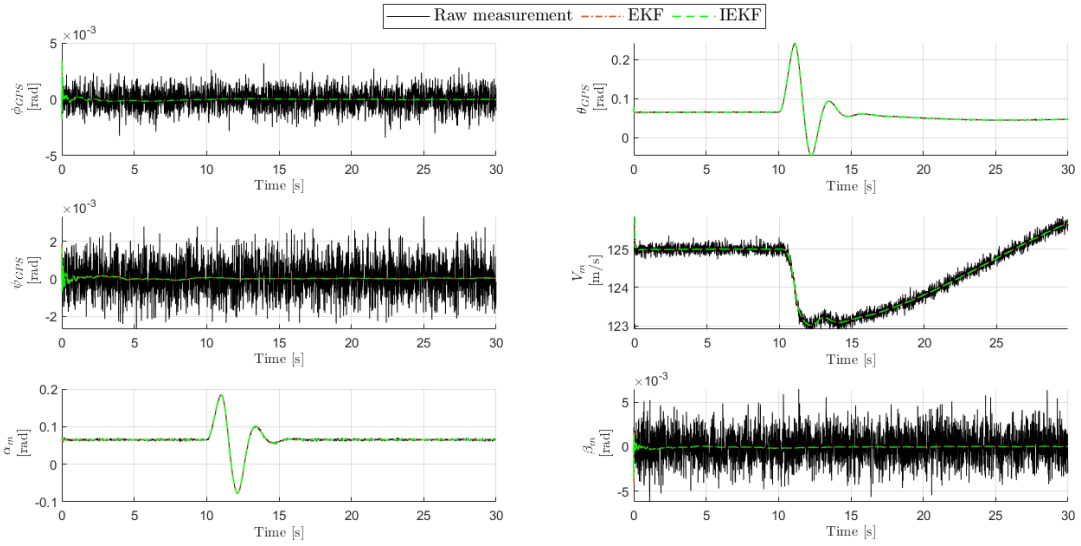

Figure 3.6: EKF and IEKF filtered attitude and air data measurements compared to raw measurements for a simulated elevator doublet

Figures presented above show that both developed EKF and IEKF converge and successfully reconstruct the true state, with the IEKF reaching convergence earlier than the EKF particularity visible for the IMU bias estimation. Ideal in this case, constant biases are relatively well predicted with little dependence on the manoeuvre dynamics, occurring for λ_x and λ_z - the primary axes of dynamic motion for an elevator doublet manoeuvre. The measurement is correctly filtered from the noise, with filter innovation being close to being independent of time.

3.2. Parameter identification

Parameter identification is the second step of the Two Step method and aims at determining the parameters used in the model definition such that the mathematical model predicts the physical system the best. Among the available parameter identification methods described in subsection 2.5.2, the Two

Step method employs the least squares estimation technique. This approach attempts to tune the model parameters such that the best fit to the measured data is found by minimising the sum of squared residuals, the difference between the estimated model output and measured data.

An Ordinary Least Squares (OLS) estimator is developed for this study to be applied on data measured and processed in the flight path reconstruction step. The principle of the OLS is first described in subsection 3.2.1, followed by a description of methods used to assess the performance of the estimator in subsection 3.2.2 and a formulation of the aerodynamic and engine models in subsection 3.2.3 and subsection 3.2.4, respectively.

The numerical implementation of the parameter identification is done in file `part3_OLS.m`, as described in Appendix D.

3.2.1. Ordinary Least Squares

The Ordinary Least Squares approach lies at the root of all least squares methods and is built upon the assumption that any function can be expressed in terms of an algebraic basis. Given N observations of an independent variable x and dependent variable $y = f(x)$, the measured data can be approximated by Equation 3.11 [29]:

$$\phi(x) = \sum_{i=1}^{m} \theta_i \varphi_i(x), \quad \varphi_i(x) = x^{i-1} \tag{3.11}$$

Where for least squares, the basis function $\varphi_i(x)$ commonly takes the given form of higher order of x. By substituting Equation 3.11 into an expression of a multivariate polynomial $P(x_1, x_2)$, here taken as a bi-variate example, with degrees of independent variables x_1 and x_2 denoted by a and b, respectively, the following can be stated:

$$P(x_1, x_2) = \theta_0 + \theta_{1,0}x_1 + \theta_{0,1}x_2 + \theta_{2,0}x_1^2 + \theta_{1,1}x_1x_2 + \ldots = \sum_{i=1}^{a+b=n} \theta_{a,b} \frac{n!}{a!b!} x_1^a x_2^b \tag{3.12}$$

With the total degree of the bi-variable polynomial given by $n = a + b$. Subsequently, a linear regression model that best fits a sequence of N measurement y can be defined as follows [75]:

$$\mathbf{y} = \mathbf{A}(\mathbf{x}) \cdot \theta + \varepsilon \tag{3.13}$$

Where y is the $N \times 1$ measurement vector, $\mathbf{A}(x)$ is the $N \times n$ regression matrix, $\mathbf{x}$ the $m \times 1$ state vector, θ the $n \times 1$ parameter vector and ε the $N \times 1$ model residual vector. The regression matrix $\mathbf{A}(\mathbf{x})$ can then be constructed as [75]:

$$\mathbf{A}(\mathbf{x}) = \begin{bmatrix} 1 & x_i(1) & x_i^2(1) & \ldots & x_i^n x_j^m(1) & \ldots & x_k^M(1) \\ 1 & x_i(2) & x_i^2(2) & \ldots & x_i^n x_j^m(2) & \ldots & x_k^M(2) \\ 1 & x_i(3) & x_i^2(3) & \ldots & x_i^n x_j^m(3) & \ldots & x_k^M(3) \\ \vdots & \vdots & \vdots & \vdots & \vdots & \vdots & \vdots \\ 1 & x_i(N) & x_i^2(N) & \ldots & x_i^n x_j^m(N) & \ldots & x_k^M(N) \end{bmatrix} \tag{3.14}$$

Subsequently, a cost function J can be defined, such that the least squares estimation of the model parameters can be found by solving for $\hat{\theta} = \arg\min J(x, \theta)$, the minimum of J. For the least squares approach, the cost function J is the sum of squared residuals ε, as given by Equation 3.15 in algebraic and vector form, respectively:

$$\begin{aligned} J(x, \theta) &= \sum_{i=1}^{N} \varepsilon_i^2 = \sum_{i=1}^{N} \left(y_i - A(x_i) \cdot \theta\right)^2 \\ J(\mathbf{x}, \theta) &= \varepsilon^\intercal \varepsilon = (\mathbf{y} - \mathbf{A}(\mathbf{x}) \cdot \theta)^\intercal \left(\mathbf{y} - \mathbf{A}(\mathbf{x}) \cdot \theta\right) \end{aligned} \tag{3.15}$$

Given that the cost function J is convex, its minimum can simply be found when its partial derivative with respect to θ is null: $\partial J(x,\theta)/\partial\theta = \partial\varepsilon^\intercal\varepsilon/\partial\theta = 0$. Expanding and rearranging for explicit formulation of θ gives the OLS solution for optimum parameters, namely $\hat{\theta}_{OLS}$, as well as the predicted model outcome $\hat{\mathbf{y}}$:

$$\hat{\theta}_{OLS} = \left(\mathbf{A}^\intercal(\mathbf{x})\cdot\mathbf{A}(\mathbf{x})\right)^{-1}\mathbf{A}^\intercal(\mathbf{x})\cdot\mathbf{y}, \quad \hat{\mathbf{y}} = \mathbf{A}(\mathbf{x})\cdot\hat{\theta}_{OLS} \tag{3.16}$$

The residuals ε as well as the Mean Squares Error (MSE) can be found with [29]:

$$\varepsilon = \mathbf{y} - \mathbf{y}, \quad \text{MSE} = \frac{1}{N}\sum_{i=1}^{N}\varepsilon^2 = \frac{1}{N}\sum_{i=1}^{N}(\mathbf{y}-\mathbf{y})^2 \tag{3.17}$$

Given the assumptions made throughout the derivation of the OLS estimator, several conditions have to be met to make the OLS Best Linear Unbiased Estimator (BLUE). The following has to be true for the application of the OLS estimator [75] [29]:

1. The model is linear in the parameter, i.e. the dependent variable y is a function of a set of superimposed independent variables x multiplied by their coefficients and includes an additional error term ε. All linear in the parameter functions can be written in a matrix-vector form, such as the one derived before.
2. The residuals ε have a constant variance for all measurements, which implies that all diagonal terms of the covariance matrix are equal to each other, or in other words, the measurement noise is independent of time and constant, $\mathbb{E}(\varepsilon\varepsilon^\intercal) = \sigma^2\mathbf{I}$.
3. The residuals ε are uncorrelated, implying that the off-diagonal terms of the covariance matrix should be equal to zero. The same expression applies, $\mathbb{E}(\varepsilon\varepsilon^\intercal) = \sigma^2\mathbf{I}$.
4. The expected value of the model residuals is zero $\mathbb{E}\{\varepsilon\} = 0$.

3.2.2. Statistical assessment

As a subsequent step of the parameter estimation, the optimal parameters $\hat{\theta}$ obtained with the given data measurements $\mathbf{y}$, the regression matrix $\mathbf{A}(\mathbf{x})$ and associated residuals ε, should be analysed to establish whether the performed estimation can be considered as BLUE and determine the level of confidence of the results. Building the covariance matrix of the parameter estimate $\hat{\theta}$ allows to access statistical information about the parameter correlation and its spread. The covariance of two parameters $\hat{\theta}_j$ and $\hat{\theta}_k$ is expressed by the $\sigma^2 d_{jk}$ element of the covariance matrix. The variance (or squared standard deviation) of a given parameter $\hat{\theta}_j$ is given by the diagonal element $\sigma^2 d_{jj}$ of the always symmetrical, $n \times n$ covariance matrix of $\hat{\theta}$, as defined by Equation 3.18:

$$\text{Cov}\{\hat{\theta}\} = \sigma^2\left(\mathbf{A}(\mathbf{x})^\intercal\cdot\mathbf{A}(\mathbf{x})\right)^{-1} \qquad \text{Var}\{\hat{\theta}\} = \text{diag}\left(\text{Cov}\{\hat{\theta}\}\right) \tag{3.18}$$

The calculation of the parameter covariance matrix requires the determination of the variance of residual σ^2 (or variance of measurement error), assumed constant for an OLS. For a flight measured time series data in which repeating exactly the same independent variable setting is assumed unlikely, an estimation of the variance can be made based on the residuals [33]:

$$\sigma^2 \approx \hat{\sigma}^2 = \frac{\varepsilon^\intercal\varepsilon}{N-n} = \frac{(\mathbf{y}-\mathbf{A}(\mathbf{x})\theta)^\intercal(\mathbf{y}-\mathbf{A}(\mathbf{x})\theta)}{N-n} \tag{3.19}$$

The variance $\text{Var}\{\hat{\theta}\}$ and covariance $\text{Cov}\{\hat{\theta}\}$ are therefore functions of both the variance of the error terms σ^2 in the population model and the sum of squares of the independent variables. The variance quantifies the confidence of the determined parameters. A smaller variance indicates the estimated coefficients are likely closer to their true population values, indicating a higher estimator reliability. A large variance suggests that the estimates are sensitive to the specific sample used, making them less reliable and potentially leading to inaccurate conclusions.

3.2.3. Aerodynamic model

The aerodynamic model expresses the nondimensionalised forces and moments acting on the aircraft in the body frame F_b in the form of multivariate polynomials. Independent variables of the polynomials of the aerodynamic model form the regression matrix $\mathbf{A}(\mathbf{x})$ and are accessed from the reconstructed flight path measurement vector $\mathbf{z}$ (α, β, V_{TAS}), input vector $\mathbf{u}$ (p, q, r) and measured aircraft control surface deflections (δ_e, δ_a, δ_r). The parameter vector θ is formed by aerodynamic and control derivatives, which are to be estimated.

The dependence of nondimensionalised forces and moments is defined by Equation 3.20 and is different for longitudinal and lateral force and moments. Throughout the study, the formulation of the aerodynamic model has been subject to corrections resulting from analysis of the determined derivatives and correlation of independent variables. Equation 3.20 includes terms that have been crossed out as a result of model structure correction.

$$\begin{aligned} C_X, C_Z, C_m &= f(\alpha, \cancel{\dot{\alpha}}, \cancel{\alpha^2}, q, \delta_e, \cancel{\Delta p_t / 0.5 \rho V^2}) \\ C_Y, C_l, C_n &= f(\beta, \cancel{\dot{\beta}}, p, r, \delta_a, \delta_r) \end{aligned} \tag{3.20}$$

For an effective use of the Ordinary Least Squares, the independent variables that are contributors to the aerodynamic forces and moments should show sufficient excitation during the manoeuvres and as little correlation as possible. Excitation allows for the OLS to differentiate between independent variables and attribute them parameter values such that the sum of the combination guarantees the least squares error fit of the observation. On the other hand, mutual correlation of independent variables makes them less distinct from each other for the OLS to attribute them a different weight (parameter). An analysis of the independent variables correlation post flight test data acquisition, as presented in section 4.4, allows to correct the model structure, removing terms that reduce its confidence. The choice of the model structure therefore aims to find the best combination of reliability of the determined coefficients (minimise their variance) while avoiding the depreciation of fitting performance, usually improved by higher number of applicable terms. Overall, correlations of variables are common and expected in aircraft system identification and the elimination of terms from the model structure might depend on an expected model format.

Because the term $\Delta p_t / 0.5 \rho V^2$ used to quantify the nondimensional power setting is not varied during the manoeuvres and not excited as a response to the manoeuvre, it becomes an additional, redundant constant term, in addition to the default $C_{()_0}$ "bin" term which takes care of any non-zero offset between the observation and model. The same principle lies behind not including the α term in the asymmetrical model nor the β term in the symmetrical model.

In contrast, the air incidence angles first time derivatives $\dot{\alpha}$ and $\dot{\beta}$ terms, which quantify the time history of α and β, have shown a high correlation with pitching rate q and yawing rate r, respectively, while the squared angle of attack, α^2, a high correlation with angle of attack α itself. The terms are therefore removed from presented the model structure. The results of parameter identification including $\dot{\alpha}$ and $\dot{\beta}$ are shown in Appendix B, where an alternative model structure is formulated. The aileron deflection δ_a shows high correlation with the roll rate p, which is rather expected. Despite this, both terms are kept in the model to maintain an influence of the aircraft change in geometry (δ_a) on its dynamic motion, at the expense of a potentially increased variance of the parameter characterising this relation.

Given that the observation moment equation Equation 3.24 is dominated by the product of rotational acceleration terms $\dot{p}$, $\dot{q}$, $\dot{r}$ and corresponding moments of inertia, an aerodynamic model structure including $\dot{p}$, $\dot{q}$, $\dot{r}$ is expected to show a very good observation fitting performance. However, being dominated by the rotational acceleration terms, such a model shows a negligible contribution of all other model terms (angles of incidence, control surface deflections) and is expected to be extremely sensitive to the inertia matrix. Its application, which has not been encountered in literature, is therefore limited.

Given the depreciating effect of excess constant terms in the aerodynamic model, coefficients associated to motion and control surfaces which are not excited during a particular manoeuvre are redundant. Therefore, the terms of C_X, C_Z, C_m are only determined from elevator manoeuvre (symmetrical), whereas C_Y, C_l, C_n are only determined from aileron and rudder manoeuvres (asymmetrical). Moreover, control derivatives corresponding to control surfaces that are inactive during a particular manoeuvre

are ignored, thus for example $C_{()_{\delta a}}$ cannot be accurately determined from an uncoupled rudder doublet, nor $C_{()_{\delta r}}$ from an uncoupled aileron doublet.

With the aforementioned being said, the final model structure can be defined. Equation 3.21 defines the nondimensionalised forces in the body frame F_b of the aircraft, while Equation 3.22 the nondimensionalised moments.

$$\begin{aligned} C_X &= C_{X_0} + C_{X_\alpha}\alpha + C_{X_q}\frac{q\bar{c}}{V} + C_{X_{\delta_e}}\delta_e \\ C_Y &= C_{Y_0} + C_{Y_\beta}\beta + C_{Y_p}\frac{pb}{2V} + C_{Y_r}\frac{rb}{2V} + C_{Y_{\delta_a}}\delta_a + C_{Y_{\delta_r}}\delta_r \\ C_Z &= C_{Z_0} + C_{Z_\alpha}\alpha + C_{Z_q}\frac{q\bar{c}}{V} + C_{Z_{\delta_e}}\delta_e \end{aligned} \tag{3.21}$$

$$\begin{aligned} C_l &= C_{l_0} + C_{l_\beta}\beta + C_{l_p}\frac{pb}{2V} + C_{l_r}\frac{rb}{2V} + C_{l_{\delta_a}}\delta_a + C_{l_{\delta_r}}\delta_r \\ C_m &= C_{m_0} + C_{m_\alpha}\alpha + C_{m_q}\frac{q\bar{c}}{V} + C_{m_{\delta_e}}\delta_e \\ C_n &= C_{n_0} + C_{n_\beta}\beta + C_{n_p}\frac{pb}{2V} + C_{n_r}\frac{rb}{2V} + C_{n_{\delta_a}}\delta_a + C_{n_{\delta_r}}\delta_r \end{aligned} \tag{3.22}$$

The nondimensional forces and moment cannot be measured directly in flight and thus have to be computed from the available reconstructed measurements $\mathbf{z_m}$, inputs $\mathbf{u}$. Equation A.5 and Equation A.13 in Appendix A define the dimensional forces and moments, respectively, which can be nondimenionalised, as given by Equation 3.23 and Equation 3.24, respectively.

$$\begin{aligned} C_X &= \frac{X}{0.5\rho V^2 S} = \frac{mA_x}{0.5\rho V^2 S} \\ C_Y &= \frac{Y}{0.5\rho V^2 S} = \frac{mA_y}{0.5\rho V^2 S} \\ C_Z &= \frac{Z}{0.5\rho V^2 S} = \frac{mA_z}{0.5\rho V^2 S} \end{aligned} \tag{3.23}$$

$$\begin{aligned} C_l &= \frac{L + L_{gyr}}{0.5\rho V^2 Sb} = \frac{\dot{p}I_{xx} + qr(I_{zz} - I_{yy}) - (pq + \dot{r})I_{xz}}{0.5\rho V^2 Sb} \\ C_m &= \frac{M + M_{gyr} + M_T}{0.5\rho V^2 S\bar{c}} = \frac{\dot{q}I_{yy} + rp(I_{xx} - I_{zz}) + (p^2 - r^2)I_{xz} + I_p(\omega_{e,f} + \omega_{e,r})r \cancel{-(\Delta z_f T_f + \Delta z_r T_r)}}{0.5\rho V^2 S\bar{c}} \\ C_n &= \frac{N + N_{gyr}}{0.5\rho V^2 Sb} = \frac{\dot{r}I_{zz} + pq(I_{yy} - I_{xx}) + (qr - \dot{p})I_{xz} - I_p(\omega_{e,f} + \omega_{e,r})q}{0.5\rho V^2 Sb} \end{aligned} \tag{3.24}$$

The $(\Delta z_f T_f + \Delta z_r T_r)$ thrust moment term in Equation 3.24 induces a constant offset into the C_m expression, provided the power setting is constant. Given that the aircraft is trimmed before each manoeuvre (and thus $C_{m(t=0)} = 0$), the thrust moment term does not add any dynamic behaviour into the longitudinal moment, which is why the term has been crossed out.

Equation 3.24 introduces terms of body rotational acceleration $\dot{p}$, $\dot{q}$ and $\dot{r}$, which have not been explicitly defined, but can be computed by applying numerical differentiation to rotational body rates p, q and r, respectively. For this purpose, the central finite difference scheme of order four has been employed throughout the core of the dataset, as defined by Equation D.1 in section D.1 of Appendix D. The order of the differentiation scheme is taken as a compromise between truncation error and noise amplification and is discussed in more details in section 4.1.

3.2.4. Engine model

The MVP-50P engine monitor measures, displays, and records a variety of engine parameters (see section 4.4), however not in the format that could directly be used in the aircraft mathematical model. The aim of the engine model is therefore to compute the variables required in the aerodynamic model such as thrust T (see Equation 3.24), power P, propeller efficiency η_p and nondimensional change in total pressure provided by the propeller $\Delta p_t/0.5\rho V^2$ (see Equation 3.21 and Equation 3.22) as function of the available engine parameters and flight conditions.

The aerodynamic model assumes an engine power setting contribution to dimensionless longitudinal forces and moments in the form of a nondimensionalised change in total pressure of the air flow through the propeller Δp_t, as proposed by [45] (see subsection 2.3.5) and defined by Equation 3.25:

$$\frac{\Delta p_t}{\frac{1}{2}\rho V^2} = a + b\frac{P}{\frac{1}{2}\rho V^3} \tag{3.25}$$

The brake power at the engine crank shaft P_{br}, as a direct measure of the useful engine power, can be related to thrust via the propeller efficiency η_p and airspeed V [28, p. 1002] for airspeeds away from zero:

$$P_{br} = \frac{TV}{\eta_p} \tag{3.26}$$

Under the assumption of steady, inviscid, incompressible, uniform and irrotational flow, the momentum theory can be applied on the flow at free stream (0) and downstream (e) of the propeller treated as an actuator disk. The free stream and downstream static pressures are equal $p_{s,0} = p_{s,e}$, if not compared in close proximity and across the propeller. The thrust force generated by the propeller can then be expressed as a change in total pressure Δp_t, here equivalent to change in dynamic pressure Δq, acting on an effective area A_{eff}:

$$T = \dot{m}_e V_e - \dot{m}_0 V_0 = \frac{1}{2}\rho\left(V_e^2 - V_0^2\right) A_{eff} = \Delta p_t A_{eff} \tag{3.27}$$

A solution to Equation 3.25 becomes $b = \frac{\eta_p}{A_{eff}}$ and $a = 0$. Indeed, the value of a experimentally determined by Mulder for the DHC-2 Beaver is small (below 0.087, [67, p. 15]). The change in total pressure across the propeller can be expressed analytically by Equation 3.28, valid for non-zero airspeed values.

$$\Delta p_t = \frac{\eta_p P_{br}}{A_{eff} V} \tag{3.28}$$

Power determination

The MVP engine monitor calculates the engine power output as function of engine rotational speed (N [rpm] or ω [rad/s]), manifold pressure p_z, altitude and mixture setting [50], yet the exact computational procedure is hidden under the black box of the monitor software. In addition, the validity of Equation 3.26 is lost at low airspeeds. As a first step, encoded in the `ac_engine_map.m` function (see section D.2 of Appendix D), the engine model determines the corrected engine power from a digitised version of the Continental IO-360 version CB and C engine performance chart [14], as presented on Figure 3.7.

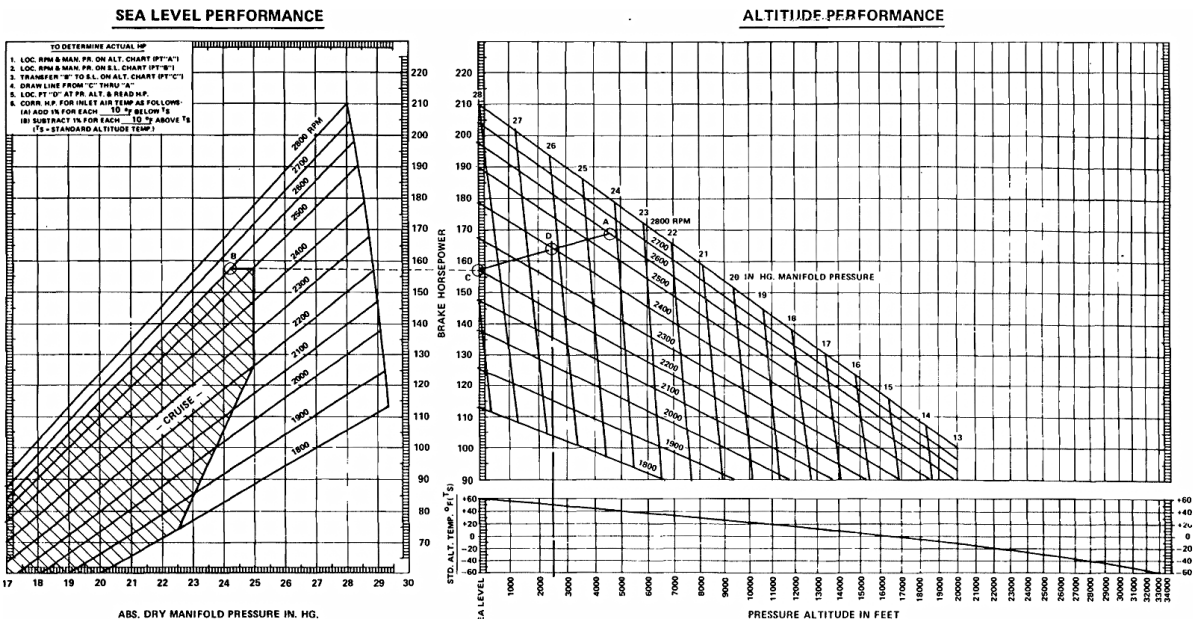

Figure 3.7: Altitude performance curves IO-360-C, CB, D, DB, G, GB, H, HB [14]

The function `ac_engine_map.m` takes the engine rotational speed N, manifold pressure p_z, pressure altitude h_p and outside air temperature OAT as inputs to compute the altitude and temperature corrected engine power as output. It contains the digitised version of the data of Figure 3.7 and follows the same steps:

1. Locate the RPM and manifold pressure on the altitude chart (point A)
2. Locate the RPM and manifold pressure on the sea level chart (point B)
3. Identify the power output of point B and transfer it to the altitude chart as point C at sea level (left margin of the altitude chart)
4. Connect points A and C with a straight line AC
5. Identify point D lying on AC at the desired pressure altitude and read off corresponding engine power
6. Correct the engine power for inlet air temperature (approximately OAT) by adding or subtracting 1% for each 10°F below or above the ISA temperature at given pressure altitude, respectively

The function interpolates linearly between the curves, as well as extrapolates linearly beyond the range included in Figure 3.7 while raising an off-range warning.

Efficiency and thrust coefficient determination

In order to determine the propeller efficiency η_p and thrust coefficient C_T, the model makes use of performance maps provided by the propeller manufacturer, MT Propellers. The maps contain information on η_p, C_T and β_p as function of advance ratio J and power coefficient C_P, at four flight levels (SL, FL25, FL75 and FL125) and for three values of N [rpm] (2400, 2600 and 2800) for ISA conditions [44]. Equation 3.29 provides the definitions of C_P, C_T and J:

$$C_P = \frac{P}{\rho N^3 D^5} \qquad C_T = \frac{T}{\rho N^2 D^4} \qquad J = \frac{V}{ND} \tag{3.29}$$

The engine model function `ac_get_eta_ct.m` takes the advance ratio J, power coefficient C_P, engine rotational speed N [rpm] and flight level FL as inputs to retrieve the corresponding propeller efficiency η_p and thrust coefficient C_T as output. Since the pressure altitude of the flight is not always aligned with a flight level, the input allows a decimal expression of the FL value, i.e. FL [ft] $= \frac{h_p[m]}{30.48}$. An example of

the format of the propeller performance maps is given by Table 3.1, providing η_p for columns of J and rows of C_P, in this case at $FL25$ and $N = 2800$ [rpm].

Table 3.1: Simplified η_p MTV-12 propeller performance map at $FL25$ and 2800 RPM by MT Propellers

$C_P \downarrow / J \rightarrow$	0.1	0.2	0.3	0.4	0.5	0.6	...	1.5
0.03	0.28603	0.49899	0.64268	0.73151	0.78258	0.80933	...	0.50332
0.04	0.25911	0.46487	0.61532	0.71746	0.78268	0.82208	...	0.67372
0.05	0.23520	0.43096	0.58222	0.69098	0.76499	0.81348	...	0.76423
0.06	0.21443	0.39940	0.54885	0.66148	0.74152	0.79628	...	0.81655
...	...	...	...	...	...	...	...	...
0.15	0.11171	0.22050	0.32579	0.42579	0.51706	0.59576	...	0.82348

The function `ac_get_eta_ct.m` accesses the η_p and C_T maps and linearly interpolates between the discrete values of J columns and C_P rows of all available maps (all FL and N). Once a value of η_p and C_T is retrieved from each map, the function interpolates linearly between the discrete values of FL and N. In case the flight conditions exceed the range of J, C_P, FL or N covered by the table, the value is extrapolated linearly, while raising a warning. Typical cruising conditions are computed to be $J_c = 1.022$ and $C_{P,c} = 0.045$ through 0.061 (from SL to $FL100$), while MCP conditions $J_{MCP} = 1.005$ and $C_{P,MCP} = 0.048$ through 0.065. Extrapolation is usually required on the ground, when N is low or the pressure altitude is negative, which can happen at EHRD airport under certain weather conditions.

Thrust and Δp_t determination

As the final step, the engine model employs the function `ac_engine.m` which takes airspeed V, pressure altitude h_p, sea level static temperature T_0, engine rotational speed N and engine power P as inputs to determine the thrust and dimensionless change in total pressure as outputs. The `ac_engine.m` function is the outer shell of the engine model and employs `ac_get_eta_ct.m` as well as an ISA atmospheric model. It uses hardcoded geometrical properties of the propeller, engine MCP and function inputs to compute J and C_P allowing to call `ac_get_eta_ct.m`. The thrust T is subsequently computed from C_T by rearranging the appropriate expression of Equation 3.15, while $\Delta p_t / 0.5 \rho V^2$ is computed with Equation 3.25.

4

Experiment Design

In the process of creating an aircraft mathematical model, the measurement data for the system identification can be obtained from different sources, such as computational fluid dynamics (CFD) simulations, scaled wind tunnel experiments, or flight testing. The latter is used in this study, given the early stage of research performed on the newly acquired Cessna Skymaster research aircraft.

Flight measurements provide the least biased information about the behaviour of the aircraft, compared to numerical or scaled models which, by definition, are approximations of reality. Flight testing comes at the cost of several challenges, which increase the complexity of data post processing and include noise, reduced control over the testing environment, instrumentation limitations or safety precautions limitations.

This chapter attempts to describe the approach to the practical side of this study, necessary to obtain the data needed for the execution of a model identification. First, a simple method of control surface deflections determination is introduced in section 4.1 discussing its principles and limitations. This is followed by a note on the fuel mass determination in section 4.2 and BOM capabilities and limitations in section 4.3. The chapter is closed by an elaboration on the flight testing approach, in section 4.4.

4.1. Control surface deflection measurement

By definition and design, the control surfaces are the main contributors influencing the change in aircraft motion. The knowledge about their deflection in time is therefore equally important as the measured aircraft output data characterising the dynamic response to their deflection. At the time of realisation of the presented study, that is between March and October 2025, the researched Cessna Skymaster N4207X is not equipped with onboard instrumentation which would allow to measure the control surface deflection and an implementation of thereof is not anticipated in the predictable future. This imposes a need to develop and implement a temporary method for the purpose of the given study, while keeping it as non-invasive to the critical control systems as possible, for safety reasons.

In this study, the control surfaces considered are the ailerons - controlling the aircraft roll (rotation about X_b) induced by rotation of the control column, elevator - controlling the aircraft pitch (rotation about Y_b) induced by translation of the control column, and rudder - controlling the aircraft yaw (rotation about Z_b) induced by pair-wise opposite pedal translation. The Cessna Skymaster is also equipped with main wing and engine cowl flaps, elevator and rudder trim tabs as well as retractable landing gear, all of which can influence the aircraft attitude and motion, yet they are not considered in this study, given its scope. Given the time available, resources, accessibility and safety limitations, the control surface deflection is measured with the help of IMU sensors attached directly on the control column or dedicated spring loaded pulleys, translating translational motion of the control column or pedals into rotation. The IMU sensor characteristics are presented in subsection 4.1.1, the measurement of the control column and pedal displacement described in subsection 4.1.2, whereas the translation of the steering to control surface deflections is given in subsection 4.1.3. A quantification of the measurement uncertainty is presented in subsection 4.1.4.

The principle of measuring the control deflections with IMUs consists of attaching the sensors to the control column and pedals in order to determine their change in position. On one hand, this approach measures the pilot's input rather than actual control deflections and thus, together with control cable extension and mechanism play, can introduce errors. On the other hand, all the sensors are placed in the cockpit and within the reach of the pilot's hand, complying with the safety requirements of minimum

interference with the control system. This results in a compromise between accuracy and measurement feasibility, as safety cannot be compromised.

4.1.1. IMU sensors

As described in subsection 2.5.1, several methods to measure the control surface deflection exist and have been considered. The choice has been made to use the Movella DOT (historically Xsens) Inertial Measurement Unit (IMU) sensors, given their availability, small size, ease of use, measurement capabilities, recording rate and precision. The Xsens IMU are designed for body motion capture, yet the measured variables, such as body attitude and accelerations, make them applicable for the purpose of this study. Table C.1 in section C.1 of Appendix C provides more detailed information on the available measurements recorded by the IMUs, either in the sensor body F_X or local Earth-fixed F_L frame.

The sensor, together with its body coordinate system definition F_X, is depicted on Figure 4.1. A single IMU weighs 11.2 [g] and has dimensions of $36.3 \times 30.4 \times 10.8$ [mm]. The variables measured, as listed on Table C.1, can be recorded in specific configurations, selecting one variable of each type at a time only. Data can be logged onto the sensor or recorded directly on a mobile device via a Bluetooth connection. Although the latter limits the recording frequency to 60 Hz (instead of 120 Hz at maximum for the former case), this method is preferred for live monitoring in flight. The accuracy of the orientation measurement in dynamic mode (chosen given the dynamic nature of the signal) is 1.0° 1σ RMS for inclination (ϕ, θ) and 2.0° 1σ RMS for heading (ψ) and a measurement latency of 30 ms. The non-orthogonality of sensors axes is within 0.05°, whereas the misalignment of the internal sensors with the hardware frame is less than 0.2° for the accelerometer [81].

Figure 4.1: Xsens DOT sensor coordinate system [81]

4.1.2. Column and pedal displacement measurement

A significant challenge anticipated in the design of control surface deflections with IMUs is the undesired interference of the aircraft dynamic motion response with the desired recording of the control excitation. To solve this issue, multiple sensor placement and recording configurations have been considered during qualification testing. Sensors have been attached to the yoke (one sensor), pedals (one sensor for each pedal) and the stationary instrumentation panel (one sensor). The purpose of the latter is to serve as reference allowing to subtract the aircraft body motion contribution from the measured yoke rotational motion, resulting in pure motion of controls with respect to the aircraft body.

Initially, measurements of sensor body F_X linear acceleration have been taken to determine the translational change in position of elevator and rudder control (yoke and pedals translation) by performing double integration with respect to time. Given the measurement noise and the drift it has caused throughout the integration process, this approach has been discarded after several stationary and ground engine run tests, despite attempts to smooth the recorded acceleration signal. Within the same test, sensor attitude measurements have shown promising behaviour and are further used to determine the control deflections.

Given the relatively low noise and high precision of the Xsens attitude measurements, an attempt is made to translate all control inputs into a rotational motion. This is naturally not needed for the aileron control measurement, since the aileron control is performed by yoke rotation. The principle of this approach is to make the IMU sensor rotate about its own Z_X axis, as the pilot executes an elevator, aileron or rudder input. In addition, this method provides decoupling of the recorded control input from the aircraft response, as long as the axis of rotation of the IMU is orthogonal to the principle body

axis of rotation of the aircraft response motion. This idea imposes a need for a construction of device translating a translational motion into a rotational motion in a predictable and controllable manner. To accomplish that, a simple modification is made to the common pull reel device (US patent number USD539122S, EU patent number 000279237.0001 [68]), as shown on Figure 4.2. Illustrations of the pulley manufacturing and its internal components can be found in section C.2 of Appendix C. In this report, the modified pull reel is referred to as pulley.

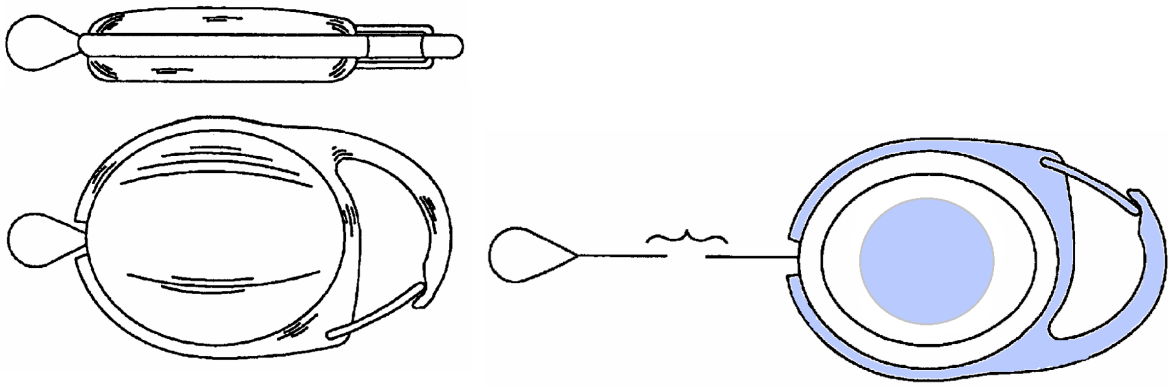

(a) Top and side views of the pull reel device (USD539122S) [68]

(b) Proposed modification of the pulley, shaded area removed

Figure 4.2: Pulley for translation to rotation transformation

The original pulley is composed of a spring loaded drum which winds any slack from an extended string. The modification consists of removing the unnecessary metal circumferential casing, and keeping the plastic protection casing and string winding drum. In addition, a circular hole of diameter of around 22 [mm] is drilled on one side of plastic casing, such that its centre coincides with the axis of rotation of the drum. This allows to access the rotating drum, while keeping it framed within the plastic casing. A connection between the drum and the Xsens sensor is established with Velcro. As a result, the Xsens sensor rotates around its Z_X axis when the string is being pulled, and returns to its original attitude when the string is released. Illustrations of the pulley and IMU assembly can be found in section C.2 of Appendix C. The schematic top and side views of the pulley with the sensor are presented on Figure C.1.

By measuring the string displacement at five full rotations of the sensor, the radius of the drum has been determined to be 12.45 [mm] with a determination coefficient $R^2 > 0.9999$, allowing to relate the determined sensor rotation to string displacement. This has also been confirmed by measuring the drum diameter with a caliper.

Given the available measurements listed on Table C.1, the sensor rotational rate r around its axis Z_X can be either measured directly, or computed from the measured attitude defined by Euler angles ϕ, θ and ψ. The Xsens measured Euler angles and rotational rates are defined with respect to the the sensor reference frame F_X and should not be confused with the aircraft body attitude and rotational rates in F_b, however the same equations of motion apply, as defined by Equation 4.1. Equation 4.1 is the result of rearranging Equation A.19 into an explicit formulation of rotational rates as function of Euler angles.

$$p = \dot{\phi} - \sin\theta\,\dot{\psi} \tag{4.1}$$

$$q = \cos\phi\,\dot{\theta} + \sin\phi\,\dot{\psi}\cos\theta \tag{4.2}$$

$$r = -\sin\phi\,\dot{\theta} + \cos\phi\,\dot{\psi}\cos\theta \tag{4.3}$$

The first time derivative of the Euler angles $\dot{\phi}$, $\dot{\theta}$, $\dot{\psi}$ is determined by applying numerical differentiation on the measured Euler angle, using the central difference of fourth order and forward and backward difference of order two on boundaries, as stated by Equation D.1 and Equation D.2 in Appendix D, respectively. The order of the differentiation scheme is chosen as a compromise between truncation error and uncertainty amplification, as discussed in more detail in subsection 4.1.4. The angle of rotation of the sensor around its axes can be determined by integrating the rotational rates p, q and r with respect

to time, which is performed numerically using the cumulative composite trapezoidal rule, as defined by Equation D.3.

Both approaches, i.e. integrated measured rotational rate r and integrated computed rotational rate r determined with Equation 4.1, have been applied to 12 stationary engine-off, ground test measurements of each control surface deflection. A consistent pattern indicating a drift of integrated measured sensor r is present at each measurement and showcased on Figure 4.3 as example. The graph shows the pulley string displacement Δs_e in time, which is a result of elevator control input, for both described methods. Figure 4.3b presents a zoomed in portion of Figure 4.3a just after the end of the input signal, showing the integrated measured r drift and integrated computed r steady.

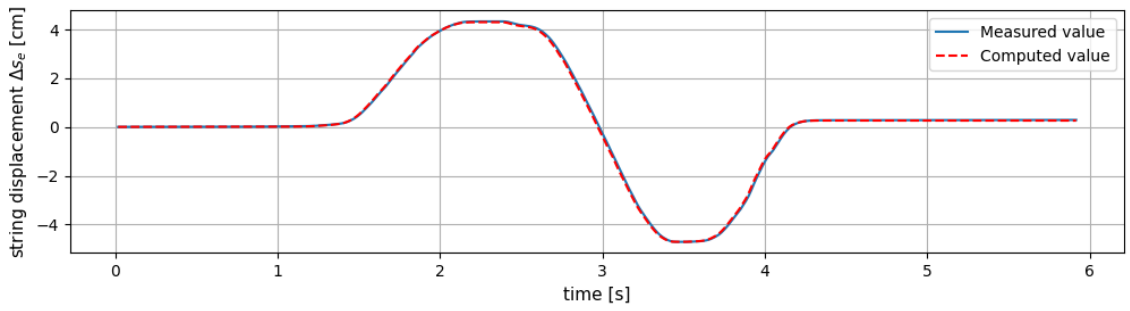

(a) Complete input signal

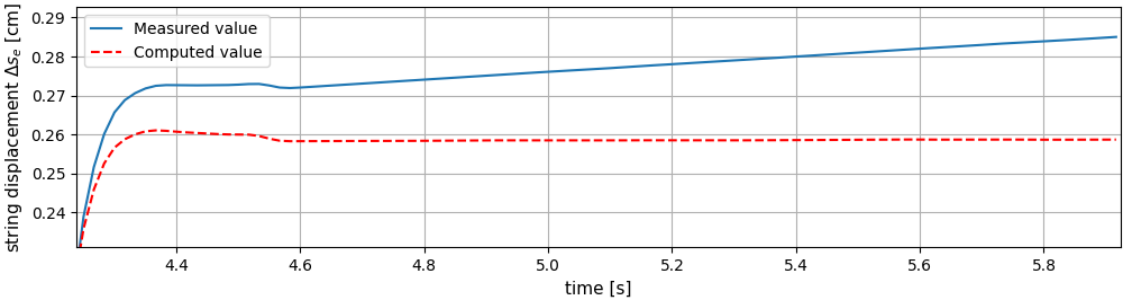

(b) Zoomed in part of signal showcasing the drift of integrated measured r

Figure 4.3: Example of string displacement of elevator control mounted pulley for a sinusoidal input signal, comparing both methods

Table 4.1 lists the quantified differences between string displacement values determined with both methods over the 12 stationary, engine-off ground measurements Δs for all control surfaces. The difference is taken at the point in time just as the signal stabilises and is scaled with respect to the maximum absolute signal recorded, allowing to be expressed in %.

	Aileron	Elevator	Rudder
$\max\{\Delta s_{meas.} - \Delta s_{comp.}\}$ [%]	10.41	2.06	8.78
$\min\{\Delta s_{meas.} - \Delta s_{comp.}\}$ [%]	1.19	0.26	0.11
$\overline{\Delta s_{meas.} - \Delta s_{comp.}}$ [%]	3.45	1.02	2.13

Table 4.1: Difference in string displacement between both methods, scaled with respect to absolute maximum signal value

Although no clear pattern linking the drift behaviour to signal characteristic has been observed throughout the test measurements, the drift is a result of noise present in the measured r, which, once integrated, gives a false indication of divergence of the string displacement. Computing the displacement Δs from measured Euler angles and their time derivatives allows to solve this problem. Numerical differentiation, as performed in this procedure, has a tendency to smooth out dynamic signals, which would be indicated by a reduced computed $\Delta s_{comp.}$ amplitude compared to measured $\Delta s_{meas.}$ amplitude. The significance of this effect is mitigated by employment differentiation schemes of higher order (see section D.1) and has not been influencing the test measurements in any noticeable

manner. Given the described phenomena, it is decided to determine $\Delta s_{comp.}$ by numerical computation from Euler angles rather than using the prone to drift measured r for further control surface deflection determination.

4.1.3. Translation of steering to control surface deflection

Section 4.1.2 described the approach to translate the rotation recorded by the Xsens sensor to the translation of the pulley string. The end of the pulley string can therefore be attached to the control column or pedals in order to record its displacement. This motion can subsequently be translated into the actual control surface deflection, the process of which is the focus of this subsection. Each steering control requires a dedicated approach of displacement measurement, as the nature of their movement is unique for each of them.

Aileron

The aileron deflection is expressed by the angle of deflection of the aileron surface downwards, with right aileron deflection downwards considered positive. Positive aileron deflection induces negative roll p and is induced by a counter-clockwise yoke rotation. Negative expressions of aileron deflections define the left aileron downward deflection. In order to solve the differential aileron deflection asymmetry problem, only downward deflections are considered. The neutral aileron position is considered when the yoke is in a laterally symmetrical position with respect to the instrument panel.

The yoke rotation is measured directly by the Xsens sensor (no pulley is used), which is attached to the yoke, such that Z_X is aligned with the yoke rotation. Since the main component of the aircraft rotation responding the aileron deflection (roll p) is aligned with Z_X, the measured yoke rotation is skewed by the aircraft body roll. In order to account for this effect, a separate sensor is attached to the instrument panel, such that it records the aircraft body roll only and can be treated as a reference measurement. In order to obtain pure yoke rotation, the reference measurement is subtracted from the measured yoke rotation skewed by aircraft body roll.

In order to translate the determined yoke rotation into aileron deflection, a series of ground, stationary, engine-off measurements have been taken, relating the orientation of the yoke to the aileron (downwards) deflection, with the use of a digital inclinometer (accuracy of ±0.1°). The results of this correlation are shown on Figure 4.4, together with a linear fit. Table 4.2 quantifies the linear fit characteristics of the correlation.

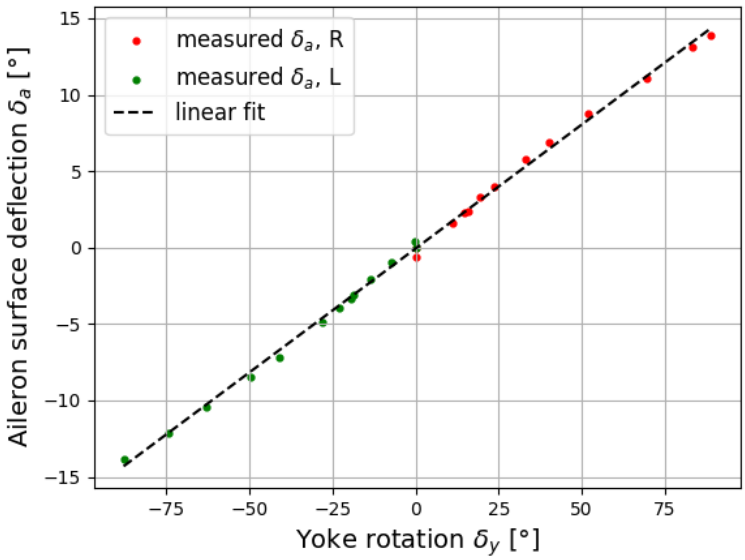

Figure 4.4: Measured aileron surface deflection corresponding to yoke orientation

	Slope	Intercept	R^2
Value	0.162	-0.060	0.998

Table 4.2: Linear fit characteristics of aileron deflection to yoke rotation correlation

Elevator

The elevator deflection is expressed by the angle of deflection of the elevator surface downwards, considering this direction as positive. Positive elevator deflection induces negative pitch q and is induced by a forwards displacement of the control column. The neutral elevator position is considered when the elevator chord is aligned with the horizontal stabiliser chord and the elevator trim is in neutral position.

The control column displacement is measured by the Xsens sensor mounted on the pulley, attached to the instrument panel, with the pulley string attached to the yoke. The translational motion of the steering column is therefore translated into rotation of the Xsens sensor around its Z_X axis. Figure 4.5 shows the IMU and pulley arrangement for column displacement measurement. Due to mechanical limitations, the extended part of pulley string of length x is not parallel to the steering column (extended to length l), which has to be taken into account when computing the control column travel.

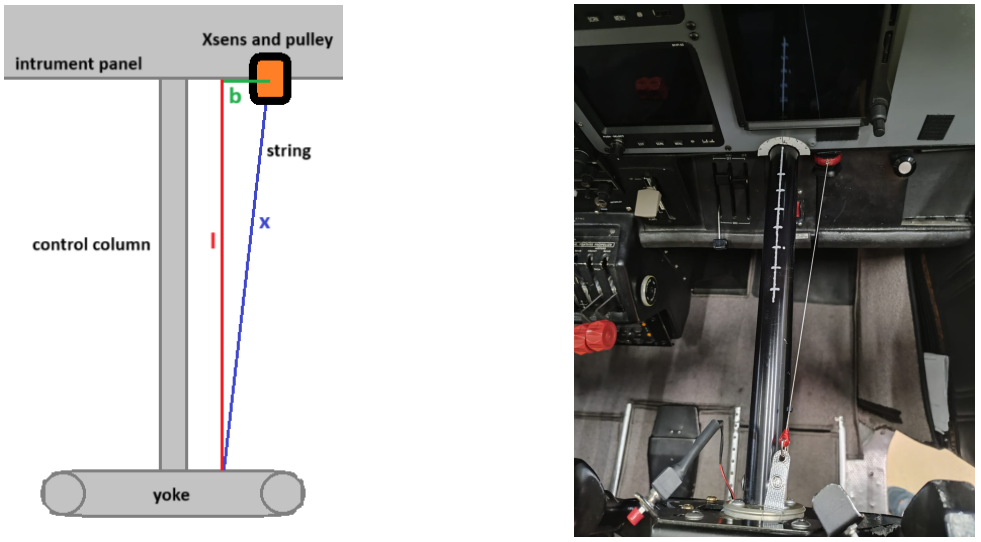

(a) Top view schematic representation

(b) Top view picture

Figure 4.5: IMU and pulley arrangement for column displacement measurement

Given the acute angle θ between the control column of length l and string x, the change in control column displacement Δl can be expressed as:

$$\Delta l = \Delta x \cos\theta, \qquad \theta = \sin^{-1}\left(\frac{b}{x}\right) \tag{4.4}$$

Substituting the expression of θ into the expression of Δl and simplifying returns:

$$\Delta l = \Delta x \cos\left(\sin^{-1}\left(\frac{b}{x_0 - \Delta x}\right)\right) = \Delta x \sqrt{1 - \left(\frac{b}{x_0 - \Delta x}\right)^2} \tag{4.5}$$

Where Δl is considered as positive control column displacement and x_0 indicates the known string length for neutral elevator position. Equation 4.5 introduces an assumption about performing any elevator control inputs around the exact neutral position. This is unrealistic in actual flight conditions, since the extension (length l) of the control column in steady horizontal flight varies with flight conditions

and trim tab position. The following brief analysis assesses the sensitivity of the control column displacement measurement on the x_0 value.

Around the neutral point, $l_0 = 20.8$ [cm], while the value of $b = 2.5$ [cm] and thus x_0 and θ can be computed as 20.9 [cm] and 14.0°. Applying Equation 4.5 to one of the recorded test measurements gives a signal control column absolute travel of 4.60 [cm]. Now, the same signal can be treated, assuming it has been started when the initial control column has not been at neutral position, but 2.1 [cm] away from it (corresponding to 5° elevator deflection difference). In this case, $l_1 = 22.9$ [cm] and $x_1 = 23.0$ [cm] and leads to an absolute control travel of 4.61 [cm]. Repeating the same for $l_{-1} = 18.7$ [cm] and $x_{-1} = 18.9$ [cm] leads to a absolute control travel of 4.60 [cm]. Given that the difference between the absolute control travels is less than 0.3% for a relatively high deviation from the neutral point (±5° elevator deflection), it is considered reasonable to assume that all signals induced in flight are performed around the neutral point, thus $x_0 = 20.9$ [cm].

In order to translate the determined control column displacement into elevator deflection, a series of ground, stationary, engine-off measurements have been taken, relating the position of the column (measured with a tape measure, ±1 [mm]) to the elevator surface deflection (measured with a digital inclinometer, ±0.1°). The results of this correlation are shown on Figure 4.6, together with a linear fit curve. Table 4.3 quantifies the linear fit characteristics of the correlation.

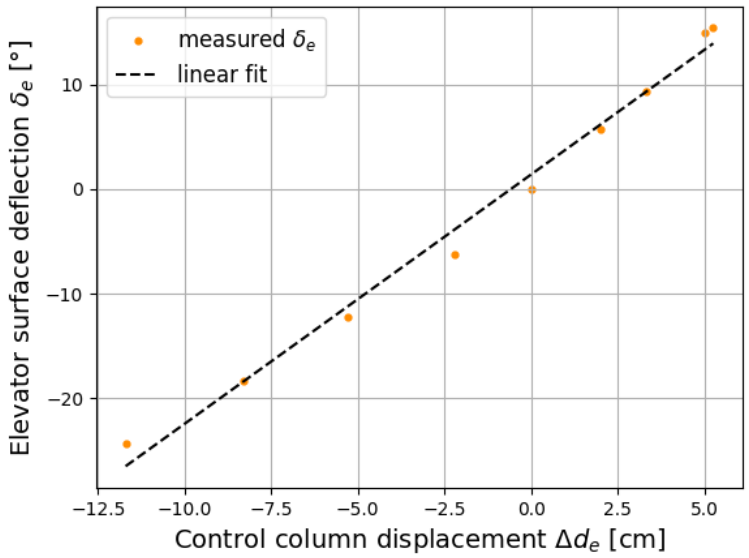

Figure 4.6: Measured elevator surface deflection corresponding to control column displacement around neutral point

	Slope	Intercept	R^2
Value	2.386	1.401	0.989

Table 4.3: Linear fit characteristics of elevator deflection to control column displacement correlation

Since the elevator is a symmetrical control surface and the relation between control surface and column motion is considered linear, the intercept value can be disregarded, even if not null. The slope value only determines the change in elevator surface deflection.

Rudder

The Cessna Skymaster has two rudders, symmetrical with respect to each other, however deflecting asymmetrically - the outboard deflection is higher than inboard. The rudder deflection is therefore expressed by the angle of deflection of the rudder surface inboard, with deflections to the left considered positive. Positive rudder deflection induces negative yaw r and is induced by a backwards right pedal

displacement and forwards left pedal displacement. The neutral rudder position is considered when both pedals are aligned, the rudder chord is aligned with the vertical stabiliser chord and the rudder trim is at neutral position.

Figure 4.7 shows an exploded view of the installation assembly drawing of the pedals [61]. The pedals do not move symmetrically around the neutral position, with a larger displacement forwards than backwards. Their motion, when pressed, is in fact a rotation around the Cross Tube (2) (see Figure 4.7), rather than a translation. In addition to steering the rudder, the pedal controls the aircraft main wheel brake, which is activated by rotating the pedal around the Brake Actuating Arm (1) (see Figure 4.7, pressing the top part of pedal). This renders the identification of pure pedal motion corresponding to rudder control relatively complex.

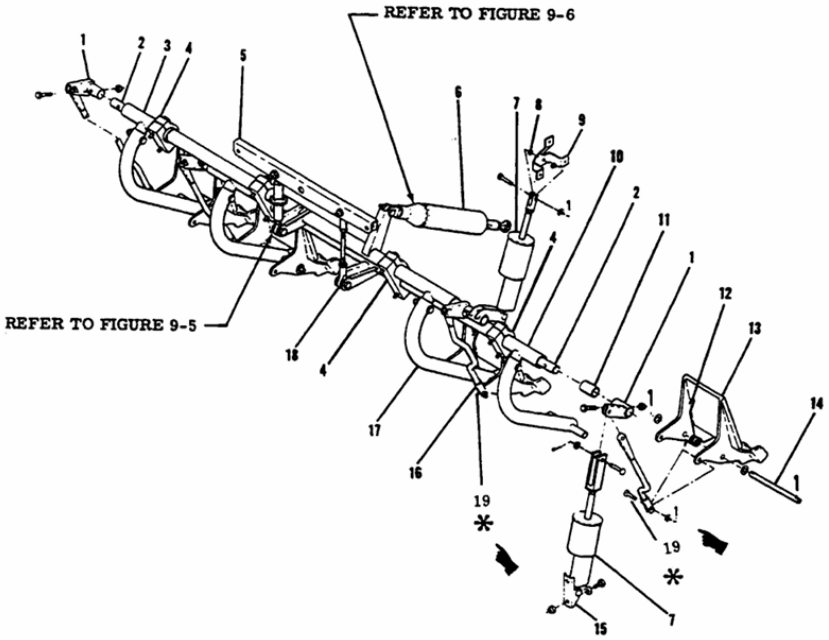

Figure 4.7: Rudder pedals installation [61]

Similarly to the elevator case, the pedal displacement is measured by the Xsens sensor mounted on the pulley, rotating about its Z_X axis. The pulley is attached on the side of the protective panel of the engine controls, in close proximity of the pedals. The end of the pulley string is routed on the side of the Pedal (13) and below the Brake Actuating Arm (1) and attached to the lower end of the Rudder Bar Assembly (10) (see illustrations in section C.2 of Appendix C). This routing aims at avoiding the pedal rotation around the Brake Actuating Arm (1) to influence the measurement of the Rudder Bar Assembly (10) displacement. For technical and safety of flight reasons, the sensors measure the displacement of the right captain pedal and left copilot pedal.

Because of the complex characteristic of the pedal movement, the translation of recorded change in pedal position into rudder deflection is realised by fitting a polynomial function into measured rudder deflection corresponding to pulley string displacement (instead of actual pedal displacement), as presented on Figure 4.8. The rudder deflection is measured by placing a Xsens sensor along the chord of the right rudder, aligned with the hinge of the control surface, in close proximity of the beacon light. A series of full rudder deflections around neutral position are induced by the pedals, the motion of whose is also recorded and expressed as string displacement Δs_r. The coefficients of polynomial of degree five are listed on Table 4.4. The subscript of the coefficient indicates the degree of corresponding term.

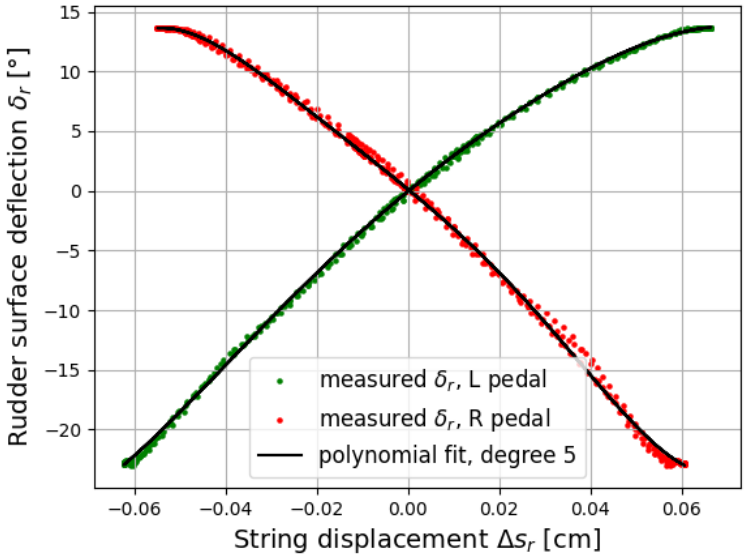

Figure 4.8: Measured right rudder surface deflection corresponding to pedal string displacement

Table 4.4: Fifth degree polynomial fit characteristics of rudder deflection to pedal string displacement correlation

Polynomial fit	a_5	a_4	a_3	a_2	a_1	a_0
Right pedal	$9.752 \cdot 10^6$	$-8.065 \cdot 10^4$	$-3.074 \cdot 10^4$	$-1.098 \cdot 10^3$	$-3.155 \cdot 10^2$	$1.207 \cdot 10^{-1}$
Left pedal	$-1.737 \cdot 10^6$	$5.275 \cdot 10^4$	$1.406 \cdot 10^3$	$-1.412 \cdot 10^3$	$3.129 \cdot 10^2$	$-5.071 \cdot 10^{-2}$

The flattening of the curves observed at the full deflection, as shown on Figure 4.8, can be due to the pedals following a combination of translational and rotational motion. The motion is approximately translational around the neutral position, but diverges at full deflections. Another effect potentially affecting the quality of recorded results is the force opposing the pedal motion, proportional to the pedal displacement. The rudder deflection is coupled with the spring loaded rotation of the nose wheel. Given the measurement has been performed on the ground, with nose wheel touching the ground, a resistive force is exerted by the spring onto the pedals, when the wheel is not free to rotate. An attempt to decrease this effect has been undertaken by placing two smooth plates separated by a layer of grease under the nose wheel, reducing its resistance to rotation.

Since the rudder moves asymmetrically, the outboard deflection has to subsequently be scaled by $13.6/22.8 \approx 0.596$, which corresponds to the recorded maximum rudder deflection inboard to outboard ratio.

4.1.4. Measurement uncertainty

The determination of control surface deflection is prone to errors which increase the uncertainty of deflection, negatively affecting the model identification of the aircraft. The errors originate from the mechanical imperfections of the aircraft mechanics, such as play or cable extension, but also the steering column measurement uncertainty and computation of the sensor rotational angle from its recorded attitude. This paragraph aims at identifying and quantifying the order of magnitude of the errors affecting the uncertainty of the control surface deflection.

Measurement standard deviation

As stated before, the manufacturer of the Xsens sensors states an accuracy of 1° 1σ RMS for inclination (ϕ, θ) and 2.0° 1σ RMS for heading (ψ) for a dynamic mode. The dynamic mode is recommended for "fast and jerky motions that last for a short time" [81], such as the execution of a doublet or 3211 control input.

In order to observe the attitude measurement noise standard deviation as well as the propagation of its effects throughout the computation of the sensor's angle of rotation around Z_X, the standard deviation σ of attitude measurements with known, expected constant value can be computed. Subsequently, numerical differentiation is applied on the Euler angles (see section D.1), the sensor rotation around Z_X axis is computed (see Equation 4.1) and integrated (see section D.1) and the standard deviation at each step of this computation can be determined. Using data recorded in a series of 12 engine-off, stationary ground measurements consisting of single doublet inputs to all control surfaces (same as introduced in section 4.1), the initial, constant part of the signal, preceding the control input, is taken for this analysis. This provides a overall 12 signal bits, during which the expected attitude of the sensor is constant, and therefore the measurement noise is isolated and expressed in the form of error standard deviation.

Table 4.5 lists the 12 measurements constant signal part average standard deviation σ of the measured sensor attitude ϕ, θ, ψ, attitude angles time derivatives $\dot{\phi}$, $\dot{\theta}$, $\dot{\psi}$, sensor body rotational rate r and angle $\int rdt$. The same analysis has been performed for the constant signal parts after the control input, yet the data is not shown for brevity and because of its similarity to the presented case.

Table 4.5: Average standard deviation values from 12 ground engine-off measurements

	$\overline{\sigma}_\phi$ [°]	$\overline{\sigma}_\theta$ [°]	$\overline{\sigma}_\psi$ [°]	$\overline{\sigma}_{\dot{\phi}}$ [°/s]	$\overline{\sigma}_{\dot{\theta}}$ [°/s]	$\overline{\sigma}_{\dot{\psi}}$ [°/s]	$\overline{\sigma}_r$ [°/s]	$\overline{\sigma}_{\int rdt}$ [°]
Aileron	0.100	0.008	0.090	1.160	0.142	1.104	0.386	0.031
Elevator	0.013	0.042	0.036	0.130	0.527	0.304	0.651	0.058
Rudder	0.008	0.167	0.013	0.108	1.633	0.254	1.632	0.168

Table 4.5 shows indeed insignificantly small values of attitude standard deviations, independent on the control surface, the measurement noise is therefore low. Expectedly, the numerical differentiation amplifies the measurement noise by around one order of magnitude, yet this seems not to affect significantly the body rotational rate r noise (given that its magnitude reaches order of 10^3 during doublet or 3211 signal inputs) nor the angle of body rotation (order of full rotations during typical signal).

Now, the same analysis is performed on a series of two engine-on stationary ground measurements, allowing to capture the engine vibration influence on the measurement noise. The average values of standard deviations at all steps are presented on Table 4.6.

Table 4.6: Average standard deviation values from two ground engine run measurements

	$\overline{\sigma}_\phi$ [°]	$\overline{\sigma}_\theta$ [°]	$\overline{\sigma}_\psi$ [°]	$\overline{\sigma}_{\dot{\phi}}$ [°/s]	$\overline{\sigma}_{\dot{\theta}}$ [°/s]	$\overline{\sigma}_{\dot{\psi}}$ [°/s]	$\overline{\sigma}_r$ [°/s]	$\overline{\sigma}_{\int rdt}$ [°]
Aileron	0.155	0.076	0.155	3.462	2.002	3.342	1.309	0.058
Elevator	0.032	0.092	0.295	0.790	1.525	1.055	0.676	0.290
Rudder	0.051	0.028	0.049	2.099	1.027	2.601	1.049	0.024

Table 4.6 shows an increased noise in the attitude measurements, yet still within the same order of magnitude as compared to the engine-off case. The noise is once more significantly amplified by numerical differentiation, yet the low values of body rotation angle imply low drift.

Computation error

The numerical differentiation and integration introduce an error, which might affect the uncertainty of the computed variable. In this case however, the integration is considered exact, since no information exists about the shape of the integrated function in between the discrete points of sampled signal, while the recording frequency of 60 [Hz] is high enough to capture all signal dynamics. Only the computational error of the numerical differentiation is therefore addressed.

The signal is sampled at the maximum available frequency in the given mode, $f = 60$ [Hz], which is significantly smaller than the optimum time step of square root of machine epsilon. The rounding error is therefore not an issue in this case. In order to minimise the estimation error of the finite difference, the order of the scheme can be increased. This, however, comes with the cost of noise amplification,

which grows with the sum of finite difference coefficients. Given the noise standard deviation σ_f can be computed with the general law of propagation of uncertainty for a function f of several variables x_i with standard deviations σ_{x_i} [34]:

$$\sigma_f = \sqrt{\sum_i \left(\frac{\partial f_i}{\partial x_i}\sigma_{x_i}\right)^2} \tag{4.6}$$

The formula can be applied for a finite difference scheme of order n, step size h and coefficients c_k, the sum of squares of which grows with n:

$$\sigma_{f'} = \frac{\sigma_{x_i}}{h}\sqrt{\sum_{k=1}^{n} c_k^2} \tag{4.7}$$

For a high dynamics, yet relatively low noise signals, the highest available sampling frequency is taken to catch the signal dynamics, however the finite difference scheme is taken of the fourth order as compromise between estimation error ($O(h^4)$) and noise amplification.

Controls mechanical inaccuracies

A challenge in the determination of errors in the control surface deflection estimation is the lack of any existing systems that could provide a source of validation data. The proposed method of surface deflection determination is essentially the first attempt to do so on the given aircraft.

In order to give an estimation of the control surface deflection information in the cockpit, an aileron deflection indicating dial has been attached to the instrument panel, around the control column tube. Markings have been made on the control column tube, which point at the aileron deflection indication on the dial (longitudinal line along the control column tube axis) as well as indicate the elevator deflection (lateral lines along the control column tube axis). Illustrations of the markings made can be seen in section C.4 of Appendix C. Because of the limited accessibility to the pedals which are hidden under the instrument panel, no visual indication has been made for rudder deflection estimation. The markings allow to estimate the magnitude of control surface deflection in flight or during ground testing.

An attempt is made to compare the maximum deflections of control surfaces, as reported by the manufacturer, measured with the on the control surface and determined by the Xsens sensor from the column/pedal deflections. The values are reported on Table 4.7.

Table 4.7: Maximum control surface deflection according to manufacturer, measured on control surface and column/pedal

Source	Aileron	Elevator	Rudder
Manufacturer's manual	down 14.5° ± 2°	down 15.0° ± 1°	inboard 15.0° + 0° − 2°[1]
	up 21.0° ± 2°	up 26.0° ± 1°	outboard 22.0° ± 2°
Inclinometer/ruler	down 13.9°	down 14.0°	inboard 14.7°
	up 20.1°[2]	up 25.8°	outboard 19.8°
Xsens sensor	down 14.7°	down 14.4°	inboard 13.6°
	up 21.3°[2]	up 24.9°	outboard 22.7°

Data presented on Table 4.7 show that nearly all measured surface control maximum deflections are within the manufacturer's uncertainty (outboard rudder exceeded by 0.2). The values of maximum control surface deflection determined by the Xsens sensor are also close to the ones measured by the inclinometer, with the maximum deviation of 2.9° for the outboard rudder deflection. Overall, Table 4.7 showcases the imperfections of the control deflection measurement and can be treated as an indication of expected inaccuracies. Maximum deflections, however, are not expected to be reached through the anticipated flight testing. The measurements reported on Table 4.7 have been taken on ground, thus excluding the potential aerodynamic force cable extension.

[1] Measured parallel to the fin water line

[2] In this study, aileron deflection is expressed as downward deflection only, the values of upward deflection are a result of scaling the downward deflection by 21/14.5.

Table 4.8 lists the measured play of both the control surfaces as well as the steering column and pedals. The presented play of the control surfaces and steering column/pedals should be treated independently, i.e. the play in yoke rotation does not translate directly to the play in the aileron hinge.

Table 4.8: Measured approximate play of control surfaces and column and pedals

Location	Aileron	Elevator	Rudder
Steering column and pedals	2°	2 [mm]	CPT: none, COP: 5 [mm]
Control surface	0.3°	0.3°	R:1.1°, L:0.8°

It is worth noting that the yoke rotation play of 2° corresponds to the discrepancy between the captain (CPT) and copilot (COP) yoke orientation. The captain's pedal is infinitesimal, however noticeable on the copilot side, as the pedals on the right side are removable (rod 17, see Figure 4.7).

Pulley winding inconsistency

The pulley described in subsection 4.1.2 winds a 0.6 [mm] diameter string on a drum of diameter 24.9 [mm] and width of 4 [mm]. As the string winds onto the drum, the effective radius of the drum increases, which is a source of error, given the drum radius is assumed constant.

As an attempt to quantify this error, the following brief analysis can be considered. Although the string winds itself onto the drum bed in a relatively random way, it tends to align itself along the smallest radius, given it is under the spring tension. It therefore takes around 6.7 full pulley rotations for the string to fully fill the drum bed width and wind onto a full layer of string, which increases the diameter of the drum to 26.1 [mm], adding twice the string diameter to the drum radius. The string displacement is now 82.0 [mm] for a full rotation, compared to the 78.2 [mm] with no winded string at all. This gives on average an increase of string displacement of less than 0.6 [mm] per rotation of the pulley, which translates to approximately 0.13° of elevator deflection.

Given that a full rudder deflection induces less than two full sensor rotations, while a ±10° elevator input induces just over one full rotation, the effect of winding inconsistency is relatively small, yet not negligible. This is also confirmed by the experimental determination of the average drum radius, as mentioned on subsection 4.1.2.

Cable extension

Finally, it is recognised that change in relative control cable length can be another source of uncertainty in control surface deflection determination. This can be caused by the difference in thermal expansion rates between the aircraft and the control cables, resulting in varying tension of the control cables, but also the aerodynamic force resisting the deflection of control surface, thus increasing the tensile stress in the control cable. Although the control surfaces can be aerodynamically balanced, the change in their deflection still requires force, which changes the tensile stress of the control cables. The determination of the cable extension is considered a complex problem and is outside of the scope of this study, in which it only recognised.

4.2. Fuel mass determination

Throughout the study, the accuracy of the fuel probe indication has been identified as relatively poor, most likely due to its age. Although its replacement is planned, it is not anticipated before the end of the study. This implies that the fuel mass displayed and recorded by the engine monitor might be off, which imposes the need for an alternative fuel mass identification method or correction of the value displayed.

In order to address this issue, an experiment is carried out during which emptied fuel tanks are gradually filled with known volumes of fuel. At each instance, the mass of fuel displayed by the monitor is noted, and the height of the fuel surface in the tank is measured with a wooden stick inserted by the fuel tap. The experiment is carried out with the aircraft standing on flat ground, while the calibrated fuel station pump guarantees a precise dosage of known volume of fuel. Measurements are taken at fuel volume steps of 10 [l], for each fuel tank. As mentioned also in subsection 5.1.3, the density of fuel has been determined to be 752.6 [kg/m^3] or, equivalently, 1.659 [lbs/l].

Table 4.9 lists the actual fuel volume and mass in the main tank and corresponding MVP displayed value. The height of the fuel level measured by the stick is given in the first column. Data from Table 4.9 is plotted on Figure 4.9, showing the displayed fuel mass against the actual fuel mass in both main tanks.

Table 4.9: Actual and MVP displayed main tank fuel mass data showcasing the MVP fuel mass deviation

Stick height [mm]	Actual fuel volume [l]	Actual fuel mass [lbs]	MVP indication L [lbs]	MVP indication R [lbs]
0	0	0.00	0	0
0	10	16.59	47	17
0	20	33.18	20	41
0	30	49.78	39	66
0	40	66.37	41	80
0	50	82.96	56	90
0	60	99.55	68	102
0	70	116.14	85	120
10	80	132.74	100	139
20	90	149.33	113	155
35	100	165.92	130	172
45	110	182.51	146	187
50	120	199.10	164	203
60	130	215.70	182	221
70	140	232.29	211	240
85	150	248.88	245	256
100	160	265.47	274	271
110	170	282.06	276	276
120	176	292.02	276	276

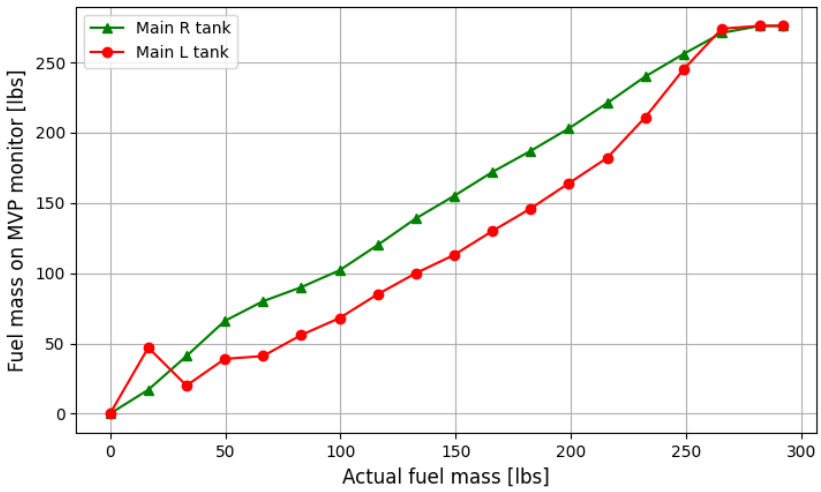

Figure 4.9: Recorded engine monitor fuel mass indication for different actual fuel mass, main tanks

Table 4.10 lists the equivalent experiment data, yet for both auxiliary tanks. It shows the mass of the auxiliary tanks fuel as displayed by the MVP for different volumes of actual fuel and its surface height measured by the stick. In a similar way to Figure 4.9, Figure 4.10 plots the displayed against actual fuel mass for the right and left auxiliary tank.

Table 4.10: Actual and MVP displayed auxiliary tank fuel mass data showcasing the MVP fuel mass deviation

Stick height [mm]	Actual fuel volume [l]	Actual fuel mass [lbs]	MVP indication L [lbs]	MVP indication R [lbs]
0	0	0.00	0	0
15	10	16.59	0	0
35	20	33.18	18	27
60	30	49.78	35	41
85	40	66.37	50	58
110	50	82.96	66	74
140	60	99.55	85	92
-	67	111.17	92	-
185	70	116.14	-	107

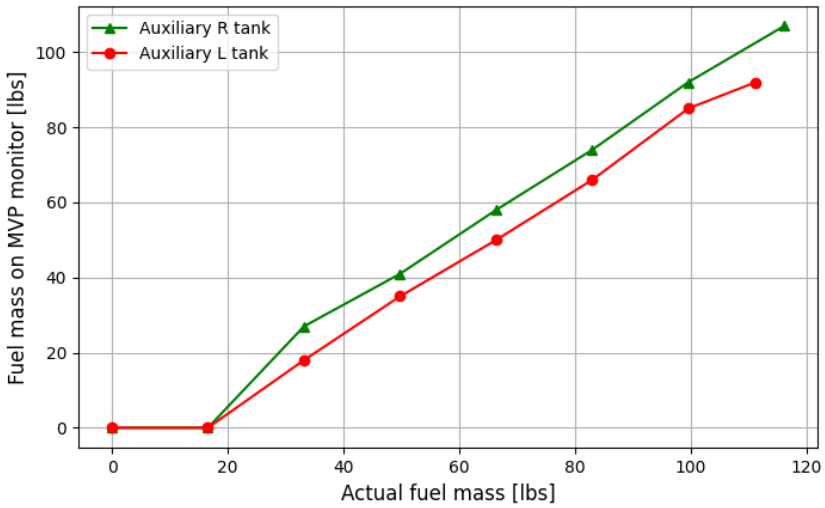

Figure 4.10: Recorded engine monitor fuel mass indication for different actual fuel mass, auxiliary tanks

The results of the measurement show that the deviation of the fuel probe from actual fuel mass can be significant, with maximum values of 36.5 and 16.2 [lbs] for the left and right main tanks, respectively, and 19.2 and 16.6 [lbs] for the left and right auxiliary tanks, respectively. The expected linear trend of displayed to actual fuel mass value is maintained throughout the middle portion of the fuel mass range, yet anomalies occur at close to full and close to empty states of the tanks. In particular, the probe seems to fail to measure the fuel mass of the auxiliary tank up to approximately 20 [lbs] and ignores the fuel in excess of around 270 [lbs] in the main tank.

The occurrence of the outlier displaying 47 [lbs] at actual 16.59 [lbs] in the left main tank suggests possible inconsistencies in the behaviour of the fuel probe indications. For this reason, the stick method can be used as a more certain solution to determine the actual fuel mass on the ground, with a range of usefulness starting from approximately 120 [lbs] for the main tank. In flight, the determined fuel probe indication correction has to be used, which is realised with the `ac_realfuel.m` function, which linearly interpolates between the data points presented on Figure 4.9 and Figure 4.10.

4.3. Broadcasting Outer Module (BOM)

The aircraft mathematical model, as defined by Equation 3.21 and Equation 3.22, is a function of the angle of attack and angle of sideslip. This implies the necessity to record the aforementioned independent variables in flight, which, at the early stage of the equipment of the aircraft with scientific instrumentation, is realised with the Levil BOM, acquired for this purpose.

4.3.1. Description

Among other variables such as IMU and GPS data, the BOM measures the angle of attack and angle of sideslip with the help of five pressure probes arranged in a cross shaped pattern against the freestream - one total pressure probe at the BOM nose, two total pressure probes arranged vertically and two static pressure probes arranged horizontally.

The BOM records data with a default frequency of 1 [Hz], which can be increased to 5 [Hz] by changing appropriate settings. This change is however applied only after a subsequent power up of the BOM, meaning that it cannot be effective in flight, when the BOM is running. This is of particular importance when recalibrating the device, which requires restoring default settings, thus automatically changing the frequency to 1 [Hz]. In order to record at 5 [Hz] during a calibration flight, it is recommended to restore default setting and change the frequency on the ground, turning off and on again the BOM before the flight.

When investigating the working principles of the BOM, it becomes clear that the air data probes are designed to serve as a stall warning system rather than an angle of attack measurement. Although the angle of sideslip is measured and outputted by the BOM in degrees, the angle of attack variable is provided as a nondimentional value between 0 and 100 (or 0.00 and 1.00, depending on the version), with 100 indicating stall and 0 indicating conditions in which the high and low probes record the same pressure. Equation 4.8 defines the BOM angle of attack indication output, as provided by the manufacturer, Levil Aviation.

$$AoA_{BOM} = c \cdot \frac{\left(\frac{p_t}{V^2} - CP_{low}\right)}{\left(CP_{high} - CP_{low}\right)} \tag{4.8}$$

Here, CP_{low} and CP_{high} correspond to airflow conditions at low and high total pressure probes at the calibration point, while c is a constant.

In order to correctly signal the stall of any aircraft, the BOM has to be calibrated in flight, by establishing a steady, level and horizontal flight at $1.15 \cdot V_{min}$, equal to 80.5 [kt] in the case of the C337 (variable depending on mass). Once established, the particular flow field around the BOM is memorised upon signalling it via the Levil ADHRS mobile application. At calibration, the $AOA_{BOM} = 85$ (or 0.85, depending on the version), suggesting a constant $c = 85$ (or 0.85).

4.3.2. Angle of attack measurement

As the AOA_{BOM} is recorded by the BOM, it has to be translated into an effective angle of attack α acting on the wing of the aircraft. It cannot be assumed that when $AOA_{BOM} = 0$ then $\alpha = 0$, as an offset might be present due to upwash and misalignment of the BOM longitudinal axis with the wing chord.

A first attempt to determine a correlation between the AOA_{BOM} and α has been made by identifying flight instances during which the flight path angle γ is zero (or rate of climb ROC or vertical speed are null). In such conditions, the angle of attack is equivalent to the aircraft pitch θ. Figure 4.11 shows the data points from two test flights, during which such condition have been isolated and the values of θ and AOA_{BOM} extracted and plotted.

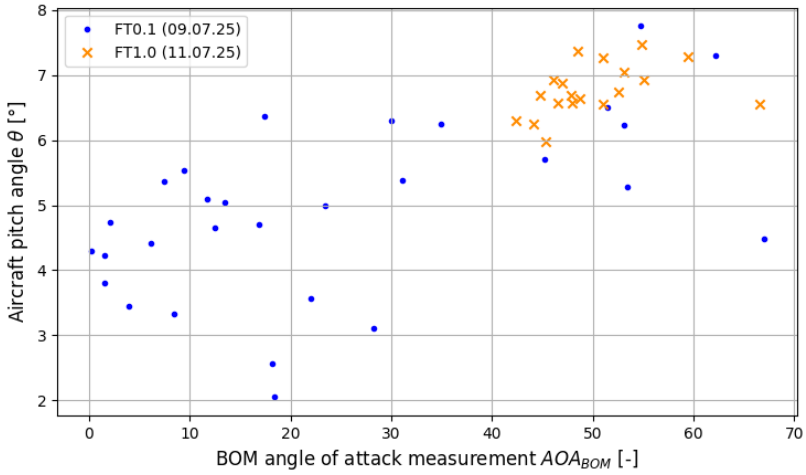

Figure 4.11: Aircraft pitch angle θ plotted against the AOA_{BOM} for $\gamma = 0$ conditions

The correlation between θ and AOA_{BOM} is poor for both flight datasets, namely the coefficient of determination R^2 is 0.542 for the FT0.2 flight and 0.406 for the FT1.0 flight. The reason for such low values of R^2 is most likely due to very brief instances of $\gamma = 0$ flight conditions, in which the vertical speed oscillates around zero, instead of remaining close to zero for a time long enough to allow the stabilisation of the aircraft attitude readings. Thus, at instances where γ crosses zero, even at low rates, the values of θ and AOA_{BOM} increase or decrease, causing a mismatch.

For the aforementioned reason, an alternative solution for the AOA_{BOM} to α translation is proposed. For a particular aircraft mass and BOM calibration point, the values of $AOA_{BOM} = [0, 85, 100]$, correspondence to zero total pressure difference across probes, calibration point and stall, each occur at particular V_{TAS} in steady, level, horizontal flight, which are easily determined in flight. With the aircraft mass and air density known, the true angle of attack α can be determined from the C337 lift curve and the application of the lift equation.

Figure 4.12 shows the C337 lift curve determined by Ramesh [58] using several numerical tools. For the purpose of this study, the viscous CFD out of ground effect (OGE) simulation results are used, indicated by the red curve. The lift curve slope is $C_{L_\alpha} = 0.086^{\circ -1}$, zero lift angle of attack is $\alpha_{C_{L=0}} = 3.879^\circ$ and lift coefficient at zero angle of attack $C_{L_{\alpha=0}} = 0.333$.

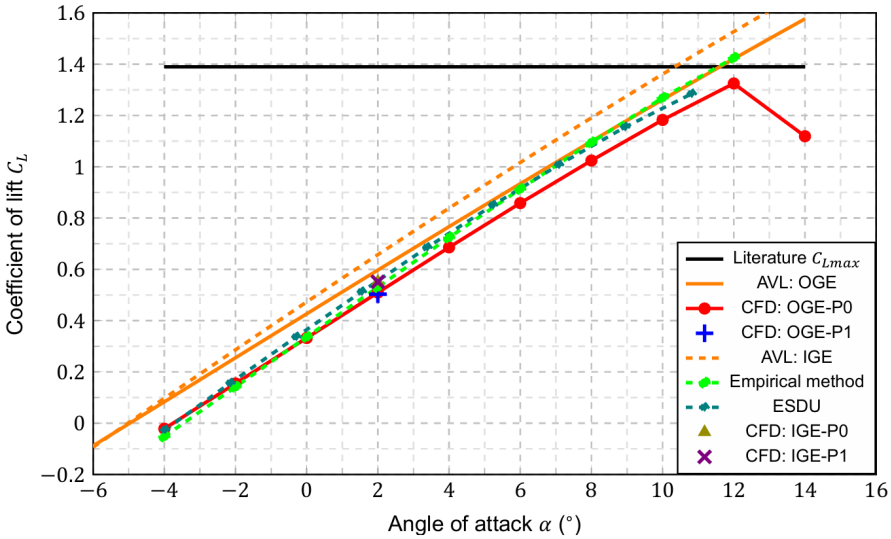

Figure 4.12: Cessna Skymaster lift coefficient as function of angle of attack determined numerically [58]

Figure 4.13 plots the angle of attack α against the AOA_{BOM} determined for values of $[0, 85, 100]$ for both the FT0.2 and FT1.0 test flights for which the aircraft mass was approximately 1,778 and 2,044 [kg], respectively. A curve is subsequently fitted through the data points to ensure a continuous correlating function. It is assumed that α can be expressed as function of AOA_{BOM} as an exponential function of the form $\alpha = e^{\sum_{k=0}^{6} a_k AOA_{BOM}^k}$, where the exponent is a polynomial of sixth degree. The degree of the polynomial is chosen as low as possible, but high enough to guarantee a continuously increasing function throughout the entire AOA_{BOM} domain. Table 4.11 lists the function coefficients, where the subscript indicates the degree of corresponding term.

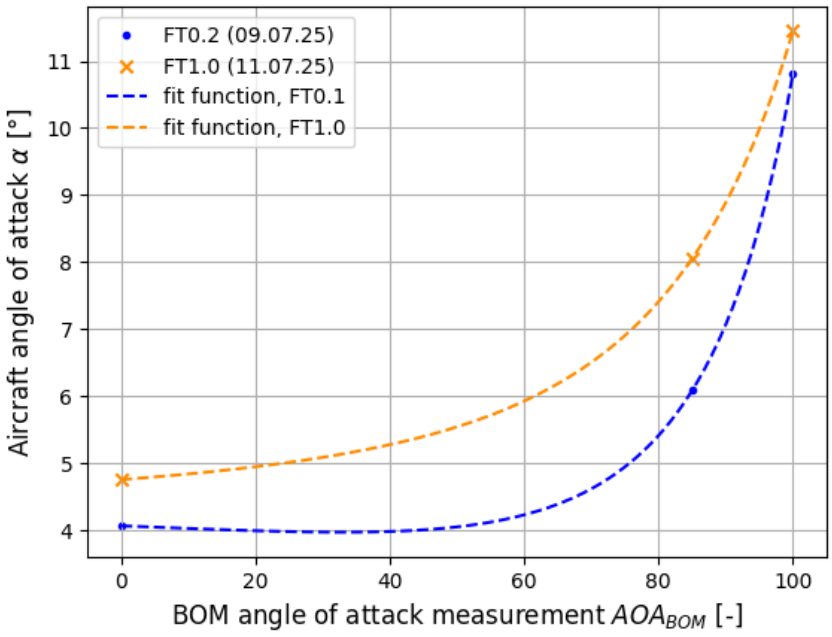

Figure 4.13: α corresponding to AOA_{BOM} values determined for FT0.2 and FT1.0 together with exponential function fit

Table 4.11: Sixth degree polynomial fit of the exponential function

Polynomial fit	a_6	a_5	a_4	a_3	a_2	a_1	a_0
FT0.1	$4.188 \cdot 10^{-13}$	$3.235 \cdot 10^{-11}$	$2.199 \cdot 10^{-9}$	$1.115 \cdot 10^{-7}$	$3.298 \cdot 10^{-7}$	$-9.854 \cdot 10^{-4}$	$1.402 \cdot 10^{0}$
FT1.0	$1.278 \cdot 10^{-13}$	$1.370 \cdot 10^{-11}$	$1.455 \cdot 10^{-9}$	$1.525 \cdot 10^{-7}$	$1.572 \cdot 10^{-5}$	$1.589 \cdot 10^{-3}$	$1.559 \cdot 10^{0}$

4.3.3. Measurement uncertainty and limitations

This described principle of working of the BOM brings significant limitations to the recording of the angle of attack α for scientific purposes. Although the α to AOA_{BOM} translation presented on Figure 4.13 remains valid for the collected data points, the fitting function remains a prediction of the actual behaviour and should be validated by collecting more data points. This requires a steady and stabilised flight at the slow end of the flight envelope, the achievement of which proves to be challenging in practice.

Moreover, the correspondence of $AOA_{BOM} = 0$ to a given airspeed (90 IAS or 96 TAS [kt] for FT0.2 and 95 IAS or 101 TAS [kt] for FT1.0) effectively limits the useful working range of the BOM to approximately 20 [kt] of airspeed between the stall speed and AOA_{BOM} point. All manoeuvres thus have to be performed within these conditions.

Several actions can be taken to mitigate the limitations of the BOM. The BOM calibration can be performed assuming a "fake" stall speed, thus shifting the working range of the AOA_{BOM} values.

The BOM can also be installed more nose up with respect to the wing chord, allowing to reach the $AOA_{BOM} = 0$ boundary at higher airspeeds (lower aircraft pitch).

4.4. Flight Testing

This section aims at reporting the approach and outcome of the flight testing campaign, stating the desired and achieved flights, describing and motivating the chosen manoeuvres in subsection 4.4.1 and defining the test points within the flight envelope in subsection 4.4.2. In addition, subsection 4.4.3 elaborates on the flight test data preprocessing.

4.4.1. Manoeuvres

The manoeuvres executed during flight testing aim at exciting the aircraft motion, such that the response to a given control input can be recorded and analysed for the derivation of the aerodynamic and control derivatives. Because the control signals are introduced by the pilot by hand, the simple doublet signal and 3211 signal are chosen to excite the aircraft motion in a particular axis.

As the aerodynamic force generated by a control surface deflection is proportional to the dynamic pressure, the aircraft load factor n during a manoeuvrer increases with airspeed and decreases with altitude for a signal of common magnitude and rate. Although it is aimed to maintain a constant magnitude and dynamics of the control input signal, which is facilitated by the visual indications on the control column (absent for pedals, see Appendix C), it can be adjusted by the pilot depending on the flight conditions at the test point. Since the signal input is generated by hand, perfect repetition of the signal is not expected anyway.

As described in subsection 4.1.2, the interference of the aircraft dynamic response to the input signal with the rotational motion of the Xsens sensor should be avoided. In order to achieve that, each control surface shall be excited independently, ideally resulting in a decoupled aircraft response. At each test point, six manoeuvres shall be executed, namely:

1.1. Aileron doublet	2.1. Elevator doublet	3.1. Rudder doublet
1.2. Aileron 3211	2.2. Elevator 3211	3.2. Rudder 3211

A steady, horizontal, symmetrical flight is established for at least 2-3 [s] before the manoeuvre input to allow for a convergence of the Kalman filter before the start of the input signal. The dynamic response of the aircraft to the manoeuvre is not to be interfered with until it is fully damped, which is judged arbitrarily by observing the onboard instruments. Figure 4.14 shows typical control deflection signals recorded throughout testing and outlines some imperfections in induced control inputs.

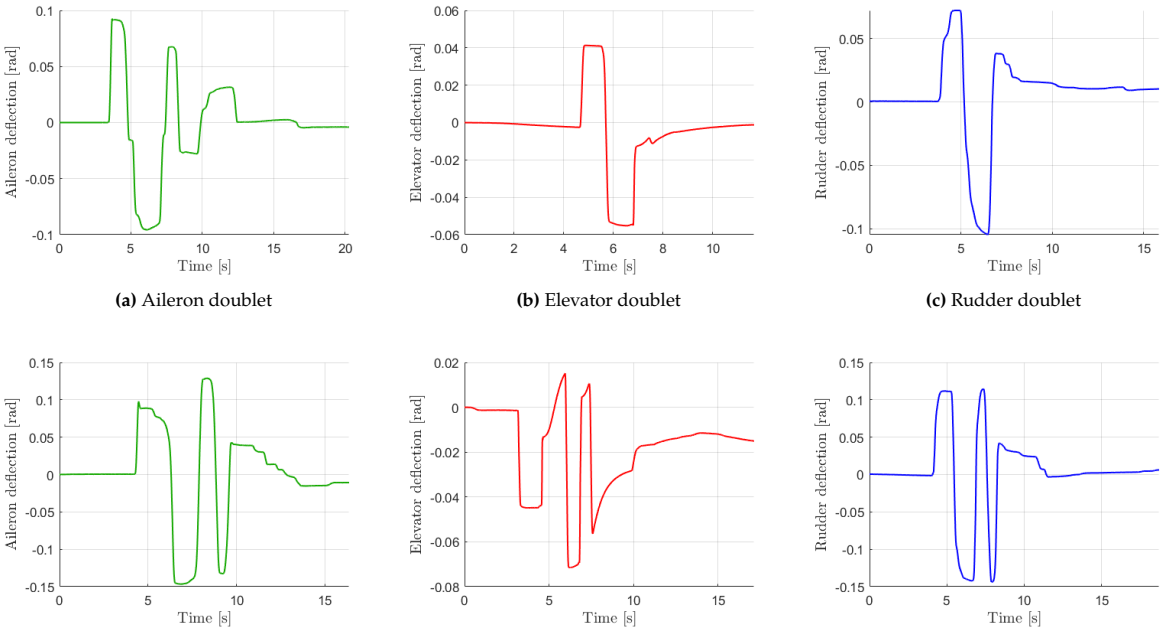

(a) Aileron doublet **(b)** Elevator doublet **(c)** Rudder doublet

(d) Aileron 3211 **(e)** Elevator 3211 **(f)** Rudder 3211

Figure 4.14: Typical control surface deflection signals recorded during identification manoeuvres

The manoeuvres are executed with the aircraft in clean configuration, retracted engine cowl flaps and stowed landing gear. The flight conditions of testing points are defined in subsection 4.4.2. No power setting is specified, other than the desired matching operation of both engines.

4.4.2. Flight testing envelope

As mentioned in Equation 2.3.4, the nondimentional aerodynamic and control coefficients dependence on airspeed and altitude is expected to be approximately linear [29]. This is why, the flight testing envelope is desired be populated with test points evenly spread in the altitude - airspeed plane. Figure 4.15 shows the altitude and airspeed of nine test points desired to be reached to investigate the dependence of aerodynamic derivatives on altitude and airspeed, but also to enlarge the envelope of validity of the provided results. Figure 4.15 compares the desired the flight test conditions to the ones that have been achieved so far.

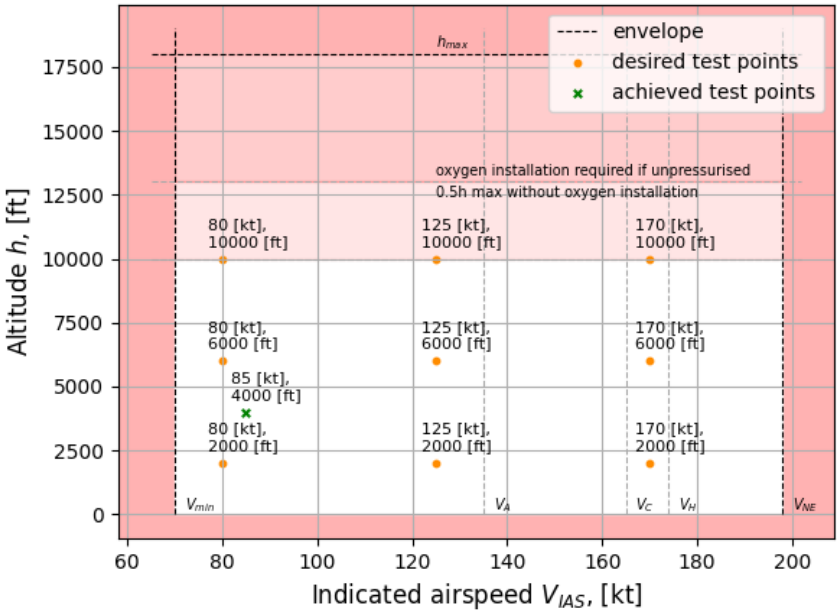

Figure 4.15: Envelope of the anticipated flight test points

The simplified flight envelope showed on Figure 4.15 is enclosed by the stall speed in clean configuration V_{min}, never exceed speed V_{NE}, ground level $h = 0$ and operational ceiling h_{max}. Because the cabin is unpressurised and the aircraft is not equipped with an oxygen installation, the flight time at altitudes above 10,000 [ft] is limited to 30 [min] and forbidden at altitudes above 13,000 [ft] [72].

The airspeed at testing points shown on Figure 4.15 is varied from the value of 80 [kt], taking a 10 [kt] margin from the clean configuration stall speed V_{min}, and 170 [kt], 4 [kt] away from V_H, the maximum speed in level flight at maximum continuous power. Although V_C and V_H are higher than the design manoeuvring speed V_A, no full control surface deflections are anticipated during testing. The altitude of the test points is varied from the value of 2,000 [ft], considered minimum for flight testing manoeuvrers and 10,000 [ft], which is the lower bound of the limited flight time at given altitude.

Until the final phase of the study, all performed manoeuvres have been performed at a common flight conditions of 4,000 [ft] and 85 [kt], due to a limited airspeed range of BOM usefulness (see section 4.3) within a single calibration. This does not provide enough data to answer research question **RQ3**, as stated in section 2.2. Table 4.12 lists the performed flights indicating their conditions and purpose. So far, only a single flight could have been dedicated to flight identification manoeuvres.

Table 4.12: List of performed flights with their conditions and purpose

Flight ID	Date	Altitude [ft]	V_{IAS} range [kt]	Purpose
FT0.1	09.05.25	4,000	80-150	Qualification of control surface deflection measurement method
FT0.2	09.07.25	3,000	80-150	BOM calibration, AOA_{BOM} to α correlation
FT1.0	11.07.25	4,000	80-90	System identification manoeuvres

During FT1.0, 23 decoupled identification manoeuvres are performed, one of which is not considered due to poor control input. Three doublet manoeuvres for each control surface as well as five elevator, three aileron and five rudder 3211 manoeuvres have been executed. 19 manoeuvres are used as identification data set, whereas three manoeuvres, representing 14% of the total dataset, are selected as validation data set (an aileron doublet as well as elevator and rudder 3211).

4.4.3. Data preprocessing

This subsection aims to present the flight test data processing from its recorded or received state, into the format used as input in the flight path reconstruction process of the Two Step method of system identification. This involves variable transformation, resampling and timestamp alignment of the signals, as well as signal reconstructing in the case of the angle of attack and angle of sideslip measurements.

Table 4.13 lists all the recorded parameters used in the study as inputs to either the flight path reconstruction, engine model or aerodynamic model fitting of the parameter identification. The table also indicates the unit, frequency and source of the data.

Table 4.13: List of recorded parameters used in the study together with their frequency and source

Symbol	Parameter	Unit	Frequency	Source
$A_{ac,x}$	Acceleration parallel to X_b	g	50	Arinc ADAHRS
$A_{ac,y}$	Acceleration parallel to Y_b	g	50	Arinc ADAHRS
$A_{ac,z}$	Acceleration parallel to Z_b	g[1]	50	Arinc ADAHRS
p	Roll rate along X_b	°/s	50	Arinc ADAHRS
q	Pitch rate along Y_b	°/s	50	Arinc ADAHRS
r	Yaw rate along Z_b	°/s	50	Arinc ADAHRS
ϕ	Roll angle	°	50	Arinc ADAHRS
θ	Pitch angle	°	50	Arinc ADAHRS
ψ	Magnetic heading	°	25	Arinc ADAHRS
V_{TAS}	True airspeed	kt	12.5	Arinc ADAHRS
OAT	Outside air temperature	°C	2.5	Arinc ADAHRS
h_p	Pressure altitude	ft	25	Arinc ADAHRS
p_s	Static pressure	inHg	12.5	Arinc ADAHRS
h_{GPS}	GPS altitude	ft	5	Arinc NAV
u_E	North-South velocity in F_E	kt	5	Arinc NAV
v_E	East-West velocity in F_E	kt	5	Arinc NAV
w_E	Vertical velocity[2] in F_E	kt	5	Arinc NAV
α	Angle of attack	-	1 or 5	BOM air data
β	Angle of sideslip	°	1 or 5	BOM air data
$m_{f,MR}$	Main right tank fuel mass	lbs	5.56	Engine MVP
$m_{f,ML}$	Main left tank fuel mass	lbs	5.56	Engine MVP
$m_{f,AR}$	Aux. right tank fuel mass	lbs	5.56	Engine MVP
$m_{f,AL}$	Aux. left tank fuel mass	lbs	5.56	Engine MVP
$p_{z,f}$	Front eng. manifold pressure	inHg	5.56	Engine MVP
$p_{z,r}$	Rear eng. manifold pressure	inHg	5.56	Engine MVP
N_f	Front eng. rotational speed	rpm	5.56	Engine MVP
N_r	Rear eng. rotational speed	rpm	5.56	Engine MVP
P_f	Front eng. horsepower[3]	hp	5.56	Engine MVP
P_r	Rear eng. horsepower[3]	hp	5.56	Engine MVP
δe	Elevator deflection angle	°	60	Xsens
δa	Aileron deflection angle	°	60	Xsens
δr	Rudder deflection angle	°	60	Xsens

Variable transformation

As first part of the data processing, all parameters listed on Table 4.13 are converted to SI units, with the exception of engine rotational speed N and manifold pressure p_z which are directly used as input to the engine model in [rpm] and [inHg]. The determination of control surface deflections $\delta e, \delta a, \delta r$ and air data angles α, β from raw measurements has been elaborated upon in section 4.1 and section 4.3,

[1] Normalised acceleration along Z_b axis, ignores gravitational component

[2] Vertical velocity measured positive upwards

[3] The engine horsepower computed by the MVP is recorded for comparison to the engine model estimation rather than for direct usage.

respectively. It is therefore not addressed in the following paragraphs, where these variables are assumed to be expressed in [rad].

Secondly, since not all measured variables correspond directly to the ones desired as inputs to the Kalman filter, they have to be calculated. As described in section 3.1, the measurement vector **z** includes the GPS position and velocity in the navigation frame. The latter is directly measured, such that $u_{GPS_m} = u_E$, $v_{GPS_m} = v_E$ and $w_{GPS_m} = -w_E$. The GPS position is determined by numerically integrating u_{GPS_m} and v_{GPS_m} with the trapezoidal rule (see section D.1), judged sufficiently accurate given the low dynamics of the signal and high upsampling frequency. The XY_E position of the aircraft is always measured with respect to the initial position of each manoeuvre. The vertical position in F_E is taken as the negative value of the GPS altitude, $z_{GPS_m} = -h_{GPS}$.

The state vector **x** includes the body velocity components u, v, w, the initial guess for which is computed with the available air data, as defined by Equation 4.9:

$$\begin{aligned} u &= V_{TAS} \cos\alpha \cos\beta \\ v &= V_{TAS} \sin\beta \\ w &= V_{TAS} \sin\alpha \cos\beta \end{aligned} \tag{4.9}$$

The acceleration parallel to aircraft body axes measured by the accelerometer $\mathbf{A_{ac}}$ behind the left PFD at location [2.03, 0.20, 1.40] [m] in F_D has to be corrected to obtain the desired acceleration of the centre of gravity in F_b, $\mathbf{A_{cg}}$. This is done using the translation of acceleration in ribig body motion, as specified by Equation 4.10:

$$\mathbf{A_{cg}} = \mathbf{A_{ac}} + \dot{\Omega} \times \mathbf{r_{cg/ac}} + \Omega \times \left(\Omega \times \mathbf{r_{cg/ac}}\right) \tag{4.10}$$

Where Ω is the body rotation rate vector $[p, q, r]^\intercal$ and $\mathbf{r_{cg/ac}}$ defines the position of the centre of gravity with respect to the accelerometer.

Resampling

Inputs to the Two Step method of system identification are logically required to be at a common frequency, chosen to be 100 [Hz] for this study. This value is chosen to allow sufficient data points for the Kalman filter convergence without being affected by the manoeuvre dynamics and has been used in application of the the Two Step method for similar aircraft [75] .

Resampling is performed using linear interpolation between measured data points while maintaining the same timestamp. The Python function `numpy.interp` is used for this purpose on all variables whose frequency is equal or higher than 2.5 [Hz]. The KF subsequently takes care of the reconstruction of the signal, including smoothing. For low quality signals, for instance when the angle of attack α and angle of sideslip β are recorded at 1 [Hz], signals are upsampled and reconstructed using the quadratic spline function, numerically implemented as `scipy.interpolate.interp1d` Python function, as demonstrated on Figure 4.16.

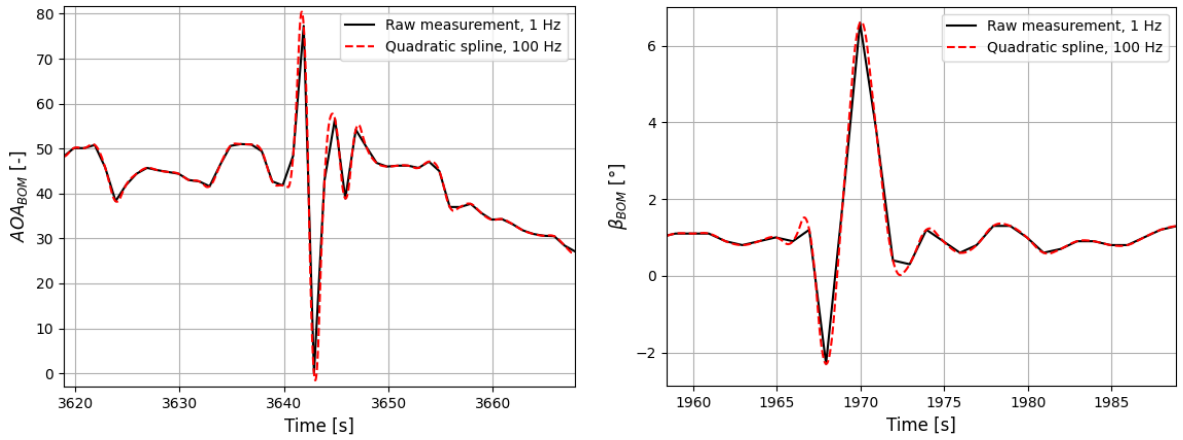

(a) BOM angle of attack during an elevator 3211 manoeuvre

(b) BOM angle of sidedlip during an aileron doublet manoeuvre

Figure 4.16: Low frequency BOM signal reconstruction and upsampling using quadratic spline function

The reason behind the reconstruction of the α and β signals before feeding them into the Kalman filter is dictated by desire to capture their high unsteadiness in opposition to for example OAT, which is steady throughout the manoeuvre and used for atmospheric conditions determination. The quadratic spline interpolation comes at the cost of the mismatch of the fitting function at the initiation and end of the manoeuvre dynamics. Given the poor quality of the raw BOM signal and relatively low fitting function mismatch, quadratic spline fitting for the AOA_{BOM} and β_{BOM} signals is considered overall beneficial.

Filtering

Although the Kalman filter takes care of noise filtering of the state **x** and measurement **z** vectors, the input vector **u** remains unfiltered. The IMU white noise is small in magnitude (see Table 4.15), however becomes important in the least squares parameter identification process, when Equation 3.22 is applied onto the numerically differentiated body rotational rates. As a result, the observation vector contains amplified noise. For this purpose, an attempt is made to filter and smooth out the signal of the input vector constituents.

This is performed in three steps. First, the original, raw signal of 50 [Hz] is processed with a moving average of window width $w = 4$. It has been observed that some of signal dynamics can be lost with window sizes $w > 4$, while keeping in mind that $w = 4$ typically embraces two white noise periods. Secondly, a polynomial interpolation of degree $d = 2$ and window width $w = 11$ is applied, which smooths out the averaged signal, distributing the polynomial coefficients around the central element of the moving window. Lastly, a quadratic spline interpolation is applied to upsample the 50 [Hz] signal to 100 [Hz] signal. The result is presented on Figure 4.17 in which the A_z acceleration is plotted against flight time during an elevator 3211 manoeuvre. Figure 4.17a shows the big picture of the signal showing that the smoothing does not significantly affect the overall amplitude and dynamics of the signal, while Figure 4.17b shows the zoomed in steady signal, picturing the decrease in white noise in four steps.

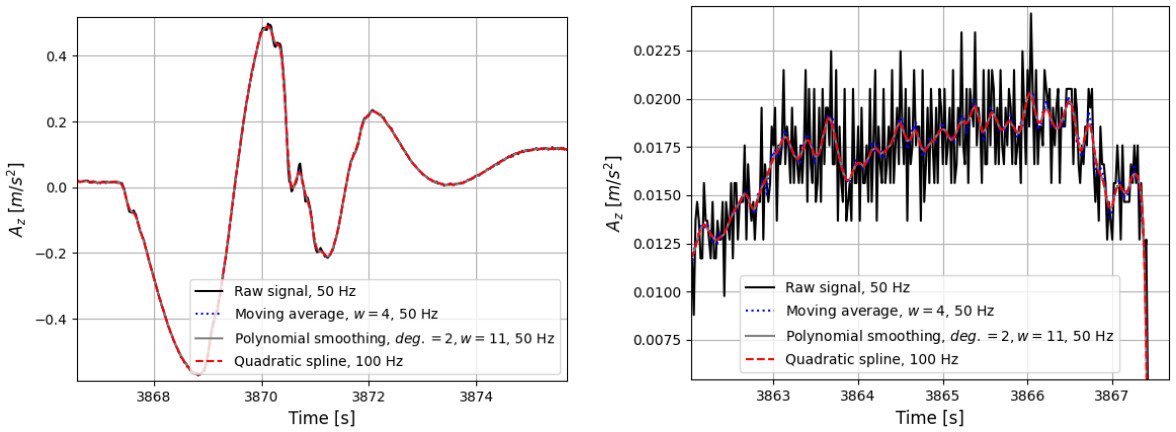

(a) Big picture of the A_z acceleration during an elevator 3211

(b) Steady A_z signal prior to elevator 3211

Figure 4.17: Effect of applying filtering, smoothing and upsampling on the input vector

The moving average window size, polynomial smoothing degree and window size have been chosen to compromise the filtering performance and loss of signal amplitude and dynamics. When increasing the moving average or smoothing polynomial window size, the signal dynamics are depreciated and amplitude reduced, although the filtering effect is more visible. Increasing the smoothing polynomial degree allows to better fit data points of the original signal into the smoothed signal.

Timestamp alignment

The parameters listed on Table 4.13 originate from five different sources, with four different internal clocks. Both the ADAHRS and navigation parameters transmitted via the Arinc are timestamped with their common, stable and high-resolution clock by hardware, while the engine MVP is timestamped in software by the CPU clock of lower accuracy. The BOM reports the UTC time for each data point to the nearest second, but also times them from power up in milliseconds. The Xsens sensors provide the recording starting time in UTC to the nearest millisecond of the recording mobile device and counts the data point sampling time since the sensors power up to the nearest microsecond.

Except of the Xsens sensors, all parameters are recorded continuously during the entire flight duration. In order to align the MVP and BOM clocks to the Arinc clock, parameters recorded in common by the three sources are compared throughout the entire flight time range. For the MVP to Arinc time alignment, aircraft load factor n and IAS are compared. For the BOM to Arinc time alignment, the IAS, pitch θ and roll ϕ are compared. The time relation of the MVP and BOM to the Arinc is subsequently expressed as $t_{arinc} = p_0 + (1 + p_1) \cdot t_{MVP}$ [s] and $t_{arinc} = p_2 + (1 + p_3) \cdot t_{BOM}$ [s], respectively. Table 4.14 lists the determined constants p_0, p_1, p_2, p_3 for performed test flights.

Table 4.14: Timestamp alignment constants for for the MVP and BOM

Flight	p_0 [s]	p_1 [-]	p_2 [s]	p_3 [-]
FT0.1	-1.720	$-4.58 \cdot 10^{-5}$	-899.790	$-1.11 \cdot 10^{-4}$
FT1.0	-0.734	$-4.51 \cdot 10^{-5}$	-258.810	$-1.43 \cdot 10^{-4}$

The flight test data including the Arinc and MVP parameters is provided by the Flight Testing Department in *.hdf5* format, together with the implementation and description (p_0 and p_1) of the aforementioned method of timestamp alignment. The timestamp alignment of other data with Arinc and determination of p_2 and p_3 has been performed as part of the presented study.

It is worth noting that after the time correction, the time mismatch between the MVP n and IAS has been determined to be 0.23 [s] for FT0.2 and 0.19 [s] for F1.0. Given that the engine parameters remain relatively steady during performed manoeuvres, this has no implication on the quality of the study. The BOM shows a mismatch between IAS (air data) and θ and ψ (GPS data) of around 0.21 [s] per 1000 [s] of flight, which indicates a potential difference in p_3 for these parameters. Since the BOM is used to

retrieve α and β, which are part of the BOM air data, the BOM timestamp is aligned with IAS, rather than with θ and ϕ.

Lastly, the Xsens sensors timestamp is aligned with the Arinc time by means of its UTC time of start of recording. For operational reasons, the Xsens sensors are not recording continuously during the entire flight, but are set to record only during the manoeuvres of interest. Since a delay exists between the "record" command and actual onset of data recording, manual alignment corrections are necessary, usually within 1.5 [s]. The manual alignment is performed to 1-2 [ms] precision by identifying the first data point of aircraft body acceleration A_x, A_y, A_z responding to a corresponding control deflection signal onset $\delta_a, \delta_r, \delta_e$. The aligning precision corresponds to the frequency of Arinc recorded aircraft body acceleration of 50 [Hz].

Although not observed consistently and only for isolated forces or moments, a time delay has noticed between the model fitting signal and observation signal. An example of such a behaviour of the C_l moment can be seen on Figure B.23 of Appendix B. A brief time shifting sensitivity analysis has eliminated errors in BOM or Xsens timestamping alignment as cause of this behaviour. Cable extension or aerodynamic delay could be reasons, yet a more consistent behaviour throughout all signals would be expected in such a case and a decreased model fitting performance (control surface contribution signal in time misaligned with remaining contribution). Nevertheless, it is strongly recommended to increase the level of confidence in time alignment between data sources for future studies, with an attempt to quantify potential sensor delays.

Noise statistics

In order to form the system and measurement noise matrices **Q** and **R** necessary for the flight path reconstruction (see subsection 3.1.1), the collected data has to be analysed to identify its noise standard deviation. This is done by identifying a time period of approximately 10 [s] when the recorded parameters are steady. The standard deviation of the parameter during the isolated time period is subsequently computed. Table 4.15 and Table 4.16 present the identified input and measurement parameter noise standard deviation, the square of which is used as diagonal elements **w** and **v** of the matrices **Q** and **R**, respectively.

Table 4.15: Input vector noise standard deviation, in SI units

	A_x	A_y	A_z	p	q	r
Raw input	$3.07e{-2}$	$5.61e{-3}$	$1.46e{-2}$	$6.22e{-4}$	$1.20e{-3}$	$6.15e{-2}$
Filtered input	$4.52e{-3}$	$4.96e{-3}$	$9.40e{-3}$	$4.62e{-4}$	$5.07e{-4}$	$5.06e{-4}$

Table 4.16: Measurement vector noise standard deviation, in SI units

x_{GPS}	y_{GPS}	z_{GPS}	u_{GPS}	v_{GPS}	w_{GPS}
$1.63e{-1}$	$8.74e{-2}$	$8.65e{-2}$	$1.86e{-2}$	$1.70e{-2}$	$5.82e{-3}$

ϕ	θ	ψ	V_{TAS}	α	β
$6.25e{-4}$	$3.52e{-4}$	$2.32e{-4}$	$5.14e{-2}$	~~$5.34e{-5}$~~	~~$1.23e{-3}$~~

The time period for noise identification is not common for all parameters. The reason for this is a high dependency of the parameter dynamics on the aircraft conditions. The IMU noise (input vector) is identified during steady flight conditions, as the IMU noise induced by the engine vibration on the ground is amplified. On the other hand, the Euler angles, navigation position or velocity components noise is most easily identified on the ground. The α and β noise can only be identified in flight, after BOM calibration.

Because the angle of attack and angle of sideslip signals have been reconstructed, their noise standard deviation is small. In contrast, when measured at 1 [Hz], the quality of the information carried by the signal might be poor. Because the Kalman filter treats the noise standard deviation as an indication of the confidence of the measurement, the α and β noise statistics are increased to values of $1e-2$,

$5e-3$ [rad], respectively to force the Kalman filter a higher innovation of these variables, based on more reliable measurements. At the same time, throughout the flight, a β offset of 0.72 [°] is identified post calibration and the applicable correction is applied.

Independent variable correlation

As indicated in subsection 3.2.3, correlation of independent variables is undesired for the Least Squares parameter identification method. This subsection addresses this issue by presenting a brief correlation analysis. The following matrices present the correlation coefficients of measured (filtered and reconstructed) independent variables characterising symmetrical and asymmetrical flight and common to the aerodynamic model structure. The presented data is used to quantitively judge the usefulness of inclusion of the given variables in the model structure. The presented data represents the averaged correlation coefficient computed from all applicable manoeuvres (i.e. symmetrical manoeuvres ignored for symmetrical variables and vice versa) throughout the FT1.0 flight.

	α	$\dot{\alpha}$	α^2	q	δe
α	1.00	0.00	0.93	0.18	−0.24
$\dot{\alpha}$	0.00	1.00	0.00	0.97	-0.58
α^2	0.93	0.00	1.00	0.14	−0.30
q	0.18	0.97	0.14	1.00	-0.61
δe	−0.24	-0.58	−0.30	-0.61	1.00

	β	$\dot{\beta}$	p	r	δa	δr
β	1.00	0.00	-0.58	−0.15	−0.02	−0.06
$\dot{\beta}$	0.00	1.00	0.21	-0.97	−0.50	0.60
p	-0.58	0.21	1.00	−0.03	-0.92	0.10
r	−0.15	-0.97	−0.03	1.00	0.36	-0.57
δa	−0.02	−0.50	-0.92	0.36	1.00	–
δr	−0.06	0.60	0.10	-0.57	–	1.00

For independent variables characterising symmetrical flight, a high correlation exists between $\dot{\alpha}$ and q as well as α^2 and α (both with correlation coefficient above 0.9, highlighted in orange). Although some correlation exits between the elevator deflection δ_e and $\dot{\alpha}$ or q, the coefficient is lower (around 0.6, highlighted in yellow).

For independent variables characterising asymmetrical flight, a high correlation exists between $\dot{\beta}$ and r as well as δ_a and p (both with correlation coefficient above 0.9, highlighted in orange). Although some correlation exists between the rudder deflection δr and $\dot{\beta}$ or r, the coefficient is lower (around 0.6, highlighted in yellow). Since the rudder and aileron deflections are decoupled (not induced within the same manoeuvre), no correlation is determined between these two independent variables.

5

Determination of Centre of Gravity and Moment of Inertia

This chapter describes the methodology employed to determine the centre of gravity of the N4207X aircraft and model its location as function of loading configuration, as presented in section 5.1. In addition, an attempt is made to determine the full moment of inertia matrix of the aircraft around the established centre of gravity, described in section 5.2. The assumptions made throughout the analysis are stated together with identifying the limitations of the model, defining its scope.

5.1. Centre of gravity

The knowledge of the centre of gravity location of the aircraft is required in the loading problem solved by the pilot prior to every flight. The centre of gravity has to fall within margins predefined by the manufacturer as excessively aft centre of gravity implies reduced stability and poor stall recovery characteristics, whereas an excessively forward centre of gravity, although increases stability, can reduce the aerodynamic performance.

Apart of safety of operation, the determination of centre of gravity location (also referred to as COG) is required by the aircraft mathematical modelling, is used as reference point for moment of inertia determination and as origin of the body axis reference frame F_b, around which the aircraft body rotates. Under the assumption of uniform gravitational field (see subsection 2.3.1), the centre of gravity coincides with the centre of mass and defines the infinitesimal point in which the integral mass of the aircraft is concentrated. Information about the distance between any force exerted on the body and the COG allows to perform a moment analysis around the aircraft. With the COG varying with loading configuration, its effect on the control and aerodynamic derivatives can also be quantified.

In this chapter, the COG is described in the F_D frame (see subsection 2.3.2), with origin at the aircraft datum point, that is 65 [in] in front of the firewall, in the symmetry plane, on the ground. The COG can also be expressed as percentage of the mean aerodynamic chord, which is defined in subsection 5.1.1.

5.1.1. Mean aerodynamic chord

The mean aerodynamic chord (also referred to as MAC) of a wing can be defined as "the chord of an imaginary airfoil which would have force vectors throughout the flight range identical with those of the actual wing" [18]. It provides ready means for evaluation of the wing moments. The aerodynamic centre can be located to lie at approximately 25% of the MAC length.

Given the half wing planform of the C337 as shown on Figure 5.1, two sections of constant taper can be identified, the inner section, spanning from the aircraft symmetry plane to the boom pylon (taken at y = 60.75 [in] = 1.54 [m]), with semispan $b/2_{in}$ = 1.54 [m], taper λ_{in} = 1 and surface area S_{in} = 2.90 [m^2], and the outer section, spanning from the boom pylon to the wing tip (excluding fairing, as in [18]), with semispan b/s_{out} = 4.10 [m], taper λ_{out} = 0.67 and surface area S_{out} = 6.43 [m^2].

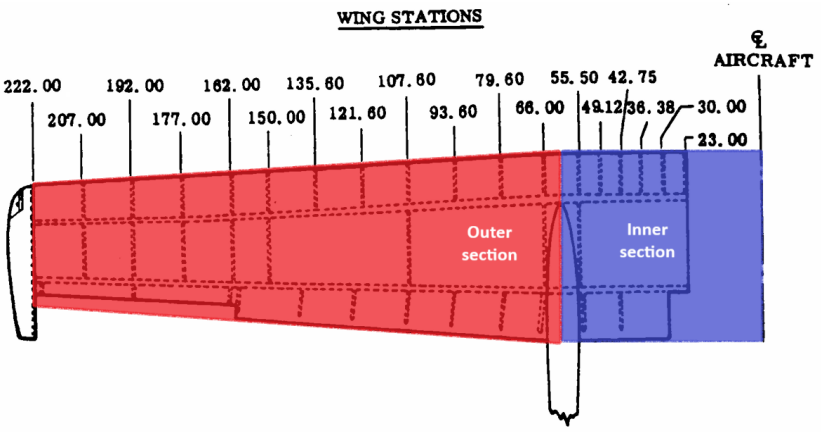

Figure 5.1: Left wing planform, divided into separate sections of constant taper, dimensions in [in] [61]

The general definition of mean aerodynamic chord length, as stated on Equation 5.1, can be specified for sections i of constant taper λ. The MAC of a wing comprised of n constant taper sections (here $n = 2$) can subsequently be computed as an average weighted by section surface area [77]:

$$MAC = \frac{2}{S}\int_0^{b/2} c^2 dy = \frac{\sum_{i=1}^{n} MAC_i S_i}{\sum_{i=1}^{n} S_i}, \qquad MAC_i = \frac{2}{3} c_{r,i}\left(\frac{1+\lambda_i+\lambda_i^2}{1+\lambda_i}\right) \tag{5.1}$$

Where c is the chord length, and subscripts r and t indicate the spanwise location - root and tip, respectively. The longitudinal and spanwise location $x_{MAX_{LE}}$ and y_{MAC} of the MAC with respect to the datum can be expressed as follows [77] for a constant taper wing section:

$$x_{MAC_{LE}} = x_r + (x_t - x_r)\frac{1+2\lambda}{3+3\lambda}, \qquad y_{MAC} = y_r + \frac{b}{2}\frac{1+2\lambda}{3+3\lambda} \tag{5.2}$$

For a wing composed of several constant taper wing sections, the average weighted by section surface area can be used, as defined by Equation 5.1, replacing MAC_i by $x_{MAC_{LE},i}$ and $y_{MAX,i}$, respectively. The application of the described method to the C337 yields results summarised on Table 5.1.

Table 5.1: Mean aerodynamic chord and its location for the C337

	$x_{MAC_{LE}}$ [m]	y_{MAC} [m]	MAC [m]
Inner section	3.09	0.77	1.88
Outer section	3.24	3.46	1.59
Half wing	3.19	2.62	1.68

5.1.2. Centre of gravity model specification

The three dimensional location of the centre of gravity of the aircraft is modelled as function of the aircraft load, namely the fuel mass in the right main tank $m_{f,MR}$, fuel mass in the left main tank $m_{f,ML}$, fuel mass in the right auxiliary tank $m_{f,AR}$ and fuel mass in the left auxiliary tank $m_{f,AL}$. Additionally, the masses of the two pilots and two passengers are taken into account as $m_{p,FR}$, $m_{p,FL}$, $m_{p,RR}$, $m_{p,RL}$ as well as the luggage/cargo m_c. It is assumed that the engine oil volume is constant and any additional load is manually incorporated in the COG model if necessary. For brevity, only the general expression to compute an arbitrary centre of gravity location is stated by Equation 5.3 and defines the COG as the mass weighted average moment arm of mass components of a body. It is assumed that the reader is familiar with such process.

$$x_{c.g.} = \frac{\sum_{i=1}^{n} x_{c.g.i} m_i}{\sum_{i=1}^{n} m_i} \tag{5.3}$$

Given the aircraft datum point defined 1.65 [m] (65 [in]) in front of the firewall, in the symmetry plane of the aircraft and on the ground (water line $WL = 0$, see Figure 2.2 in chapter 2), the local COG locations of the fuel tanks, crew on board and cargo are summarised on Table 5.2. The fuel tanks are located in between the front and rear spars, corresponding to 0.2 and 0.6 of the local chord length c. The main fuel tanks span between wing stations 66.0 and 150.0 [in] (see Figure 5.1), while the auxiliary tanks between wing stations 23.0 and 55.5 [in] [61]. Given the maximum thickness to chord ratio of 12% at root and 9% at tip, the height of the fuel tanks is approximated as constant 15 [cm]. The main fuel tank shape is therefore assumed as trapezoidal prism with the COG lying at midpoint of the segment connecting both bases centroid. The auxiliary fuel tank shape is assumed as a rectangular cuboid. The $\Gamma = 3°$ wing dihedral angle is taken into account.

The COG of crew and passengers on board is taken to be in the symmetry plane of each seat, 23 [cm] above the seat surface, 20 [cm] in front of the backrest, as found by [19] for an unclothed, average male human body, with the pilot seats in a forward (in flight) position. The additional luggage COG is taken at station 168 [in] = 4.27 [m] [12], in the plane of symmetry, 0.90 [m] above the ground level.

Table 5.2 summarises the COG location of individual components contributing to the calculation of the global COG. In addition, the points of ground contact of the nose and main landing gear tires are reported.

Centre of gravity model component	x [m]	y [m]	z [m]
DATUM	0.0	0.0	0.0
Nose gear[1]	1.45	0.0	0.0
Main gear right[1]	3.84	1.24	0.0
Main gear left[1]	3.84	-1.24	0.0
Main right fuel tank	3.83	2.71	2.01
Main left fuel tank	3.83	-2.71	2.01
Auxiliary right fuel tank	3.83	1.00	1.90
Auxiliary left fuel tank	3.83	-1.00	1.90
Copilot (front, right)	2.59	0.28	1.11
Captain (front, left)	2.59	-0.28	1.11
Passenger (rear, right)	3.61	0.28	1.11
Passenger (rear, left)	3.61	-0.28	1.11
Additional luggage	4.27	0.0	0.90

Table 5.2: Measured COG of individual variable mass components of the aircraft together with reference measurements, in F_D

5.1.3. Centre of gravity experimental determination

In order to determine the COG travel with change of loading of the aircraft, the knowledge of a reference COG of an empty configuration aircraft is desired. The determination of the COG of the aircraft at operational empty weight can be performed experimentally, as described in this section.

From the most recent Mass and Balance supplement (17.05.2022, FAA A&P 3289471), the $x_{c.g.,OEW}$ is calculated as 3.57 [m] (140.47 [in]), for an OEW of 1,382 [kg] (3,047 [lbs]). This mass includes the engine oil, trapped fuel and fixed onboard equipment, but excludes fuel mass, people on board or any cargo. The Pilot's Operating Manual [12] reports the $LEW + m_{oil}$ of a sample aircraft at 2,832 [lbs] with a moment of 397,200 [lbs in], which translates into a $x_{c.g.,LEW+m_{oil}}$ of 3.56 [m] (140.25 [in]). The $x_{c.g.,OEW}$ is treated as reference value from which a travel can be computed depending on aircraft loading. The $y_{c.g.}$ is assumed to be 0.0, given the lateral symmetry of the aircraft and is confirmed experimentally. The $z_{c.g.}$ is determined from a series of measurements of the aircraft tyres ground reaction forces at different fuselage pitch.

The experimental determination of vertical centre of gravity location is performed by measuring the landing gear ground reaction forces of the aircraft. Given that the three points of contact of the aircraft with the ground are spread in the XY plane, the $x_{c.g.}$ and $y_{c.g.}$ can be determined from a single

[1] Nose and main gear locations reported at point of contact of the tyre with the ground.

measurement. However, a series of measurements (at least two) is necessary to determine $z_{c.g.}$ by varying the aircraft pitch θ, while assuming a fixed COG location within the measurement series. Two series of measurements are therefore performed on the aircraft, varying the pitch for two separate total aircraft weights. One measurement series is performed with low fuel level resulting in a total aircraft mass of 1,586 [kg] (averaged from three measurements), and one with maximum fuel level resulting in a total aircraft mass of 1,750 [kg] (averaged from four measurements).

During the experimental measurement, the aircraft mass consisted of the OEW (as reported in chapter 2, including trapped oil and fuel) and fuel only, while the front seats have been placed in forward, in-flight position. The pitch has been varied by placing boxes of different height under the nose wheel, as shown schematically on Figure 5.2. Scales have been placed under each wheel and included the weight of the box, which subsequently has been subtracted from the nose wheel scale reading. The factor limiting the maximum attainable pitch is the condition past which the aircraft tilts backwards, thus the nose wheel reaction force is zero.

Figure 5.2 defines the difference between the measured ground pitch θ_g, being the angle between the horizontal ground and line connecting the longitudinal point of contact of the landing gear with the artificial, inclined ground as well as the aircraft pitch $\theta_{a/c}$, being the angle between the body X_b axis and the horizontal ground. θ_g is determined from the distance between tyres ground contact and the box height with the use of trigonometry, whereas $\theta_{a/c}$ is measured with an inclinometer.

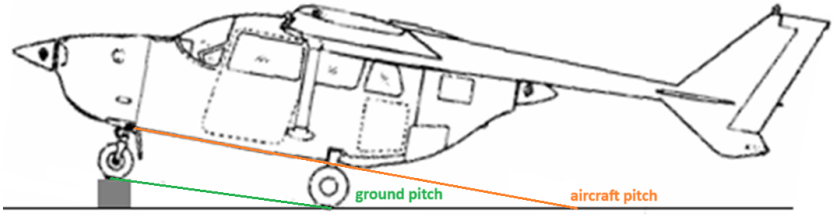

Figure 5.2: Schematic side view of the experimental setup for $z_{c.g.}$ determination

Due to an uncalibrated on board fuel probe at the time of the measurement, the fuel mass in the aircraft in each measurement is determined from the calibrated fuel pump readings. When all tanks are filled with fuel, as done for the full fuel measurement, each main tank holds 46.5 [gal] = 176.0 [l], whereas each auxiliary tank holds 19 [gal] = 71.9 [l]. Given that the total change in aircraft weight between measurements is recorded as 164 [kg], and that 217.9 [l] of fuel has been pumped, the average fuel (AVGAS) density is 752.6 [kg/m^3]. Table 5.3 summarises the fuel volume and mass added to each tank between the low fuel and full fuel measurements.

Table 5.3: Fuel volume and mass added to each of the tanks between measurements, volume given by fuel pump

	main tank, right	main tank, left	auxiliary tank, right	auxiliary tank, left
V_f [l]	78.5	74.4	31.8	33.2
m_f [kg]	59.1	56.0	24.0	25.0

The recorded results of the two, low fuel and full fuel, measurement series are summarised on Table 5.4 and Table 5.5, respectively. The tables report the computed ground pitch angle θ_g, and aircraft pitch angle $\theta_{a/c}$ and roll angle $\phi_{a/c}$ [°] measured with an inclinometer of accuracy ±0.1°, computed fuel masses m_f in respective fuel tanks [kg], nose and main wheel reaction forces F_n and F_m [kg] measured with a scale of accuracy ±1 [kg] and the total measured reaction force F_{total}, which is a sum of the individual wheel reaction forces.

Table 5.4: Measured wheel reaction forces for different aircraft pitch attitude, low fuel level

θ_g	$\theta_{a/c}$	$\phi_{a/c}$	$m_{f,MR}$	$m_{f,ML}$	$m_{f,AR}$	$m_{f,AL}$	F_n	$F_{m,R}$	$F_{m,L}$	F_{total}
0.0	0.7	0.3	73.4	76.5	30.2	29.2	168	707	710	1585
2.6	6.0	0.5	73.4	76.5	30.2	29.2	88	749	751	1588
7.2	11.5	0.6	73.4	76.5	30.2	29.2	14	784	787	1585

Table 5.5: Measured wheel reaction forces for different aircraft pitch attitude, full fuel level

θ_g	$\theta_{a/c}$	$\phi_{a/c}$	$m_{f,MR}$	$m_{f,ML}$	$m_{f,AR}$	$m_{f,AL}$	F_n	$F_{m,R}$	$F_{m,L}$	F_{total}
0.0	1.6	0.3	132.5	132.5	54.1	54.1	158	804	791	1753
2.6	6.9	0.3	132.5	132.5	54.1	54.1	78	841	831	1750
1.3	5.4	0.4	132.5	132.5	54.1	54.1	103	827	819	1749
4.9	9.3	0.3	132.5	132.5	54.1	54.1	38	858	852	1748

It can be observed that the ground pitch θ_g and aircraft pitch $\theta_{a/c}$ do not have a constant offset, but rather tend to diverge from each other with increasing pitch. In addition, the increased fuel load also increases the aircraft pitch when the landing gear stands on horizontal flat ground. This is due to the increasing deflection of the main landing gear strut, as the main landing gear transfers higher loads with increasing pitch or fuel, at the same time relaxing the load on the nose wheel, which increases the protrusion of the nose gear strut from the shock absorber. This showcases the limitation of the rigid body assumption and should be noted, as it has influence on the computed vertical location of the centre of gravity.

According to the measured data reported on Table 5.4 and Table 5.5, longitudinal and lateral COG location for the low fuel level measurement with wheels on flat ground ($\theta_g = 0°$) is 3.59 and 0.0 [m], respectively, while for the full fuel level measurement, 3.62 and 0.01 [m], respectively.

In order to determine the vertical COG position of the aircraft, $z_{c.g.}$, the sum of moments can be taken about the datum point and the three dimensional COG location has to be assumed constant throughout the measurement series. Figure 5.3 schematically shows the force contribution to the moments taken around the datum, in this case aligned with the line connecting the points of contact of the landing gear wheels with the scales. Assuming a counter-clockwise positive direction, the following moment balance can be stated, for a static series of measurements:

$$\sum_{c.c.+} M_{m,datum} = l_n F_n \cos\theta_g + l_m(F_{m,R} + F_{m,L})\cos\theta_g - x_{c.g.}F_{total}\cos\theta_g - z_{c.g}F_{total}\sin\theta_g = 0 \qquad (5.4)$$

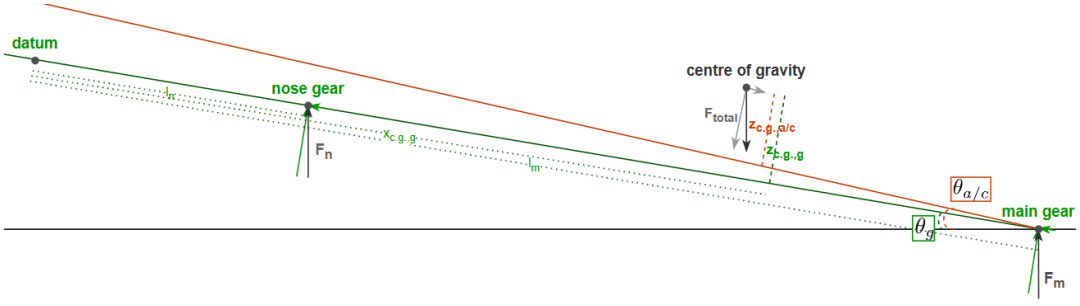

Figure 5.3: Schematic representation of the moments taken around the datum of the aircraft

Where l_n is the longitudinal position of the nose gear and l_m the longitudinal position of the main gear, with respect to the datum (see Table 5.2). Equation 5.4 can be rearranged into a linear relation, in which the average moment arm is expressed as being proportional to the tangent of pitch θ_g, with slope and intersect corresponding to $z_{c.g.}$ and $x_{c.g.}$, respectively, as reported on Equation 5.5:

$$\frac{l_n F_n + l_m(F_{m,R} + F_{m,L})}{F_{total}} = z_{c.g.}\tan\theta_g + x_{c.g.} \qquad (5.5)$$

The results of the measurement series reported on Table 5.4 and Table 5.5 can therefore be substituted into Equation 5.5, which is graphically presented on Figure 5.4a and Figure 5.4b, respectively, together with a linear fit curve.

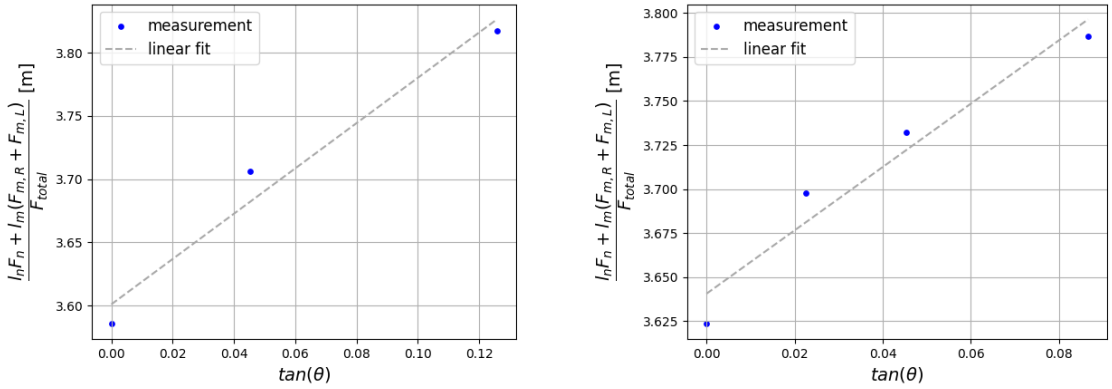

(a) Low fuel level measurement series

(b) Full fuel level measurement series

Figure 5.4: Graphical determination of $x_{c.g.}$ and $z_{c.g.}$ from experimental measurements

The results determined from the linear regression shown on Figure 5.4 are presented on Table 5.6, together with the coefficient of determination R^2. The values are determined with respect to the line passing through the landing gear contact points with the ground. This value can thus be corrected for the main gear strut deflection by taking into account the difference $\Delta\theta$ between $\theta_{a/c}$ and θ_g (see Figure 5.3):

$$z_{c.g.,a/c} = z_{c.g.,g} - (l_m - x_{c.g.,g}) \tan\left(\overline{\Delta\theta}\right) \tag{5.6}$$

Table 5.6: $x_{c.g.,g}$ and $z_{c.g.,g}$ from linear regression of experimental measurements together with corrected term $z_{c.g.,a/c}$ and linear regression coefficient of determination R^2

Measurement series	$\overline{\Delta\theta}$ [°]	$x_{c.g.,g}$ [m]	$x_{c.g.}$ [%MAC]	$z_{c.g.,g}$ [m]	$z_{c.g.,a/c}$ [m]	R^2
Low fuel	2.8	3.60	24.4	1.79	1.78	0.983
Full fuel	3.6	3.64	26.8	1.80	1.79	0.972

The observation of backwards travel of the $x_{c.g.}$ with increasing the fuel mass is logical, so is the upwards travel of the $z_{c.g.}$. The correction applied to the $z_{c.g.,g}$ to obtain the $z_{c.g,a/c}$ is indeed small in magnitude (around 1 [cm]).

The reference empty weight vertical COG location, $z_{c.g.,OEW}$ can be computed backwards using the values reported in Table 5.6 and assuming no fuel in the tanks. This can be performed using $z_{c.g.,a/c}$ values determined for the low and full fuel measurement series, and results in values of $z_{c.g,OEW}$ of 1.74 [m] and 1.73 [m], respectively. Although expected identical, the difference can be due to violations of some of the assumptions, as stated earlier. Taking the average, the $z_{c.g,OEW}$ can be reported as 1.74 [m]. The reference, operational empty weight COG location of the aircraft is thus stated on Table 5.7.

Table 5.7: Reference, operational empty weight COG location of the aircraft

$x_{c.g,OEW}$ [m]	$x_{c.g.}$ [%MAC]	$y_{c.g,OEW}$ [m]	$z_{c.g,OEW}$ [m]
3.57	22.6	0.00	1.74

5.1.4. Centre of gravity model validation

Now, a comparison can be made between the modelled and measured COG of the aircraft, making use of the collected data. The numerical implementation of the model is done on the `Matlab` file `ac_cg.m`,

as described in Appendix D. Table 5.8 provides values of the modelled and measured COG location for the low and full fuel aircraft state, reporting also the error. The measured COG are taken at the lowest recorded pitch angle, for which the effect of fuel displacement in the tanks is the smallest.

Table 5.8: Comparison of the model prediction and measured COG location for the low fuel and full fuel cases

Measurement series	Modelled [m]			Measured [m]			Difference [m]		
	$x_{c.g.}$	$y_{c.g.}$	$z_{c.g.}$	$x_{c.g.}$	$y_{c.g.}$	$z_{c.g.}$	$\Delta x_{c.g.}$	$\Delta y_{c.g.}$	$\Delta z_{c.g.}$
Low fuel	3.60	0.00	1.77	3.59	0.00	1.78	0.01	0.00	0.01
Full fuel	3.62	0.00	1.79	3.62	0.01	1.79	0.00	0.01	0.00

Table 5.8 shows discrepancies of up to 1 [cm], which is also the reported precision of the COG location. 1 [cm] corresponds to less than 0.6% of the MAC, suggesting that the model error is relatively small. On the other hand, the experimental results have shown a travel of the longitudinal COG location with aircraft pitch change, resulting from the change in fuel COG, which is against the model assumptions. The COG model is thus limited for cases in which the pitch angle θ is small. Similarly, the divergence of $\theta_{a/c}$ from θ_g with increasing pitch has increased the complexity of determining $z_{c.g.}$, potentially increasing the uncertainty of computed values, and showcases the limitations of the rigid body assumptions.

5.1.5. Centre of gravity envelope

To close the description of the COG determination of the N4207X aircraft, the envelope of the longitudinal centre of gravity is reported on Table 5.9 for reference, based on the Pilot's Operating Handbook [12].

Table 5.9: Longitudinal centre of gravity envelope corners [12]

	Weight		Moment [lbs in/10^3]		$x_{c.g.}$ [m]		$x_{c.g.}$ [% MAC]	
	[lbs]	[kg]	min	max	min	max	min	max
OEW	3047	1382	410	436	3.42	3.63	13.6	26.4
MLW	4400	1996	604	630	3.49	3.64	17.7	26.6
MTOW	4630	2100	648	662	3.56	3.63	21.7	26.3

It can be noticed that the values found in subsection 5.1.3 exceed the maximum location of $x_{c.g.}$ for positive θ_g. It should be noted that the COG envelope is defined for the loading problem to be solved at conditions $\theta_g = 0°$, for which the determined $x_{c.g.}$ values are always within the envelope bounds. In addition, the pilot weight always negatively contributes the longitudinal COG travel (COG shifts forwards), while the experimentally found $x_{c.g.}$ includes the OEW and fuel only.

5.2. Moment of inertia

The mass moment of inertia (also referred to as MOI) corresponds to the ratio between the torque applied and resulting angular acceleration of a body around its rotational axis. It can therefore be described as resistance to angular acceleration in rotational motion, in the same way as mass resists linear acceleration in linear motion. It describes the distribution of mass around a body rotational axis, given a body shape. As stated in Equation A.12 of Appendix A, section A.2, a body, in this case aircraft, mass moment of inertia can be described by the symmetrical inertia tensor matrix:

$$\begin{bmatrix} I_{xx} & -I_{xy} & -I_{xz} \\ -I_{xy} & I_{yy} & -I_{yz} \\ -I_{xz} & -I_{yz} & I_{zz} \end{bmatrix} \tag{5.7}$$

Since the aircraft rotates around its body axes, the inertia tensor matrix is taken around the centre of gravity, which is the origin of the F_b frame of reference. Because of the aircraft symmetry in the body XY plane, the terms I_{xy} and I_{yz} are expected to be close to 0.

The knowledge of the aircraft inertia is necessary for the determination of the moments acting in the body frame F_b on the aircraft, as defined by Equation A.13. In this chapter, the moment of inertia tensor

is defined around the aircraft COG, while the COG is defined with respect to the aircraft datum, as described in section 5.1.

The approach of MOI determination of the aircraft is based on methods proposed by Lanham's Inertia Calculation Procedure for Preliminary Design report for the USAF [37] as well as the USAF DATCOM chapter 8.1 [22]. It involves decomposing the aircraft into major component groups, to which a percentage of aircraft total mass is attributed. The local MOI taken with respect to local COG of individual component group are subsequently determined. The MOI of individual components are then translated to be expressed with respect the integral aircraft COG and summed.

The presented approach does not exactly follow any of the mentioned methods, but is adapted to the available resources and data to increase the accuracy of the result. Most importantly, in this study, the MOI of the C337 is computed given a fully designed aircraft for which the MOI data is not available, while most MOI determination methods are developed for preliminary MOI estimation at early design phase. This implies that although in this study several weights, such as integral aircraft, fuel or engine weights are readily available, the mass distribution around the aircraft still has to be determined.

5.2.1. Aircraft component group mass attribution

For the purpose of this MOI determination, the aircraft total weight, expressed as the maximum take-off weight, is decomposed into the following fixed mass component groups:

1. Wing - the structural mass of the wing, including empty fuel tanks, wing control surfaces and high lift devices.
2. Fuselage - the structural mass of the fuselage, assumed to span between the front and rear engine firewalls, excluding any fixed equipment such as instrumentation, environmental control system or seats.
3. Empennage - structural mass of the horizontal tail and two parallel vertical tails, including the control surfaces.
4. Tail booms - structural mass of both tail booms, from tail boom station 0.0 to station 168.0 [in] [61], including the control and electrical cables.
5. Nacelle - structural mass of engine mounts, the front and rear engine cowlings, ending at the firewalls and excluding any propulsion system equipment.
6. Landing gear - nose and main landing gear, including tyres, wheels, brakes and struts.
7. Powerplant - the summed structural mass of the engines, propellers, trapped oil and supporting powerplant systems such as air induction, fuel supply, starters and controls.
8. Fixed equipment - mass of non-removable aircraft equipment such as instrumentation, environmental control system, seats, flight test data acquisition system etc.

In addition, the following are considered as components of variable mass, or removable, effectively changing the aircraft MOI. The mass of the listed removable is known:

1. Fuel - the mass of the fuel in the tanks, including trapped fuel.
2. Crew - the mass of people on board with maximum of four, including pilots and passengers.
3. Luggage/cargo - the mass of luggage located behind the passenger's seats (fuselage station 168 [in] [12]).

In order to attribute mass to individual component groups, a class II weight estimation is performed with three methods, as described by Roskam in Airplane Design, Part V: Component Weight Estimation [59]. The employed methods are the Cessna method applicable to small, low performance airplanes with $V_{max} < 200$ [kt], Torenbeek method applicable to light transport airplanes with $MTOW < 12,500$ [lbs], and the United States Air Force method applicable to light and utility type airplanes with $V_{max} < 300$ [kt]). For the class II weight estimation, known aircraft data is used as listed in [2] [12] [61] or measured. The maximum and minimum load factors are taken as 3.8 and -1.52, respectively [70] and multiplied by a 1.5 constant according to CS 23.2230(a)(2) [10] to obtain a positive ultimate load of 5.7.

In addition, component mass data is collected for nine twin piston propeller engine aircraft of design mission similar to the C337 to provide comparison to class II weight estimation. The empirical data is collected from [59] and describes the following aircraft: Beech 65QA, Beech E18S, Beech G50TB, Beech 95TA, Cessna 310C, Cessna 404-3, Cessna 414A, Cessna TP441 and Rockwell 690B. The results of the class II weight estimation as well as averaged empirical data are presented in Table 5.10, and expressed as percentage value of aircraft MTOW attributed to a particular component group.

Table 5.10: Percentage of MTOW mass associated to aircraft component group based on Cessna, Torenbeek and USAF class II weight estimations and averaged empirical data

Component group	Cessna [%]	Torenbeek [%]	USAF [%]	Empirical average [%]
Wing	5.3	4.5	9.6	9.6
Fuselage	4.8	- [1]	5.3	8.5
Empennage	3.1	1.7	2.2	2.2
Nacelle	1.1	0.7	- [2]	3.4
Landing gear	5.1	- [1]	1.9	5.0
Powerplant	- [1]	16.2	19.1	20.5

Results shown on Table 5.10 show significant variation in component group mass between methods and often underestimate values of percentages of MTOW compared to empirical average values. This is why, in this MOI estimation, the mass attribution is based on the determined empirical average values and presented on Table 5.11. In addition to the empirical mass fraction and absolute mass value, the standard deviation σ of the particular fraction is given.

Table 5.11: Attribution of mass to aircraft component groups based on empirically determined MTOW fractions

Component group	Empirical fraction of MTOW [%]	Empirical data σ [%]	Attributed mass [kg]
MTOW	100	29.0	2100.0
OEW (actual)	65.8	-	1382.1
OEW (statistical)	63.1	28.4	1325.4
Wing	9.6	0.8	201.6
Fuselage	8.5	0.2	177.6
Empennage	2.2	0.2	45.5
Nacelle	3.4	0.6	71.1
Landing gear	5.0	1.0	105.7
Powerplant	20.5	3.9	431.2 $\rightarrow$ 447.4
Fixed equipment	14.1	3.3	296.8 $\rightarrow$ 324.6

Table 5.11 states two values of OEW, one which corresponds to the actual C337 OEW and includes the trapped fuel and engine oil, while the other one - to the statistical OEW, predicted by empirical data. The difference between the actual and statistically predicted OEW is around 4%, which can be considered small. Since the sum of the component group masses does not add up exactly to the actual OEW, the powerplant mass is increased by the engine oil mass (16.2 [kg]), and the fixed equipment mass is increased to reach the actual OEW mass less the trapped fuel (8.6 [kg]), which is not part of the fixed equipment. Moreover, the estimated tail boom mass is also excluded from the increased mass of fixed equipment.

In the following paragraphs, the distribution of mass within each of the component group and determination of MOI around its local centroid is described. The computation is supported with the 3D CAD model and 3D scan of the N4207X realised by Ramesh [58].

Wing group

As the great majority of the C337 aircraft structure, the wing spars, ribs and skin are made of aluminum 2024 [2], which has a density of $2,780$ [kg/m^3] [3]. As reported in Table 5.11, the wing component

[1] Method not applicable to the C337 aircraft.

[2] For the USAF class II weight estimation, the nacelle weight is included in Powerplant weight.

group weights 201.6 [kg] and its mass is distributed along the surface of the empty shell wing body. The thickness of the equivalent wing skin which includes all the wing group structural weight is determined to be $t = 1.9$ [mm]. Figure 5.5 shows an isometric view of the wing model.

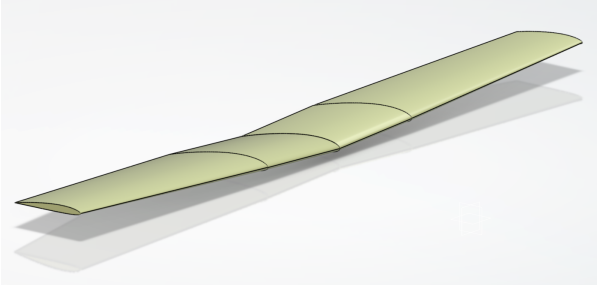

Figure 5.5: Isometric view of the wing group model, based on file `skymaster_adimsc_mainwing` [58]

The wing group centroid (coinciding with COG) with respect to the aircraft datum is located at [3.95, 0.0, 1.98] [m], and the diagonal elements of the inertia tensor around the wing group centroid are $\text{diag}\left(\bar{I}\right) = [2001.0, 49.9, 2045.1]$ [kg m^2].

Fuselage group

The fuselage is assumed to be located between the engines' firewalls, as indicated on Figure 5.6 by beige colour elements. The structure of the fuselage, namely bulkheads and skin, is fabricated of aluminum 2024 [2]. Following the same approach as for the wing group, the fuselage of weight 177.6 [kg] is treated as shell of shape given on Figure 5.6 has an equivalent thickness of $t = 4.1$ [mm].

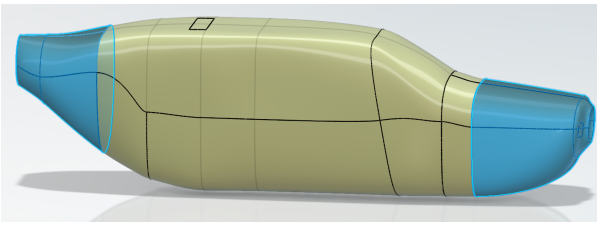

Figure 5.6: Isometric view of the fuselage (beige) and nacelle (light blue) group model, based on file `skymaster_adimsc_fuselage` [58]

The fuselage group centroid with respect to the aircraft datum is located at [3.40,0.0,1.32] [m], and the diagonal elements of the inertia tensor around the wing group centroid are $\text{diag}\left(\bar{I}\right) = [86.6, 216.5, 204.9]$ [kg m^2].

Empennage group

The empennage is composed of the horizontal tail and two vertical tails the structure of which (spars, extrusions and skin) are made of alumnium 2024 [2]. A mass of 22.5 [kg] is attributed to the horizontal tail and a mass of 23.0 [kg] to the vertical tails, based on the ratio of the tails wetted area. The mass is distributed along the surface of the empty body shell, resulting in a skin equivalent thickness of $t = 1.3$ [mm] for both the horizontal and vertical tails. Figure 5.7 shows an isometric view of the horizontal and vertical tails models.

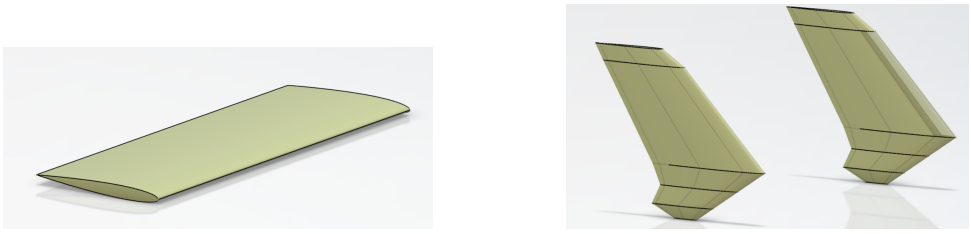

(a) Horizontal tail **(b)** Vertical tail

Figure 5.7: Isometric view of the empennage group model, based on files `skymaster_adimsc_ht` and `_vt` [58]

The centroids with respect to the aircraft datum are located at [7.91, 0.0, 1.80] and [8.44, 0.0, 2.12] [m] for the horizontal and vertical tails, respectively. The diagonal elements of the inertia tensor around the respective centroids are diag $\left(\overline{I}\right)$ = [18.3, 1.9, 20.1] and [56.7, 7.6, 56.4] [kg m^2].

Tail boom group

The tail boom mass has to be estimated from available information on boom structure, as it is not predicted by the empirical attribution of percentage mass to components. Figure 5.9b shows the structural overview of the aft part of the boom (boom stations 70 to 168, as defined on Figure 5.8), for which the stringers, bulkheads and skin are made of aluminum 2024. The skin has a thickness of t = 0.016 [in] [2], and is reinforced with six bulkheads dividing the aft part of the boom into seven sections. The first two sections are reinforced with 12 T shaped stringers (assumed of thickness t = 0.016 [in] and side size 1.5 [cm]), sections 3 and 4 by ten stringers and sections 5, 6 and 7 by six stringers.

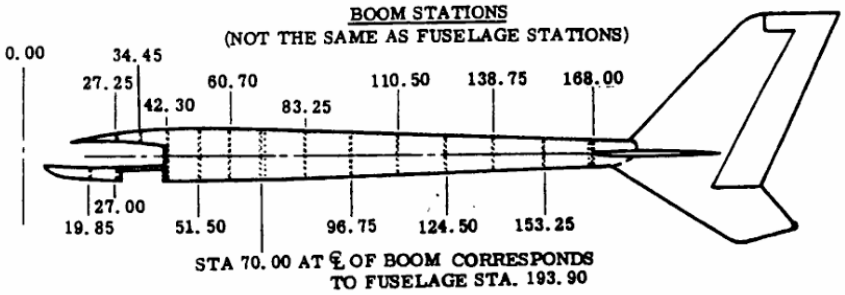

Figure 5.8: Tail boom stations definition, dimensions in [in] [61]

For a single boom, the aft section skin weight can be determined to be approximately 2.05 [kg], while the stringers alone 0.74 [kg]. Given the elliptical cross sectional shape of the booms with a semimajor axis of 17.7 [cm] and semi-minor axis of 10.0 [cm] at station 70, with taper 1 : 1.9 at station 168 [2], the bulkheads are estimated to be of elliptical hollow shape of local size corresponding to local boom cross section, a flange of 2 [cm] and thickness 0.016 [in]. The summed mass of a single boom aft section bulkheads is thus approximated as 0.02 [kg]. Given the measured diameter of control cables being 3.5 [mm] for rudder and 3.0 [mm] for elevator, their mass per unit length can be approximated as 0.06 [kg/m] [17]. Two pair of control wires are routed through each boom, thus their mass within the aft boom section can be estimated to be around 0.43 [kg]. The total determined mass of 3.24 [kg] is further rounded up to the nearest 0.5 [kg] to account for the mass of rivets, paint and electrical cables and obtain 3.5 [kg] per aft boom section. Since the aft boom section describes the boom from stations 70 to 168, the mass is linearly scaled up for the full boom, accounting for the full length from 0 to 168. The total mass of a single boom is thus estimated as 6.0 [kg], making a total of 12.0 [kg] for the tail boom group.

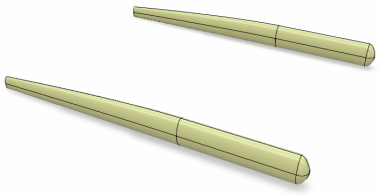

(a) Isometric view of the tail booms, based on file `skymaster_adimsc_boom` [58]

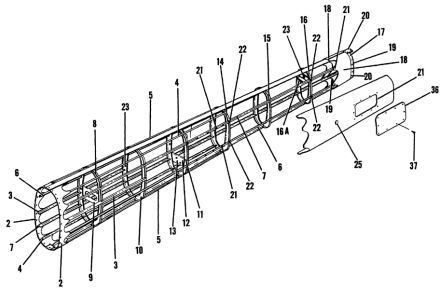

(b) Tail boom structural overview from boom station 70 to 168 [11]

Figure 5.9

The tail boom group centroid (both booms) with respect to the aircraft datum is located at [5.37, 0.0, 1.87] [m], and the diagonal elements of the inertia tensor around the wing group centroid are diag $\left(\bar{I}\right)$ = [0.2, 16.3, 16.2] [kg m^2].

Nacelle group

The front and rear nacelles close the shape of the fuselage and are assumed to be separated from it by the firewalls. The nacelle geometry is represented in light blue on Figure 5.6 and, similarly to other component groups, its mass is distributed over the surface. The total nacelle group mass of 71.1 [kg] is split equally between the front and rear structure, resulting in equivalent thickness of t = 3.8 [mm] for the front and t = 5.7 [mm] for the rear nacelle.

The centroids with respect to the aircraft datum are located at [1.17, 0.0, 1.14] and [5.46, 0.0, 1.55] [m] for the front and rear nacelle, respectively. The diagonal elements of the inertia tensor around the respective centroids are diag $\left(\bar{I}\right)$ = [8.7, 6.8, 7.8] and [6.6, 5.2, 4.9] [kg m^2].

Landing gear group

The structural weight attributed to the landing gear is 105.7 [kg]. This weight is further distributed between the nose gear (20.9 [kg]) and two main landing gear (42.4 [kg] each) based on their respective length, approximated as 0.37 [m] and 0.75 [m], respectively. Given that the MOI is approximated in flight configuration, the landing gear is assumed to be stowed and its shape is simplified to slender rods, with their local COG at mid-length.

As the nose gear retracts forwards, its centroid is located at [1.37, 0.0, 0.37] [m], in front of the nose wheel ground contact point. The main landing gear struts retract rearwards and their centroids are therefore taken at [4.21, 0.50, 0.37] and [4.21, -0.50, 0.37] [m] respectively. The diagonal elements of the inertia tensor around the landing gear local centroids are determined to be diag $\left(\bar{I}\right)$ = [0.0, 0.96, 0.96] for the nose gear and [0.0, 7.95, 7.95] [kg m^2] for each of the main gear.

Powerplant group

The powerplant group is attributed a total mass of 447.4 [kg], which is equally split between the front and rear propulsive units. Within the 223.7 [kg] per propulsive unit, 25.0 [kg] is given as propeller mass, 126.0 [kg] is the dry mass of a single engine and 8.1 [kg] is mass of the engine oil, leaving 64.6 [kg] for the remaining powerplant systems. The propeller is idealised as three constant diameter slender rods of length equal to the propeller radius of r_p = 0.96 [m] and constant density. The engine dry mass, trapped oil and supporting systems are concentrated in a rectangular cuboid of dimensions 898, 839, 570 [mm], which encloses the engine.

The centroids of the propellers with respect to the aircraft datum are located at [0.57, 0.0, 1.26] and [5.95, 0.0, 1.47] [m], while the cuboids of the power plant are at [1.14, 0.0, 1.26] and [5.26, 0.0, 1.47] [m]. The diagonal elements of the inertia tensor around the centroids are diag $\left(\bar{I}\right)$ = [7.7, 3.8, 3.8] for the propeller and [17.0, 18.7, 25.0] [kg m^2] for the powerplant cuboid.

Fixed equipment
As reported on Table 5.11, the mass attributed to the fixed equipment is 324.6 [kg] and it is distributed evenly throughout the aircraft volume, resulting in an equivalent constant density of 35.8 [kg/m^3]. Figure 5.10 shows the 3D scan of the aircraft in flight configuration used to determined the local centroid and MOI around it.

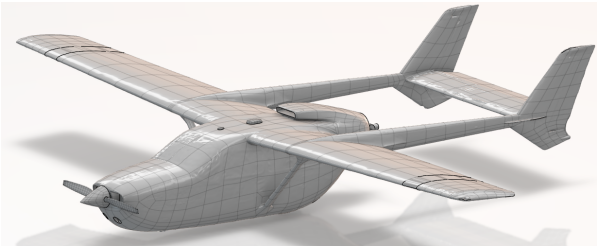

Figure 5.10: Isometric view of the integral aircraft scan, based on file `skymaster_3dscan_configflight` [58]

The centroid of the scanned aircraft of constant density is determined to be at [3.63, -0.05, 1.45] [m], and given the distributed mass, the diagonal elements of the inertia tensor around it are diag $\left(\bar{I}\right)$ = [830.2, 778.4, 1482.8] [kg m^2].

Fuel
As described in subsection 5.1.2, the main and auxiliary fuel tanks fill the space between the front and rear spar of the wing and are assumed to be of a spanwise constant height of 15 [cm]. The main fuel tank spans between wing stations 66.0 and 150.0 [in], while the auxiliary tanks between stations 23.0 and 55.5 [in] (see Figure 5.1). Figure 5.11 shows the layout of the main and auxiliary fuel tank geometry.

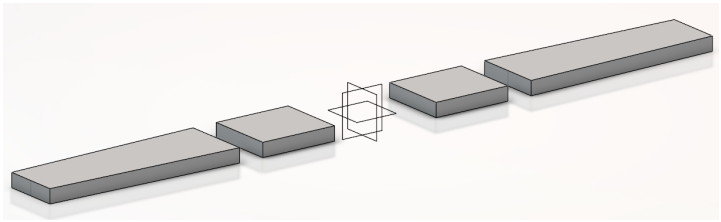

Figure 5.11: Isometric view of the main and auxiliary fuel tanks model for MOI estimation

The centroids, coinciding with the COGs of the fuel tanks are reported on Table 5.2 in subsection 5.1.2. The diagonal elements of the inertia tensor around the fuel tanks centroids are diag $\left(\bar{I}\right)$ = [50.37, 5.15, 55.02] and [3.17, 2.49, 5.46] [kg m^2] for a single main and auxiliary tank, respectively. The reported values are applicable to full tanks, containing 132.5 and 54.1 [kg] of fuel each, respectively. The fuel tank MOI around own centroid scales linearly with mass.

Crew
As for the fuel, the crew represents a removable and variable mass in the aircraft, which influences the MOI. The crew centroids, coinciding with the COG are reported on Table 5.2 in subsection 5.1.2. The MOI of humans around their centroid has been determined for an average, 74.7 [kg] male of 1.75 [m], unclothed [19] sitting in an in-flight position, and is scaled linearly with mass. The diagonal elements of the inertia tensor around the centroid of the sitting human are diag $\left(\bar{I}\right)$ = [6.36, 7.51, 3.2] [kg m^2].

Luggage
The luggage, also being a removable and variable mass, is assumed to have dimensions of [$l = 0.5, w = 0.5, h = 0.2$] [m]. Its centroid is located at [4.27, 0.0, 1.0] [m] and allowable mass depends on the loading configuration of the aircraft. Its diagonal elements of the inertia tensor around its centroid can be computed as diag $\left(\bar{I}\right) = [\frac{m}{12}(w^2 + h^2), \frac{m}{12}(l^2 + h^2), \frac{m}{12}(l^2 + w^2)]$ [kg m^2].

5.2.2. Parallel axis theorem application

In subsection 5.2.1, the MOI determination around local centroids of the aircraft component groups has been presented. Now, given the aircraft COG model determined in section 5.1, the parallel axis theorem can be applied to the local MOI values to determine individual component group MOI contribution around the aircraft global COG.

Equation 5.8 states the parallel axis theorem for the diagonal terms of the inertia tensor matrix in three dimensional space of the aircraft, in which the MOI around local centroid, $\overline{I}$, is translated by the product of component group mass m and distance between the parallel axes of rotation. $[\overline{x}_{c.g.}, \overline{y}_{c.g.}, \overline{z}_{c.g.}]$ define the coordinates of the local component group centroid, while $[x_{c.g.}, y_{c.g.}, z_{c.g.}]$ define the aircraft centre of gravity location for a given loading.

$$\begin{aligned} I_{xx} &= \overline{I}_{xx} + m\left((\overline{y}_{c.g.} - y_{c.g.})^2 + (\overline{z}_{c.g.} - z_{c.g.})^2\right) \\ I_{yy} &= \overline{I}_{yy} + m\left((\overline{x}_{c.g.} - x_{c.g.})^2 + (\overline{z}_{c.g.} - z_{c.g.})^2\right) \\ I_{zz} &= \overline{I}_{zz} + m\left((\overline{x}_{c.g.} - x_{c.g.})^2 + (\overline{y}_{c.g.} - y_{c.g.})^2\right) \end{aligned} \tag{5.8}$$

Equation 5.9 defines the parallel axis theorem for the off-diagonal terms of the aircraft inertia tensor matrix, the product moment of inertia terms.

$$\begin{aligned} I_{xy} &= \overline{I}_{xy} + m(\overline{x}_{c.g.} - x_{c.g.})(\overline{y}_{c.g.} - y_{c.g.}) \\ I_{xz} &= \overline{I}_{xz} + m(\overline{x}_{c.g.} - x_{c.g.})(\overline{z}_{c.g.} - z_{c.g.}) \\ I_{yz} &= \overline{I}_{yz} + m(\overline{y}_{c.g.} - y_{c.g.})(\overline{z}_{c.g.} - z_{c.g.}) \end{aligned} \tag{5.9}$$

Table 5.12 summarises all the mass m of component groups in [kg], local centroid location with respect to the datum point, in [m], and the determined MOI around it, in [kg m^2], as listed in subsection 5.2.1. In addition, the parallel axis theorem is applied onto the local MOI of the component groups to determine their MOI around the integral aircraft COG.

The purpose of Table 5.12 is to track the process of the aircraft MOI determination and show the dominant terms of the calculation. Since the off-diagonal terms of the inertia tensor matrix are significantly smaller (at least one order of magnitude), for brevity reasons, they are not included in Table 5.12. The presented data is specific to the case of the aircraft with full fuel tanks and four crew members of the given mass and luggage of 45.9 [kg], resulting in a MTOW configuration with COG at [3.56, 0.0, 1.68] [m].

Table 5.12: Summarised mass, local centroids and MOI data of individual component groups

Component group	m	$\overline{x}_{c.g.}$	$\overline{y}_{c.g.}$	$\overline{z}_{c.g.}$	$\overline{I}_{xx}$	$\overline{I}_{yy}$	$\overline{I}_{zz}$	I_{xx}	I_{yy}	I_{zz}
Wing	201.6	3.95	0.00	1.98	2001.0	49.9	2045.1	2019.3	98.3	2075.1
Fuselage	177.6	3.40	0.00	1.32	86.6	216.5	204.9	109.8	244.2	209.4
Horz. tail	22.5	7.91	0.00	1.80	18.3	1.9	20.1	18.6	428.2	446.1
Vert. tail	22.6	8.44	0.00	2.12	56.7	7.6	56.4	61.0	549.1	593.7
R boom	6.0	5.37	1.53	1.87	0.1	8.1	8.1	14.4	27.9	41.7
L boom	6.0	5.37	-1.53	1.87	0.1	8.1	8.1	14.4	27.9	41.7
Front nacelle	35.5	1.17	0.00	1.14	8.7	6.8	7.8	19.2	220.7	211.2
Rear nacelle	35.5	5.46	0.00	1.55	6.6	5.2	4.9	7.2	133.6	132.7
Nose gear	20.9	1.37	0.00	0.37	0.0	1.0	1.0	35.9	137.6	101.7
Main gear, R	42.4	4.21	0.50	0.37	0.0	8.0	8.0	83.2	98.9	36.5
Main gear, L	42.4	4.21	-0.50	0.37	0.0	8.0	8.0	83.2	98.9	36.5
F. powerplant	198.7	1.14	0.00	1.26	17.0	18.7	25.0	52.1	1216.5	1187.8
R. powerplant	198.7	5.26	0.00	1.47	17.0	18.7	25.0	26.2	604.9	602.0
F. propeller	25.0	0.57	0.00	1.26	7.7	3.8	3.8	12.1	232.3	227.9
R. propeller	25.0	5.95	0.00	1.47	7.7	3.8	3.8	8.8	147.4	146.3
Fixed equip.	324.6	3.63	-0.05	1.45	830.2	778.4	1482.8	848.4	797.6	1485.4
Main tank, R	132.5	3.83	2.71	2.01	50.4	5.2	55.0	1037.3	29.3	1037.0
Aux. tank, R	54.1	3.83	1.00	1.90	3.2	2.5	5.5	59.6	9.0	63.2
Main tank, L	132.5	3.83	-2.71	2.01	50.4	5.2	55.0	1037.3	29.3	1037.0
Aux. tank, L	54.1	3.83	-1.00	1.90	3.2	2.5	5.5	59.6	9.0	63.2
Captain (F, L)	74.7	2.65	-0.28	1.11	6.4	7.5	3.2	36.5	93.5	70.8
Copilot (F, R)	74.7	2.65	0.28	1.11	6.4	7.5	3.2	36.5	93.5	70.8
Pax (R, L)	74.7	3.49	-0.28	1.11	6.4	7.5	3.2	36.5	32.1	9.4
Pax (R, R)	74.7	3.49	0.28	1.11	6.4	7.5	3.2	36.5	32.1	9.4
Luggage	45.9	4.27	0.00	1.00	1.1	1.9	1.1	22.3	46.1	24.1

Finally, the I_{xx}, I_{yy} and I_{zz} terms of Table 5.12 can be summed and reported together with the determined off-diagonal terms of the aircraft inertia tensor matrix, which is presented on Equation 5.10 in [kg m^2]:

$$\begin{bmatrix} I_{xx} & -I_{xy} & -I_{xz} \\ -I_{xy} & I_{yy} & -I_{yz} \\ -I_{xz} & -I_{yz} & I_{zz} \end{bmatrix} = \begin{bmatrix} 5775.50 & 1.37 & -296.16 \\ 1.37 & 5438.03 & -1.88 \\ -296.16 & -1.88 & 9960.24 \end{bmatrix} \tag{5.10}$$

The low values of products moments of inertia, in particular I_{xy} and I_{yz} confirm the assumption stated in subsection 2.3.1. The numerical implementation of the moment of inertia model is done in the `ac_moi.m` file, as described in Appendix D.

5.2.3. Comparison to empirical estimation

The outcome of the moment of inertia model determined in this chapter can be compared to an estimation based on empirical data, as proposed by Roskam in [59, pp. 17–21]. Its class I method for preliminary aircraft inertia estimation assumes that a radius of gyration $R_{x,y,z}$ in each F_b axis can be identified within each airplane category. A nondimensionalised radius of gyration $\overline{R}$ can be associated with each R component and the moment of inertia determined accordingly, as defined by Equation 5.11 [59].

$$\begin{aligned} &I_{xx} = R_x^2 \cdot m \quad I_{yy} = R_y^2 \cdot m \quad I_{zz} = R_z^2 \cdot m \\ &\overline{R}_x = \frac{2R_x}{b} \qquad \overline{R}_y = \frac{2R_y}{l} \qquad \overline{R}_z = \frac{2R_z}{e}, \quad e = \frac{b+l}{2} \end{aligned} \tag{5.11}$$

Given that airplanes of similar mission and configuration tend to have similar values of dimensionless radius of gyration $\overline{R}$ [59, p. 18], data of single and twin engine propeller aircraft is collected, including models such as: Beech N-35, Cessna 150M, Cessna 172M, Cessna 177A, Cessna R182, Cessna 210K, Beech

55, Beech 95, Beech D-50, Beech D18S, Cessna 402, Cessna 404, Cessna 441. The database, provided by [59, pp. 198–199], also includes different mass configurations of the same aircraft model. Values of $\overline{R}$ components have to be chosen for the Cessna 337, which is presented on Figure 5.12 and summarised on Table 5.13. The choice is made subjectively by proximity to other existing designs.

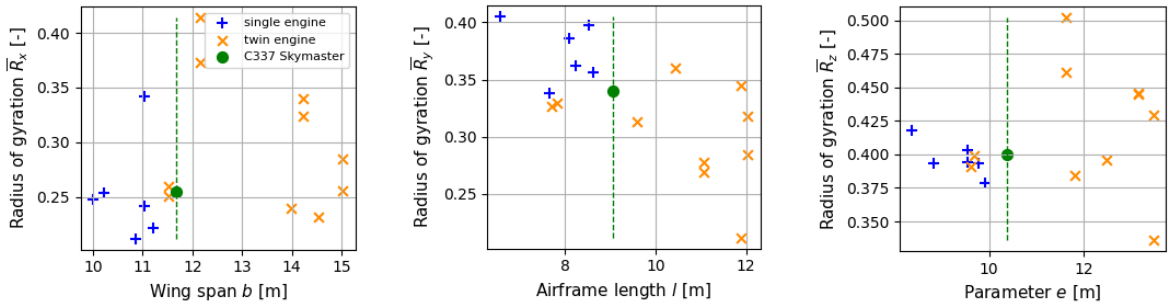

(a) $\overline{R}_x$ against span b **(b)** $\overline{R}_y$ against length l **(c)** $\overline{R}_z$ against e

Figure 5.12: Single and twin propeller engine aircraft radii of gyration $\overline{R}$ together with values chosen for the C337

Table 5.13: Values of dimensionless radius of gyration $\overline{R}$ chosen for the Cessna Skymaster class I inertia estimation

$\overline{R}_x$	$\overline{R}_y$	$\overline{R}_z$
0.26	0.34	0.40

Now, the moment of inertia terms can be computed with Equation 5.11 for the aircraft at OEW and MTOW and compared with values predicted by the analytical model derived in this chapter as well as aircraft of similar mass and configuration. This is presented on Figure 5.13, whereas the actual values are summarised on Table 5.14.

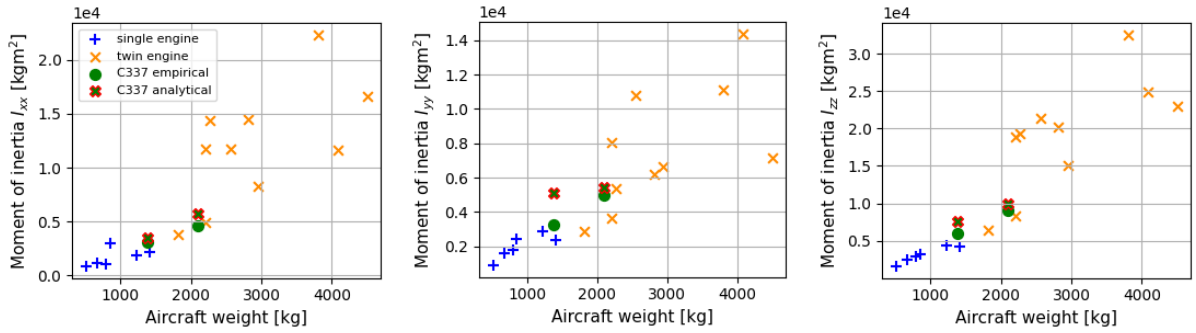

(a) I_{xx} against aircraft mass **(b)** I_{yy} against aircraft mass **(c)** I_{zz} against aircraft mass

Figure 5.13: Moment of inertia terms of the C337 estimated empirically and determined analytically, compared to existing aircraft

Table 5.14: Empirically estimated moment of inertia terms for the C337, expressed in [kg m^2]

m	$\overline{R}_x$	$\overline{R}_y$	$\overline{R}_z$
OEW	3066.7	3284.3	5951.2
$MTOW$	4659.9	4990.6	9043.1

The empirical estimation method has shown a reasonably good prediction of the analytically determined moment of inertia terms, while consistently underestimating them. Logically, the highest difference in is observed in I_{yy} prediction. This is due to the C337 engines being located on both sides of the Y_b

axis and with a relatively high moment arm compared to classical configuration aircraft. The latter is also the main limitation in the validity of the Roskam empirical class I inertia estimation. Given that the C337 engine and tail configuration is relatively unique, comparing it to aircraft of a classical configuration might not provide accurate results. The presented analysis should therefore be treated as a comparison, allowing to place the C337 aircraft in the context of its competitors, rather than source of MOI determination. Moreover, the class I estimation is a method designed for a preliminary aircraft design phase and does not allow to estimate the product of inertia terms.

5.2.4. Moment of inertia model limitations

The presented analysis of the aircraft moment of inertia is a compromise between accuracy of obtained inertia tensor matrix and time and effort spent on the analysis of mass distribution within the aircraft. The scope of the model assumes only a few variable mass component groups, limited to fuel tanks, crew and luggage. The remaining component groups mass distribution is determined as constant. In the following paragraphs, the effect of simplifications made throughout the MOI determination is discussed.

Modelling of most of the structural group components as empty shells of mass distributed along surface aims at mimicking the actual aircraft structural layout, in which the skin, stiffeners and bulkheads are responsible for most of structural weight. However, this approach assumes empty bodies and constant equivalent thickness, which is a significant simplification of the reality. Empty shell modelling therefore tends to overestimate the MOI, given that it concentrates all the mass on the outer skin surface, moving it away from the centroid. Concentrated structural weight associated with the fuselage to wing connection, control surface mechanisms or local strengthening due to presence of cutouts is ignored by the employed methods. This can either have an overestimating or underestimating effect on the MOI, depending on the location of the structural anomaly with respect to the axis of revolution.

The mass determination of the tail booms is prone to uncertainty. The C337 booms are a rather unique feature, which is also the reason for which their mass has been estimated from available information rather than statistics of component group mass attribution. The determined 6 [kg] per boom can seem relatively small and has been determined from the limited information provided in [2] [61] or measured, rather than being deducted from the fuselage mass. Given a shorter fuselage of the C337 compared to similar mission, classic configuration aircraft on which the mass attribution statistics are based on, as well as relatively light booms, the MOI can be underestimated with the described method.

The approximation of the landing gear as slender rods ignores the wheel shape as well as curvature of the main lading gear struts. The uniform distribution of the mass along the slender rod ignores the retraction mechanism of the landing gear and wheel, which likely concentrates mass at both ends of the gear struts. This simplification is judged to underpredict the MOI around the longitudinal axis, I_{xx}, and potentially overpredict it around the lateral and vertical axis, given that the rods are positioned longitudinally, along the fuselage.

The powerplant less propeller MOI is concentrated in a cuboid emboxing the engine. Although the engine itself represents the majority of the powerplant less propeller mass, in reality, the supporting powerplant systems representing the remaining powerplant mass are spread around the engine box. This simplification therefore underestimates the powerplant less propeller MOI, unless the systems are located closer to the COG than the powerplant box centroid itself. The propeller is simplified to three slender rods only and thus ignores the spinner and propeller blade taper. Therefore, it over-distributes the mass of the spinning body, resulting in an overestimated MOI.

One of the largest single contributors to the determined inertia tensor is the fixed equipment, as reported in Table 5.12. This is caused by its relatively high mass and the assumption of its uniform spread within the aircraft volume. It could be argued, that most fixed equipment mass is present in the fuselage (instrumentation, seats etc.), however a further, more detailed analysis would be required to confirm this. Nevertheless, most likely the MOI due to fixed equipment is overestimated.

The variable mass and removable component groups, namely fuel, crew and luggage is of known mass, yet approximated shape. The fuel tanks are taken as constant spanwise height, which overestimates I_{xx} and I_{zz} terms. The shape of the crew members is based on a study with male humans of average height of 1.75 [m], although deviations from this are considered negligible for the overall aircraft MOI.

Finally, the presented MOI model relies on the integral aircraft COG location around which the inertia tensor is determined, therefore any inaccuracies in the centre of gravity location, as presented in section 5.1, affect the validity of the computed MOI.

6
Results

This chapter presents the results of the aircraft mathematical model identification for the Cessna Skymaster TU Delft research aircraft in an attempt to quantitatively answer the research question, as defined in section 2.2. This is done by describing intermediate outcomes of the system identification processes. First, the Kalman filter performance of the flight path reconstruction is presented in section 6.1. Subsequently, the parameter estimation performed with ordinary least squares approach is shown in section 6.2, the result of which is a complete list of aerodynamic and control derivatives of the aircraft. Finally, the engine performance model is shown in section 6.3, where modelled engine power is compared to the estimated engine monitor output.

6.1. Flight path reconstruction

The flight path reconstruction is performed by feeding the developed Extended and Iterated Extended Kalman filters with the measured input and measurement vectors **u** and **z**. The **u** and **z** vectors' elements are preprocessed as described in subsection 4.4.3. The initial guess of the state vector, $\mathbf{x_0}$, is computed from the unfiltered measurement vector and input vector with the help of the kinematic and navigation relations, as defined in chapter 3.

Throughout this section, a single elevator doublet manoeuvre is used as an example in the graphical representation of the flight path reconstruction. The input vector **u**, namely the aircraft body accelerations and rotational rates as well as control surface deflections for the example elevator doublet manoeuvre are given on Figure 6.1. Graphs of other symmetrical and asymmetrical manoeuvres can be found in section B.1 of Appendix B.

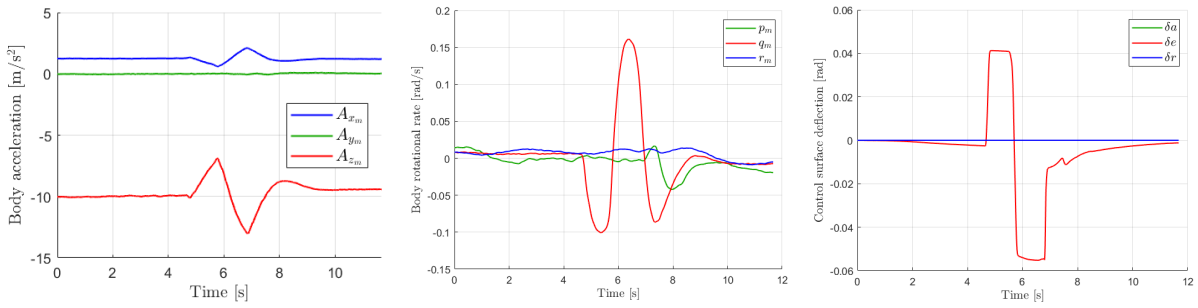

(a) Body acceleration **(b)** Body rotational rate **(c)** Control surface deflection

Figure 6.1: Aircraft body acceleration, rotational rate and control surface deflection for an elevator doublet

6.1.1. State estimation

The compared performance of the EKF and IEKF state estimation of an exemplary elevator doublet manoeuvre is presented on Figure 6.2 and Figure 6.3. Figure 6.2 shows the estimated aircraft GPS position x_E, y_E, z_E in the navigation frame, body velocity components u, v, w[1] as well as the Euler attitude angles ϕ, θ, ψ as function of the time throughout the manoeuvre.

Figure 6.2 shows a straight advancement of the aircraft in the XY_E plane, as shown by the reconstructed x_E and y_E position. The flight is however not perfectly level and steady, as shown by the overall

[1]Note, that the shown body vertical and lateral velocities v and w are expressed left and up positive, contrary to F_b

decreasing z_E (gaining altitude), positive mean vertical body velocity component w and increasing pitch θ. This is indeed observed for most of the performed manoeuvres, which increases the challenge of isolation of the manoeuvre effect on the flight dynamic motion.

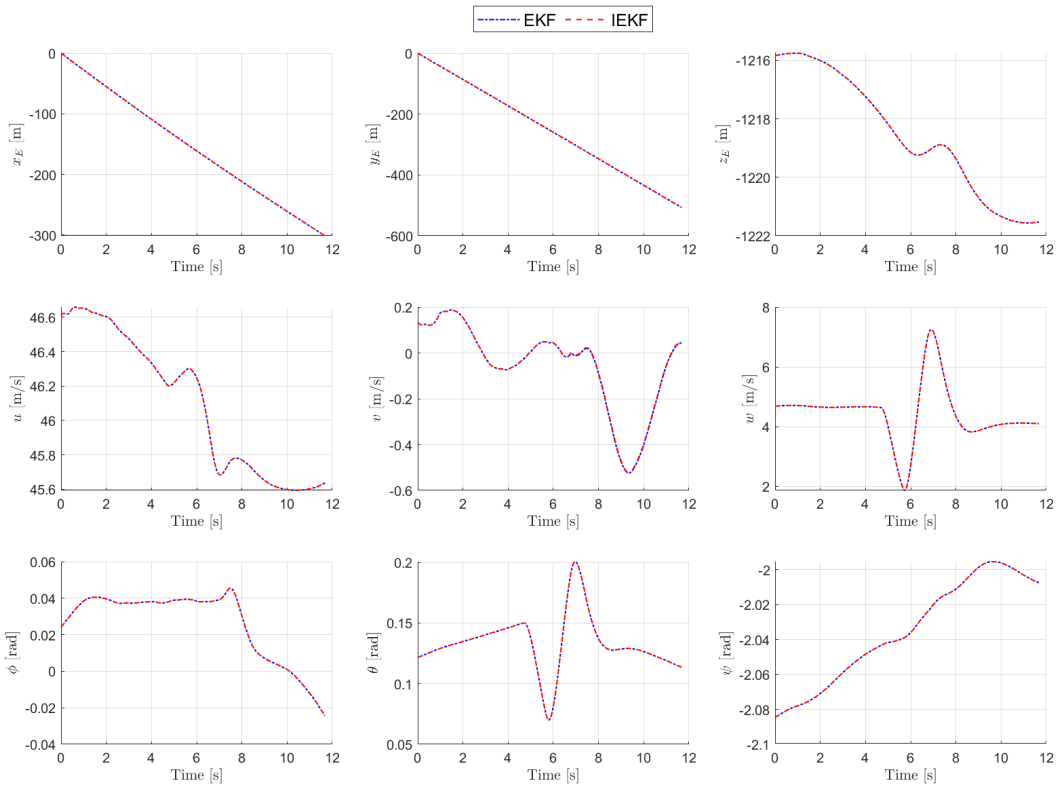

Figure 6.2: Unaugmented state estimation of EKF and IEKF for an elevator doublet manoeuvre[1]

Figure 6.3 shows the estimated augmented part of the state vector, namely the wind components in the navigation frame W_{x_E}, W_{y_E}, W_{z_E} and the accelerometer and gyro biases $\lambda_x, \lambda_y, \lambda_z, \lambda_p, \lambda_q, \lambda_r$ as function of the time throughout the manoeuvre.

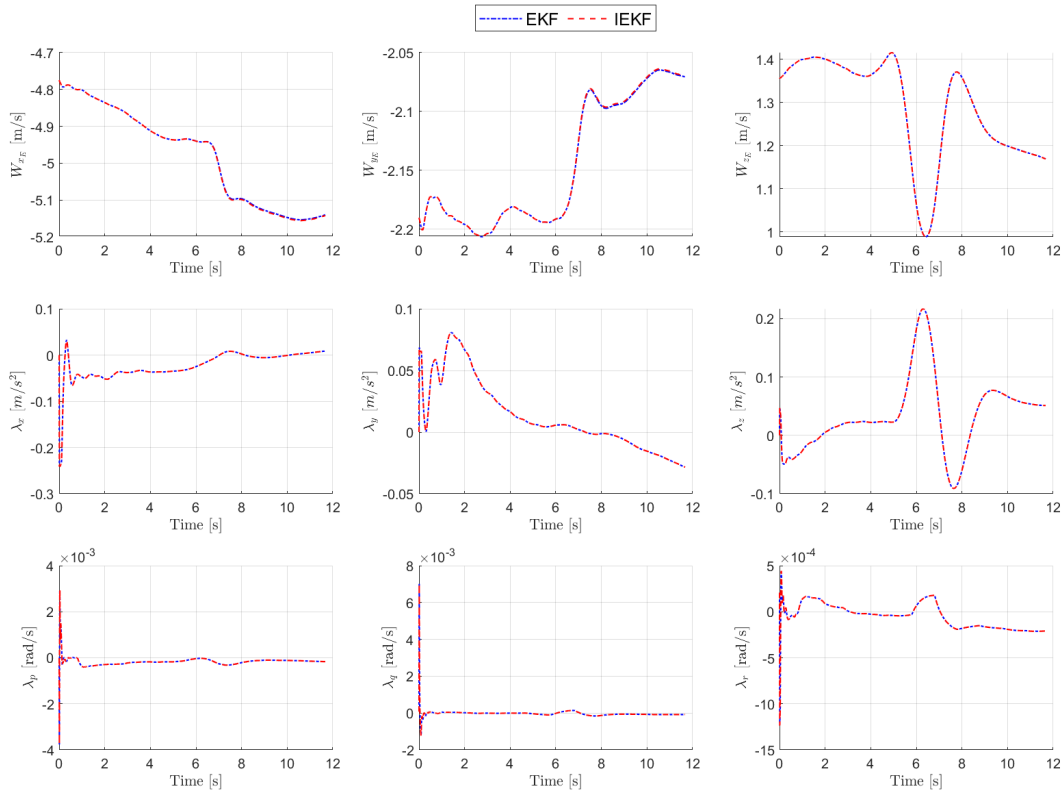

Figure 6.3: Wind and IMU bias estimation of EKF and IEKF for an elevator doublet manoeuvre

The estimated wind velocity components and IMU biases show some variation in time, yet limited in magnitude. The dependence of wind and biases tends to follow the aircraft dynamic motion for the case of W_{z_E} and λ_z, thus in the primary axis of excitation during the manoeuvre. This behaviour is observed throughout both symmetrical and asymmetrical manoeuvres.

The wind and bias statistics for the integrity of performed manoeuvres are presented on Table 6.1 and Table 6.2. The mean $\overline{\lambda}$ of wind velocity components and IMU biases are reported, together with their standard deviation σ_λ, minimum λ_{min} and maximum λ_{max} values across the population of recorded manoeuvres. Table 6.1 presents values estimated with the EKF, while Table 6.2 values presented with the IEKF. The λ values are determined for each manoeuvre by taking the mean of the last 100 estimated values, equivalent to 1 [s], in order to eliminate the potential influence of the dynamic motion and initial convergence phase on the λ value.

Table 6.1: Mean, maximum, minimum and standard deviation values of EKF estimated biases over performed manoeuvres

	$\overline{\lambda}$	σ_λ	λ_{min}	λ_{max}
W_{x_E} [m/s]	-5.73	2.04	-9.44	-3.19
W_{y_E} [m/s]	-1.94	2.35	-6.02	2.80
W_{z_E} [m/s]	1.22	0.48	0.37	2.56
λ_x [m/s^2]	-6.37e-3	2.78e-2	-5.32e-2	6.90e-2
λ_y [m/s^2]	-1.11e-2	2.33e-2	-6.60e-2	3.99e-2
λ_z [m/s^2]	2.06e-2	2.75e-2	-3.97e-2	6.94e-2
λ_p [rad/s]	7.75e-6	3.23e-4	-8.62e-4	7.40e-4
λ_q [rad/s]	3.33e-6	1.29e-4	-2.91e-4	3.06e-4
λ_r [rad/s]	-1.40e-4	2.31e-4	-7.24e-4	3.13e-4

Table 6.2: Mean, maximum, minimum and standard deviation values of IEKF estimated biases over performed manoeuvres

	$\overline{\lambda}$	σ_λ	λ_{min}	λ_{max}
W_{x_E} [m/s]	-5.73	2.04	-9.44	-3.19
W_{y_E} [m/s]	-1.94	2.35	-6.02	2.81
W_{z_E} [m/s]	1.22	0.48	0.37	2.56
λ_x [m/s^2]	-6.35e-3	2.78e-2	-5.31e-2	6.91e-2
λ_y [m/s^2]	-1.12e-2	2.33e-2	-6.60e-2	3.99e-2
λ_z [m/s^2]	2.06e-2	2.75e-2	-3.97e-2	6.94e-2
λ_p [rad/s]	7.79e-6	3.23e-4	-8.62e-4	7.40e-4
λ_q [rad/s]	3.30e-6	1.29e-4	-2.91e-4	3.06e-4
λ_r [rad/s]	-1.40e-4	2.31e-4	-7.24e-4	3.13e-4

As expected, the EKF and IEKF are consistent in predicting the state, as shown by the overlying curves of Figure 6.2 and Figure 6.3. The bias reported on Table 6.1 and Table 6.2 differs for few data point only and at a insignificant level of magnitude. As expected, the IEKF outperforms the EKF in the rate of convergence of the state estimation (not explicitely shown), which is most notable for the IMU biases. Once convergence is achieved for both filters, no difference is observed between the estimated states.

In an ideal, simulated flight scenario, all bias terms are expected to converge to a constant value, independent of the aircraft dynamic motion. Figure 6.3 shows however some variation of the estimated biases with time. This can be due to the fact that the augmented part of the state vector (formed by bias terms) acts as a bin for any offset values when the actual measured flight path does not exactly follow the kinematic interdependences.

6.1.2. Measurement reconstruction

Figure 6.4 and Figure 6.5 illustrate the reconstructed measurement vector for the exemplary elevator doublet manoeuvre as performed by the EKF and IEKF. Figure 6.4 shows the reconstructed GPS position x_{GPS}, y_{GPS}, z_{GPS} and velocity components u_{GPS}, v_{GPS}, w_{GPS} in the navigation frame, while Figure 6.5 shows the reconstructed attitude angles ϕ, θ. ψ and air data V_{TAS}, α and β.

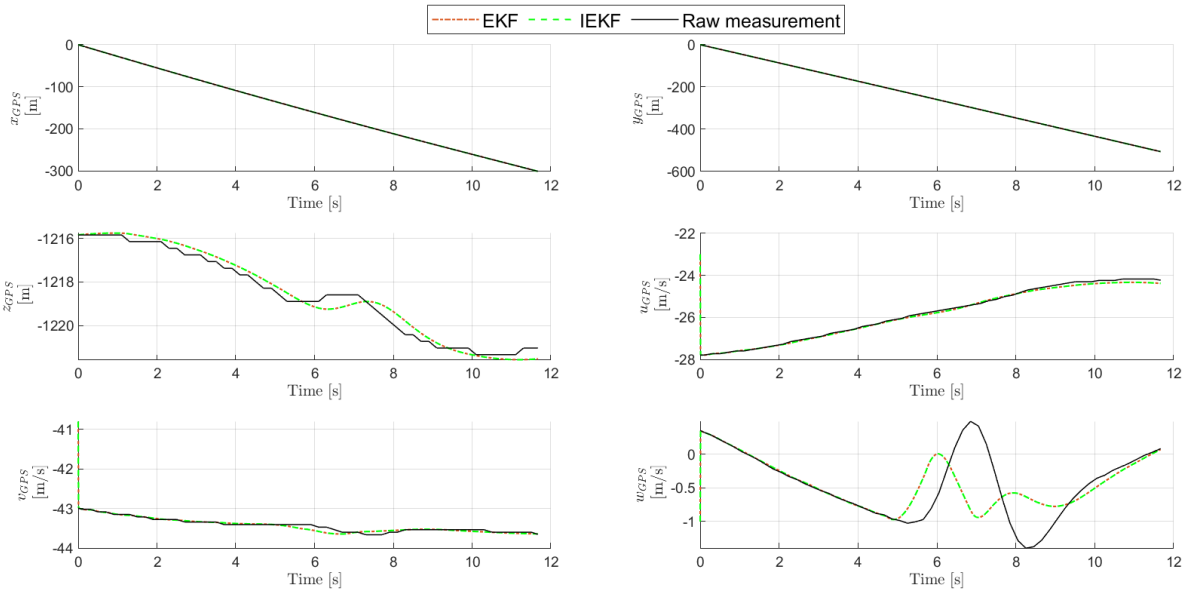

Figure 6.4: Measurement vector GPS terms reconstructed by the EKF and IEKF for an elevator doublet manoeuvre

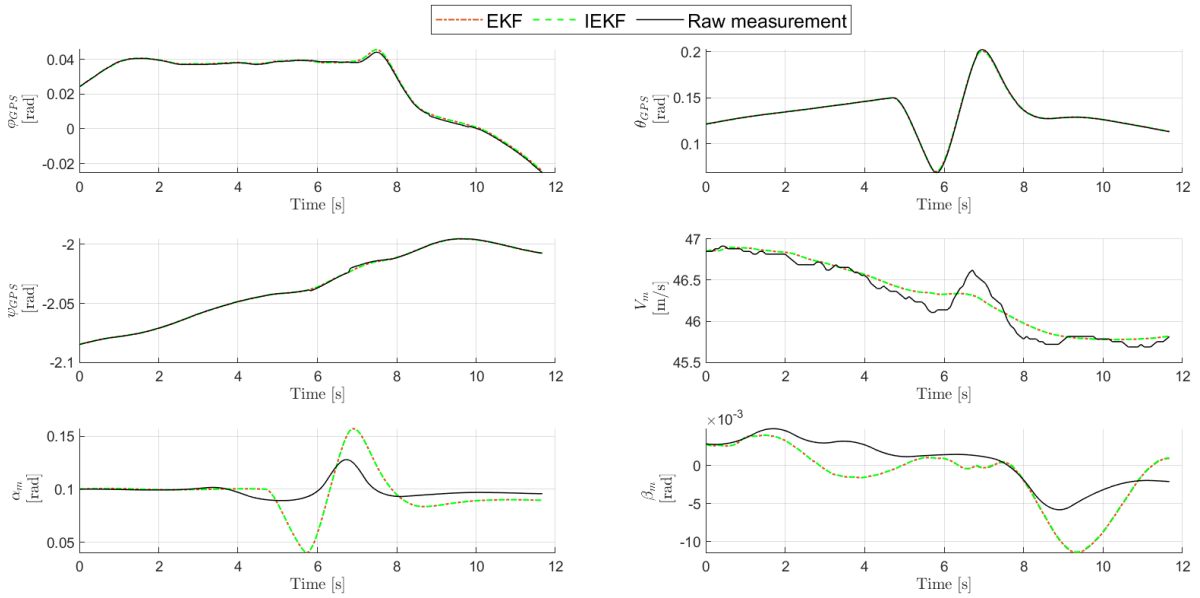

Figure 6.5: Measurement vector attitude and air data terms reconstructed by the EKF and IEKF for an elevator doublet manoeuvre

The EKF and IEKF are consistent in reconstructing the measurement vector, showing the same filter innovation, which is further isolated and captured as function of time in subsection 6.1.3. As the raw measurement noise is relatively small (see Table 4.16), the IEKF acts more as a smoother and innovator rather than white noise filter. Variables of high confidence, such as lateral and longitudinal GPS position or attitude angles show little to no innovation, while unsmooth signals such as the z_{GPS} or V_{TAS} are smoothed. Variables of low confidence, such as α or β show a large innovation, essentially correcting the raw measured signal. Because of the air data coupling, also the V_{TAS} shows high innovation, which in turn affects the reconstruction of vertical velocity w_{GPS}. The onset of the signal dynamics began by a pitch down (nose down) in the fifth second is observed throughout all affected, reconstructed variables.

6.1.3. Filter innovation

The innovation, which quantifies the corrections made by the Kalman filter to the raw measurement, is determined as the difference between the reconstructed and raw measurements. Figure 6.6 and Figure 6.7 plot the innovation of the exemplary doublet manoeuvre as determined by both the EKF and IEKF.

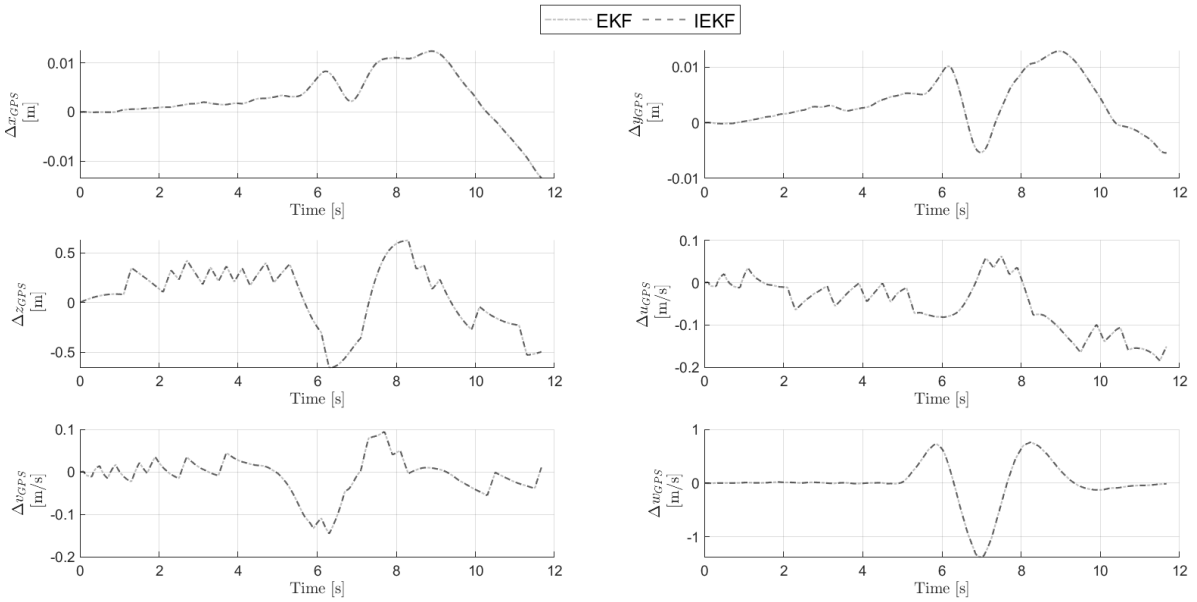

Figure 6.6: Measurement innovation of the GPS terms by EKF and IEKF for an elevator doublet manoeuvre

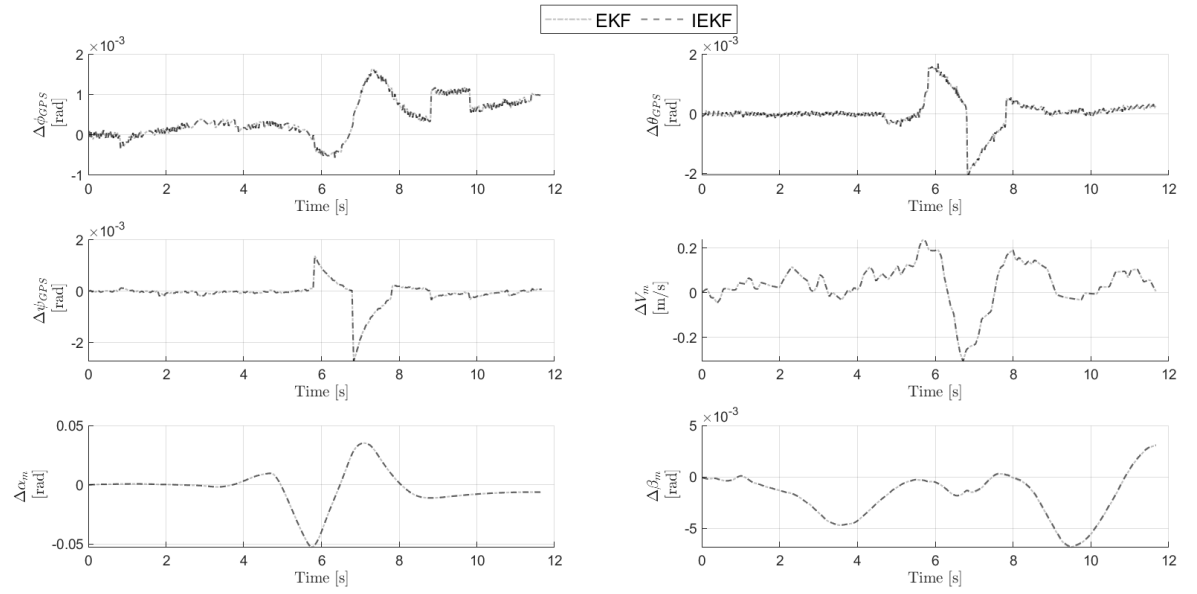

Figure 6.7: Measurement innovation of the attitude and air data terms by EKF and IEKF for an elevator doublet manoeuvre

The highest innovation can be observed for the reconstructed air data, which is triggered by the high uncertainty of the raw measurement quantified by the noise, as defined in subsection 4.4.3. Throughout all observed manoeuvres, the Kalman filter tends to amplify both the angle of attack and angle of sideslip signals, while keeping β within the raw measurement period and decreasing the period of α. Significant corrections are also applied to the navigation frame velocity components, as they are coupled with the air data via the estimated body velocity components and attitude (the latter shows relatively low innovation). The z_{GPS} signal is smoothed, while keeping the overall trend of the raw measurement. The innovation is usually kept within the 2σ confidence interval during steady flight, while it exceeds it for most of the manoeuvre dynamics, which suggests that the Kalman filter plays a significant role in adjusting the signal dynamics rather than only filtering noise.

6.2. Parameter estimation

This section presents the outcome of the parameter estimation, which has been performed with an Ordinary Least Square estimator developed as the second part of the Two Step method. The aerodynamic model of dimensionless forces and moments consisting of parameters θ and the regression matrix $\mathbf{A}(\mathbf{x})$ of the structure defined by Equation 3.21 and Equation 3.22 is fitted onto the observation (or measurement) $\mathbf{y}$, computed from the measured data with Equation 3.23 and Equation 3.24 in subsection 3.2.3.

Throughout this section, an elevator doublet and aileron 3211 manoeuvres are used as examples in the graphical representation of the Two Step method performance. Graphs of other manoeuvres can be found in section B.2 of Appendix B.

6.2.1. OLS model fit

The performance of the OLS estimator fitting the model to the observation can be visualised by plotting the observation $\mathbf{y}$ together with the model fit $\mathbf{y}$, as done on Figure 6.8 and Figure 6.9. Figure 6.8 shows the fit of the model to the computed symmetrical forces C_X, C_Z and moment C_m during an elevator doublet, while Figure 6.9 shows the fit of the model into the computed asymmetrical force C_Y and moments C_l, C_n during an aileron 3211.

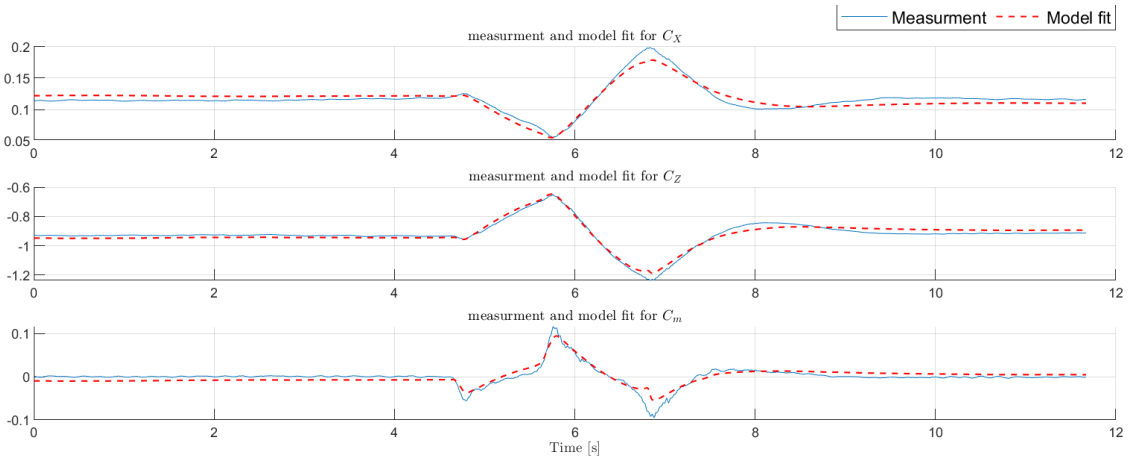

Figure 6.8: Observation and OLS model fit of the symmetrical dimensionless forces and moment for an elevator doublet

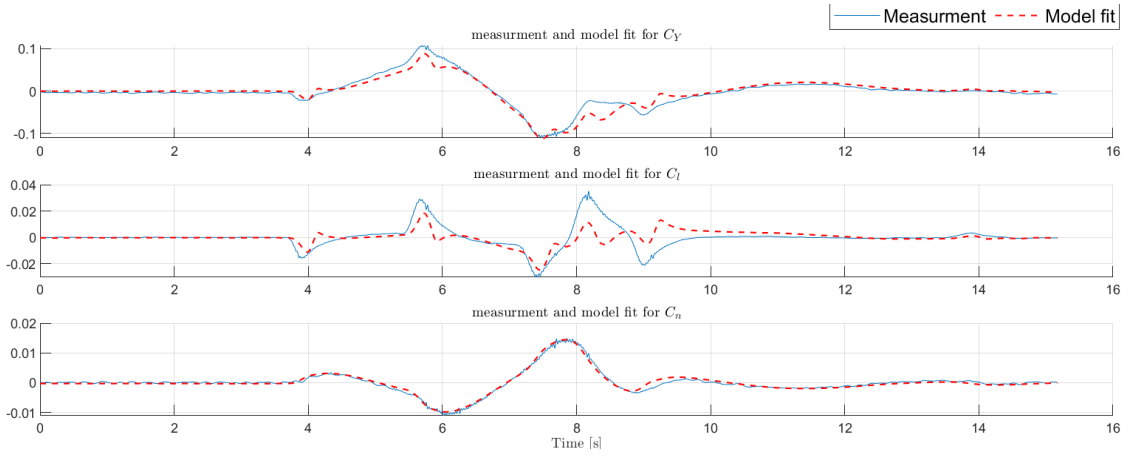

Figure 6.9: Observation and OLS model fit of the asymmetrical dimensionless force and moments for an aileron 3211

Throughout the recorded manoeuvres, the model of the chosen structure tends to fit most of the observation signals relatively well, as illustrated by the examples shown on Figure 6.8 and Figure 6.9. The rolling moment C_l shows the poorest fitting performance, in particular in the high dynamics part of

the 3211 manoeuvre. Although a better C_l fitting performance is observed for aileron doublets (not shown explicitly here, see section B.2), it remains the worst fitted moment in general, as also shown in the following paragraphs. In general, the model fails to exactly follow the extremities of the observation $\mathbf{y}$, most prominently observed for the C_l force, and to a lower extent C_X, C_Z or C_m. For the latter symmetrical forces, the post manoeuvre damping dynamics can also be underestimated by the model fit. The residual of the model fit are further described in subsection 6.2.2.

6.2.2. Model residual

The model residual is the difference between the observed force and moment $\mathbf{y}$ and the modelled force and moment $\mathbf{y}$, as defined by Equation 3.17. Figure 6.10 and Figure 6.11 plot the residual of the model as function of time for the elevator doublet and aileron 3211 manoeuvres, respectively.

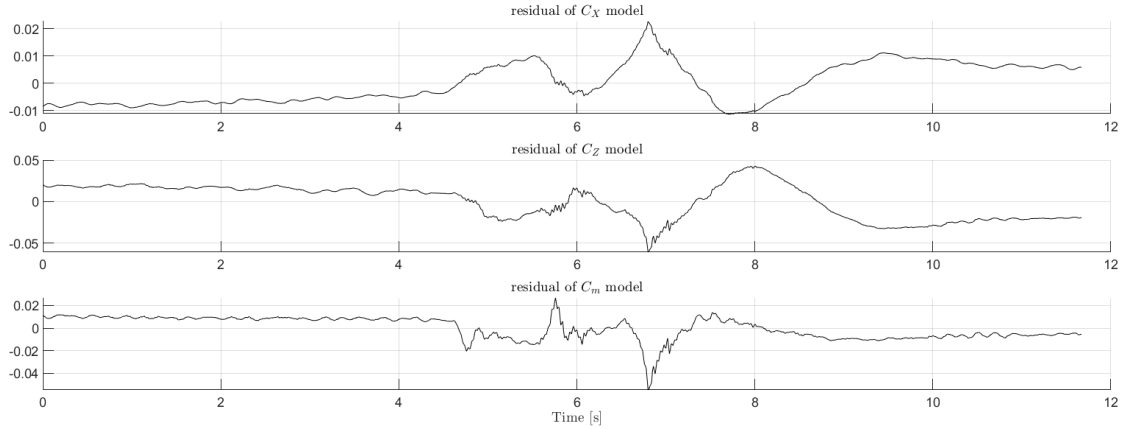

Figure 6.10: Model residual of the symmetrical dimensionless forces and moment for an elevator doublet

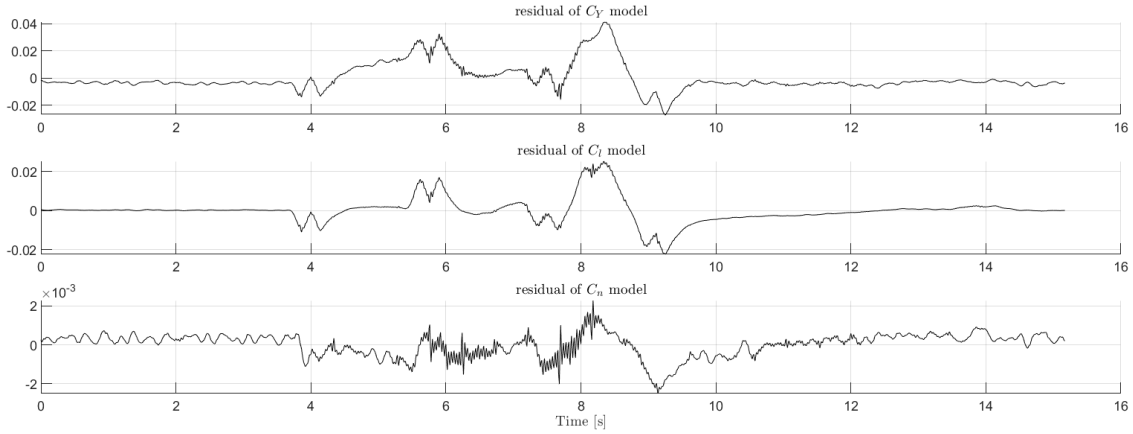

Figure 6.11: Model residual of the asymmetrical dimensionless force and moments for an aileron 3211

As the model is desired to fit the observation as close as possible, the residual is expected to have a mean of zero and consist of observation noise only (part of the BLUE condition, see subsection 3.2.1). As observed on Figure 6.10 and Figure 6.11, the residual stays indeed close to zero throughout the manoeuvre compared to the forces and moments excitation magnitudes, however, a time dependence of the residual can be observed around the extremities of reached aerodynamic forces and moments or at post manoeuvre damping. This is a consequence of limited observation fitting performance and is considered a limitation of the model. It should be noted that the smoothing and filtering of the input vector $\mathbf{u}$, as described in subsection 4.4.3, removes a significant part of the noise, otherwise visible as white noise oscillating around values close to zero on the residual plots.

In order to assess the overall performance of the OLS model fitting, rather than individual cases shown above, Table 6.3 lists the average, minimum and maximum relative root mean squared value of the residual throughout all manoeuvres. The RMS_{rel} is computed as the $RMS/|\mathbf{y}|_{\mathbf{max}}$ and therefore can be expressed as percentage. Values presented on Table 6.3 are computed as average from all applicable manoeuvres used in the identification process, thus two for symmetrical and five for asymmetrical forces and moments.

Table 6.3: Average, minimum and maximum of the relative root mean squared value of the residual, in %

	$\overline{RMS}_{rel}$	$\{RMS_{rel}\}_{min}$	$\{RMS_{rel}\}_{max}$
C_X	5.6	3.7	7.1
C_Y	5.9	3.0	9.3
C_Z	2.9	1.7	4.0
C_l	13.4	4.7	20.5
C_m	12.4	8.5	16.2
C_n	5.9	2.8	10.3

The root mean square of residual analysis shows the best fitting of the forces with mean RMS_{rel} up to 6% of the signal maximum absolute magnitude. The worst fitting performance concerns the C_m and C_n moments, where the mean RMS_{rel} reaches above 13% of the signal maximum absolute magnitude. There exists however variance of the model fitting performance with manoeuvres, indicated by the difference in minimum and maximum observed RMS_{rel} value. In gerenal, dimensionless forces and C_m moment is better fitted during doublets than 3211, whereas rudder excitation signals are better fitted overall than aileron excitation signals. Reasons for that and ways to improve fitting by model structure modification are suggested in chapter 7.

6.2.3. Aerodynamic and control derivatives

With the given OLS model fitting performance, the aerodynamic and control derivatives of C_X, C_Y, C_Z, C_l, C_m, C_n can be determined and are reported on Table 6.4, Table 6.5, Table 6.6, Table 6.7, Table 6.8 and Table 6.9, respectively. The parameter mean $\overline{\theta}$, minimum θ_{min} and maximum θ_{max} value among all applicable manoeuvres are presented, together with the mean, minimum and maximum encountered variance $Var\{\theta\}$, computed as defined by Equation 3.18.

As mentioned before, the symmetrical forces and moment aerodynamic and control derivatives are determined from three elevator doublets and four 3211 manoeuvres. The asymmetrical force and moments aerodynamic derivatives are determined from two aileron doublets, three aileron 3211s, three rudder doublets and four rudder 3211s. The asymmetrical control derivatives ($C_{()_{\delta a}}$, $C_{()_{\delta r}}$) are derived from manoeuvres exciting the particular control surface only.

Table 6.4: Estimated parameters of the C_X model, listing their mean, minimum and maximum determined values and variance

	$\overline{\theta}$	θ_{min}	θ_{max}	$\overline{Var}\{\theta\}$	$Var\{\theta\}_{min}$	$Var\{\theta\}_{max}$
C_{X_0}	0.029	0.022	0.038	1.17e-6	7.56e-7	1.67e-6
C_{X_α}	0.796	0.612	0.983	1.00e-4	7.26e-5	1.40e-4
C_{X_q}	2.823	1.221	5.734	2.07e-2	1.38e-2	3.83e-2
$C_{X_{\delta e}}$	0.126	-0.111	0.522	1.74e-4	1.04e-4	3.35e-4

Table 6.5: Estimated parameters of the C_Y model, listing their mean, minimum and maximum determined values and variance

	$\overline{\theta}$	θ_{min}	θ_{max}	$\overline{Var\{\theta\}}$	$Var\{\theta\}_{min}$	$Var\{\theta\}_{max}$
C_{Y_0}	0.001	-0.006	0.009	5.68e-8	1.83e-8	1.14e-7
C_{Y_β}	-0.515	-0.657	-0.390	8.32e-5	1.32e-5	4.05e-4
C_{Y_p}	0.262	-1.018	1.404	4.23e-3	4.38e-4	1.79e-2
C_{Y_r}	0.651	0.356	0.931	6.48e-4	1.66e-4	1.52e-3
$C_{Y_{\delta a}}$	0.046	-0.423	0.389	3.14e-4	2.76e-4	4.00e-4
$C_{Y_{\delta r}}$	0.169	0.145	0.196	1.97e-5	6.66e-6	5.44e-5

Table 6.6: Estimated parameters of the C_Z model, listing their mean, minimum and maximum determined values and variance

	$\overline{\theta}$	θ_{min}	θ_{max}	$\overline{Var\{\theta\}}$	$Var\{\theta\}_{min}$	$Var\{\theta\}_{max}$
C_{Z_0}	-0.521	-0.560	-0.495	1.25e-5	9.27e-6	1.69e-5
C_{Z_α}	-3.868	-4.143	-3.349	1.05e-3	9.37e-4	1.22e-3
C_{Z_q}	-18.509	-29.293	-12.735	2.11e-1	1.52e-1	3.06e-1
$C_{Z_{\delta e}}$	-0.767	-2.173	0.363	1.75e-3	1.05e-3	2.67e-3

Table 6.7: Estimated parameters of the C_l model, listing their mean, minimum and maximum determined values and variance

	$\overline{\theta}$	θ_{min}	θ_{max}	$\overline{Var\{\theta\}}$	$Var\{\theta\}_{min}$	$Var\{\theta\}_{max}$
C_{l_0}	0.000	-0.001	0.001	1.05e-8	4.95e-10	3.55e-8
C_{l_β}	-0.007	-0.098	0.045	7.91e-6	4.54e-7	2.25e-5
C_{l_p}	0.001	-0.753	0.719	5.21e-4	1.86e-5	1.46e-3
C_{l_r}	0.296	0.210	0.501	1.57e-4	1.07e-6	5.52e-4
$C_{l_{\delta a}}$	-0.001	-0.278	0.220	1.18e-4	5.56e-5	1.60e-4
$C_{l_{\delta r}}$	0.003	-0.002	0.009	5.19e-7	4.31e-8	1.92e-6

Table 6.8: Estimated parameters of the C_m model, listing their mean, minimum and maximum determined values and variance

	$\overline{\theta}$	θ_{min}	θ_{max}	$\overline{Var\{\theta\}}$	$Var\{\theta\}_{min}$	$Var\{\theta\}_{max}$
C_{m_0}	0.080	0.070	0.085	4.43e-6	2.12e-6	6.63e-6
C_{m_α}	-0.843	-0.924	-0.719	3.70e-4	2.26e-4	5.69e-4
C_{m_q}	-1.321	-6.455	2.191	7.08e-2	5.30e-2	8.39e-2
$C_{m_{\delta e}}$	-0.424	-0.977	0.030	5.82e-4	3.41e-4	7.55e-4

Table 6.9: Estimated parameters of the C_n model, listing their mean, minimum and maximum determined values and variance

	$\overline{\theta}$	θ_{min}	θ_{max}	$\overline{Var\{\theta\}}$	$Var\{\theta\}_{min}$	$Var\{\theta\}_{max}$
C_{n_0}	-0.001	-0.001	0.000	3.31e-9	6.50e-11	1.33e-8
C_{n_β}	0.042	-0.008	0.063	7.36e-6	8.81e-8	4.72e-5
C_{n_p}	-0.210	-0.534	-0.143	3.37e-4	7.28e-6	2.08e-3
C_{n_r}	-0.113	-0.167	-0.068	2.32e-5	1.54e-6	6.54e-5
$C_{n_{\delta a}}$	-0.010	-0.015	-0.003	1.03e-6	6.51e-7	1.48e-6
$C_{n_{\delta r}}$	-0.078	-0.087	-0.067	1.59e-6	4.02e-7	3.26e-6

The reliability of the determined parameters can be addressed by assessing their variance. Because the range of magnitude of the determined parameters $\overline{\theta}$ makes the variances listed in subsection 6.2.3 difficult to compare, the relative variance can be computed as $Var_{rel} = \sqrt{Var}/|\overline{\theta}|$.

In the C_X force model, the C_{X_α} term has the lowest relative variance (1.26e-2). This implies a consistent determination of the angle of attack contribution to the longitudinal body force. Since the C_X force

quantifies the force resisting the forward longitudinal aircraft motion, an increase of α it is expected to have a positive effect on the resistive force, drag being the main contributor. While the constant term C_{X_0} is also determined relatively consistently, the elevator deflection term $C_{X_{\delta e}}$ shows the highest relative variance (1.04e-1), changing sign depending on the manoeuvre. The elevator should not have major influence on the longitudinal force, thus this behaviour does not significantly downgrade the model robustness.

In the C_Y force model, the aileron deflection term $C_{Y_{\delta a}}$ has the highest relative variance (3.86e-1), followed by the rolling rate term C_{Y_p} (2.48e-1). This is caused not only by a overall variance of coefficient determination, but also the small absolute value of the coefficient average, increasing the relative variance. The side force dependence on rolling is expected negative yet its determination from aileron and rudder excitation has caused a high variance of C_{Y_p} value, to the extent its value changes sign from one manoeuvre to another. The same has been observed for $C_{Y_{\delta a}}$, which is determined inconsistently throughout aileron excitation. The side force dependence on β has been determined with highest confidence (relative variance of 1.77e-2), followed by the dependence on the rudder deflection δ_r (relative variance of 2.62e-2).

In the C_Z force model, the $C_{Z_{\delta e}}$ term shows the highest variance (5.46e-2). Although the variance is highest among the force model, it is still relatively low compared to other modelled forces and moments. The inconsistency of $C_{Z_{\delta e}}$ determination is most likely caused by one elevator 3211 outlier manoeuvre, during which the parameter is determined as positive. The C_{Z_0} (relative variance of 6.77e-3), closely followed by C_{Z_α}, are determined most consistently. Given that C_Z models the body downwards force, negative constant and angle of attack terms are affected mostly by the aircraft lift coefficient at trimmed conditions and lift curve, respectively. Overall, the confidence level of the C_Z force determination within the model is relatively high.

In the C_l moment model, the C_{l_0} term happens to show the highest relative variance, yet extremely small absolute variance. This is due to the parameter average being very close to zero (as expected), while being determined as positive or negative throughout the manoeuvres. Low confidence is also stated for C_{l_p}, to the extent that its average is small, even though its value determined from individual manoeuvres are in order of magnitude of 10^{-1}. In general, the C_l model is determined with relatively low confidence - the determined parameters show a rather inconsistent behaviour, having a positive or negative sign, depending on the manoeuvre, particularly for terms associated to highly correlated variables (p with δ_a) and the one subsequently showing coefficient correlation (p with δ_a and r) and during aileron excitation. This issue is further addressed in chapter 7. The lowest relative variance is computed for C_{l_r} (4.23e-2), $C_{l_{\delta r}}$ (2.37e-1) and C_{l_β} (3.89e-1).

In the C_m moment model, the C_{m_q} term shows the highest relative variance (2.01e-1) and has occasionally been determined as positive by outlier manoeuvres. The outliers have thus shifted its average to a less negative value, which can later affect the model validation performance. Unsurprisingly, the angle of attack term C_{m_α} and constant term C_{m_0} show the lowest variance (2.28e-2, 2.63e-2, respectively) and thus are determined consistently. Logically, they have a positive and negative sign, respectively, fulfilling the necessary conditions for aircraft longitudinal static stability.

In the C_n moment model, the $C_{n_{\delta a}}$ term shows the highest relative variance (1.06e-1). Within the C_n moment model, the C_{n_β} term only have been inconsistently determined with both positive and negative sign and, overall, determination from rudder excitation has shown more consistent results than from aileron excitation. Similarly to the C_l model, the constant term shows an increased relative variance due to its mean value close to zero, as expected. The lowest variance is computed for the rudder deflection term $C_{n_{\delta r}}$ (1.61e-2), followed by C_{n_r} and C_{n_β} (4.28e-2, 6.46e-2).

The high variance of the determined terms might be explained by the correlation of independent variables constituting the given force or moment. For symmetrical terms, the outstanding correlation relates the pitching rate q and elevator deflection δ_e, yet its value is at an acceptable level of -0.61. For asymmetrical terms, a strong correlation exists most notably between the rolling rate p and aileron deflection δ_a (-0.92). The yawing rate r and rudder deflection show a moderate correlation of -0.57.

In addition to independent variables correlation, the parameter correlation is determined from the covariance matrix (see Equation 3.18) and has shown similar correlation trends (moderate $q - \delta_e$ and

$r - \delta_r$, high $p - \delta_a$). An additional coupling is observed between parameters characterising the the contribution of rolling rate p and yawing rate r to C_Y force and C_l moment. Further analysis is given in chapter 7, together with suggestions for improvement of the model performance.

The aerodynamic and control derivatives for an alternative model structure including the $\dot{\alpha}$ and $\dot{\beta}$ terms in respective symmetrical and asymmetrical forces and moments are presented in section B.3 of Appendix B. As expected, the increase of number of terms in the model improves its fitting performance. This improvement is small because of the high correlation of the added independent variables with q and r, respectively. The latter causes an inconsistent determination of some of the parameters (increased variance), therefore, it is not superior to the model structure defined by Equation 3.21 and Equation 3.22.

Identification with doublet and 3211 control input

The aerodynamic and control derivatives presented in subsection 6.2.3 are averaged throughout all manoeuvres. However, a difference can be observed between the values determined from 3211 and doublet manoeuvres and is addressed on Figure 6.12. Figure 6.12a through Figure 6.12f plot the average derivatives as determined from 3211 and doublet manoeuvres separately, together with a single standard deviation range of their determination population.

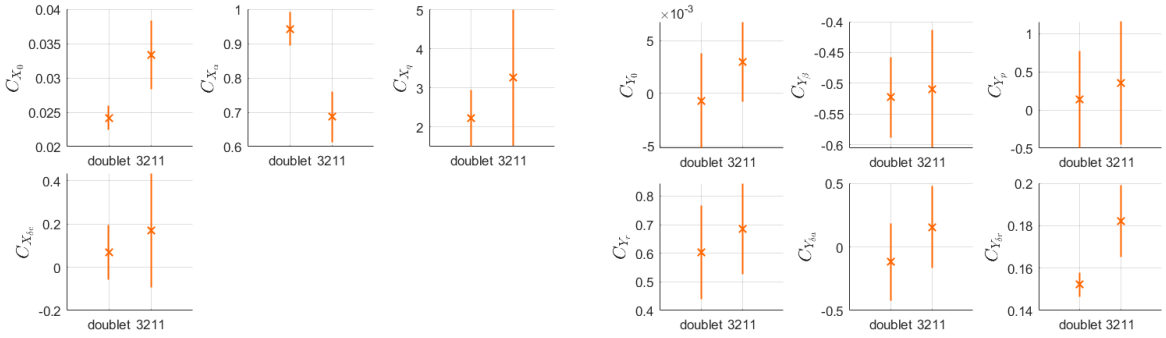

(a) C_X model terms

(b) C_Y model terms

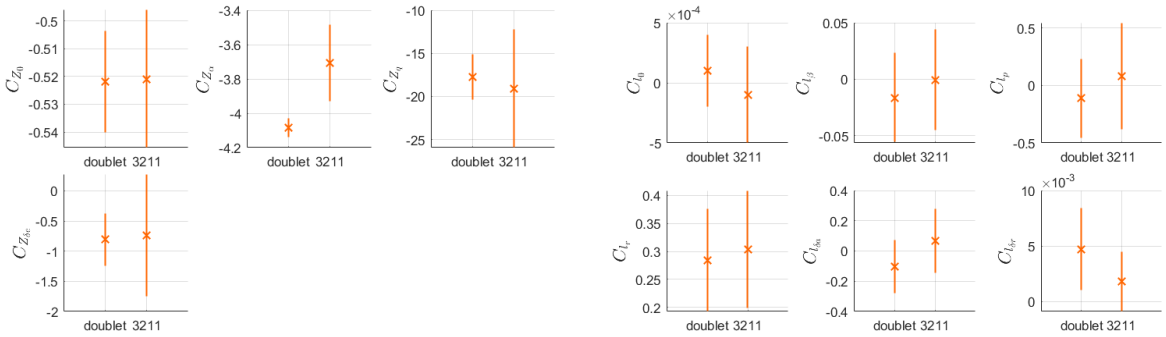

(c) C_Z model terms

(d) C_l model terms

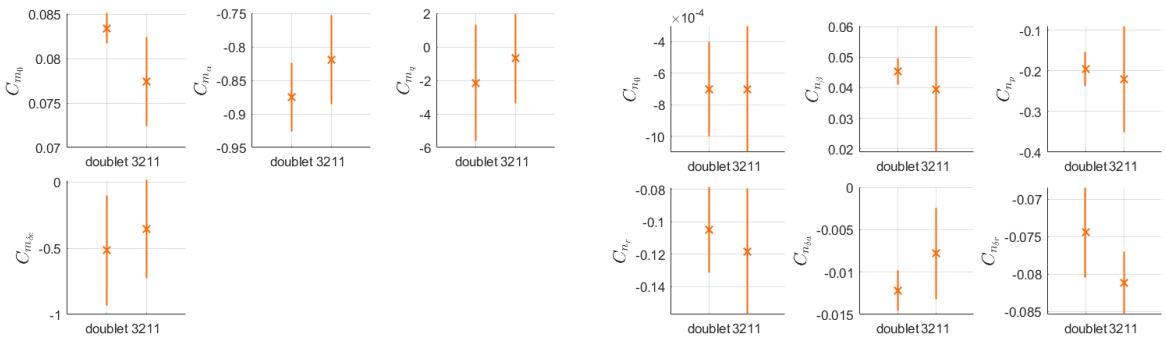

(e) C_m model terms

(f) C_n model terms

Figure 6.12: Average and standard deviation 1σ range of parameters determined with doublet and 3211 control inputs

Although no clear trend can be observed suggesting a different dynamic behaviour of the aircraft depending on the manoeuvre, Figure 6.12 provides valuable information about the variance of determined coefficients. Coefficients such as C_{Y_p}, $C_{Y_{\delta a}}$, C_{l_β}, C_{l_p} and $C_{l_{\delta a}}$ have a significant relative variance, to the extent of being determined with different signs, depending on the manoeuvre (as mentioned before in subsection 6.2.3). This suggests a high degree of randomness in the determination of such terms, implying a low confidence. Although terms such as C_{Y_0} and C_{l_0} are also determined with high relative variance from both types of manoeuvres, their value is, as expected, very close to zero and therefore their change in sign can be accepted. For some parameters, such as $C_{Y_{\delta r}}$ or C_{n_β}, the standard deviation differs significantly from one manoeuvre to the other. This suggests that a particular type of manoeuvrers might be more beneficial in terms of confidence in the identification of a particular parameters. Since this trend is observed for single parameters, rather than entire forces or moments constituents, no conclusion can be made about superiority of a particular manoeuvre over another.

Force and moment model constituents

In order to analyse the significance of the determined derivatives, the forces and moments of the aerodynamic model can be decomposed into their individual contributors, resulting from the model structure. An attempt to do so is presented on Figure 6.13, which shows how each product of the independent variable and corresponding parameter contributes to the overall forces C_X, C_Y, C_Z and moments C_l, C_m, C_n. The analysis is performed on doublet manoeuvres with excitation of the three control surfaces.

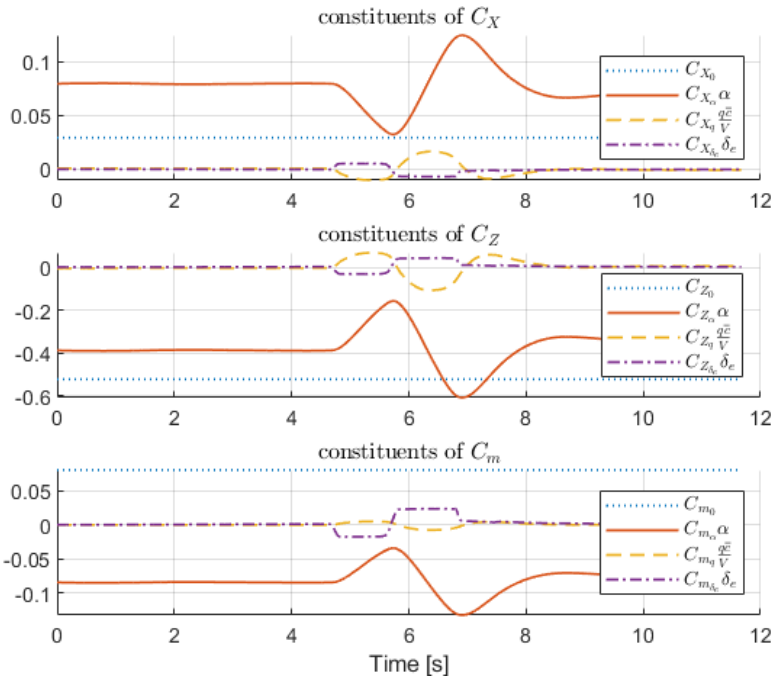

(a) Symmetrical forces and moment during an elevator doublet

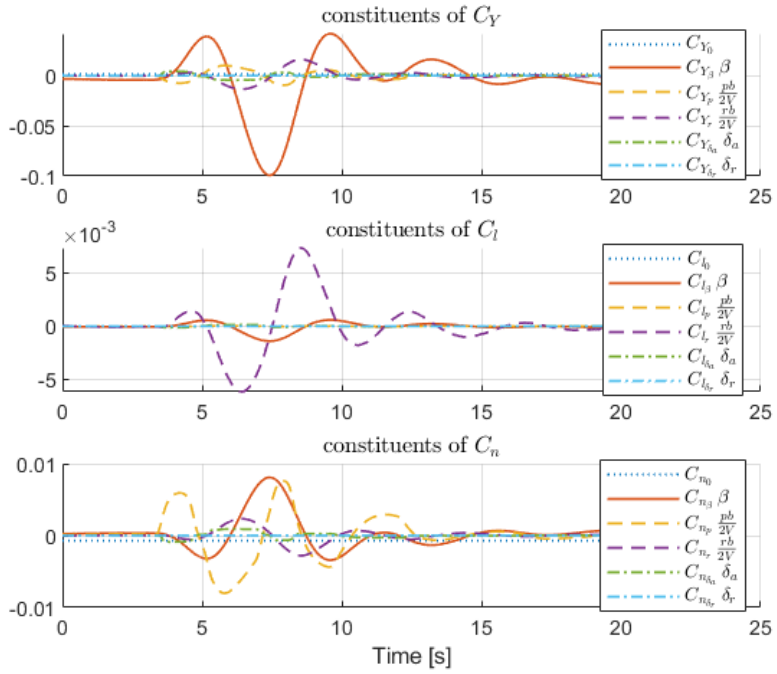

(b) Asymmetrical force and moments during aileron doublet

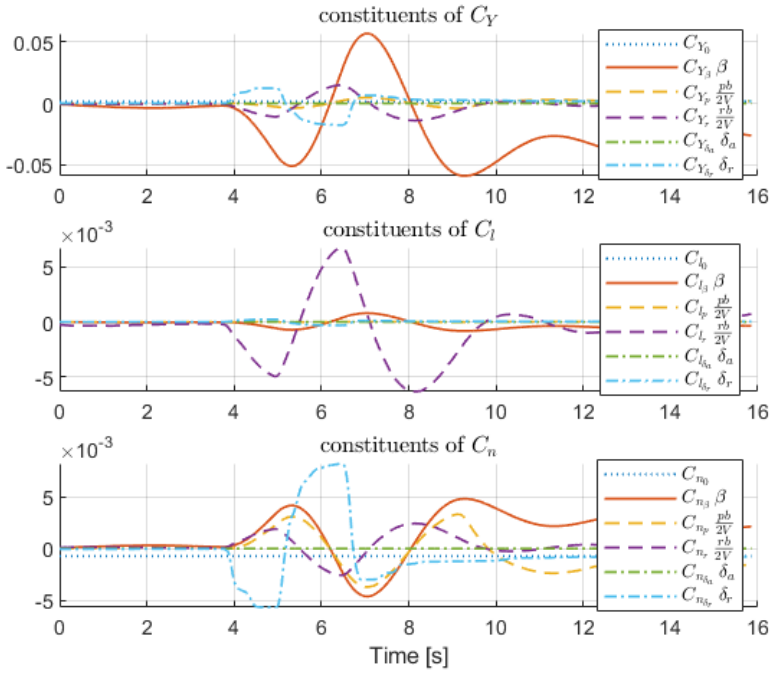

(c) Asymmetrical force and moments during rudder doublet

Figure 6.13: Contribution of constituents of force and moment model during doublet manoeuvre

Figure 6.13 shows that forces tend to be dominated by the incidence angle terms, with little control surface contribution, which is expected. This is visible on Figure 6.13a, where the α term is dominant, as well as Figure 6.13b and Figure 6.13c, where the β term is dominant. The rotational rates tend to be the second most significant terms constituting dimensionless forces. As shown on Figure 6.13c, the rudder deflection is as significant as the yawing rate for modelling the side force C_Y during a rudder doublet.

The symmetrical moment C_m is dominated by the α terms, however none of the three time varying

constituents overshadows the contribution of others. The relative similarity of the constituting terms (shape and period) might be the cause of relatively poor fitting of the complex C_m moment observation, as shown earlier in subsection 6.2.3. The rolling moment C_l is clearly dominated by the yawing term r, which is rather unexpected, as one would expect a high contribution of rolling term p and aileron deflection δ_a. Since the latter terms are determined inconsistently, their average is close to zero, ultimately reducing their contribution to the model. The C_n parameters are determined more consistently and show an even distribution of significance in the contribution to the dimensionless moment. As expected, the rudder deflection δ_r contribution is important in the yawing moment prediction.

6.3. Engine performance modelling

This section presents the engine performance estimated by the engine model, as described in subsection 3.2.4. The primary function of the model is to compute individual engine power P, thrust T and dimensionless change in total pressure $\Delta p_t/0.5\rho V^2$, which is done as function of the measured engine rotational speed N [rpm], manifold pressure p_z [inHg] and flight conditions. Once calibrated with engine specific values, the MVP engine monitor computes the engine power, which allows to compare the model and MVP estimation of the power value. Values used to calibrate the MVP engine monitor are presented in subsection 6.3.1, whereas the comparison and potential reasons of differences in estimated power are addressed in subsection 6.3.2.

6.3.1. Engine monitor calibration

The MVP engine monitor so called "Horsepower Calibration" is performed by identifying values of parameters listed on Table 6.10 specific for the Continental IO-360 engine. The specified parameters can be found in the Pilot's Operating Handbook [12], the engine manual [14] and the MVP manual itself [50].

Table 6.10: Engine characteristic values collected for the calibration of the MVP engine monitor, as per [50]

Maximum Continuous Power (MCP)	210 [hp]
N at MCP	2800 [rpm]
p_z at MCP	28.0 [inHg]
Percent of MCP at cruise	75 [%]
N at cruise power	2600 [rpm]
p_z at cruise power	24.3-25.0 [inHg]
Cruising altitude	5500 [ft]
Calibration factor	2.9
Richest cylinder No.	FWD: 4, AFT: 3
Richest cylinder EGT	FWD: 1367 [°F], AFT: 1390 [°F]

Although the exact computation procedure of the horsepower by the MVP remains a black box, it is specified to take the rotational speed N, manifold pressure p_z, altitude h and the mixture setting as input. In contrast to the derived model, it includes the mixture setting contribution, but potentially excludes the outside air temperature.

6.3.2. Modelled engine parameters

Since the monitored engine parameters are relatively constant during the identification manoeuvres (see subsection 3.2.3), the engine performance during the entire flight profile is addressed to capture its full range. The flight taken for this analysis is the FT1.0 and has been divided into phases of different power settings. Because of its low dynamics, the engine model input data is resampled to 2 [Hz].

Figure 6.14 shows the model and MVP estimated engine horsepower throughout the enire flight for the front and aft engine, as well as the difference in power estimation for both engines. The flight profile is marked with phases such as taxi, engine run up (engine test prior to take-off), idle, take-off, climb, BOM calibration, testing at 90 [kt] (for parameter identification), cruise at 150 [kt], descent and landing.

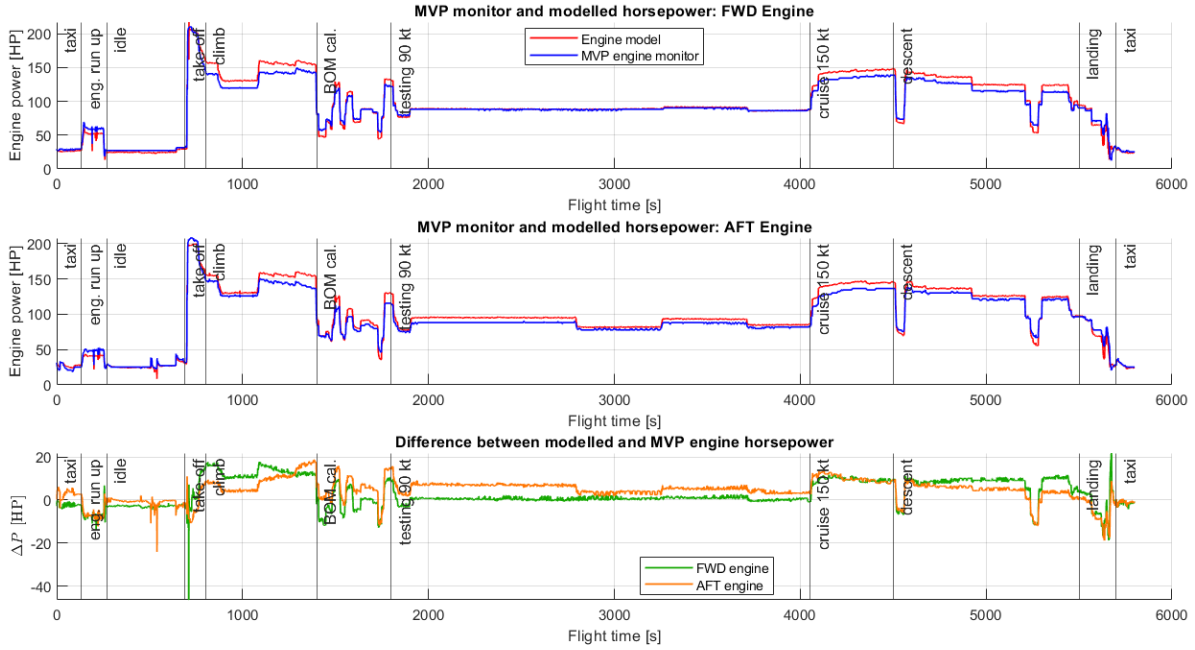

Figure 6.14: Power estimated with engine model and MVP throughout the FT1.0 flight profile

From each of the flight phases, a time instance is chosen for which the primary monitored and modelled parameters are determined for both engines and listed on Table 6.11. This allows to picture typical engine parameters values throughout the flight profile. On Table 6.11, t defines the flight time instance for which data is assembled, N the engine rotational speed, p_z the manifold pressure, P_{mod} and P_{MVP} the model and MVP estimated power, respectively, T the thrust and $\Delta p_t/0.5\rho V^2$ the dimensionless change in total pressure. Since during taxi, engine run up and idle phases the airspeed is null, no value exists for the $\Delta p_t/0.5\rho V^2$ at these instances.

Table 6.11: Engine monitored and estimated parameters during different phases of the flight profile

	t	N [rpm]		p_z [inHg]		P_{mod} [hp]		P_{MVP} [hp]		T [N]		$\frac{\Delta p_t}{0.5\rho V^2}$ [-]	
	[s]	FWD	AFT	FWD	AFT	FWD	AFT	FWD	AFT	FWD	AFT	FWD	AFT
Taxi	100	1180	1180	17.2	16.2	26.81	27.67	29.4	25.2	1073.1	1076.6	-	-
Engine run up	245	1770	1780	18.9	16.6	52.37	41.52	59.2	50.4	1857.8	1603.9	-	-
Idle	400	1100	1080	17.1	17.0	24.68	24.29	27.3	25.2	944.9	913.2	-	-
Take-off	720	2770	2730	27.9	27.9	206.59	197.32	210.0	207.9	2828.2	2722.2	1.040	1.001
Climb	850	2509	2510	24.8	24.6	156.45	154.57	140.7	147.0	1692.3	1673.4	0.296	0.293
BOM calibration	1600	2340	2320	15.6	17.3	69.88	83.16	75.6	77.7	914.4	1088.2	0.261	0.311
Testing, 90 [kt]	3000	2350	2350	17.7	17.0	88.26	82.30	88.2	79.8	1145.0	1068.3	0.323	0.301
Cruise, 150 [kt]	4200	2330	2340	24.7	24.5	142.69	142.08	132.3	130.2	1158.8	1153.6	0.111	0.111
Descent	4800	2300	2290	24.7	24.8	136.06	135.88	128.1	130.2	1222.3	1221.2	0.139	0.139
Landing	5660	1960	2174	12.7	15.2	21.27	46.84	39.9	62.2	309.6	671.0	0.094	0.203

Figure 6.14 and Table 6.11 clearly show that a difference ΔP exists between the engine power estimated with the derived engine model and MVP monitor. Since ΔP varies with time, attempts are made to identify correlations of ΔP with other engine parameters, which is explored in the following paragraphs.

Prior to that, the MVP estimated engine power is plotted against the modelled power on Figure 6.15 to graphically show their correlation, which is further quantified on Table 6.12 listing the coefficient of determination R^2 and the absolute root mean square difference, RMS. The coefficient of determination R^2 quantifies the proportionate variation of a model fitting an observation in a linear regression model and is the square of the correlation coefficient. The RMS is computed with Equation 3.17.

In this case, the MVP estimation is thus treated as the observation value fitted by the derived model. This does not truly picture the purpose of the derived engine model, as it aims to fit the observed

engine performance, rather than the MVP estimated engine performance, which has not been validated. However, the R^2 statistics are shown for the sake of comparison. The RMS quantifies the difference, rather than error, as the MVP estimation is not validated.

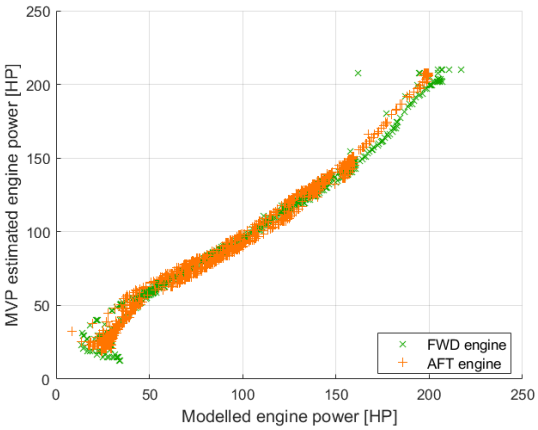

Figure 6.15: MVP estimated horsepower data plotted against the modelled horsepower

Table 6.12: Coefficient of determination and absolute root mean square difference between the modelled and MVP estimated engine horsepower

	R^2 [-]	RMS [hp]
Front engine	0.989	6.88
Aft engine	0.988	6.74

Data shown on Figure 6.15 deviates slightly from the perfect linear correlation, which is also captured by the high R values from Table 6.12. The modelled engine power fits the observed MVP power well, as given by the high R^2.

In order to identify potential sources of the non-zero ΔP, it is evaluated against other engine parameters and flight conditions for their potential correlation, namely the modelled engine power P_{mod}, manifold pressure p_z, static pressure p_s, outside air temperature OAT, rotational speed N, true airspeed V_{TAS} and pressure altitude h_p. The resulting correlation coefficients are listed on Table 6.13.

Table 6.13: Correlation coefficients of engine parameters and flight conditions with ΔP

	$R_{P_{mod}}$	R_{p_z}	R_{p_s}	R_{OAT}	R_N	$R_{V_{TAS}}$	R_{h_p}
Front engine	0.811	0.847	0.052	-0.182	0.404	0.648	-0.063
Aft engine	0.613	0.516	-0.497	-0.583	0.434	0.520	0.491

Among the variables presented on Table 6.13, P_{mod}, p_z and p_s are chosen as the ones that have relatively high correlation (within the population), while also showing a clear trend when presented graphically, as shown on Figure 6.16. While V_{TAS} is reported to have a relatively high correlation coefficient for both engines, no clear trend is observed when plotted. Logically, the p_s and h_p show similar behaviour because of their interdependence.

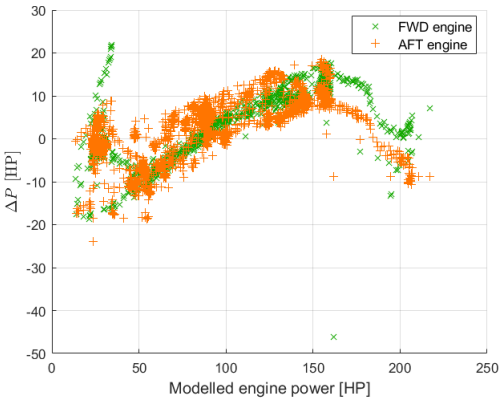

(a) ΔP against modelled engine horsepower

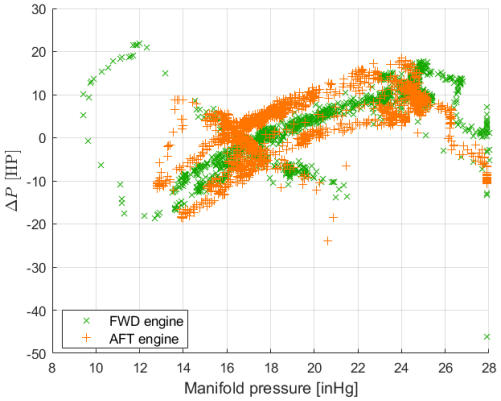

(b) ΔP against manifold pressure

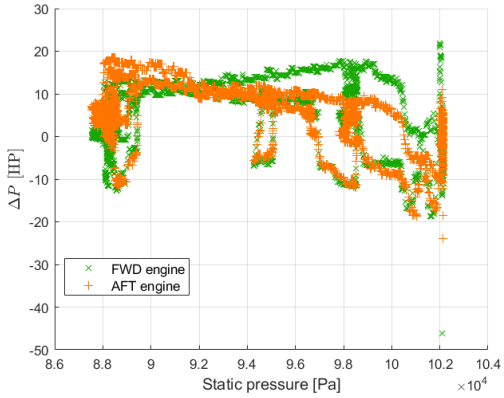

(c) ΔP against static pressure

Figure 6.16: ΔP represented against engine parameters and flight conditions of relatively high correlation coefficient

Lastly, the MT Propeller performance maps used in the derived model are presented on Figure 6.17. Although the model uses the a set of maps spanning between SL and FL125 as well as N of 2400 through 2800, the presented charts are assembled for the SL and $N = 2600$ [rpm] conditions. Figure 6.17a shows the propeller efficiency η_p and Figure 6.17b the thrust coefficient C_T dependence on the advance ratio J for a range of power coefficient values C_P.

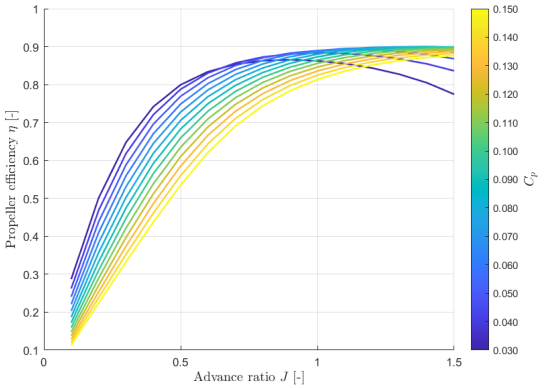

(a) Propeller efficiency η_p

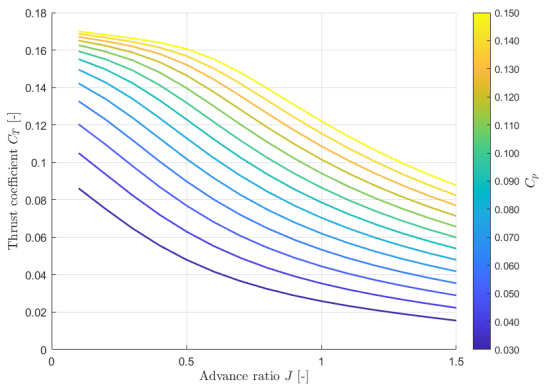

(b) Thrust coefficient C_T

Figure 6.17: η_p and C_T dependence on J for a range of C_P

7
Evaluation

This chapter evaluates the results of the system identification presented in chapter 6. This is done by comparing the determined aerodynamic model to flight data in a validation process described in section 7.1. Additionally, a sensitivity analysis is performed on the aerodynamic and engine models in section 7.2. The obtained results in the context of presented statistical analysis, validation and sensitivity analysis are discussed in section 7.3. Finally, an attempt is made to qualitatively answer the research question, as done in section 7.4.

7.1. Validation

This section presents the validation of the aircraft aerodynamic model being the result of the system identification process explained in chapter 3 and reported in section 6.2. Its numerical implementation is done in file `part4_vadidation.m`, as listed in Appendix D. Validation concerns the identified aerodynamic model only. The engine model is not validated, but its outcome is compared to the MVP output, which has been done and presented in subsection 6.3.2. In order for the data provided by the MVP engine monitor to be treated as source of validation, its calibration should be validated with dedicated experiments, which is outside of the scope of this study (see section 8.2).

The identified aerodynamic model of the symmetrical and asymmetrical forces and moments has been applied to a validation set of flight data consisting of 14% of the total recorded flight data, as specified in section 4.4. The validation data set includes three manoeuvres, each exciting a particular axis of the body reference frame, namely: an elevator 3211, aileron doublet and rudder 3211.

Figure 7.1 shows the symmetrical forces and moment C_X, C_Z and C_m predicted by the aerodynamic model compared to the observation flight data during an elevator 3211 manoeuvre.

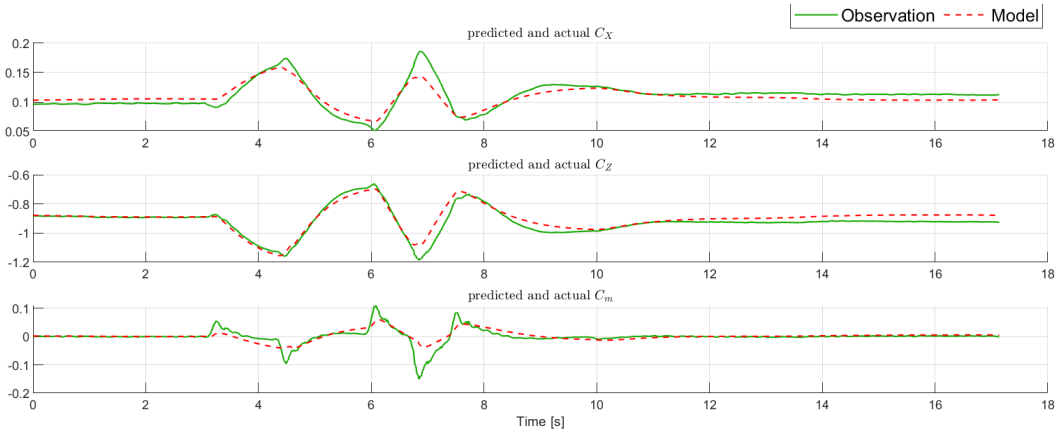

Figure 7.1: Observed and modelled symmetrical forces and moment for an elevator 3211 manoeuvre

Figure 7.2 shows the asymmetrical force and moments C_Y, C_l and C_n predicted by the aerodynamic model compared to the observation flight data during an aileron doublet manoeuvre.

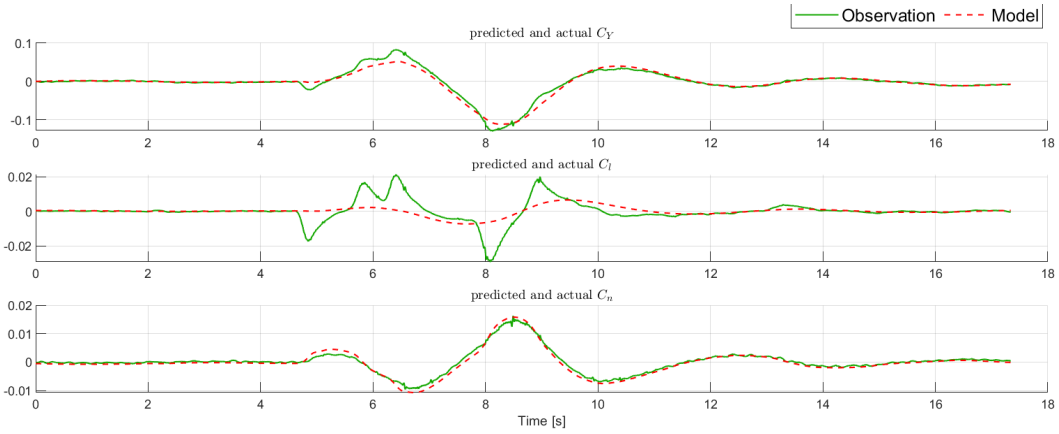

Figure 7.2: Observed and modelled symmetrical force and moments for an aileron doublet manoeuvre

Figure 7.3 shows the asymmetrical force and moments C_Y, C_l and C_n predicted by the aerodynamic model compared to the observation flight data during a rudder 3211 manoeuvre.

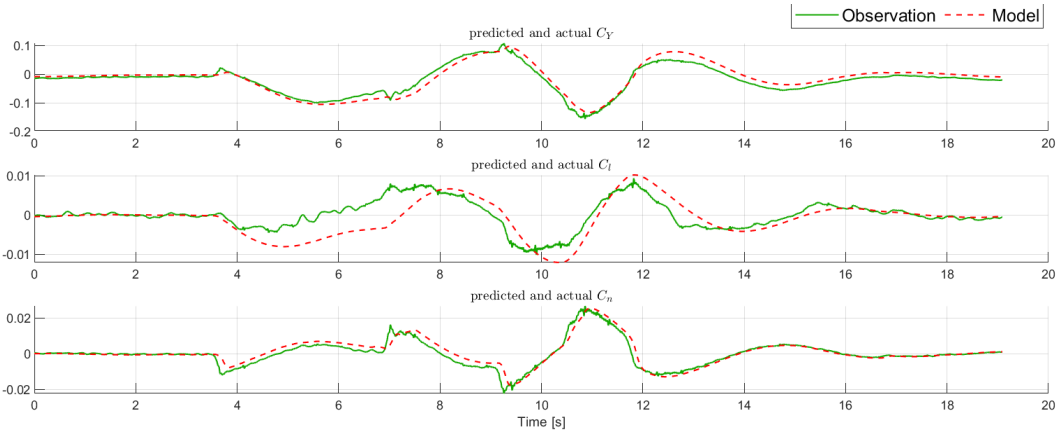

Figure 7.3: Observed and modelled asymmetrical force and moments for a rudder 3211 manoeuvre

The model behaviour shows similar trends to the ones observed for the OLS observation fit presented in subsection 6.2.1. Forces and moments that tend to be modelled the best are C_Z, C_Y and C_n, while the C_l model seems to fail to reach extremities of the moment signal, predicting only the overall trend. The C_l model performs better during the rudder excitation, while C_n slightly better during the aileron excitation - manoeuvres in which their respective axes excitation is a result of coupling, rather than direct control input and shows lower dynamics. The C_X and C_m show the tendency to fail to reach the extremities of the signal, however fitting the overall signal relatively well. For the latter terms in particular, the model tends to overdamp the signal post manoeuvre, reducing the amplitude of signal during the damping phase.

In order to quantitatively present the validity of the aerodynamic model, fitting statistics are presented. The relative root mean squared model error (in percent) and coefficient of determination are listed on Table 7.1 as averaged values over the validation manoeuvres for the six dimensionless forces and moments. The model error shows similar behaviour to the fitting residual presented in subsection 6.2.2 and oscillates around a mean zero value, while capturing the reaming unfiltered observation noise and model weaknesses mentioned above.

Table 7.1: Fit statistics of the aerodynamic model averaged over the three validation manoeuvres

	C_X	C_Y	C_Z	C_l	C_m	C_n
$\overline{RMS}_{rel}$ [%]	5.4	7.8	2.8	23.8	10.8	6.9
$\overline{R^2}$ [-]	0.834	0.939	0.901	0.462	0.585	0.944

The modelled forces and yawing moment show a relatively high correlation with the validation set observation signal, C_Y, C_Z and C_n exceeding 0.9. In contrast, the rolling and pitching moment show a low correlation with values below 0.6. The latter moments also show high relative RMS values. Although well correlated, the asymmetrical force C_Y also show a high relative RMS value.

7.2. Sensitivity analysis

This section addresses the sensitivity of both the aerodynamic and engine models' output to change in their input parameters. The aim of the section is to identify results that might be overly sensitive to a change in some input variables, in particular if the latter have a considerable uncertainty. It is therefore an attempt to asses the robustness of the results, independently of their validity presented in section 7.1.

The sensitivity analysis is carried out by determining the partial derivatives of the results (output C_a - aerodynamic model derivatives and engine output parameters) with respect to selected variables (input a), computed around specified nominal conditions a_0. This is done by linearising the gradient of the outputs around ±5% of the nominal input conditions: dividing the change in output by the change in input, as explained by Equation 7.1. Since the partial derivatives are local, their values can be considered valid around the specified nominal conditions only. subsection 7.2.1 presents the sensitivity analysis of the aerodynamic model, whereas subsection 7.2.2 - the sensitivity analysis of the engine model.

$$\frac{\partial C_a}{\partial a} \approx \frac{C_{a,a=1.05a_0} - C_{a,a=0.95a_0}}{1.05a_0 - 0.95a_0} \tag{7.1}$$

Rather than analysing the impact on the dynamics of the aircraft or engine, this analysis aims at isolating single variables potentially affecting the output and assessing the severity of a potential error in the estimation of a particular variable influencing the value of the resulting output. A derivation of the influence of change in the centre of gravity location on the aerodynamic and control derivatives can be found in [67, p. 18].

7.2.1. Aerodynamic model

The sensitivity of the aerodynamic model is evaluated by determining the partial derivatives of the aerodynamic and control derivatives (coefficients) with respect to variables that have been determined throughout this study and thus can carry a non-negligible uncertainty. These variables are the aircraft centre of gravity location, moment of inertia and control surface deflections. In addition, measurements such as the angle of attack, angle sideslip as well as main and auxiliary tank fuel mass have been incorporated to the analysis as they are identified to have a non-negligible uncertainty caused by instrumentation limitations.

COG and MOI

Table 7.2, Table 7.3 and Table 7.4 list the partial derivatives of the rolling, pitching and yawing moment constituents with respect to the centre of gravity location $x_{c.g.}$, $y_{c.g.}$, $z_{c.g.}$ and inertial properties of the aircraft I_{xx}, I_{yy}, I_{zz}, I_{xz}, respectively. The derivative is computed around ±5% MAC of the nominal centre of gravity location and ±5% of the nominal inertia matrix. The nominal conditions for this analysis are COG of [3.53, 0.00, 1.68 (-0.01)] [m] in F_D and [I_{xx}, I_{yy}, I_{zz}, I_{xz}] = [5,493 (-134), 5,411 (-6), 9,689 (-131), 311 (-2)] [kg m^2]. The change of nominal conditions throughout all the manoeuvres has been indicated in parentheses.

Table 7.2: Partial derivatives of rolling moment constituents with respect to centre of gravity and moment of inertia

	$\partial x_{c.g.}$ [% MAC]	$\partial y_{c.g.}$ [% MAC]	$\partial z_{c.g.}$ [% MAC]	∂I_{xx} [kg m^2]	∂I_{yy} [kg m^2]	∂I_{zz} [kg m^2]	∂I_{xz} [kg m^2]
∂C_{l_0}	5.71e-7	-1.55e-9	-2.01e-7	-3.71e-9	5.97e-10	-5.83e-10	8.26e-8
∂C_{l_β}	-3.19e-5	-3.77e-7	-6.96e-6	-1.01e-6	2.72e-8	-2.65e-8	-4.62e-6
∂C_{l_p}	1.60e-4	-3.50e-7	-6.23e-5	-1.08e-6	-1.53e-7	1.49e-7	2.31e-5
∂C_{l_r}	7.75e-5	1.86e-5	7.97e-4	5.11e-5	4.98e-7	-4.86e-7	1.12e-5
$\partial C_{l_{\delta a}}$	7.66e-6	-9.92e-8	-8.77e-6	-3.54e-7	-7.45e-8	7.28e-8	1.11e-6
$\partial C_{l_{\delta r}}$	6.14e-5	2.89e-8	-1.40e-5	1.14e-7	3.60e-8	-3.51e-8	8.89e-6

Table 7.3: Partial derivatives of pitching moment constituents with respect to centre of gravity and moment of inertia

	$\partial x_{c.g.}$ [% MAC]	$\partial y_{c.g.}$ [% MAC]	$\partial z_{c.g.}$ [% MAC]	∂I_{xx} [kg m^2]	∂I_{yy} [kg m^2]	∂I_{zz} [kg m^2]	∂I_{xz} [kg m^2]
∂C_{m_0}	-5.91e-5	0	2.21e-4	-1.45e-9	1.46e-5	1.50e-9	-1.59e-8
∂C_{m_α}	6.23e-4	0	-2.33e-3	2.37e-8	-1.54e-4	-2.45e-8	1.37e-7
∂C_{m_q}	8.78e-4	0	-3.63e-3	-9.61e-7	-2.41e-4	9.93e-7	-1.28e-5
$\partial C_{m_{\delta e}}$	3.05e-4	0	-1.16e-3	2.46e-8	-7.67e-5	-2.54e-8	-7.09e-7

Table 7.4: Partial derivatives of yawing moment constituents with respect to centre of gravity and moment of inertia

	$\partial x_{c.g.}$ [% MAC]	$\partial y_{c.g.}$ [% MAC]	$\partial z_{c.g.}$ [% MAC]	∂I_{xx} [kg m^2]	∂I_{yy} [kg m^2]	∂I_{zz} [kg m^2]	∂I_{xz} [kg m^2]
∂C_{n_0}	3.29e-7	-2.73e-8	-6.50e-9	-1.18e-9	1.23e-9	-7.48e-8	3.56e-9
∂C_{n_β}	-9.28e-6	1.43e-6	-2.06e-6	-6.68e-8	7.00e-8	4.05e-6	1.12e-6
∂C_{n_p}	9.50e-5	-7.38e-6	-2.64e-6	3.05e-9	-2.94e-9	-2.06e-5	1.43e-6
∂C_{n_r}	-3.67e-4	-3.85e-6	1.09e-4	-3.61e-7	3.78e-7	-1.04e-5	-5.92e-5
$\partial C_{n_{\delta a}}$	7.45e-6	-4.06e-7	-8.97e-7	-7.14e-8	7.46e-8	-1.06e-6	4.88e-7
$\partial C_{n_{\delta r}}$	3.16e-5	-2.83e-6	3.12e-7	1.50e-8	-1.58e-8	-7.90e-6	-1.69e-7

From the determined partial derivatives presented on Table 7.2, Table 7.3 and Table 7.4 it can be observed that C_{l_p}, C_{l_r}, C_{m_q} and C_{n_p}, C_{n_r} show the highest overall sensitivity to change in centre of gravity location and aircraft moment of inertia. The change in centre of gravity location influences the inertial properties of the aircraft around the COG, but in this analysis changing the moment of inertia does not influence the centre of gravity location. Since the dimensionless aircraft moments dominating term is the product of the moment of inertia and rotational acceleration around the moment axis (see Equation 3.24), it is logical for the rotational rate coefficients to show the highest sensitivity to COG and MOI change. Nevertheless, no coefficient has partial derivative higher than order of magnitude 10^{-3}. The lowest sensitivity is observed for constant terms. Dimensionless forces coefficients are insensitive to change in COG and MOI.

Control deflection and air angles

The sensitivity of control coefficients on corresponding measured control deflections is presented on Table 7.5, whereas the sensitivity of α and β coefficients on the angle of attack and angle of sideslip is presented on Table 7.6. Logically, no other coefficients than presented are sensitive to changes in the control deflection and air incidence angles.

Since the control deflection and air incidence angles are signals recorded as function of time rather than as constant throughout manoeuvres, the sensitivity analysis addresses constant scaling of the signal. This aims at mimicking uncertainty in computation of the control deflection and air angles from measured data by applying an erroneous scaling. The partial derivative is thus determined as ratio between difference in coefficients (output) and difference in angle signals (input) scaled by 105% and 95%.

Table 7.5: Partial derivatives of control coefficients with respect to control deflections

	$\partial\delta e$ [%]	$\partial\delta a$ [%]	$\partial\delta r$ [%]
$\partial C_{X_{\delta e}}$	-1.27e-3	-	-
$\partial C_{Y_{\delta a}}$	-	-4.61e-4	-
$\partial C_{Y_{\delta r}}$	-	-	-1.70e-3
$\partial C_{Z_{\delta e}}$	7.69e-3	-	-
$\partial C_{l_{\delta a}}$	-	1.41e-5	-
$\partial C_{l_{\delta r}}$	-	-	-3.04e-5
$\partial C_{m_{\delta e}}$	4.25e-3	-	-
$\partial C_{n_{\delta a}}$	-	9.57e-5	-
$\partial C_{n_{\delta r}}$	-	-	7.85-4

Table 7.6: Partial derivatives of coefficients with respect to angle of attack and sideslip

	$\partial\alpha$ [%]	$\partial\beta$ [%]
∂C_{X_α}	-7.98e-3	-
∂C_{Y_β}	-	5.16e-3
∂C_{Z_α}	3.88e-2	-
∂C_{l_β}	-	7.25e-5
∂C_{m_α}	8.45e-3	-
∂C_{n_β}	-	-4.21e-4

In the case of control deflection and air angles, the partial derivatives of the coefficients are approximately equal to the negative coefficient values themselves, when expressed in decimal (instead of % scaling). This implies that for every percent change in scaling of the signal, the corresponding coefficient value changes by one percent and shows the effective linearisation of the coefficient dependence on the angles around nominal conditions.

Fuel mass

Table 7.7, Table 7.8, Table 7.9, Table 7.10, Table 7.11 and Table 7.12 list the derivatives of the constituents of the C_X, C_Z, C_m, C_Y, C_l and C_n forces and moments with respect to the fuel mass in the main ($m_{f,M}$) and auxiliary ($m_{f,A}$) tank, respectively. The change in fuel mass affects the centre of gravity location, moment of inertia and overall aircraft weight. The derivative is computed around ±5% of the nominal fuel mass in the tanks, being [$m_{f,M}$, $m_{f,A}$] = [231.7 (-16.7), 100.9] [kg].

Table 7.7: Partial derivatives of longitudinal force constituents with respect to fuel mass

	$\partial m_{f,M}$ [kg]	$\partial m_{f,A}$ [kg]
∂C_{X_0}	1.37e-5	1.45e-5
∂C_{X_α}	3.71e-4	3.94e-4
∂C_{X_q}	1.31e-3	1.40e-3
$\partial C_{X_{\delta e}}$	5.84e-5	6.26e-5

Table 7.8: Partial derivatives of vertical force constituents with respect to fuel mass

	$\partial m_{f,M}$ [kg]	$\partial m_{f,A}$ [kg]
∂C_{Z_0}	-2.43e-4	-2.58e-4
∂C_{Z_α}	-1.80e-3	-1.91e-3
∂C_{Z_q}	-8.61e-3	-9.15e-3
$\partial C_{Z_{\delta e}}$	-3.56e-4	-3.79e-4

Table 7.9: Partial derivatives of pitching moment constituents with respect to fuel mass

	$\partial m_{f,M}$ [kg]	$\partial m_{f,A}$ [kg]
∂C_{m_0}	4.88e-6	3.65e-6
∂C_{m_α}	-5.15e-5	-3.85e-5
∂C_{m_q}	-8.22e-5	-6.17e-5
$\partial C_{m_{\delta e}}$	-2.57e-5	-1.93e-5

Table 7.10: Partial derivatives of lateral force constituents with respect to fuel mass

	$\partial m_{f,M}$ [kg]	$\partial m_{f,A}$ [kg]
∂C_{Y_0}	6.99e-7	7.12e-7
∂C_{Y_β}	-2.51e-4	-2.53e-4
∂C_{Y_p}	1.28e-4	1.29e-4
∂C_{Y_r}	3.17e-4	3.20e-4
$\partial C_{Y_{\delta a}}$	2.26e-5	2.26e-5
$\partial C_{Y_{\delta r}}$	8.20e-5	8.33e-5

Table 7.11: Partial derivatives of rolling moment constituents with respect to fuel mass

	$\partial m_{f,M}$ [kg]	$\partial m_{f,A}$ [kg]
∂C_{l_0}	-2.56e-8	3.77e-9
∂C_{l_β}	-9.25e-6	-1.79e-6
∂C_{l_p}	-4.48e-6	1.23e-6
∂C_{l_r}	4.24e-4	6.53e-5
$\partial C_{l_{\delta a}}$	-2.27e-6	-2.60e-7
$\partial C_{l_{\delta r}}$	1.86e-6	1.07e-6

Table 7.12: Partial derivatives of yawing moment constituents with respect to fuel mass

	$\partial m_{f,M}$ [kg]	$\partial m_{f,A}$ [kg]
∂C_{n_0}	-6.04e-7	-8.93e-8
∂C_{n_β}	3.19e-5	4.83e-6
∂C_{n_p}	-1.63e-4	-2.42e-5
∂C_{n_r}	-9.30e-5	-1.90e-5
$\partial C_{n_{\delta a}}$	-9.04e-6	-1.27e-6
$\partial C_{n_{\delta r}}$	-6.25e-5	-9.35e-6

The sensitivity of the coefficients to fuel tank mass per [kg] is highest for the symmetrical forces C_X and C_Z, particularity the pitching moment terms, which happen to be the highest in magnitude. Nevertheless, an unrealistic fuel mass uncertainty of order 10^2 [kg] would be required to have significant influence on the determined parameters.

Overall, no aerodynamic nor control derivatives showed excessive sensitivity to any particular parameters, indicating that changes to nominal conditions or errors in its accurate determination do not significantly affect the values of identified aerodynamic and control derivatives. It should however be noted, that the sensitivity analysis aimed at identifying the effect of uncertainty in determined variables around nominal conditions - anticipating the computed or measured aircraft state being different from reality. The analysis does not take into account the effect of change in variables on the dynamic response of the aircraft, for which a dedicated experimental campaign would be necessary. In addition, the sensitivity of results in conditions different than nominal might be different from the one presented.

7.2.2. Engine model

Similarly to the aerodynamic model case, the sensitivity of the engine model can be identified by independently varying its inputs. As described before (see subsection 3.2.4), in contrast to the aerodynamic model, the engine model is composed of several embedded functions, rather than being identified by optimising for least squares error. To assess the sensitivity of the engine model, partial derivatives of its outputs, namely engine horsepower P, thrust T and dimensionless change in total pressure $\Delta p_t/0.5\rho V^2$ are computed with respect to the model inputs, namely the engine rotational speed N (±5 [rpm]), manifold pressure p_z (±0.05 [inHg]), static temperature at sea level $T_{h=0}$ (±0.125 [K]), pressure altitude h_p (±0.15 [m]) and true airspeed V_{TAS} (approximately ±0.016 [m/s]). The derivatives are computed around ±5% of the variable value at two different nominal conditions - cruise conditions and testing conditions.

Table 7.13 lists the partial derivatives of the engine model for cruise conditions, determined as $N = 2600$ [rpm], $p_z = 24.5$ [inHg], $T_{h=0} = 288.15$ [K], $h_p = 1,676$ [m] and $V_{TAS} = 85$ [m/s]. At these conditions, the engine is modelled to have a power of $P = 172.8$ [hp], thrust $T = 1,348.6$ [N] and $\Delta p_t/0.5\rho V^2 = 0.128$ [-].

Table 7.13: Partial derivatives of engine power, thrust and dimensionless Δp_t with respect to inputs at cruise conditions

	∂N [rpm]	∂p_z [inHg]	$\partial T_{h=0}$ [K]	∂h_p [m]	∂V_{TAS} [m/s]
∂P [hp]	6.95e-2	9.55e0	-3.11e-1	7.72e-3	0
∂T [N]	4.36e-1	7.44e1	-2.42e0	5.97e-2	-1.49e1
$\partial \frac{\Delta p_t}{0.5\rho V^2}$ [-]	4.08e-5	7.06e-3	1.39e-4	1.85e-5	-4.45e-3

In a similar way, Table 7.14 lists the partial derivatives of the engine for testing conditions, determined as $N = 2350$ [rpm], $p_z = 17.5$ [inHg], $T_{h=0} = 296.65$ [K], $h_p = 1,219$ [m] and $V_{TAS} = 46$ [m/s]. At these conditions, the engine is modelled to have a power of $P = 86.7$ [hp], thrust $T = 1,172.7$ [N] and $\Delta p_t/0.5\rho V^2 = 0.372$ [-].

Table 7.14: Partial derivatives of engine power, thrust and dimensionless Δp_t with respect to inputs at testing conditions

	∂N [rpm]	∂p_z [inHg]	$\partial T_{h=0}$ [K]	∂h_p [m]	∂V_{TAS} [m/s]
∂P [hp]	6.17e-2	8.47e0	-1.72e-1	8.22e-3	0
∂T [N]	7.31e-1	1.11e2	-2.41e0	1.07e-1	-1.88e1
$\partial \frac{\Delta p_t}{0.5\rho V^2}$ [-]	2.33e-4	3.52e-2	4.35e-4	6.97e-5	-2.29e-2

Given the aforementioned precision of the recorded variables, the uncertainty in the engine model output can be estimated. Thus, the precision of the engine model output is mostly affected by the rotational speed and manifold pressure reading precision and can be off by up to around 0.5 [hp] for power, 6 [N] for thrust and 0.002 [-] for dimensionless change in total pressure. As demonstrated, the sensitivity changes with flight conditions.

7.3. Discussion

In this study, the aircraft aerodynamic model has been identified with the Two Step method, in which the flight path of the aircraft if first reconstructed with an Iterated Extended Kalman Filter, and followed by aerodynamic model parameter identification with an Ordinary Least Squares estimator. The choice of the Two Step method is dictated by its applicability to complex models which are based on measurements with high level of noise or uncertainty.

Because of the nonlinearity of the mathematical aircraft model, an Extended Kalman Filter is developed for the first part of the Two Step method based on available simulation data. In order to increase the convergence rate, it is upgraded to an Iterated EKF, which expectedly provides the same results, at a slightly improved convergence rate. Overall, the flight testing performed has provided data with relatively low noise levels but high uncertainty of actual value of some measurements, such as the angles of attack and sideslip. As a result, the IEKF behaves differently on the flight test data than on the simulated data used for its development and verification, that is, it smooths signals recorded with lower resolution and shows high innovation on air data measurements such as V_{TAS}, α or β. This is caused by the filter assigning more weight (Kalman gain) to the variable computed by the embedded navigation model, rather than relying on the raw measured data. This behaviour can suggest, but does not imply, a mismatch between individual terms of the recorded measurements in terms of physical relationships and could be caused by low instrumentation resolution or delays. In any case, high innovation of V_{TAS}, α and β terms that exceeds the filtering of white noise only implies that the reconstructed flight path differs from the recoded flight path, regardless whether it is caused by instrumentation limitation or the actual measurements not exactly following the kinematic equations.

The reconstructed flight path is subsequently used in the Ordinary Least Squares estimator, which performs as the best linear unbiased estimator (BLUE) only if its assumptions hold. These are addressed as follows to assess whether the developed OLS indeed acts as BLUE: (1) The model is indeed linear in the parameters, thus can be written in a matrix-vector form. (2) The measurement noise is constant and independent of time. Nevertheless, the residuals ε do show some dependence on the manoeuvre dynamics due to limitations of the model structure and related fitting performance. (3) The correlation of the parameters in the eventually chosen model structure is little for the symmetrical part ($q \quad \delta_e$). The asymmetrical part of the model shows high correlation between rolling p and aileron deflection δ_a. (4) The mean value of the model residuals is indeed very close to zero.

Although expected, the correlation of independent variables and correlation of parameters are a limitation to its aerodynamic model parameters identification as they decrease the consistency of the determined parameters and therefore limit their reliability. This is captured by the variance of the parameters, which is high for correlated terms, to the extent of changing the sign of determined parameters (such as $C_{Y_{\delta a}}$, C_{Y_p}, $C_{l_{\delta a}}$, C_{l_p}) across different manoeuvres. The first time derivatives of air angle terms $\dot{\alpha}$ and $\dot{\beta}$ have been originally considered in the model structure, as they provide contribution to the force and moment dynamics by a signal that is shifted in time with respect to α and β, respectively, thus improving model fitting, yet their high correlation with q and r, respectively, has a depreciating influence on the parameter reliability. The correlation of variables is undesired as is 'does not add' any meaningful carrier for the model to fit the observation. It is also for this reason that extending the model structure by an additional constant term is destructive to its quality, as a constant term is already implemented for each dimensionless force and moment, acting as bin for any offsets. The α term in asymmetrical part of the model, similarly to the engine contribution Δp_t in symmetrical part of the model, has demonstrated little variation in time, and thus insufficient excitation.

The aforementioned discussion visualises the limitations of the OLS estimator, in which a better model fitting performance might have to be compromised with repetitiveness of identifying parameters and thus their robustness. In addition to the nature of the least squares estimation methods, the robustness of the model can be affected by the consistency of identification manoeuvres. Identification performed on doublets and 3211 manoeuvres separately has resulted in different sets of parameters, therefore averaging them makes the model more universal, but less performing on a particular type of manoeuvre.

The engine model is determined purely analytically and is composed of a digitised engine power and propeller performance charts, which is also what constitutes its potential limitations. Discrete data performance charts have to be interpolated between and extrapolated beyond discrete data lines to

provide output for continuous engine model inputs. In general, the aircraft shows an excess of power available throughout its testing envelopes, thus performance charts are extrapolated at conditions such as taxi or flight at low airspeed and implies a lower confidence of the model at such conditions. The model estimates both engines as identical twins, which has been shown to be different from reality. This could either be a result of normal manufacturing differences between the engines, miscalibrated sensors of input variables (N, p_z) or different aerodynamic conditions of both engines, such as one being in the slipstream of the other.

Upon calibration with the aircraft specifications, the MVP engine monitor estimation of engine horsepower has shown a difference with respect to the engine model power estimation, even though the overall both estimations are highly correlated. Although within 10 [hp] in most cases, the difference in power prediction has shown dependence against manifold pressure (proportional for both engines) and against static pressure (proportional for front, inversely proportional for rear engine).

7.4. Answer to the research question

In this section, the research question formulated in section 2.2 divided into guiding questions is addressed by providing a quantitative answer or referring to parts of the report answering it explicitly.

The longitudinal aerodynamic derivatives constituting the C_X, C_Z forces and C_m moment characterise the contribution of angle of attack α, pitching rate q and constant offset, whereas control derivatives characterise the contribution of the elevator deflection δ_e. They have been determined from a series of elevator doublets and 3211 manoeuvres and are listed in Table 6.4, Table 6.6 and Table 6.8 of section 6.2.

The lateral aerodynamic derivatives constituting the C_Y force and C_l, C_n moments characterise the contribution of the angle of sideslip β, rolling rate p, yawing rate r and constant offset. The lateral control derivatives characterise the contribution of the aileron δ_a and rudder δ_r deflection. They have been determined from a series of aileron and rudder doublets and 3211 manoeuvres and are listed in Table 6.5, Table 6.7 and Table 6.9 of section 6.2.

The propulsion system of the aircraft is modelled as an engine - propeller system outputting values of system thrust, altitude and temperature corrected horsepower and dimensionless total pressure change across the propeller as function of engine rotational speed N, manifold pressure p_z and flight conditions. The model employs digitised versions of the engine power charts and propeller efficiency charts, which are interpolated for continuous input and output.

The presented aerodynamic model has been identified in flight conditions described in section 4.4, at an altitude of around $h_p = 4,000$ [ft] and airspeed of around $V_{IAS} = 85$ [kt] and thus is valid for these conditions. Expanding the flight testing envelope is necessary as further step in the study to increase the envelope of validity of the model. **RQ3** remains unanswered as gathering data at a range of airspeed and altitude is necessary. The engine model scope is described by the range of applicability of the propeller and engine power charts, as defined in subsection 3.2.4.

The validity of the aerodynamic model has been assessed in a validation described in section 7.1 and sensitivity analysis in section 7.2. The model seems to show correct prediction of longitudinal and lateral forces as well as the yawing moment. The pitching C_m and rolling C_l moments show higher model errors, particularly at moments' observation extremities. This originates from both insufficiently diverse model structure and thus lower observation fitting performance, which in contrast is limited by observed correlation of contributing variables. Correlation of p and r increases the variance of the corresponding parameters.

The engine model horsepower estimation is overall in line with the black box estimation of the calibrated, yet unvalidated MVP monitor. The developed model assumes the identical behaviour of both engines, which is contested by the MVP output. The difference between the model and MVP output predicted horsepower has shown some dependence with parameters such as static pressure p_s and manifold pressure p_z.

8

Conclusions and recommendations

8.1. Conclusions

This report describes the process and outcome of a study aiming at identifying a mathematical model of the Cessna Skymaster. The aircraft mathematical model has been decomposed into an aerodynamic model and an engine model, developed separately. The former has been determined with the Two Step system identification method, whereas the latter is a digitised version of coupled engine performance and propeller efficiency maps. As an intermediate step required to reach this objective, the aircraft three dimensional centre of gravity location model has been built upon experimental results. The inertia matrix is analytically modelled around the determined centre of gravity by statistical mass allocation to aircraft component groups. A simple, non-invasive method of control surface deflection determination is developed, consisting in correlating it with the change in position of the control column and rudder, which is measured by IMU sensors.

The Two Step method decomposes the system identification into a flight path reconstruction process, performed with an Iterated Extended Kalman Filter, followed by the parameter identification done with the Ordinary Least Squares approach. With the flight test data being characterised by relatively low noise, but low resolution and high uncertainty of some variables, the IEKF shows high innovation of strongly coupled angle of attack, angle of sideslip and true airspeed.

Due to strong correlation of $\dot{\alpha}$ and $\dot{\beta}$ with the pitch rate q and yaw rate r, respectively, the terms have been removed from the aerodynamic model structure. Nonetheless, in order to catch the influence of aileron deflection δ_a on rolling moment C_l, while following the common aerodynamic model structure convention, δ_a remains a constituent of asymmetrical force and moments, despite its strong correlation with the roll rate p.

The aerodynamic model shows a robust performance for symmetrical forces C_X, C_Z and yawing moment C_n. The C_l estimation is rather weak, as several of its parameters have been determined with a high variance, thus low confidence, likely caused by the strong correlation of δ_a and p, particularity excited for aileron-induced rolling moment. The model is also limited by the observation fitting performance, which is dependent on the model structure. As a result, the extremities of observation forces and moments, notably C_m and C_l, are sometimes poorly captured, thus underestimating the amplitude of the signal. A sensitivity analysis shows little influence of potential uncertainty in determination of centre of gravity, inertia, fuel mass or control deflection on the model parameters.

With the engine manifold pressure and rotational speed as main inputs, the engine model provides the engine horsepower, thrust and dimensionless change in total pressure across the propeller. The engine model horsepower estimation shows high correlation with its MVP estimated counterpart, yet their difference, ΔP, varies in time. A trend can be observed relating ΔP with engine horsepower and manifold pressure, showcasing a potential dependence of the ΔP on flight conditions. In contrast, the front and rear engine show opposite trends of ΔP dependence on static pressure. Given the resolution of available engine model input variables, a sensitivity analysis has shown an uncertainty of around 6 [N] in thrust and 0.5 [hp] in power, in cruise conditions.

The scope of the aerodynamic model is limited by the envelope of its identification flight tests, which have been performed at 90 [kt] and 4,000 [ft]. The model structure specifies the terms contributing to the modelled aircraft dynamics and includes the incidence angles, rotational rates and control surface deflections, but excludes the engine dynamics, wing and cowl flaps or landing gear. The scope of the

engine model is limited by the range of applicability of the engine performance and propeller efficiency maps.

8.2. Recommendations

The present study represents the first attempt to identify the aerodynamic and engine models of the Cessna Skymaster TU Delft research aircraft. Several tools and methods used throughout this process have been developed from scratch to reach this target, yet further improvement is desired to improve the overall quality of the model.

Firstly, the acquisition of the aircraft control surface deflection angles data should be improved. The system presented in this study has been developed as a compromise between time, costs and safety constraints and measures the deflections of the steering column and pedals, rather than the physical deflections of control surfaces. Although the steering column and pedals motion has been correlated with control surface deflection on the ground, in flight dynamic effects, control cable extension or airframe thermal expansion can negatively impact the robustness of this correlation. Future studies should therefore target an implementation of sensors measuring actual control surface deflection, preferably integrated into the Arinc time frame.

Secondly, the quality of the angle of attack and angle of sideslip in flight measurement should be improved. Throughout the study, the BOM has been judged to be a stall warning device rather than angle of attack indicator. The nature of functioning of the BOM angle of attack probe requires a recalibration every time the mass of the aircraft or testing airspeed changes, while only allowing effective measurements within a limited airspeed range. The correlation of the measured AOA_{BOM} to true angle of attack is based on the aircraft lift curve, which should be further studied. An angle of attack vane, whose operation is independent from basic flight conditions such as airspeed or aircraft mass is desired, outputting a raw angle measurement rather than transformed nondimensional value to be post processed, as it is the case for the BOM. The BOM angle of sideslip measurement should be further studied for its validity, as the consistent IEKF innovation trend applied on this measurement suggests a potential underestimation of the actual β signal amplitude in flight.

Thirdly, the MVP engine monitor should be given a designated validation campaign. Although calibrated with constants specific to the aircraft and engine specifications, the engine monitor estimation of variables such as engine rotational speed N or manifold pressure p_z should be validated, the more that these are subsequently used within the MVP black box estimation of the engine horsepower. With available propeller performance charts, validation of the MVP and developed engine model static thrust and horsepower can be performed experimentally by measuring the tension in a cable strained by the stationary aircraft on the ground. Results showing correlation of difference in MVP and engine model estimated horsepower with several variables (static or manifold pressure) and the difference in behaviour of the front and rear engines at seemingly same conditions sparkle the onset for a further investigation that is beyond the scope of this study. In addition, small timestamping misalignments have been noticed between individual variables recorded by the MVP, which are not consistent across recorded flights. Although the is negligible for the sake of this study due to low engine dynamics across executed manoeuvres, it is believed to be of high significance for any further study using the MVP output variables.

Fourthly, more time can be given to improvement of the centre of gravity and moment of inertia determination. The vertical centre of gravity determination can improved by increasing the number of measurements performed at different aircraft pitch angles. The moment of inertia can be best determined experimentally by swinging the aircraft around different axis, or from flight testing, provided a high confidence aerodynamic model is available. A more detailed decomposition of the aircraft structural components can be performed to increase the confidence of the moment of inertia estimation. The accuracy of fuel determination should be improved by replacing the old fuel probes in each of the four tanks to decrease the uncertainty in fuel mass estimation in flight.

Fifthly, a separate study is recommended on the topic of calibration and quantification of noise and delay of the sensors used to acquire flight test data for system identification. In the present study, sensor calibration, noise quantification and timestamp aligned have been performed to the extent limited by available instrumentation and knowledge about it, within the given time constraints of the project.

However, a more in detail verification and validation of available data sources and their alignment would allow to increase the confidence of the presented study. Needless to say, recording actual control deflection (not steering column deflection), IMU, GPS and air data (incidence angles and airspeed) within a single flight test data acquisition system with common clock is an ideal desired state for system identification of an aircraft.

Sixthly, the stabilisation of the aircraft prior to the manoeuvre execution can be improved. Flight path reconstruction has shown that the vertical speed w_{GPS} prior to the manoeuvre is always around ±1 [m/s] away from zero, resulting in climb or descent up to even 10 [m] throughout the manoeuvre, which often exceeds the recorded amplitude of symmetrical manoeuvres altitude signal. This has implications on the steadiness of variables such as w or V_{TAS} prior to excitation. Although it does not disvalidate the data, it adds unnecessary dynamics to it, while the purpose of executed flight testing is to isolate the manoeuvres dynamics only. Improving flight stabilisation can be done by avoiding turbulent or thermally active air bubbles or increasing the airspeed. Flight testing at 90 [kt] is judged to be relatively close to the slow end of the flight envelope.

Given the aforementioned potential improvement in aircraft state precision and flight data quality, the following addresses the refinement of the aerodynamic model. This can be done by increasing its reliability by (decreasing the variance of coefficients), improving the observation fitting performance and increasing the model scope.

Although the coupling of roll and yaw is an unchangeable aerodynamic characteristic of the aircraft, an attempt to decrease the negative effect of parameter correlation on coefficient variance might be the simultaneous excitation of motion in both X_b and Z_b axes in a coupled aileron-rudder manoeuvre. This way, both of the observation moments C_l and C_n have sufficient dynamics to be fitted by p and r terms, respectively. Since validation has shown limitated model performance in high frequency forces and moments prediction, the frequency of the manoeuvres might be decreased accordingly. In addition, with the observed high damping of the rolling motion, an attempt to model the C_l moment in an aileron step input might be beneficial. The reliability of the model can also be addressed by a better stabilisation of the aircraft flight prior to the manoeuvre and repetitiveness of the control inputs throughout manoeuvres. This increases the quality of the manoeuvre by eliminating random noise from control surface inputs. The observation vector noise can also be addressed by developing a more effective filtering and smoothing algorithm for the input vector $\mathbf{u}$. Increasing the number of identification and validation manoeuvres would allow for a higher model confidence.

The observation fitting performance can be changed by varying the aerodynamic model structure. Although the presented structure is considered optimal for the performed manoeuvres and correlation of terms have lead to removal of terms, introduction of new manoeuvres or varying the their amplitude might impose the need to expand the model structure. The implementation of α^2 term might be beneficial to capture the induced drag contribution to C_X at high amplitude manoeuvres, while in instances of high angle of attack, α^2 term might be required to model the flow separation in C_Z or C_m.

In the final iteration of the aerodynamic model structure, the engine contribution is avoided as the variable quantifying its power setting is not sufficiently excited during the identification manoeuvres. In order to identify aerodynamic model parameters quantifying the engine contribution to the longitudinal forces and moment, dedicated manoeuvres shall be performed, such as engine power doublets. In the present study, because the engine has shown relatively low dynamics compared to the airframe, the model has relaxed requirements in terms of numerical computation performance due to accessing data stored in external look-up performance maps. It is recommended to improve the engine model computational efficiency if further studies are to be focused on dynamic changes of the engine parameters.

Finally, the scope of the model should be expanded by enlarging the airspeed and altitude flight envelope of parameter identification manoeuvres and identify the expected relationship between identified parameters and V_{TAS} and h_p and thus allow to answer **RQ3**. Apart of the δ_a, δ_e, δ_r control surfaces contribution to aerodynamic forces and moments, the wing flaps, cowl flaps, engine controls and landing gear can be incorporated into the model structure, provided that their signals are excited during dedicated manoeuvres.

References

[1] 2008. URL: https://docs.scipy.org/doc/scipy/reference/generated/scipy.integrate.cumulative_trapezoid.html.

[2] D. J. Ahrens. "The Cessna Skymaster". In: *Society of Automotive Engineers* S354 (1963).

[3] *Aluminum 2024 T-3*. URL: https://asm.matweb.com/search/specificmaterial.asp?bassnum=ma2024t3.

[4] J. Anderson. *Fundamentals of Aerodynamics*. 6th ed. United States: Mc Graw Hill Education, 2017. ISBN: 978-1-259-12991-9.

[5] M. Baarspul. "A review of flight simulation techniques". In: *Progress in Aerospace Sciences* (Aug. 1989), pp. 1–120. DOI: 10.1016/0376-0421(90)90006-6.

[6] M. Baarspul and J.A. Mulder. "The synthesis of flight simulation models: DATCOM techniques versus flight test identification". In: Delft University of Technology (Oct. 1993).

[7] M. Baarspul et al. "Mathematical model identification for flight simulation, based on flight and taxi tests". In: (Apr. 1988).

[8] I. Boneschansker. "TU Delft welcomes laboratory plane at Rotterdam The Hague Airport". In: (Jan. 2025). URL: https://www.tudelft.nl/en/2025/lr/tu-delft-welcomes-laboratory-plane-at-rotterdam-the-hague-airport.

[9] A. Bucharles et al. "An Overview of Relevant Issues for Aircraft Model Identification." In: *Journal Aerospace Lab* 4 (May 1, 2012). MAG ID: 2968579831.

[10] *Certification Specifications for Normal Category Aeroplanes (CS-23)*. CS-23 Amendment 6. European Union Aviation Safety Agency, Feb. 2023.

[11] *Cessna 337 Ilustrated Parts Catalog*. Cessna Aircraft Company, 1973, pp. 1–574.

[12] *Cessna Super Skymaster Owner's Manual*. Pilot Operating Manual. 1971, pp. 1–63.

[13] Q.P. Chu, J.A. Mulder, and P.T.L.M. van Woerkom. "Aircraft flight path reconstruction with nonlinear adaptive filters". In: 2 (1995), 1196–1200 vol.2. DOI: 10.1109/ACC.1995.520939.

[14] *Continental Aircraft Engine IO-360 Maintenance and Operator's Manual*. Maintenance and Operator's Manual. 2011, pp. 1–104.

[15] M. Cook. *Flight Dynamic Principles*. 2nd ed. Florida, United States of America: Elsevier Aerospace Engineering Series, 2007.

[16] *D-005 BOM (Broadcasting Outer Module) Pilot's Guide*. Levil Aviation.

[17] *Detail Specification. General Specification for Flexible Wire Rope for Aircraft Control*. MIL-DTL-83420M. Departament of Defence Specifications and Standards, 2005.

[18] W. S. Diehl. "The Mean Aerodynamic Chord and the Aerodynamic Center of a Tapered Wing". In: *National Advisory Comittee for Aeronautics* No. 751 (1948).

[19] J DuBois et al. "Moments of Inertia and Centers of Gravity of the Living Human Body Encumbered by a Full-Pressure Suit". In: *North American Aviation, Inc* AMRL-TR-64-i 10 (1964).

[20] E. L. Duke, R. F. Antoniewicz, and K. D. Krambeer. "Derivation and Definition of a Linear Aicraft Model". In: Ames Research Center. Dryden Flight Research Facility, NASA (1988). DOI: null.

[21] B. Etkin. *Dynamics of Atmospheric Flight*. New York, United States: Dover Publications Inc., 1972.

[22] R.D. Finck and D.E. Hoak. *The USAF Stability and Control DATCOM. Volume IV, Section 8: Mass and Inertia*. McDonnell Douglas Astronautics Company, 1978.

[23] *Fixed Wing Stability and Cntrol. Theory and Flight Test Techniques. Flight Test Manual*. U.S. Naval Test Pilot School, Jan. 1997.

[24] F. R. Garza and E. A. Morelli. *A Collection of Nonlinear Aircraft Simulations in MATLAB*. NASA/TM-2003-212145. MAG ID: 1536807716. Langley Research Center Hampton, Virginia 23681-2199: National Aeronautics and Space Administration, Jan. 2003.

[25] O. H. Gerlach. *The determination of stability derivatives and performance characteristics from dynamic manoeuvres*. Jan. 1, 1971.

[26] Z. Goraj. "Flight Dynamics Models Used in Different National and International Projects". In: *Aircraft Engineering and Aerospace Technology: An International Journal* 86.3 (2014), pp. 166–178. DOI: 10.1108/AEAT-02-2013-0036.

[27] J. A. Grauer and E. A. Morelli. "A Generic Nonlinear Aerodynamic Model for Aircraft". In: *American Institude of Aeronautics and Astronautics* (2014).

[28] S. Gudmundsson. *General Aviation Aircraft Design: Applied Mthods and Procedures*. 1st ed. Kansan, United States of America: Elsevier Inc., 1997. ISBN: 1-884885-44-6.

[29] A. M. van den Heok. "Design, Identification and Implementation of a High-Fidelity Cessna Citation II Flight Simulation Model". Master Thesis. Delft: Delft University of Technology, Sept. 8, 2006.

[30] T. A. Horne. "Skymasters". In: *Aircraft Owners and Pilots Association* (Nov. 1982).

[31] S. J. Julier and J. Uhlmann. "New extension of the Kalman filter to nonlinear systems". In: *Defense, Security, and Sensing* (1997). DOI: 10.1117/12.280797.

[32] V. Klein. "Estimation of aircraft aerodynamic parameters from flight data". In: *Progress in Aerospace Sciences* 26.1 (1989), pp. 1–77. ISSN: 0376-0421. DOI: https://doi.org/10.1016/0376-0421(89)90002-X. URL: https://www.sciencedirect.com/science/article/pii/037604218990002X.

[33] V. Klein and E. A. Morelli. *Aircraft System Identification*. Virginia, United States: American Institute of Aeronautics and Astronautics, Inc., 2006. ISBN: 1-56347-832-3.

[34] H. H. Ku. "Notes on the Use of Propagation of Error Formulas". In: *Journal of Research of the National Bureau of Standards - C. Engineering and Instrumentation* 70C, No. 4 (1966), pp. 263–273.

[35] R. Kumar and A. K. Ghosh. "Parameter Estimation using Maximum Likelihood Method from Flight Data at High Angles of Attack". In: *World Academy of Science, Engineering and Technology, International Journal of Mechanical, Aerospace, Industrial, Mechatronic and Manufacturing Engineering* 5 (2011), pp. 2350–2355. URL: https://api.semanticscholar.org/CorpusID:16553069.

[36] M. Laban. "On-Line Aircraft Aerodynamic Model Identification". PhD Thesis. Delft: Delft University of Technology, May 31, 1994.

[37] C. Lanham. *Inertia Calculation Procedure for Preliminary Design*. ASD-TR-79-5004. Wright-Patterson Air Force Base, Ohio, USA: Aeronautical Systems Division. Air Force Systems Command, 1963.

[38] R. Larsson. "Flight Test System Identification". In: *Linköping studies in science and technology, Dissertations* (June 12, 2019). MAG ID: 2945427322. ISSN: 0345-7524. DOI: 10.3384/diss.diva-156694.

[39] M. Lasek and P. Lichota. "Aircraft dynamic model identification on the basis of flight data recorder registers". In: *Challenges of Modern Technology* 4.1 (Jan. 2013). MAG ID: 2125338239.

[40] T. Lombaerts. "Fault Tolerant Flight Control". PhD Thesis. Delft: Delft University of Technology, May 25, 2010.

[41] Matlab. *Optimal State Estimator Algorithm*. Apr. 2017. URL: https://www.youtube.com/watch?v=VFXf1lIZ3p8&list=PLn8PRpmsu08pzi6EMiYnR-076Mh-q3tWr&index=4.

[42] E. A. Morelli. "Determining Aircraft Moments of Inertia from Flight Test Data". In: *Journal of Guidance, Control and Dynamics*. NASA Langley Research Center, Hampton, Virginia, 23666 (Jan. 2021). DOI: https://doi.org/10.2514/1.G006072.

[43] B. C. Moulton and D. F. Hunsaker. "Simplified Mass and Inertial Estimates for Aircraft with Components of Constant Density". In: *AIAA Scitech 2023 Forum* (2023). DOI: 10.2514/6.2023-2432.

[44] *MTV-12 propeller performance maps*. MT-Propeller.

[45] J. A. Mulder. "Design and evaluaion of dynamic flight test manoeuvres". In: *Delft University of Technology* LR-497 (Oct. 1986).

[46] J. A. Mulder, J. G. den Hollander, and Binkhorst H. "Aerodynamic Model Identification from Dynamic Flight Test Data and Windtunnel Experiments". In: *Delft University of Technology* (Oct. 1982).

[47] J. A. Mulder, J. K. Sridhar, and J. H. Breeman. "AGARD Flight Test Techniques Series. Volume 3. Identification of Dynamic Systems-Applications to Aircraft. Part 2. Nonlinear Analysis and Manoeuvre Design". In: (1994).

[48] J. A. Mulder et al. *AE3202 Flight Dynamics Lecture Notes*. Delft University of Technology, Faculty of Aerospace Engineering, Mar. 24, 2013.

[49] J.A. Mulder et al. "Non-liner Aircraft Flight Path Reconstruction Review and New Advances". In: *Progress in Aerospace Sciences* 35.7 (Oct. 1999). MAG ID: 2066615546, pp. 673–726. DOI: 10.1016/s0376-0421(99)00005-6.

[50] *MVP-50P Operating Instructions*. Electronics International Inc.

[51] M. R. Napolitano and J. M. Spagnolo. "Determination of the Stability and Control Derivatives of the NASA F/A-18 HARV Using Flight Data". In: *NASA Dryden Flight Research Center* (Dec. 1993).

[52] National Museum of the United States Air Force. *Cessna O-2A Skymaster*. 2025. URL: https://www.nationalmuseum.af.mil/Visit/Museum-Exhibits/Fact-Sheets/Display/Article/196063/cessna-o-2a-skymaster/ (visited on 03/16/2025).

[53] B. F. Niehaus and V. O. Hoehne. *The USAF Stability and Control Digital DATCOM. Volume I, Users Manual*. AFFDL-TR-79-3032. St. Louis, Missouri 63166: McDonnell Douglas Astronautics Company, Apr. 1979.

[54] Inc. Northrop Aircraft. *Dynamics of the Airframe*. 1st ed. United States: Bureau of Aeronautics, Navy Department, 1952.

[55] J. Oliveira et al. "Output Error Method and Two Step Method for Aerodynamic Model Identification". In: *American Institute of Aeoroautics and Astronautics* 6440 (2005).

[56] J. P. Pegram and W. A. Anemaat. "Preliminary Estimation of Airplane Momens of Inertia using CAD Solid Modeling". In: *General Aviation Technology Conference and Exposition* (2000).

[57] D. H. Perry. *Measurments of the Moments of Inertia of the Avro 707B Aicraft*. C.P. No. 647. London, United Kingdom: Ministry of Aviation. Aeronautical Research Council, 1963.

[58] A. Ramesh. "Evaluating the feasibility of studying propeller-wing interaction through ground-based high-speed experimental taxi-tests". Master Thesis. Delft: Delft University of Technology, July 17, 2022.

[59] J. Roskam. *Airplane Design. Part V: Component Weight Estimation*. 1st ed. Kansas, United States: Data, Analysis and Research Corportation, 1985. ISBN: 978-1-884885-50-1.

[60] A. Ruiz Garcia et al. "Aerodynamic Model Identification of the Flying V from Sub-Scale Flight Test Data". In: *AIAA SCITECH 2022 Forum* (2022). DOI: 10.2514/6.2022-0713.

[61] *Service Manual, 1974 Thru 1980 Model 337 & Turbo Series*. Change 8. Wichita, Kansas, USA: Cessna Aircraft Company, 1996.

[62] "Skymaster Production". In: *Skymaster Owners And Pilots Association* (Jan. 2005).

[63] V. Strejc. "Least Squares Parameter Estimation". In: *IFAC Proceedings Volumes* 12.8, Supplement 1 (1979). Tutorials presented at the 5th IFAC Symposium on Identification and System Parameter Estimation, Darmstadt, Germany, September, pp. 535–550. ISSN: 1474-6670. DOI: https://doi.org/10.1016/S1474-6670(17)53975-0. URL: https://www.sciencedirect.com/science/article/pii/S1474667017539750.

[64] O. Stroosma. "AE4322-24 Piloted Flight Simulation - Vehicle Dynamics". Lecture. Lecture. Mar. 2025.

[65] J. A. Thelander. *Aircraft Motion Analysis*. California, United States, 1965.

[66] J. Thurstan. *Jane's All the World's Aircraft 1969–70*. Vol. 74. 1970.

[67] R.T.H. Tjee and J.A. Mulder. "Stability and control derivatives of the De Havilland DHC-2 "Beaver" aircraft". In: Delft University of Technology (LR-556 Jan. 1, 1988).

[68] H. Tsai. *Pull reel, United States Design Patent US D539.122 S*. Mar. 2007.

[69] H. L. Turner. "Measurment of the Moment of Inertia of an Airplane by a Simplified Method". In: *National Advisory Committee for Aeronautics* (1950).

[70] *Type Certificate Data Sheet NO. A23EU*. A23EU, Revision 8. United States of America: Department of Trasportation, Federal Aviation Administration, Apr. 2019.

[71] *Type Certificate Data Sheet No. A6CE*. 40. Department of Transportation Federal Aviation Administration, Nov. 3, 2004, pp. 15–16.

[72] *UK Air Operations Regulation, SPO.OP.195 Use of supplemental oxygen*. Annex VIII (Part SPO) Subpart B. United Kingdom: United Kingdom Civil Aviation Authority.

[73] C. C. de Visser, Mulder. J.A., and Q. P. Chu. "A new approach to linear regression with multivariate splines". In: *Automatica* (2009).

[74] C. C. de Visser, J. Mulder, and Q. P. Chu. "A Multidimensional Spline Based Global Nonlinear Aerodynamic Model for the Cessna Citation II". In: (2010). DOI: 10.2514/6.2010-7950.

[75] C. C. de Visser and D. Pool. "AE4320 System Identification of Aerospace Vehicles". Lecture. Delft University of Technology, 2025.

[76] C. C. de Visser and D. M. Pool. "Stalls and Splines: Current Trends in Flight Testing and Aerodynamic Model Identification". In: *Journal of Aircraft: devoted to aeronautical science and technology* 60 (Sept. 2023). DOI: 10.2514/1.c037283.

[77] T. Vogeltanz. "Application for Calculation of Mean Aerodynamic Chord of Arbitrary Wing Planform". In: *American Institute of Physics* No. 751 (2016). DOI: 10.1063/1.4951901.

[78] E. de Weerdt, Q. P. Chu, and J. A. Mulder. "Neural Network Aerodynamic Model Identification for Aerospace Reconfiguration". In: (). DOI: 10.2514/6.2005-6448. eprint: https://arc.aiaa.org/doi/pdf/10.2514/6.2005-6448. URL: https://arc.aiaa.org/doi/abs/10.2514/6.2005-6448.

[79] L. N. Wener. "Measurment of Aircraft Moments of Inertia". In: *Advisory Group for Aeronautical Research and Development, NATO* (1959).

[80] J. Wiącek. *Aerodynamic Model Identification using the Two-Step Approach. AE4320 - System Identification of Aerospace Vehicles assignment*. Delft University of Technology, 2025.

[81] *Xsens DOT User Manual*. G. Xsens Technologies.

A

Equations of Motion

The equations of motion define the movement of a body within a frame of reference. This chapter aims at defining the ways the aircraft dynamics are described within this study, under the assumptions stated in subsection 2.3.1 and within the frames of reference defined in subsection 2.3.2. Starting by equating the forces to the change of momentum in time, the aircraft motion is further categorised into three subsets, namely the translational motion in section A.1, the rotational motion in section A.2 and relative frames attitude dynamics in section A.3. Finally, the equations describing the kinematic model of the aircraft are presented in section A.4.

A.1. Translational motion

Derived from the Newton's laws of motion, the general motion of the mass varying aircraft with respect to inertial frame F_I can be described by Equation A.1 [48]:

$$\mathbf{F}^I_{ext} = m\frac{d^2\mathbf{r}^I_{cm}}{dt^2} + 2\mathbf{\Omega}^I_{bI} \times \int_m \frac{\delta\tilde{\mathbf{r}}}{\delta t}\, dm + \int_m \frac{\delta^2\tilde{\mathbf{r}}}{\delta t^2}\, dm \tag{A.1}$$

Where the total external forces as components of the inertial frame $\mathbf{F}^I_{ext}$ are function of the distance of aircraft centre of mass to the inertial reference frame origin $\mathbf{r^I_{cm}}$, the rotational rate of the body with respect to the inertial frame $\mathbf{\Omega}^I_{bI}$ and aircraft varying mass m, while $\tilde{\mathbf{r}}$ symbolises the location of a mass element with respect to the body centre of mass. Equation A.1 expresses the external forces in the inertial frame F_I, as sum of three individual components, namely the mass times acceleration of the body, the Coriolis force and a relative force due time varying mass distribution, respectively.

Considering an aircraft moving with a velocity $\mathbf{V}_C = d\mathbf{r}^C_{cm}/dt$ with respect to the rotating Earth-Centered Earth Fixed frame F_C at a distance $\mathbf{r}^C_{cm}$ from the reference frame origin (centre of rotating body), the external forces $\mathbf{F}^C_{ext}$ can be expressed by Equation A.2 [48], with $\mathbf{\Omega}^C_{CI} = (0, 0, \Omega_t)^\intercal$ expressing the Earth rotation:

$$\mathbf{F}^C_{ext} = m\frac{d^2\mathbf{r}^C_{cm}}{dt^2} + 2m\mathbf{\Omega}^C_{CI} \times \frac{d\mathbf{r}^C_{cm}}{dt} + m\mathbf{\Omega}^C_{CI} \times \left(\mathbf{\Omega}^C_{CI} \times \mathbf{r}^C_{cm}\right) \tag{A.2}$$

After reformulating the external forces, position, rotation and velocity vectors in the navigation frame of reference (vehicle carried North-East-Down, NED) F_E, the accelerations along the X_E, Y_E, Z_E axes can be expressed by Equation A.3, where the spherical position is defined with the distance to Earth centre R, latitude δ and longitude τ:

$$\begin{aligned}
\dot{V}_N &= \frac{F^E_x}{m} - 2\Omega_t V_E \sin\delta - \Omega_t^2 R \sin\delta\cos\delta - \frac{V_E^2\tan\delta - V_N V_D}{R} \\
\dot{V}_E &= \frac{F^E_y}{m} + 2\Omega_t(V_D\cos\delta + V_N\sin\delta) + \frac{V_E}{R}(V_N\tan\delta + V_D) \\
\dot{V}_D &= \frac{F^E_z}{m} - 2\Omega_t V_E\cos\delta - \Omega_t^2 R\cos^2\delta - \frac{V_E^2 + V_N^2}{R}
\end{aligned} \tag{A.3}$$

The equations of translational motion can be transformed from the navigation frame F_E to the aircraft body frame F_b as described by Equation A.4 in order to express the time rate of change of the velocity in the body frame [29]:

$$\left.\frac{d\mathbf{V}}{dt}\right|_E^b = \left.\frac{d\mathbf{V}}{dt}\right|_b^b + \mathbf{\Omega}_{bE}^b \times \mathbf{V}_b \tag{A.4}$$

Where $\mathbf{V}_b = (u, v, w)^\intercal$ represents the aerodynamic velocity components of the aircraft within its body frame. After manipulation and simplification of Equation A.4 applied to Equation A.3, the forces acting on the aircraft expressed in F_b can be defined as function of the vehicle rotational rates $\mathbf{\Omega}_{bI}^b = (p, q, r)^\intercal$ and angular orientation expressed in Euler angles ϕ, θ, ψ, as done by Equation A.5 [29, p. 54] [15, p. 72] [67, p. 7]:

$$\begin{aligned} X &= m\left(\dot{u} + qw - rv\right) + mg\sin\theta \\ Y &= m\left(\dot{v} + ru - pw\right) - mg\cos\theta\sin\phi \\ Z &= m\left(\dot{w} + pv - qu\right) - mg\cos\theta\cos\phi \end{aligned} \tag{A.5}$$

A.2. Rotational motion

The general expression of a body rotating at a rate $\mathbf{\Omega}_{bI}^b$, moving with respect to the inertial frame F_I can be described by Equation A.6 [48]:

$$\begin{aligned} \mathbf{M}_{cm}^b = &\int_m \mathbf{r} \times \left(\frac{d\mathbf{\Omega}_{bI}^b}{dt} \times \mathbf{r}\right) dm + \int_m \mathbf{r} \times \left[\mathbf{\Omega}_{bI}^b \times \left(\mathbf{\Omega}_{bI}^b \times \mathbf{r}\right)\right] dm + \\ &+ 2\int_m \mathbf{r} \times \left(\mathbf{\Omega}_{bI}^b \times \frac{\partial \mathbf{r}}{\partial t}\right) dm + \int_m \mathbf{r} \times \frac{\delta^2 \mathbf{r}}{\delta t^2}\, dm \end{aligned} \tag{A.6}$$

Where the total external moment about the vehicle centre of mass $\mathbf{M}_{cm}^b$ is expressed as function of four independent components, namely the apparent moment due to angular acceleration o the vehicle with respect to F_I, apparent moment due to angular velocity of the vehicle with respect to F_I, Coriolis moment and relative moment due to time variations in mass distributions, respectively.

Given the angular momentum for a rigid body can be expressed as product of the inertia tensor $\mathbf{I}$ and rotational rate $\mathbf{\Omega}$ [48]:

$$\mathbf{B}_{cm} = \mathbf{I} \cdot \mathbf{\Omega} \tag{A.7}$$

Its time derivative, defining the moments, $\mathbf{M}_{cm}$ can be expressed as:

$$\mathbf{M}_{cm} = \frac{\delta \mathbf{B}_{cm}}{\delta t} + \mathbf{\Omega} \times \mathbf{B}_{cm} \tag{A.8}$$

With the first term $\dfrac{\delta \mathbf{B}_{cm}}{\delta t}$ being expanded as:

$$\frac{\delta \mathbf{B}_{cm}}{\delta t} = \frac{\delta \mathbf{I}}{\delta t} \cdot \mathbf{\Omega} + \mathbf{I} \cdot \frac{\delta \mathbf{\Omega}}{\delta t} = \mathbf{I} \cdot \frac{\delta \mathbf{\Omega}}{\delta t} \tag{A.9}$$

By substituting Equation A.9 into Equation A.8 and applying once more Equation A.7, the following expression of angular momentum time derivative can be obtained:

$$\mathbf{M}_{cm} = \mathbf{I} \cdot \dot{\mathbf{\Omega}} + \mathbf{\Omega} \times \mathbf{I} \cdot \mathbf{\Omega} \tag{A.10}$$

According to the Principle of Solidification, Equation A.10 is also applicable to rotational motion of varying mass non rigid bodies [48, p. 63]. The expression of the general formulation of Equation A.10 can be rearranged to express the rotational acceleration in the body frame F_b, as expressed by Equation A.11:

$$\dot{\mathbf{\Omega}}^b_{bI} = \mathbf{I}^{-1}\left(\mathbf{M^b_{cm}} - \mathbf{\Omega}^b_{bI} \times \mathbf{I} \cdot \mathbf{\Omega}^b_{bI}\right) \tag{A.11}$$

Equation A.11 can be expanded into components of moments, inertial tensor and rotational rates expressed in the body axes, to give:

$$\begin{bmatrix}\dot{p}\\ \dot{q}\\ \dot{r}\end{bmatrix} = \begin{bmatrix} I_{xx} & -I_{xy} & -I_{xz}\\ -I_{xy} & I_{yy} & -I_{yz}\\ -I_{xz} & -I_{yz} & I_{zz}\end{bmatrix}^{-1}\left(\begin{bmatrix}L\\ M\\ N\end{bmatrix} - \begin{bmatrix}p\\ q\\ r\end{bmatrix} \times \begin{bmatrix} I_{xx} & -I_{xy} & -I_{xz}\\ -I_{xy} & I_{yy} & -I_{yz}\\ -I_{xz} & -I_{yz} & I_{zz}\end{bmatrix}\begin{bmatrix}p\\ q\\ r\end{bmatrix}\right) \tag{A.12}$$

Given the assumption stated in subsection 2.3.1, the off-diagonal elements of the inertia tensor $\mathbf{I}$ are negligible due to aircraft symmetry, $I_{xy} = I_{yz} = 0$. Rearranging Equation A.12 for explicit expression of the the moments acting in the body frame F_b gives Equation A.13:

$$\begin{aligned} L &= I_{xx}\dot{p} - \left(I_{yy} - I_{zz}\right) qr - I_{xz}\left(\dot{r} + pq\right)\\ M &= I_{yy}\dot{q} + \left(I_{xx} - I_{zz}\right) pr + I_{xz}\left(p^2 - r^2\right)\\ N &= I_{zz}\dot{r} - \left(I_{xx} - I_{yy}\right) pq + I_{xz}\left(qr - \dot{p}\right)\end{aligned} \tag{A.13}$$

Equation A.13, expresses the moments acting in the body frame of the aircraft due to the airframe inertia and its movement. It ignores however the contribution of the rotating propellers, which cause a gyroscopic effect as well as the engine contribution to pitching moment, caused by the thrust vector being applied off the vertical centre of mass of the aircraft.

Assuming a thrust acting along X_b, the angular momentum $\mathbf{h}_e$ of the engine rotating mass in F_b can be expressed as $\mathbf{h}_e = [I_p\omega_e \;\; 0 \;\; 0]^\intercal$ [33] [45]. For a constant engine rotational speed ω_e, the gyroscopic moment from the rotating mass can be expressed by Equation A.14:

$$\mathbf{M_{gyr}} = \omega_\mathbf{e} \times \mathbf{h_e} = \begin{bmatrix}L_{gyr}\\ M_{gyr}\\ N_{gyr}\end{bmatrix} = \begin{bmatrix} 0 & -r & 0\\ r & 0 & -p\\ -q & p & 0\end{bmatrix}\begin{bmatrix}I_p\omega_e\\ 0\\ 0\end{bmatrix} = \begin{bmatrix}0\\ I_p\omega_e r\\ -I_p\omega_e q\end{bmatrix} = \begin{bmatrix}0\\ I_p(\omega_{e,f} + \omega_{e,r})r\\ -I_p(\omega_{e,f} + \omega_{e,r})q\end{bmatrix} \tag{A.14}$$

While the net momentum of counterrotating propellers of the Cessna Skymaster cancels out provided the same rotational speed, the gyroscopic effect of two rotating propellers is double the one caused by a single propeller rotation, provided the same rotational speed.

Now, assuming that both engines lie in the aircraft plane of symmetry and that the engine thrust acts in X_b only, the following expression can be formulated for the contribution to sum of moments from both the front and rear engines:

$$\mathbf{M_T} = \mathbf{r} \times \mathbf{T} = \begin{bmatrix}x_e - x_{c.g.}\\ y_e - y_{c.g.}\\ z_e - z_{c.g.}\end{bmatrix} \times \begin{bmatrix}T\\ 0\\ 0\end{bmatrix} = \begin{bmatrix}0\\ (z_e - z_{c.g.})T\\ 0\end{bmatrix} \tag{A.15}$$

The contributions are split per engine and marked with subscripts f indicating the front, and r indicating the rear engine, while both propellers are assumed to have the same rotating mass inertia I_p (see chapter 5), but not necessarily thrust. These contributions are added in Equation 3.22 of section 3.2.

A.3. Attitude equations

The attitude equations define the orientation of the body frame F_b with respect to the navigation frame F_E and are functions of the Euler angles: roll ϕ, pitch θ and yaw ψ. The Euler angles arise from a successive transformation of the F_E frame to the F_b frame, which can be defined as [48]:

$$\mathbb{T}_{bE} = |_b\mathbb{T}_x(\phi)|_{E''}\mathbb{T}_y(\theta)|_{E'}\mathbb{T}_z(\psi)|_E = \begin{bmatrix}1 & 0 & 0\\ 0 & \cos\phi & -\sin\phi\\ 0 & \sin\phi & \cos\phi\end{bmatrix} \cdot \begin{bmatrix}\cos\theta & 0 & \sin\theta\\ 0 & 1 & 0\\ -\sin\theta & 0 & \cos\theta\end{bmatrix} \cdot \begin{bmatrix}\cos\psi & -\sin\psi & 0\\ \sin\psi & \cos\psi & 0\\ 0 & 0 & 1\end{bmatrix} \tag{A.16}$$

Based on Equation A.11, the time rate of change of the body attitude can be defined as [48]:

$$\begin{aligned} \dot{\phi} &= \tilde{p} + \tilde{q}\sin\phi\tan\theta + \tilde{r}\cos\phi\tan\theta \\ \dot{\theta} &= \tilde{q}\cos\phi - \tilde{r}\sin\phi \\ \dot{\psi} &= \tilde{q}\frac{\sin\phi}{\cos\theta} + \tilde{r}\frac{\cos\phi}{\cos\theta} \end{aligned} \tag{A.17}$$

With $\tilde{p}$, $\tilde{q}$ and $\tilde{r}$ being defined as:

$$\begin{aligned} \tilde{p} &= p + \cos\theta\sin\psi\dot{\delta} - [\cos\delta\cos\psi\cos\theta + \sin\delta\sin\theta](\dot{\tau} + \Omega_t) \\ \tilde{q} &= q + (\sin\psi\sin\theta\sin\phi + \cos\psi\cos\phi)\dot{\delta} - [\cos\delta(\cos\psi\sin\theta\sin\phi - \sin\psi\cos\phi) - \\ &\quad - \sin\delta\cos\theta\sin\phi](\dot{\tau} + \Omega_t) \\ \tilde{r} &= r + (\sin\psi\sin\theta\cos\phi - \cos\psi\sin\phi)\dot{\delta} - [\cos\delta(\sin\psi\sin\phi + \cos\psi\sin\theta\cos\phi) - \\ &\quad - \sin\delta\cos\theta\cos\phi](\dot{\tau} + \Omega_t) \end{aligned} \tag{A.18}$$

With the assumptions of non rotating ($\Omega_t = 0$) and flat Earth ($\dot{\tau} = \dot{\delta} = 0$, $\tilde{p} = p$, $\tilde{q} = q$, $\tilde{r} = r$), Equation A.18 can be simplified to obtain the well known set of first order differential equations for the Euler angles given by Equation A.19, also referred to as the attitude equations:

$$\begin{aligned} \dot{\phi} &= p + q\sin\phi\tan\theta + r\cos\phi\tan\theta \\ \dot{\theta} &= q\cos\phi - r\sin\phi \\ \dot{\psi} &= q\frac{\sin\phi}{\cos\theta} + r\frac{\cos\phi}{\cos\theta} \end{aligned} \tag{A.19}$$

A.4. Kinematic model

The kinematic equations of aircraft motion are a set of first order ordinary differential equations defined as functions of aircraft measured variables in F_b such as linear accelerations A_x, A_y, A_z and rotational rates p, q, r rather than control inputs and aerodynamic properties [29] [45]. They allow a formulation of a navigation model used in the flight path reconstruction (see section 3.1), allowing to numerically solve for a time histories of aircraft position in F_E, translational velocity components and the body attitude angles in F_b. In the kinematic model, the forces along the body axes can be expressed using the Newton second law of motion, as stated by Equation A.20:

$$\begin{aligned} X &= mA_x \\ Y &= mA_y \\ Z &= mA_z \end{aligned} \tag{A.20}$$

Substitution of Equation A.20 into Equation A.5 and rearranging for explicit formulation of the $\dot{\mathbf{V}}_b$ as function of $\mathbf{V}_b$ components, body accelerations, rotational rates and Euler angles gives:

$$\begin{aligned} \dot{u} &= A_x - g\sin\theta - qw + rv \\ \dot{v} &= A_y + g\cos\theta\sin\phi + pw - ru \\ \dot{w} &= A_z + g\cos\theta\cos\phi - pv + qu \end{aligned} \tag{A.21}$$

The change in aircraft position in the navigation frame F_E can be expressed by applying transition $\mathbb{T}_{Eb}$ from F_b to F_E onto the body velocity components $\mathbf{V}_b$ and including a wind term $\mathbf{W}$ expressed in the navigation frame, as defined by Equation A.22:

$$\begin{bmatrix} \dot{x}_E \\ \dot{y}_E \\ \dot{z}_E \end{bmatrix} = \mathbb{T}_{Eb} \begin{bmatrix} u \\ v \\ w \end{bmatrix} + \begin{bmatrix} W_{x_E} \\ W_{y_E} \\ W_{z_E} \end{bmatrix} \tag{A.22}$$

The $\mathbb{T}_{Eb}$ transition is expressed as follows, being the transpose of $\mathbb{T}_{bE}$:

$$\mathbb{T}_{Eb} = |_E\mathbb{T}_z(\psi)|_{E'}\mathbb{T}_y(\theta)|_{T_{E''}}\mathbb{T}_x(\phi)|_b = \mathbb{T}_{bE}^T \tag{A.23}$$

Expanding Equation A.22 into individual position components in the navigation frame F_E gives the expression stated by Equation A.24:

$$\begin{aligned} \dot{x}_E &= \left[u\cos\theta + \left(v\sin\phi + w\cos\phi\right)\sin\theta\right]\cos\psi - \left(v\cos\phi - w\sin\phi\right)\sin\psi + W_{x_E} \\ \dot{y}_E &= \left[u\cos\theta + \left(v\sin\phi + w\cos\phi\right)\sin\theta\right]\sin\psi + \left(v\cos\phi - w\sin\phi\right)\cos\psi + W_{y_E} \\ \dot{z}_E &= -u\sin\theta + \left(v\sin\phi + w\cos\phi\right)\cos\theta + W_{z_E} \end{aligned} \tag{A.24}$$

The kinematic model defines the time derivative of the navigation frame position components $\dot{x}_E, \dot{y}_E, \dot{z}_E$, airpseed components $\dot{u}, \dot{v}, \dot{w}$ and attitude angles $\dot{\phi}, \dot{\theta}, \dot{\psi}$. It is therefore expressed by Equation A.24, Equation A.21 and Equation A.19.

B

Extension to results

This chapter represents the extension to the results presented in chapter 6 by providing a higher variety of system identification manoeuvres than presented in the main part of the report (section B.1 and section B.2) as well as providing results of an alternative model structure in section B.3.

B.1. Flight path reconstruction

This section graphically presents the outcome of the flight path reconstruction on doublet and 3211 symmetrical and asymmetrical manoeuvres and is extension to the elevator doublet manoeuvre presented in section 6.1 of chapter 6.

Elevator 3211

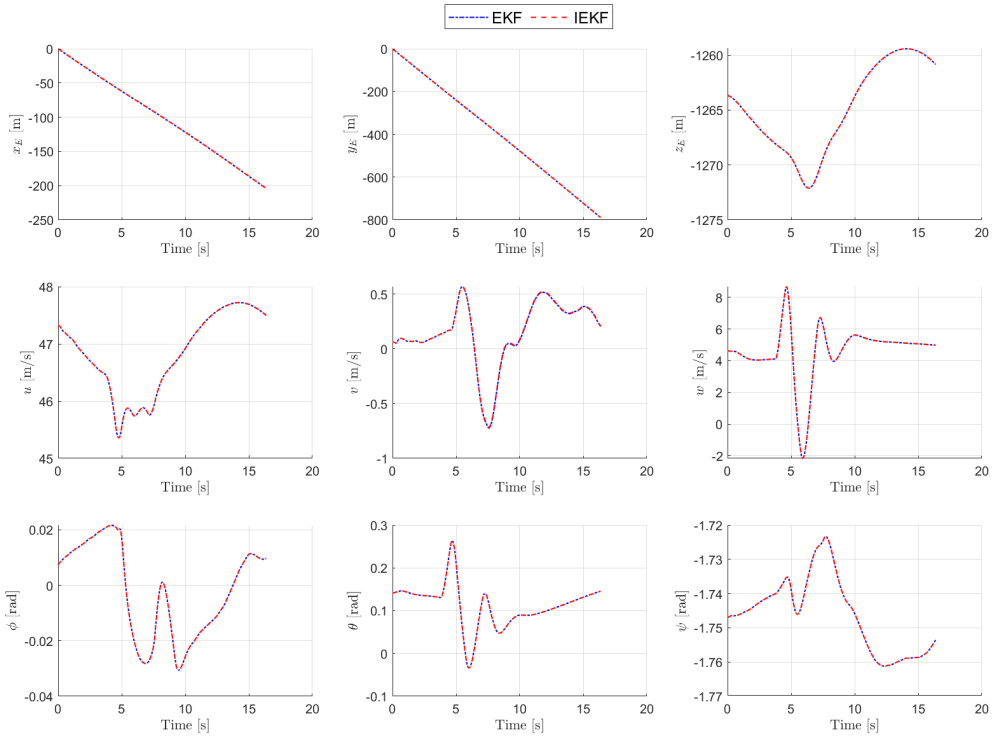

Figure B.1: Unaugmented state estimation of EKF and IEKF for an elevator 3211 manoeuvre

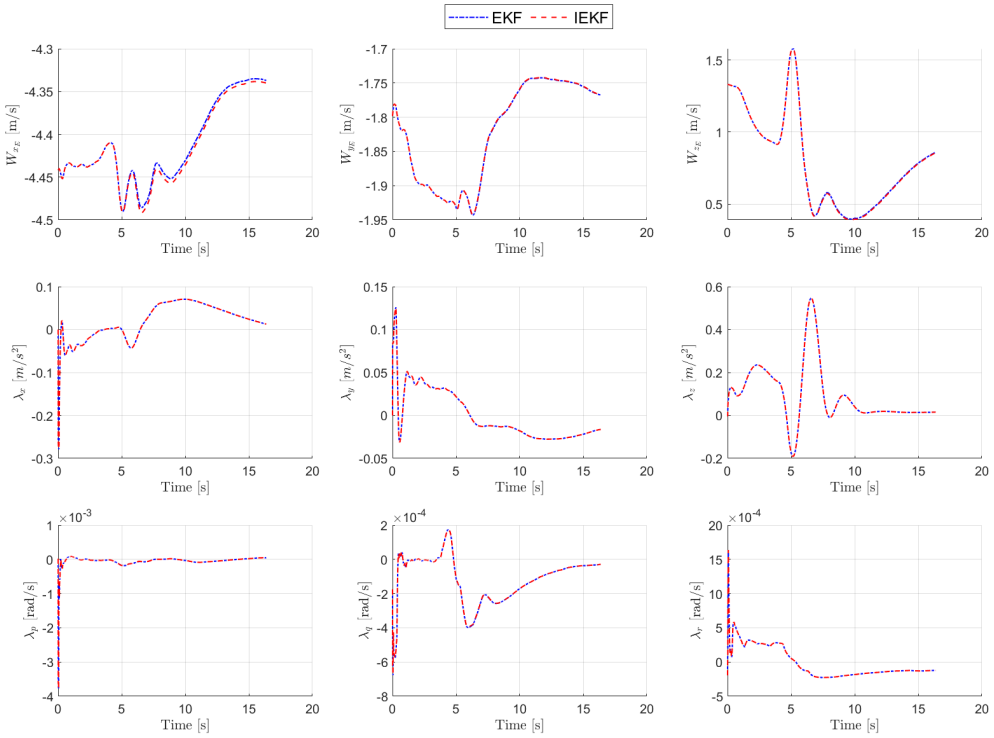

Figure B.2: Wind and IMU bias estimation of EKF and IEKF for an elevator 3211 manoeuvre

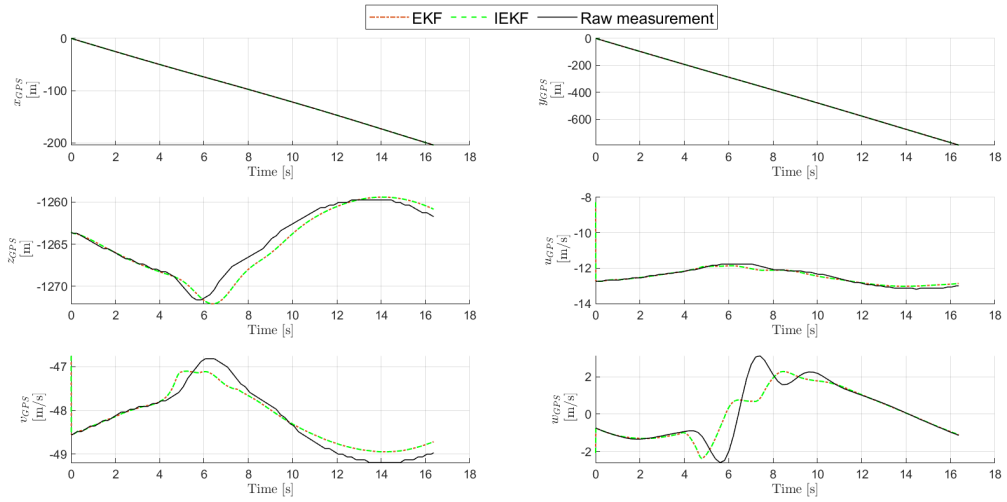

Figure B.3: Measurement vector GPS terms reconstructed by the EKF and IEKF for an elevator 3211 manoeuvre

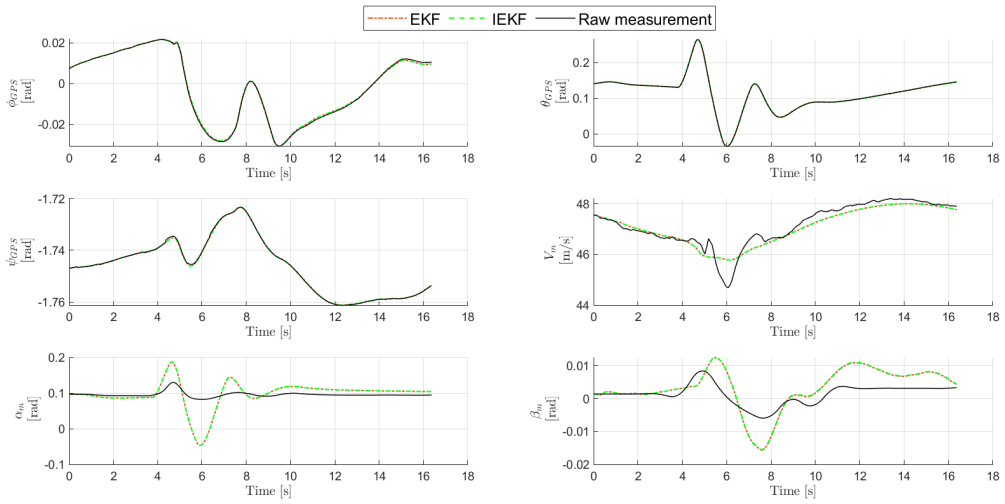

Figure B.4: Measurement vector attitude and air data terms reconstructed by the EKF and IEKF for an elevator 3211 manoeuvre

Aileron 3211

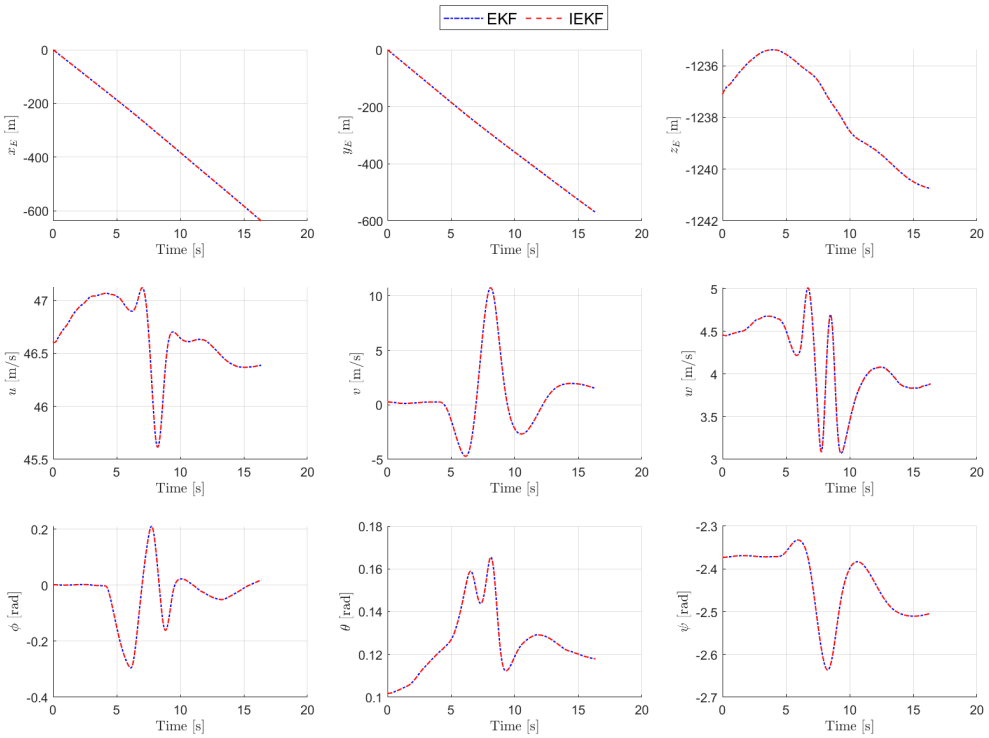

Figure B.5: Unaugmented state estimation of EKF and IEKF for an aileron 3211 manoeuvre

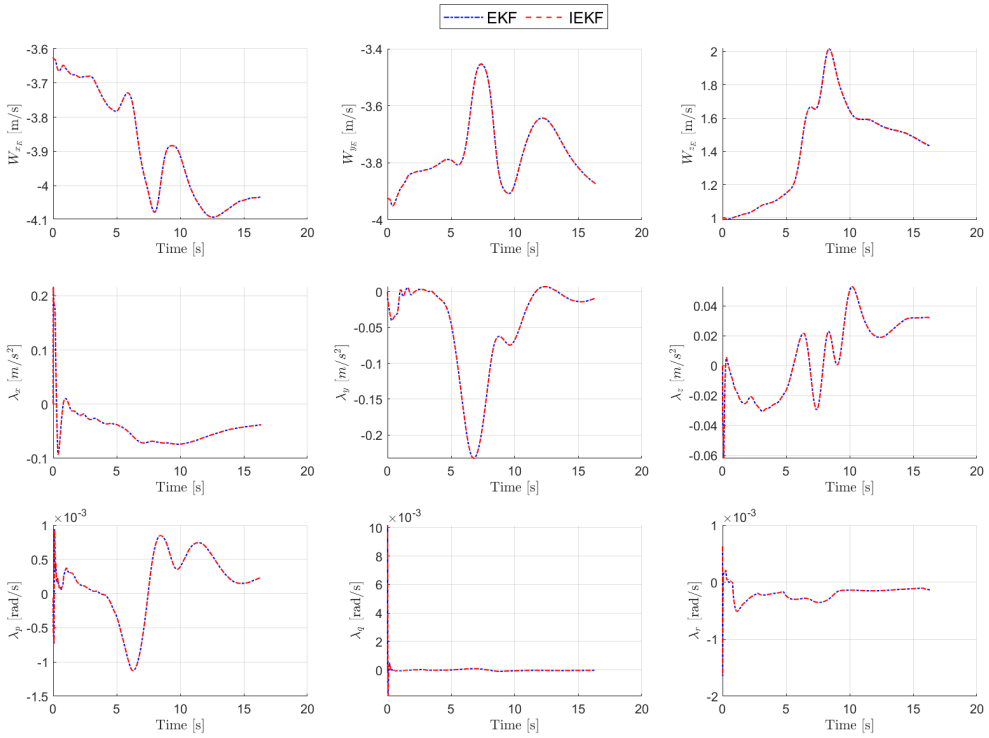

Figure B.6: Wind and IMU bias estimation of EKF and IEKF for an aileron 3211 manoeuvre

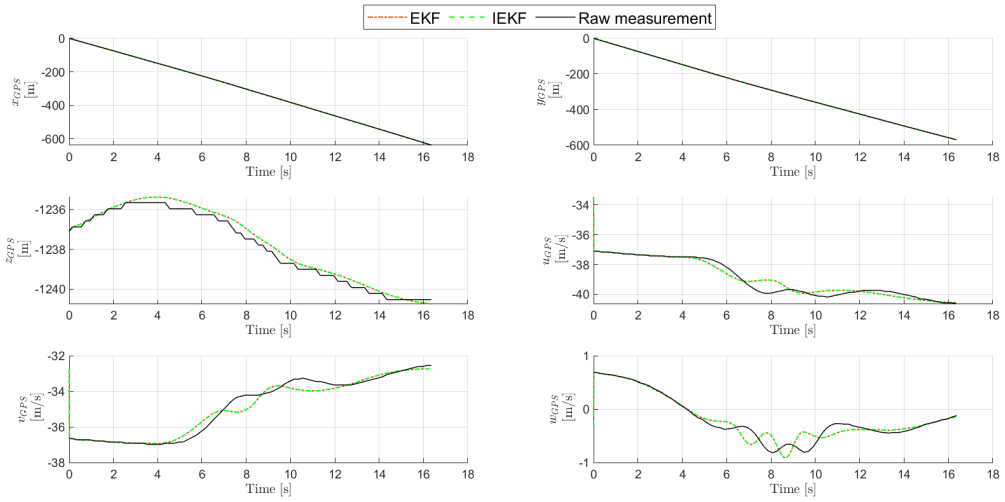

Figure B.7: Measurement vector GPS terms reconstructed by the EKF and IEKF for an aileron 3211 manoeuvre

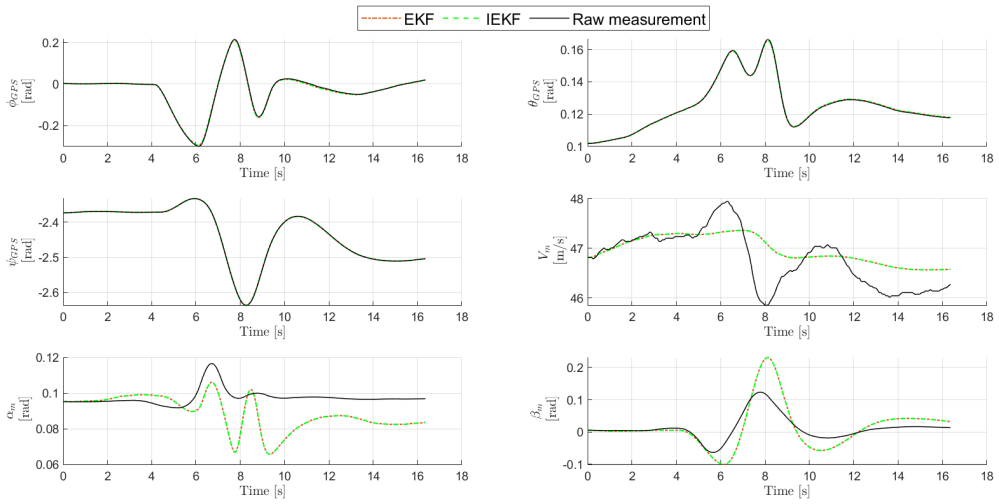

Figure B.8: Measurement vector attitude and air data terms reconstructed by the EKF and IEKF for an aileron 3211 manoeuvre

Aileron doublet

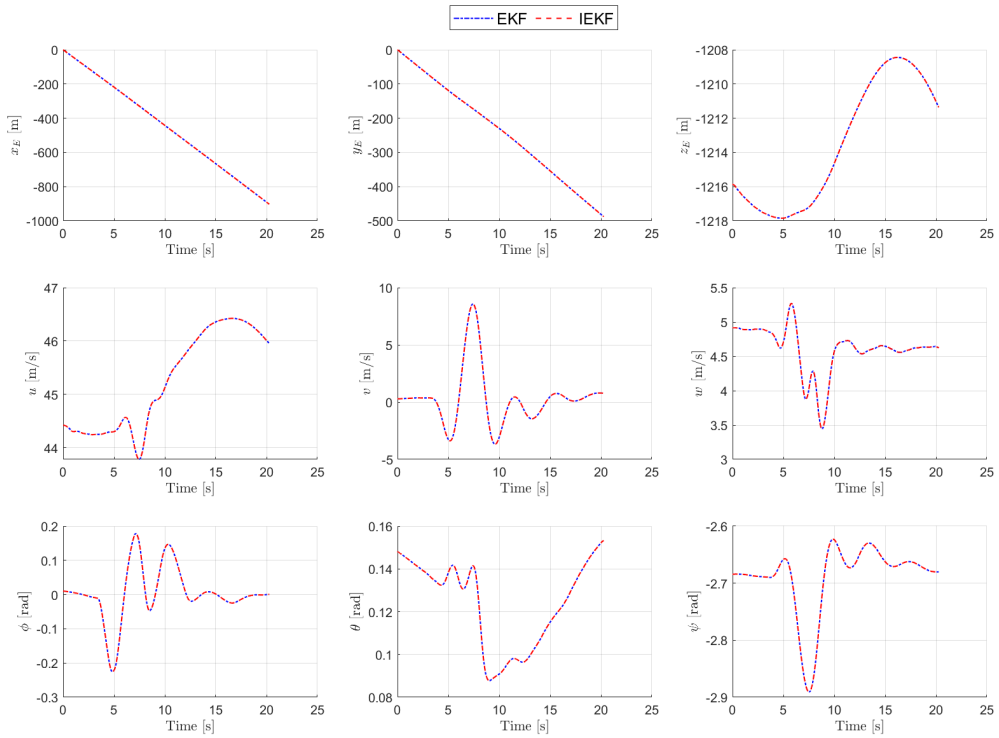

Figure B.9: Unaugmented state estimation of EKF and IEKF for an aileron doublet manoeuvre

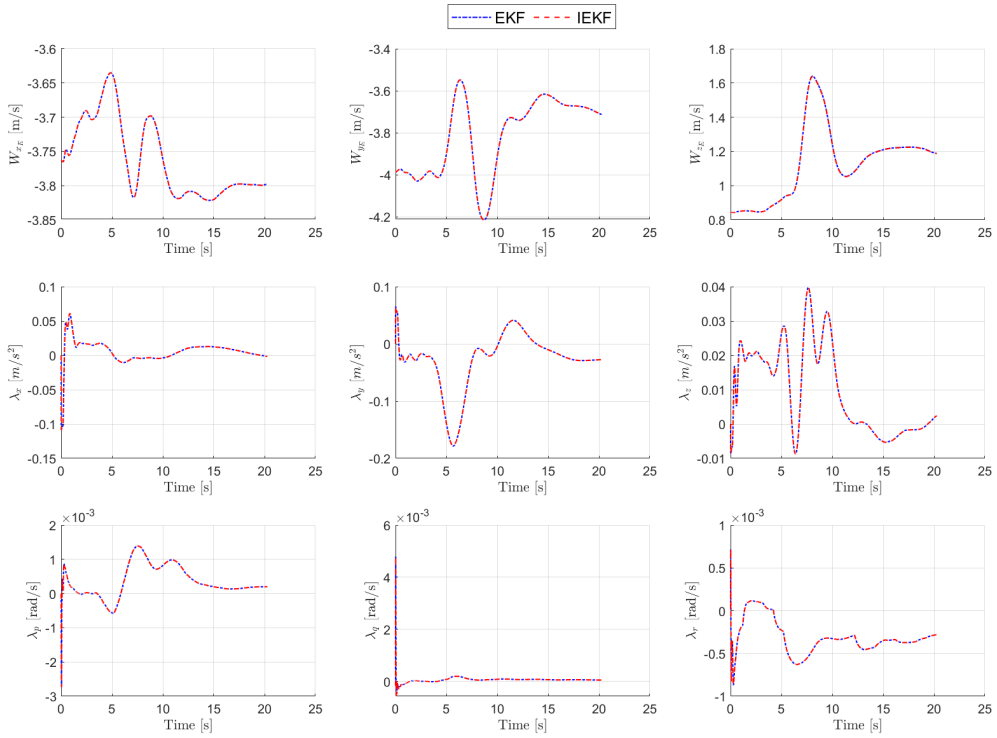

Figure B.10: Wind and IMU bias estimation of EKF and IEKF for an aileron doublet manoeuvre

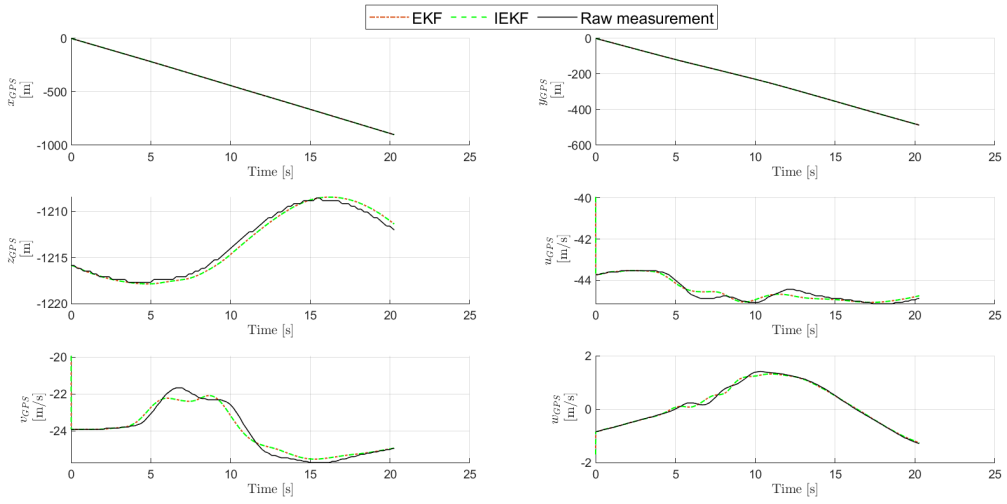

Figure B.11: Measurement vector GPS terms reconstructed by the EKF and IEKF for an aileron doublet manoeuvre

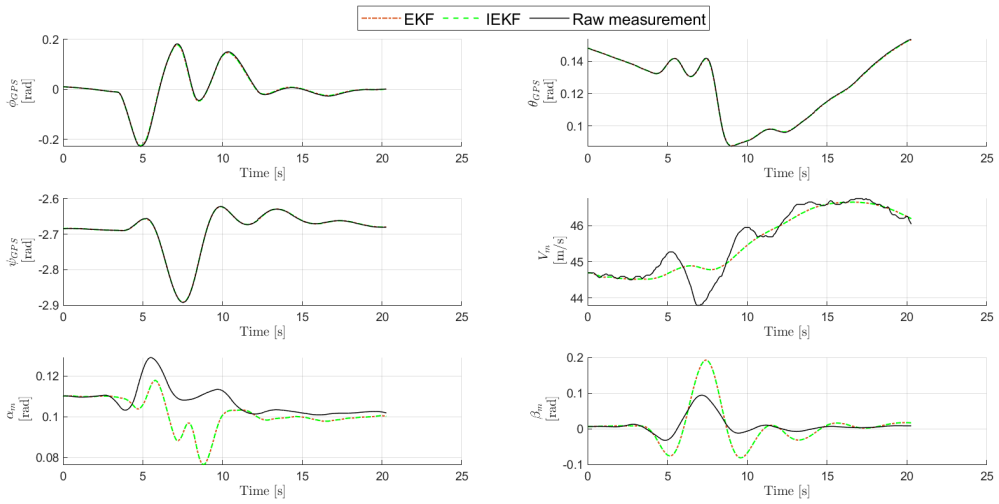

Figure B.12: Measurement vector attitude and air data terms reconstructed by the EKF and IEKF for an aileron doublet manoeuvre

Rudder 3211

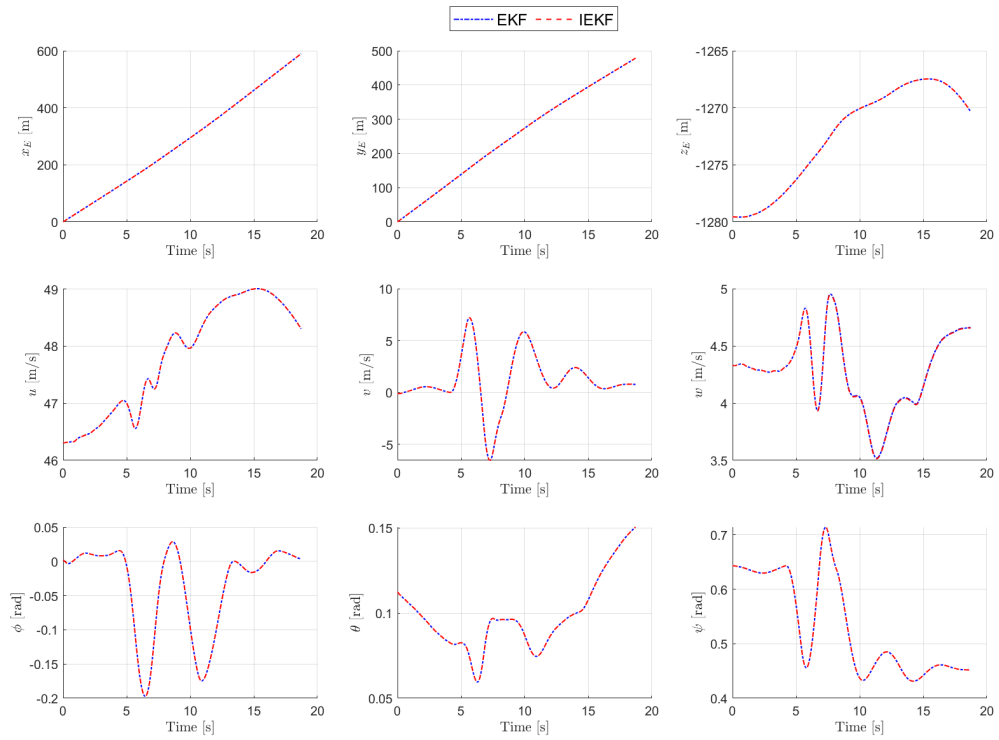

Figure B.13: Unaugmented state estimation of EKF and IEKF for a rudder 3211 manoeuvre

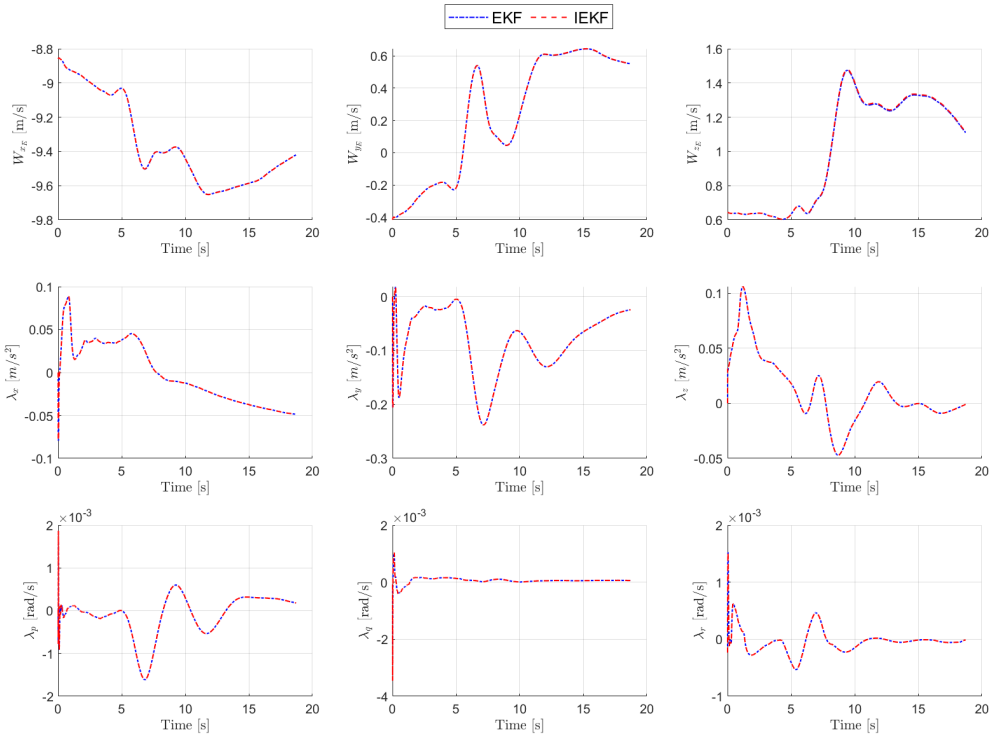

Figure B.14: Wind and IMU bias estimation of EKF and IEKF for a rudder 3211 manoeuvre

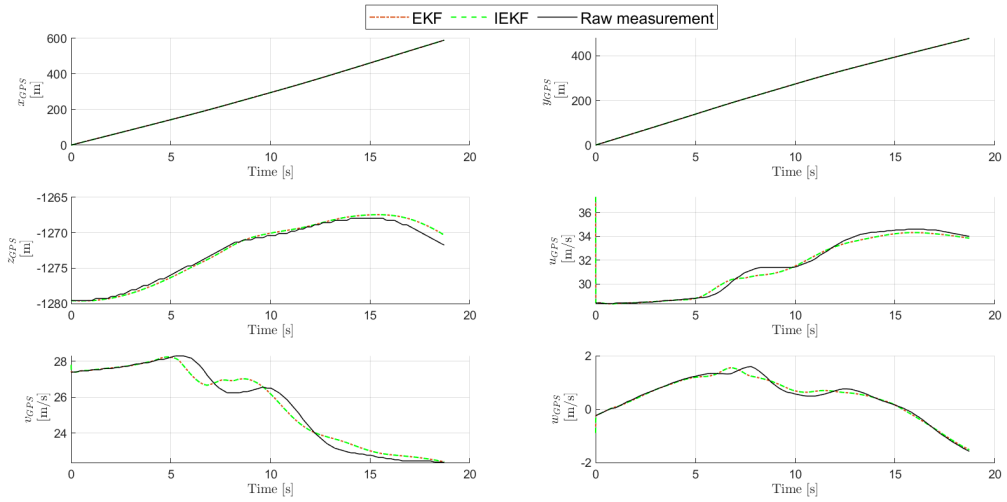

Figure B.15: Measurement vector GPS terms reconstructed by the EKF and IEKF for a rudder 3211 manoeuvre

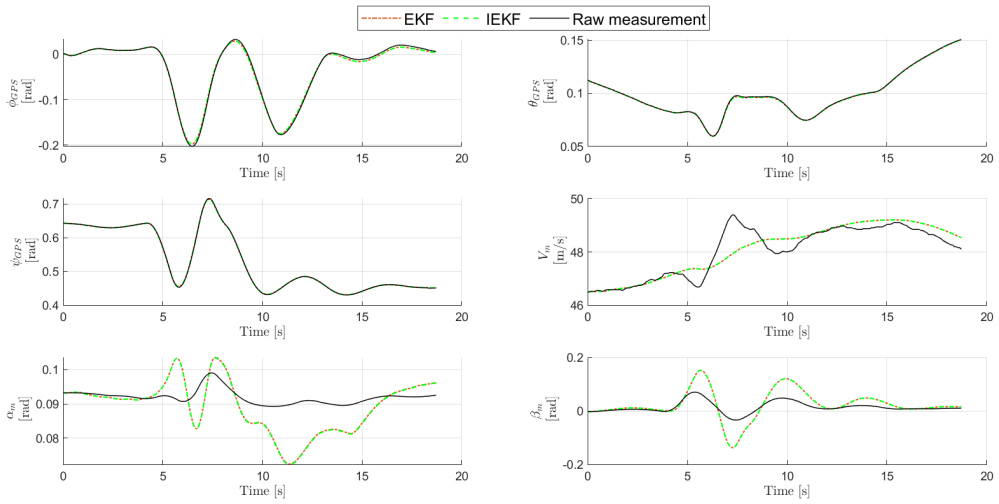

Figure B.16: Measurement vector attitude and air data terms reconstructed by the EKF and IEKF for a rudder 3211 manoeuvre

Rudder doublet

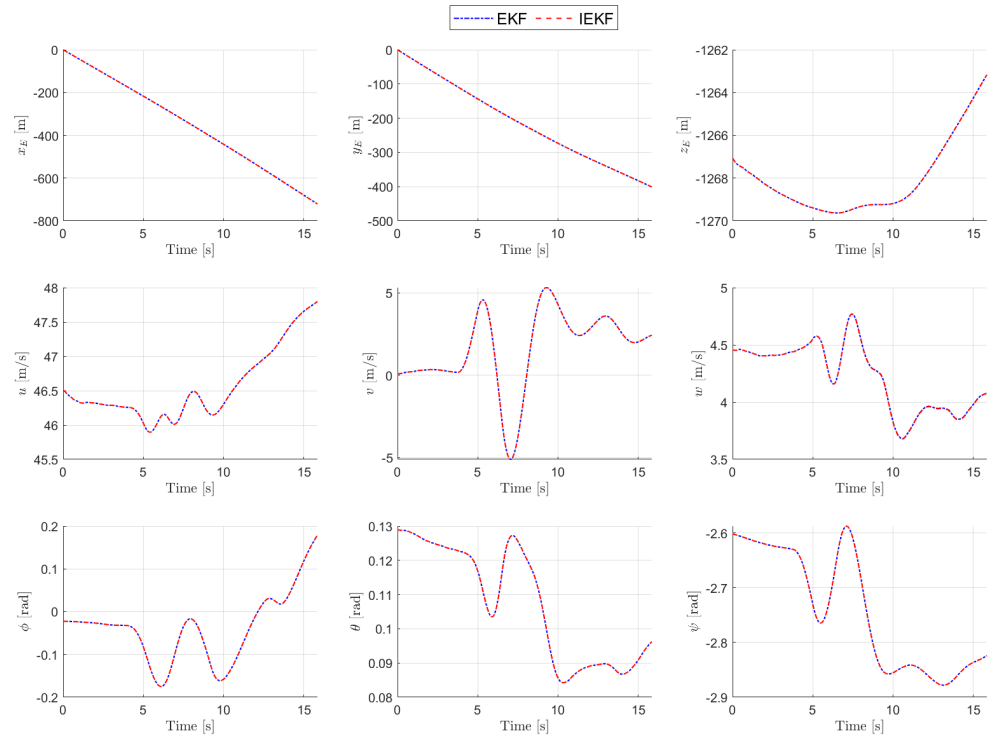

Figure B.17: Unaugmented state estimation of EKF and IEKF for a rudder doublet manoeuvre

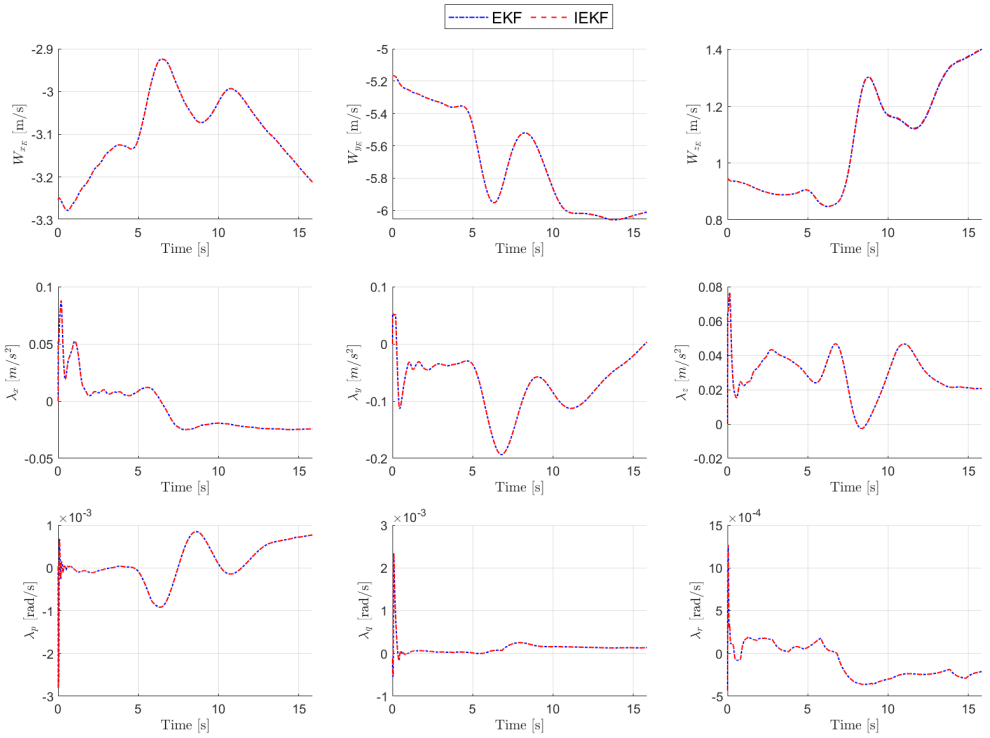

Figure B.18: Wind and IMU bias estimation of EKF and IEKF for a rudder doublet manoeuvre

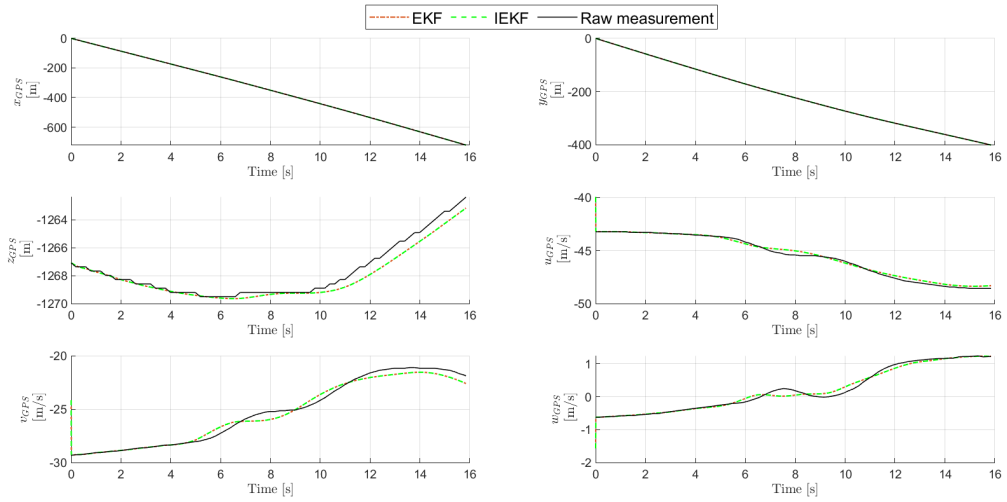

Figure B.19: Measurement vector GPS terms reconstructed by the EKF and IEKF for a rudder doublet manoeuvre

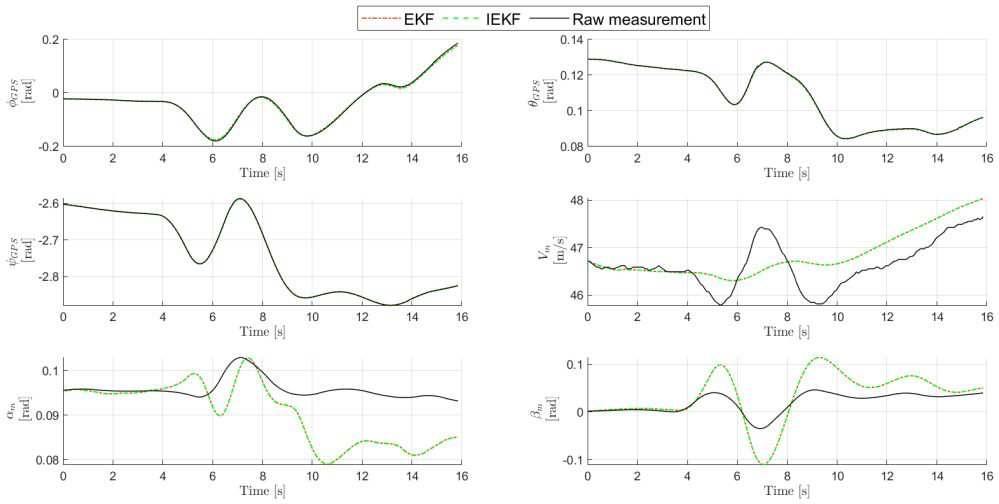

Figure B.20: Measurement vector attitude and air data terms reconstructed by the EKF and IEKF for a rudder doublet manoeuvre

B.2. Parameter estimation

This section graphically presents the model observation fitting for doublet and 3211 symmetrical and asymmetrical manoeuvres and is an extension to the elevator doublet and aileron 3211 manoeuvres presented in section 6.2 of chapter 6.

Elevator 3211

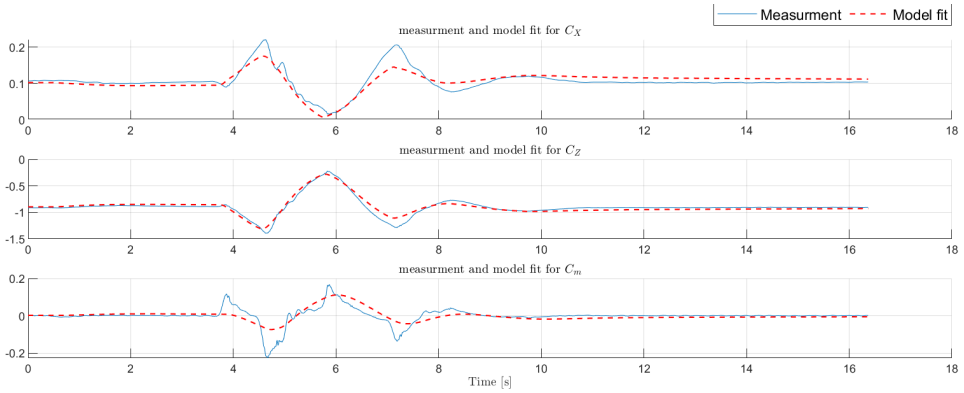

Figure B.21: Observation and OLS model fit of the symmetrical dimensionless forces and moment for an elevator 3211

Aileron 3211

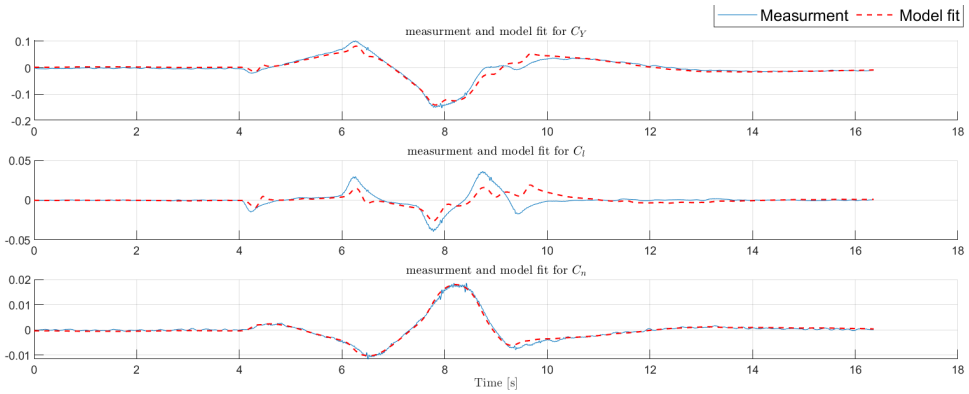

Figure B.22: Observation and OLS model fit of the asymmetrical dimensionless force and moments for an aileron 3211

Aileron doublet

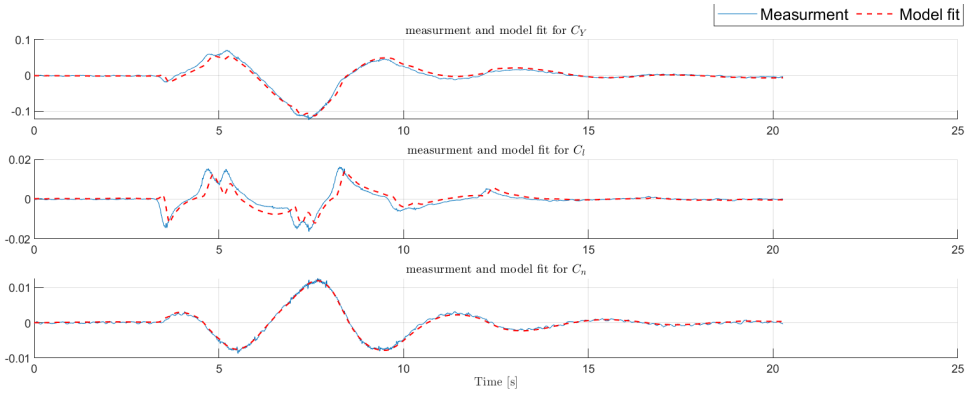

Figure B.23: Observation and OLS model fit of the asymmetrical dimensionless force and moments for an aileron doublet

Rudder 3211

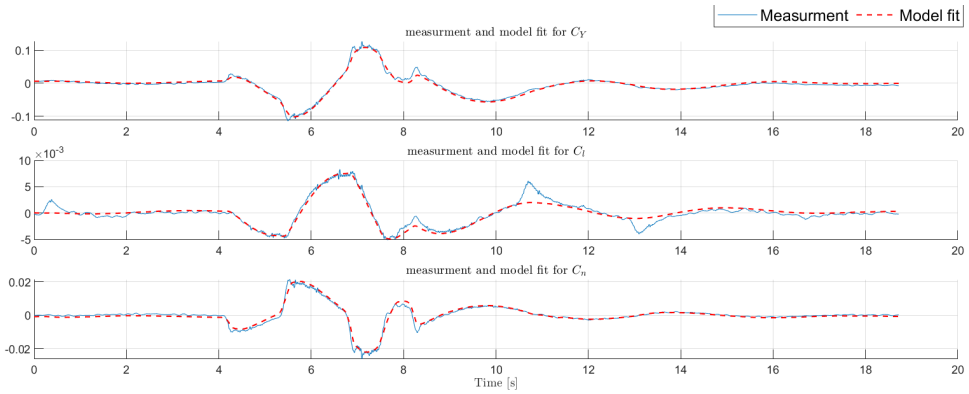

Figure B.24: Observation and OLS model fit of the asymmetrical dimensionless force and moments for a rudder 3211

Rudder doublet

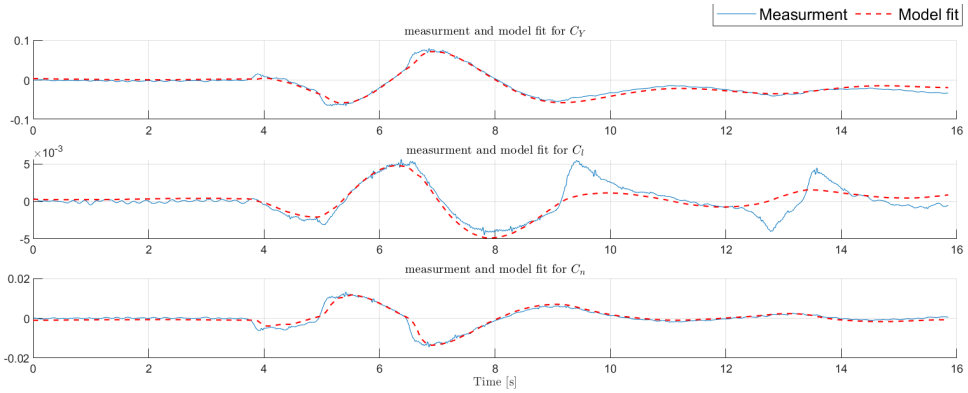

Figure B.25: Observation and OLS model fit of the asymmetrical dimensionless force and moments for a rudder doublet

B.3. Alternative model structure

This section presents the results of parameter identification of an alternative model structure, including the terms of first time derivative of incidence angles, $\dot{\alpha}$ and $\dot{\beta}$, as defined on Equation B.1 and Equation B.2. Overall, the observation fitting is improved due to higher number of terms in the model, however the variance of determined coefficients is increased, due to a high correlation of q with $\dot{\alpha}$ and r with $\dot{\beta}$.

$$
\begin{aligned}
C_X &= C_{X_0} + C_{X_\alpha}\alpha + C_{X_{\dot{\alpha}}}\dot{\alpha} + C_{X_q}\frac{q\bar{c}}{V} + C_{X_{\delta_e}}\delta_e \\
C_Y &= C_{Y_0} + C_{Y_\beta}\beta + C_{Y_{\dot{\beta}}}\dot{\beta} + C_{Y_p}\frac{pb}{2V} + C_{Y_r}\frac{rb}{2V} + C_{Y_{\delta_a}}\delta_a + C_{Y_{\delta_r}}\delta_r \\
C_Z &= C_{Z_0} + C_{Z_\alpha}\alpha + C_{Z_{\dot{\alpha}}}\dot{\alpha} + C_{Z_q}\frac{q\bar{c}}{V} + C_{Z_{\delta_e}}\delta_e
\end{aligned}
\tag{B.1}
$$

$$
\begin{aligned}
C_l &= C_{l_0} + C_{l_\beta}\beta + C_{l_{\dot{\beta}}}\dot{\beta} + C_{l_p}\frac{pb}{2V} + C_{l_r}\frac{rb}{2V} + C_{l_{\delta_a}}\delta_a + C_{l_{\delta_r}}\delta_r \\
C_m &= C_{m_0} + C_{m_\alpha}\alpha + C_{m_{\dot{\alpha}}}\dot{\alpha} + C_{m_q}\frac{q\bar{c}}{V} + C_{m_{\delta_e}}\delta_e \\
C_n &= C_{n_0} + C_{n_\beta}\beta + C_{n_{\dot{\beta}}}\dot{\beta} + C_{n_p}\frac{pb}{2V} + C_{n_r}\frac{rb}{2V} + C_{n_{\delta_a}}\delta_a + C_{n_{\delta_r}}\delta_r
\end{aligned}
\tag{B.2}
$$

Table B.1 lists the average, minimum and maximum relative root mean squared value of the residual throughout all manoeuvres for the alternative model structure. The RMS is slightly improved due to better fitting of the observation.

Table B.1: Average, minimum and maximum of the relative root mean squared value of the residual, in %

	$\overline{RMS}_{rel}$	$\{RMS_{rel}\}_{min}$	$\{RMS_{rel}\}_{max}$
C_X	5.3	2.9	7.0
C_Y	4.7	2.9	7.0
C_Z	2.7	1.2	4.0
C_l	11.6	4.4	17.4
C_m	11.6	8.2	14.7
C_n	5.4	2.2	8.7

Table B.2 through Table B.7 lists the estimated parameters of the alternative model structure, listing their mean, minimum and maximum determined values and variance for all forces and moments. The variance is slightly increased due to additional correlation between independent variables.

Table B.2: Estimated parameters of the C_X model, listing their mean, minimum and maximum determined values and variance

	$\overline{\theta}$	θ_{min}	θ_{max}	$\overline{Var}\{\theta\}$	$Var\{\theta\}_{min}$	$Var\{\theta\}_{max}$
C_{X_0}	0.013	-0.021	0.044	3.61e-6	2.07e-6	5.10e-6
C_{X_α}	0.966	0.523	1.460	3.97e-4	1.85e-4	6.32e-4
$C_{X_{\dot{\alpha}}}$	0.358	-0.205	1.048	1.46e-3	3.49e-4	2.91e-3
C_{X_q}	-5.082	-18.922	6.721	7.66e-1	2.18e-1	1.50e+0
$C_{X_{\delta e}}$	0.190	-0.116	0.525	1.88e-4	1.14e-4	4.01e-4

Table B.3: Estimated parameters of the C_Y model, listing their mean, minimum and maximum determined values and variance

	$\overline{\theta}$	θ_{min}	θ_{max}	$\overline{Var}\{\theta\}$	$Var\{\theta\}_{min}$	$Var\{\theta\}_{max}$
C_{Y_0}	0.001	-0.008	0.010	4.77e-8	7.55e-9	1.15e-7
C_{Y_β}	-0.531	-0.629	-0.394	8.87e-5	8.12e-6	4.07e-4
$C_{Y_{\dot{\beta}}}$	-0.332	-0.950	0.251	3.02e-4	7.76e-5	5.90e-4
C_{Y_p}	0.708	-0.587	2.277	3.92e-3	4.65e-4	1.98e-2
C_{Y_r}	-2.019	-7.029	2.540	2.01e-2	4.77e-3	4.14e-2
$C_{Y_{\delta a}}$	0.148	-0.225	0.410	1.62e-4	9.39e-5	2.47e-4
$C_{Y_{\delta r}}$	0.175	0.124	0.216	1.69e-5	6.90e-6	2.98e-5

Table B.4: Estimated parameters of the C_Z model, listing their mean, minimum and maximum determined values and variance

	$\overline{\theta}$	θ_{min}	θ_{max}	$\overline{Var}\{\theta\}$	$Var\{\theta\}_{min}$	$Var\{\theta\}_{max}$
C_{Z_0}	-0.462	-0.539	-0.391	3.78e-5	2.32e-5	6.60e-5
C_{Z_α}	-4.506	-5.643	-3.598	4.17e-3	2.38e-3	8.18e-3
$C_{Z_{\dot{\alpha}}}$	-1.366	-3.494	-0.260	1.53e-2	4.49e-3	3.77e-2
C_{Z_q}	11.759	-23.040	53.206	8.12e+0	2.80e+0	1.95e+1
$C_{Z_{\delta e}}$	-1.005	-2.188	0.274	1.80e-3	1.16e-3	2.48e-3

Table B.5: Estimated parameters of the C_l model, listing their mean, minimum and maximum determined values and variance

	$\overline{\theta}$	θ_{min}	θ_{max}	$\overline{Var}\{\theta\}$	$Var\{\theta\}_{min}$	$Var\{\theta\}_{max}$
C_{l_0}	0.000	-0.003	0.001	8.77e-9	4.87e-10	3.27e-8
C_{l_β}	-0.019	-0.099	0.019	6.34e-6	4.05e-7	1.61e-5
$C_{l_{\dot{\beta}}}$	-0.162	-0.481	-0.006	8.21e-5	7.98e-7	3.19e-4
C_{l_p}	0.199	-0.464	1.206	5.29e-4	1.26e-5	1.81e-3
C_{l_r}	-1.014	-3.547	0.194	5.57e-3	5.43e-5	2.24e-2
$C_{l_{\delta a}}$	0.040	-0.224	0.230	8.96e-5	4.83e-5	1.13e-4
$C_{l_{\delta r}}$	0.006	-0.001	0.018	4.25e-7	4.05e-8	1.49e-6

Table B.6: Estimated parameters of the C_m model, listing their mean, minimum and maximum determined values and variance

	$\overline{\theta}$	θ_{min}	θ_{max}	$\overline{Var}\{\theta\}$	$Var\{\theta\}_{min}$	$Var\{\theta\}_{max}$
C_{m_0}	0.062	0.002	0.113	1.32e-5	9.51e-6	2.14e-5
C_{m_α}	-0.623	-1.224	0.096	1.46e-3	8.50e-4	2.65e-3
$C_{m_{\dot{\alpha}}}$	0.526	-0.643	1.881	5.37e-3	1.60e-3	1.22e-2
C_{m_q}	-13.452	-40.862	6.955	2.84e+0	1.00e+0	6.31e+0
$C_{m_{\delta e}}$	-0.386	-1.195	0.277	6.48e-4	4.05e-4	1.07e-3

Table B.7: Estimated parameters of the C_n model, listing their mean, minimum and maximum determined values and variance

	$\overline{\theta}$	θ_{min}	θ_{max}	$\overline{Var}\{\theta\}$	$Var\{\theta\}_{min}$	$Var\{\theta\}_{max}$
C_{n_0}	-0.001	-0.001	0.001	2.97e-9	4.06e-11	9.75e-9
C_{n_β}	0.035	-0.033	0.060	6.77e-6	5.48e-8	3.44e-5
$C_{n_{\dot{\beta}}}$	-0.025	-0.166	0.036	1.58e-5	4.17e-7	6.48e-5
C_{n_p}	-0.195	-0.352	-0.115	2.60e-4	7.47e-6	1.68e-3
C_{n_r}	-0.318	-1.437	0.156	1.03e-3	2.56e-5	4.01e-3
$C_{n_{\delta a}}$	-0.012	-0.024	-0.002	9.77e-7	6.75e-7	1.53e-6
$C_{n_{\delta r}}$	-0.075	-0.090	-0.054	1.46e-6	5.04e-7	2.50e-6

C

Extension to experiment design

This chapter illustrates the experimental part of the project by providing additional sensor data in section C.1, pictures from different measurements performed in section C.2, section C.3, section C.4 and exemplary flight test sheets in section C.5.

C.1. IMU sensor

This section provides additional details on the data recorded by the Xsens IMU sensor, as listed by Table C.1.

Table C.1: Xsens IMU sensor measured parameters [81]

Symbol	Variables	Unit	Coordinate system	Type
$\dot{u}_S, \dot{v}_S, \dot{w}_S$	Acceleration in X_X, Y_X, Z_X	[m/s^2]	sensor body F_X	inertial
p, q, r	Angular velocity about X_X, Y_X, Z_X	[°/s]	sensor body F_X	inertial
mg_X, mg_Y, mg_Z	Magnetic field normalised	[a.u.][2]	sensor body F_X	magnetic
de_0, de_x, de_y, de_z	Change in quaternion per dt	[-]	F_X to F_L	calibrated de
du, dv, dw	Change in velocity per dt	[m/s]	sensor body F_X	calibrated dV_s
ϕ, θ, ψ	Attitude in Euler angles	[°]	F_X to F_L	orientation
e_o, e_x, e_y, e_z	Attitude in quaternions [3]	[-]	F_X to F_L	orientation
$\dot{u}_L, \dot{v}_L, \dot{w}_L$	Gravity deduced free acceleration	[m/s^2]	local F_L	free acc.

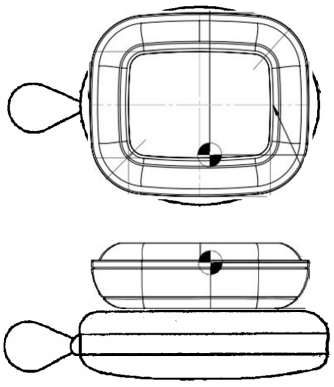

Figure C.1: Top and side view of the Xsens sensor and pulley installation together with sensor centre of gravity location

[2] One a.u. is the magnetic field strength during calibration at Xsens calibration lab, approximately 40 [uT].

[3] Quaternions are an extension to complex numbers allowing for using nondimensionalised values in the determination of Euler angles [64]

C.2. Control deflection measurement

This section illustrates the manufacturing details of the pulley used to translate the translational motion of the control column/pedals motion into the rotation of the Xsens sensor. It also pictures the physical interfaces of the control deflection measurement with the aircraft.

(a) Top view of IMU sensor on pulley

(b) Side view of IMU sensor on pulley

Figure C.2

(a) Pulley cover with drilled hole

(b) Pulley spring loaded string drum

Figure C.3

(a) IMU on yoke for aileron deflection, the sensor is moved under the clip pad in FT1.0

(b) IMU and pulley arrangement for elevator deflection

Figure C.4

(a) Pulley arrangement for rudder (pedal) deflection

(b) Attachment of pulley string behind pedal via Velcro

Figure C.5

Figure C.6: Control column marked with lateral marks each 2.1 [cm] and dot marked neutral elevator position, together with aileron deflection dial

C.3. BOM

This section illustrates the BOM and its interface with the aircraft wing

(a) BOM front view, illustrating its pressure probes

(b) BOM side view, temporarily installed with increased pitch with respect to wing chord, for calibration at higher airspeed range

Figure C.7

C.4. COG determination

This section illustrates the experimental determination of centre of gravity by measuring the wheel reaction forces with the ground at several aircraft attitudes. A fuel density test has also been performed, yet its low precision caused the result not to be taken for calculations.

(a) 3D centre of gravity determination

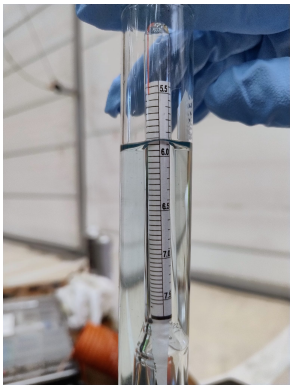

(b) AVGAS fuel density measurement

Figure C.8

C.5. Flight Test cards

This section presents the flight test cards of flight FT1.0.

Note on flight safety

The use of the presented methods have been extensively discussed with the aircraft mechanics as well as flight test pilots and accepted by them. The connection of the IMUs to the pulleys and of the pulleys to the aircraft structure is realised with Velcro and is thus detachable at any moment. The connection of the pulled string to the yoke is realised by an easily breakable wire and a clip. The connection of the pulled string to the pedals is done with Velcro patches. The system has been checked on the ground to clear out any interference of the measuring devices hardware with the controls in their full deflection range and with the ergonomic body movements of the pilots.

Test Flight Cover Sheet
Flight Test Operations

A/C type:	C337	A/C reg.:	N4207X	Date:	11.07.2025	Flt.nr.:	1.0
Captain		Alexander in't Veld		FTE			
Co-pilot							
Experiment lead							

Flight purpose:	1. Check feasibility of data acquisition within 70-90 kt range 2. Data acquisition by 3211 and doublet manoeuvres in 3 aircraft axes 3. (Recalibration of BOM for higher stall speed)
Configuration:	• pulleys and Xsens IMUs for control surface deflection ON • BOM ON • FTD acquisition system via arinc ON
Restrictions:	BOM AOA measurement IAS range 70-90 kt
Notes:	• Purpose of the flight is collect flight data during isolated doublet and 3211 manoeuvres using BOM, Xsens and arinc
	• FTD acquisition system to be turned on after engine start. BOM is automatic. Xsens measurement initiation from mobile phone and data collected on Xsens memory card.
	• Two in flight measurements (all control surfaces excitation)
	• Xsens recording custom mode 5 (quaternions)
	• (If needed, recalibrate BOM to higher stall speed)
Routing/test area:	
Flight profile:	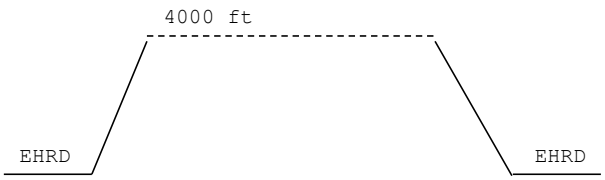

Contents of Test Flight:

Test card nr.	Version/date	Description	Duration [h:min:s]
1	V1/11JUL2025	In-flight doublet test	0:10:00
2	V1/11JUL2025	In-flight 3211 test	0:10:00
3	V1/11JUL2025	BOM AOA calibration (if needed)	0:10:00
		Estimated flight time:	0:30h + 0:20 ferry

FLIGHT TEST CARD

GENERAL		
PROJECT	:	Thesis – Jan Wiacek
TEST CARD NUMBER / VERSION	:	1 V1/11JUL2025
SUBJECT	:	
REFERENCE	:	
NOTES	:	In-flight doublet test
EST. DURATION OF TEST RUN	:	0:10:00
HAZARD CATEGORY	:	~~ROUTINE~~ / LOW / ~~MEDIUM~~ / ~~HIGH~~

INITIAL CONDITIONS					
ALT/FL	:	4000 ft	ENGINE SETTING	:	CRUISE, const.
IAS	:	70-90 kt	FLAP SETTING	:	CLEAN
MACH	:	-	LANDING GEAR	:	UP
MASS	:	-	OTHER	:	Trimmed and horiz
C.G.	:	-			

TEST PROCEDURE

Ground engine on control surface measurement

- Establish horizontal steady flight, trimmed conditions
- Check sensors in place, connected and synchronized
- Note down time stamp AND
- Within 5 second, START recording of Xsens
- Wait 3-5 seconds
- Give DOUBLET input within indicated range
- Wait until aircraft returns to steady flight (or 1 min)
- STOP recording of Xsens
- Perform FOR aileron, elevator, rudder
- For aileron, move one sensor to instrument panel for reference measurement

END OF TEST

- IF high vertical wind gust, repeat particular measurement

MATRIX

Recording order	Garmin time stamp	Recording mode	Control surface	Direction order	Estimated magnitude	other
1.1		5	Aileron	R/L		
1.2		5	Aileron	L/R		
1.3		5	Elev	Dn/up		
1.4		5	Elev	Dn/up		
1.5		5	Rudder	R/L		
1.6		5	Rudder	L/R		
Fuel[lbs] level		Main R	Main L	Aux R	Aux L	Altitude [ft]

DATE : 11.07.25 FLT.NR. :1.0 Skymaster

FLIGHT TEST CARD

GENERAL		
PROJECT	:	Thesis – Jan Wiacek
TEST CARD NUMBER / VERSION	:	2 V1/11JUL2025
SUBJECT	:	
REFERENCE	:	
NOTES	:	In-flight 3211 test
EST. DURATION OF TEST RUN	:	0:10:00
HAZARD CATEGORY	:	~~ROUTINE~~ / LOW / ~~MEDIUM~~ / ~~HIGH~~

INITIAL CONDITIONS					
ALT/FL	:	4000 ft	ENGINE SETTING	:	CRUISE, const.
IAS	:	70-90 kt	FLAP SETTING	:	CLEAN
MACH	:	-	LANDING GEAR	:	UP
MASS	:	-	OTHER	:	Trimmed and horiz
C.G.	:	-			

TEST PROCEDURE

Ground engine on control surface measurement

- Establish horizontal steady flight, trimmed conditions
- Check sensors in place, connected and synchronized
- Note down time stamp AND
- Within 5 second, START recording of Xsens
- Wait 3-5 seconds
- Give 3211 input within indicated range
- Wait until aircraft returns to steady flight (or 1 min)
- STOP recording of Xsens
- Perform FOR aileron, elevator, rudder
- For aileron, move one sensor to instrument panel for reference measurement

END OF TEST

- IF high vertical wind gust, repeat particular measurement

MATRIX

Recording order	Garmin time stamp	Recording mode	Control surface	Direction order	Estimated magnitude	other
2.1		5	Aileron	R/L		
2.2		5	Aileron	L/R		
2.3		5	Elev	Dn/up		
2.4		5	Elev	Dn/up		
2.5		5	Rudder	R/L		
2.6		5	Rudder	L/R		
Fuel[lbs] level		Main R	Main L	Aux R	Aux L	Altitude [ft]

DATE : 11.07.25 FLT.NR. :1.0 Skymaster

FLIGHT TEST CARD

GENERAL		
PROJECT	:	Thesis – Jan Wiacek
TEST CARD NUMBER / VERSION	:	3 V1/11JUL2025
SUBJECT	:	BOM calibration
REFERENCE	:	
NOTES	:	BOM Attitude, AOA calibration, adjustment for IAS and altitude
EST. DURATION OF TEST RUN	:	0:10:00
HAZARD CATEGORY	:	ROUTINE / ~~LOW~~ / ~~MEDIUM~~ / ~~HIGH~~

INITIAL CONDITIONS					
ALT/FL	:	Unspecified	ENGINE SETTING	:	CRUISE, const.
IAS	:	100 kt	FLAP SETTING	:	CLEAN
MACH	:	-	LANDING GEAR	:	UP
MASS	:	-	OTHER	:	Steady, symm., level
C.G.	:	-			

TEST PROCEDURE

BOM attitude calibration

- Establish steady and level, symmetrical flight (alt unspecified, IAS unspecified)
- Maintain for 5 sec, FTE to “CAGE” established conditions on App
- Compare App artificial horizon indication to PFD

BOM AOA calibration

- Establish steady and level, symmetrical flight at IAS=100 kt
- Maintain for 5 sec, FTE to “CALIBRATE AOA” at established conditions on the App
- Test if AOA indicator responds logically (full stall at 87 kt), check upper limit

Adjust BOM IAS, alt

- Establish steady and level, symmetrical flight (altimeter set to 1013.25, IAS unspecified)
- Maintain for 5 sec, FTE to adjust BOM IAS and BOM ALT with values from PFD
- Test if BOM IAS and ALT correspond to PFD

END OF TEST

FTE Checklist

Order	Command	CHECK	other
1	Connect to BOM via WIFI, S/N 2053		
2	Test two-ways communications (Device config./BOM)		
3	Confirm BOM reset to default settings. Device config./General config./Commands/Restore defaults		
4	Attitude calibration in Device config./BOM/Horizon adjustment. “CAGE” when ready.		Test
5	AOA calibration in Device config./BOM/AOA calibration. “CALIBRATE AOA” when ready, IAS 100 kt.		
6	Confirm AOA yellow/red boarder at 100 kt. Confirm full stall at 87 kt.		Test
7	Determine upper IAS limit when AOA=0.0		Upper IAS limit
8	Adjust IAS and pressure altitude on BOM		

D

Code documentation

This chapter reports the methods of numerical differentiation and integration used in the study as well as lists the structure of the code developed for the engine model and Two Step identification of the aerodynamic model.

D.1. Numerical computation methods

Numerical differentiation is performed with the central finite difference scheme, here described for order four by Equation D.1, where $f'(x)$ describes the first time derivative of function $f(x)$ and the step size dt is h.

$$f'(x) = \frac{-f(x+2h) + 8f(x+h) - 8f(x-h) + f(x-2h)}{12h} + O(h^4) \tag{D.1}$$

At boundaries up the the third array position, the forward and backward finite difference schemes of order two can be employed, respectively, as per Equation D.2.

$$f'(x) = \frac{-3f(x) + 4f(x+h) - f(x+2h)}{2h} + O(h^2) \quad f'(x) = \frac{3f(x) - 4f(x-h) + f(x-2h)}{2h} + O(h^2) \tag{D.2}$$

Numerical integration of a discrete, measured signal can be performed with the cumulative trapezoidal rule. In this approach, the integral of the n times sampled function $f(x)$ is approximated by assuming a linear relationship over two consecutive sampled points $f(x_k)$ and $f(x_{k+1})$, essentially summing the areas of trapezoidal slices of $f(x)$ of height $x_k - x_{k-1}$ [1], as expressed by Equation D.3. The global error is $O(h^2)$.

$$\int_a^b f(x)\,dx \approx \frac{1}{2}\sum_{k=1}^{n}(x_k - x_{k-1})\left(f(x_{k-1}) + f(x_k)\right) = \sum_{k=1}^{n} 0.5h\left(f(x_{k-1}) + f(x_k)\right) \tag{D.3}$$

For a higher order of accuracy, more suitable for non-stiff problems, the Runge-Kutta scheme can be employed. With a function $x(t)$, such that $\frac{dx}{dt} = f(x,t)$, the one-step-ahead term x_{k+1} can be predicted with a higher function gradient approximation, as stated on Equation D.4.

$$\begin{aligned} x_{k+1} &= x_k + \frac{k_1 + 2k_2 + 2k_3 + k_4}{6} \\ k_1 &= hf(x_k, t_k) \\ k_2 &= hf\left(x_k + \frac{k_1}{2}, t_k + \frac{h}{2}\right) \\ k_3 &= hf\left(x_k + \frac{k_2}{2}, t_k + \frac{h}{2}\right) \\ k_4 &= h\left(x_k + k_3, t_k + h\right) \end{aligned} \tag{D.4}$$

D.2. Code structure

Table D.1 lists the `Matlab` files comparison the Two Step method, engine model and additional tools together with their description. The initial data preprocessing including manoeuvre isolation, upsampling, input vector filtering and smoothing and control surface computation from recorded

IMU data is performed with Python, the files of which are not included in the description. The implementation of Kalman filter and state observability check are built as adapted versions of the algorithm of [75].

Table D.1: List of Matlab files together with their description

File name	Description
part1_preprocess.m	Transforms the available flight test data into the inputs of the Kalman filter and OLS, storing in noisy_data
part2_EKF.m	Reconstructs the aircraft measurements and estimates the state employing the EKF, storing in filtered_data
part2_IEKF.m	Reconstructs the aircraft measurements and estimates the state employing the IEKF, storing in filtered_data
part3_OLS.m	Estimates values of the parameters with OLS method by fitting a predefined model onto computed observation, storing in parameters, computes fit statistics
part4_validation.m	Superimposes the identified model onto computed observation of the validation data set, computes fit statistics
nav_model_f.m	Computes the time derivatives of states, given the state and input vectors
nav_model_Fx.m	Calculates the numerical value of the Jacobian of the system dynamics equations $\mathbf{f}[\cdot]$
nav_model_h.m	Computes the output if the navigation system given state and input vectors
nav_model_Hx.m	Calculates the numerical value of the Jacobian of the output equations $\mathbf{h}[\cdot]$
kf_calcNonlinObsRank.m	Checks the state observability rank of the nonlinear aircraft system [75]
ac_cg.m	Computes the aircraft three dimensional centre of gravity given variable fuel, crew and cargo mass
ac_engine_map.m	Provides engine temperature and altitude corrected horsepower given N, p_z, h_p and T_0 by interpolating between curves of the engine performance map
ac_get_eta_ct.m	Provides propeller efficiency and thrust coefficient given J, C_p, N and flight level by interpolating between retrieved propeller performance maps
ac_engine.m	Computes thrust and dimensionless change in total pressure across propeller using ac_get_eta_ct.m and flight condition inputs
ac_mass.m	Computes the total aircraft mass given variable fuel, crew and cargo mass
ac_moi.m	Computes the aircraft MOI around given COG for variable fuel, crew and cargo mass. Includes hardcoded invariant MOI components
ac_realfuel.m	Converts the MVP fuel indication into a corrected value in [kg]
atmosphere.m	ISA model valid up to 11,000 [m], with altitude, sea level pressure and temperature as inputs
num_diff.m	Computes the numerical derivative of an array given a time step, with choice of order
rk4.m	Computes the numerical integral of an array given a function and time step with Runge Kutta of order four

Note on use of Artificial Intelligence

Throughout this study, Artificial Intelligence has not been used for critical thinking tasks. The Open IA's ChatGPT (version 5) has been used to support the generation of `Matlab` and `Python` graph generation code or `Latex` thesis report formatting, but not text generation. Some functions creased in programming languages have incorporated efficiency improvements suggested by the IA and have subsequently been tested.

E

DATCOM

This chapter states the outcome of a Digital DATCOM analysis of a simplified Cessna Skymaster model input, despite the program limitations in handling the unconventional aircraft configuration, as described in subsection 2.5.2. Results of the computation are summarised in section E.1, whereas the input and output files of are reported in section E.2 and section E.3, respectively.

E.1. Control and aerodynamic derivatives

In this section, the stability, dynamic and control derivatives computed by the Digital DATCOM are presented on Table E.1. The flight conditions specified in the program mimic the ones recorded during the flight test FT1.0, namely airspeed around 46 [m/s], altitude of 1,130 [m] and angle of attack of 0.1 [rad] $\approx 6°$. The full DATCOM output file can be inspected in section E.3.

Table E.1: Selected stability and control derivatives determined by Digital DATCOM for a simplified C337 input

C_{L_α} [1]	C_{m_α}	C_{Y_β}	C_{l_β}	C_{n_β}	C_{L_q} [1 2]
6.224	-0.707	-0.722	0.119	-0.106	5.480

C_{m_q} [2]	$C_{L_{\dot\alpha}}$ [1 2]	$C_{m_{\dot\alpha}}$ [2]	$C_{L_{\delta e}}$ [1 3]	$C_{m_{\delta e}}$ [3]	$C_{l_{\delta a}}$ [3]
-7.229	1.248	-3.076	0.264	-0.608	-0.690

Although the presented results should not be directly compared with the results determined from flight test and reported in chapter 6 due to the program limitations, it can be noticed that the derivative values remain in the same order of magnitude (except for $C_{l_{\delta a}}$ and C_{l_β}) and have the correct sign (except for C_{l_β} and C_{n_β}). The footnotes provide additional context into understanding some of the differences in the derivatives computations, while the Digital DATCOM documentation should be consulted for details and is referenced as [53].

E.2. Input file

This section presents the input file of the Digital DATCOM defining a simplified C337 aircraft in flight testing conditions, with the assumptions described in subsection 2.5.2.

```
CASEID ----- Cessna Skymaster: Body, Wing, Htail, Twin Vpanel, elevator -----
DIM M
DERIV RAD
BUILD
 $FLTCON
  NMACH=1.0,
  MACH(1)=0.137,
  NALT=1.0,
  ALT(1)=1130.0,
```

[1] Digital DATCOM expresses the dimensionless force coefficients in the stability (wind) reference frame. Because the dimensionless drag contribution is not provided, the force coefficients are not translated into the F_b frame.

[2] Digital DATCOM computes both symmetrical and asymmetrical dynamic derivatives with respect to variables nondimensionalised with double the airspeed: $C_{i_a} = \frac{\partial C_i}{\partial(a\bar{c}/2V)}$ [53, p. 96]. In this report, symmetrical dynamic derivatives are scaled with V, as defined by Equation 3.21 and Equation 3.22.

[3] Linearised around neutral control surface position from increment in dimensionless force or moment due to control deflection.

```
 NALPHA=16.0,
 ALSCHD=-2.0,-1.0,0.0,1.0,2.0,3.0,4.0,5.0,6.0,7.0,8.0,9.0,10.0,11.0,12.0,13.0,
 WT=20012.0,
 GAMMA=0.0,
 LOOP=2.0$
$OPTINS
 SREF=18.7,
 CBARR=1.68,
 BLREF=11.68,
 ROUGFC=1.016E-03$
$SYNTHS
 XCG=3.53,
 ZCG=0.42,
 XW=3.08,
 ZW=0.60,
 ALIW=2.0,
 ALIH=-2.0,
 XH=7.39,
 ZH=0.51$
$BODY
 NX=13.0,
 ITYPE=1.0,
 METHOD=1.0,
  X(1)=0.28,0.61,0.73,1.65,1.93,2.49,3.64,4.15,4.65,5.11,5.65,5.89,6.32,
  P(1)=0.15,1.05,2.19,3.66,3.84,4.67,4.74,4.81,4.47,3.57,2.24,1.44,0.15,
  S(1)=0.002,0.09,0.36,1.02,1.12,1.63,1.64,1.67,1.47,0.96,0.39,0.17,0.002,
  R(1)=0.025,0.17,0.34,0.57,0.6,0.72,0.72,0.73,0.68,0.55,0.35,0.23,0.025,
  ZU(1)=0.025,0.17,0.24,0.35,0.42,0.76,0.82,0.82,0.8,0.73,0.66,0.66,0.455,
  ZL(1)=0.0,-0.17,-0.3,-0.66,-0.66,-0.7,-0.7,-0.7,-0.58,-0.39,0.05,0.2,0.41$
$WGPLNF
 CHRDTP=1.26,
 CHRDBP=1.88,
 SSPNOP=4.16,
 CHRDR=1.88,
 SSPNDD=4.15,
 TWISTA=-2.0,
 SSPNE=5.26,
 SSPN=5.84,
 SAVSO=0.0,
 DHDADI=3.0,
 CHSTAT=0.5,
 SAVSI=0.0,
 TYPE=1.0$
$HTPLNF
 CHRDTP=1.0,
 CHRDR=1.0,
 TWISTA=0.0,
 SSPNE=1.53,
 SSPN=1.53,
 SAVSO=0.0,
 DHDADI=0.0,
 CHSTAT=0.5,
 SAVSI=0.0,
 TYPE=1.0$
$TVTPAN
 BVP=1.07,
 BH=3.05,
 VLP=4.43,
 BV=1.56,
 SV=1.51,
 ZP=0.15,
 BDV=0.0,
 VPHITE=11.0$
$SYMFLP
 FTYPE=1.0,
 NTYPE=1.0,
 NDELTA=9.0,
 DELTA(1)=-25.0,-20.0,-15.0,-10.0,-5.0,0.0,5.0,10.0,15.0,
 CHRDFI=0.39,
 CHRDFO=0.39,
 SPANFI=0.0,
```

```
  SPANFO=0.765$
NACA-W-4-2412
NACA-H-4-0009
SAVE
NEXT CASE
CASEID ----- Cessna Skymaster: Body, Wing, Htail, Twin Vpanel, aileron -----
 $ASYFLP
  STYPE=4.0,
  NDELTA=9.0,
  DELTAL=14.5,12.0,8.0,4.0,0.0,-5.8,-11.6,-17.4,-21.0,
  DELTAR=-21.0,-17.4,-11.6,-5.8,0.0,4.0,8.0,12.0,14.5,
  CHRDFI=0.38,
  CHRDFO=0.38,
  SPANFI=4.11,
  SPANFO=5.56$
DAMP
```

E.3. Output file

This section presents the output file of the Digital DATCOM simplified C337 aircraft. Note that the program wrongly computes the freestream temperature, pressure and Reynolds number in lines 58 and 243 when providing control surface output. This behaviour has been observed in multiple cases found in literature and has an impact on the validity of the computed results.

```
1                            AUTOMATED STABILITY AND CONTROL METHODS PER APRIL 1976 VERSION OF DATCOM
                                     CHARACTERISTICS AT ANGLE OF ATTACK AND IN SIDESLIP
                                WING-BODY-HORIZONTAL TAIL-TWIN VERTICAL PANEL CONFIGURATION
                           ----- Cessna Skymaster: Body, Wing, Htail, Twin Vpanel, elevator -----

 ----------------------  FLIGHT CONDITIONS  -------------------------           --------------  REFERENCE DIMENSIONS  ------------
  MACH    ALTITUDE   VELOCITY    PRESSURE    TEMPERATURE     REYNOLDS              REF.      REFERENCE LENGTH    MOMENT REF. CENTER
 NUMBER                                                      NUMBER               AREA       LONG.     LAT.      HORIZ       VERT
              M         M/SEC      N/ M**2       DEG K          1/ M              M**2         M         M         M          M
 0 0.137    1130.00      46.02   8.8469E+04     280.806     2.8670E+06            18.700      1.680    11.680     3.530     0.420
 0                                                                    -------------------DERIVATIVE (PER RADIAN)-------------------
 0 ALPHA     CD        CL       CM       CN       CA       XCP         CLA          CMA          CYB          CNB          CLB
 0
    -2.0    0.022     0.197    0.0594   0.196    0.029    0.303     5.626E+00   -6.441E-01   -7.223E-01    1.188E-01   -9.152E-02
    -1.0    0.024     0.295    0.0480   0.295    0.030    0.163     5.685E+00   -6.616E-01                             -9.311E-02
     0.0    0.027     0.395    0.0363   0.395    0.027    0.092     5.767E+00   -6.800E-01                             -9.474E-02
     1.0    0.031     0.497    0.0243   0.497    0.023    0.049     5.880E+00   -7.345E-01                             -9.644E-02
     2.0    0.037     0.600    0.0107   0.601    0.016    0.018     5.994E+00   -8.208E-01                             -9.820E-02
     3.0    0.043     0.706   -0.0044   0.707    0.006   -0.006     6.076E+00   -8.597E-01                             -1.000E-01
     4.0    0.050     0.812   -0.0194   0.814   -0.007   -0.024     6.134E+00   -8.292E-01                             -1.019E-01
     5.0    0.059     0.920   -0.0333   0.922   -0.022   -0.036     6.182E+00   -7.638E-01                             -1.038E-01
     6.0    0.068     1.028   -0.0460   1.030   -0.039   -0.045     6.224E+00   -7.072E-01                             -1.058E-01
     7.0    0.079     1.137   -0.0580   1.138   -0.060   -0.051     6.272E+00   -7.022E-01                             -1.078E-01
     8.0    0.092     1.247   -0.0705   1.248   -0.083   -0.057     6.024E+00   -7.174E-01                             -1.098E-01
     9.0    0.103     1.348   -0.0830   1.347   -0.110   -0.062     5.398E+00   -8.049E-01                             -1.115E-01
    10.0    0.114     1.436   -0.0986   1.434   -0.137   -0.069     4.851E+00   -9.101E-01                             -1.126E-01
    11.0    0.125     1.517   -0.1148   1.513   -0.167   -0.076     4.456E+00   -9.395E-01                             -1.134E-01
    12.0    0.135     1.591   -0.1314   1.585   -0.198   -0.083     4.038E+00   -9.613E-01                             -1.139E-01
    13.0    0.146     1.658   -0.1484   1.648   -0.231   -0.090     3.597E+00   -9.797E-01                             -1.140E-01
 0                                     ALPHA     Q/QINF    EPSLON  D(EPSLON)/D(ALPHA)
 0
                                       -2.0      1.000      1.893        0.549
                                       -1.0      1.000      2.441        0.547
                                        0.0      1.000      2.987        0.547
                                        1.0      1.000      3.535        0.548
                                        2.0      0.985      4.084        0.549
                                        3.0      0.953      4.633        0.548
                                        4.0      0.918      5.181        0.547
                                        5.0      0.892      5.727        0.545
                                        6.0      0.885      6.270        0.541
                                        7.0      0.900      6.810        0.528
                                        8.0      0.930      7.326        0.510
                                        9.0      0.970      7.829        0.453
                                       10.0      0.997      8.232        0.398
                                       11.0      1.000      8.624        0.378
                                       12.0      1.000      8.988        0.350
                                       13.0      1.000      9.325        0.337
 0*** VEHICLE WEIGHT =  20012.00 N.
 0*** LEVEL FLIGHT LIFT COEFFICIENT = 4.09551
 1                          AUTOMATED STABILITY AND CONTROL METHODS PER APRIL 1976 VERSION OF DATCOM
                                     CHARACTERISTICS OF HIGH LIFT AND CONTROL DEVICES
                                       TAIL PLAIN TRAILING-EDGE FLAP CONFIGURATION
                                ----- Cessna Skymaster: Body, Wing, Htail, Twin Vpanel, elevator -----
 ----------------------  FLIGHT CONDITIONS  -------------------------           --------------  REFERENCE DIMENSIONS  ------------
  MACH    ALTITUDE   VELOCITY    PRESSURE    TEMPERATURE     REYNOLDS              REF.      REFERENCE LENGTH    MOMENT REF. CENTER
 NUMBER                                                      NUMBER               AREA       LONG.     LAT.      HORIZ       VERT
              M         M/SEC      N/ M**2       DEG K          1/ M              M**2         M         M         M          M
 0 0.137    1130.00      46.02   3.8590E+01     909.812     2.6635E+05            18.700      1.680    11.680     3.530     0.420
 0          ---------INCREMENTS DUE TO DEFLECTION---------               ---DERIVATIVES (PER DEGREE)---
 0     DELTA     D(CL)     D(CM)    D(CL MAX)    D(CD MIN)                (CLA)D     (CH)A       (CH)D


       -25.0    -0.073     0.1713     0.046      0.01057                  NDM      -6.979E-03  -1.477E-02
       -20.0    -0.069     0.1618     0.039      0.00741                  NDM                  -1.426E-02
       -15.0    -0.065     0.1511     0.032      0.00521                  NDM                  -1.345E-02
       -10.0    -0.046     0.1061     0.023      0.00272                  NDM                  -1.324E-02
        -5.0    -0.023     0.0531     0.012      0.00118                  NDM                  -1.324E-02
         0.0     0.000    -0.0001     0.000      0.00000                  NDM                  -1.324E-02
         5.0     0.023    -0.0531     0.012      0.00118                  NDM                  -1.324E-02
        10.0     0.046    -0.1061     0.023      0.00272                  NDM                  -1.324E-02
        15.0     0.065    -0.1511     0.032      0.00521                  NDM                  -1.345E-02
 0  *** NOTE * HINGE MOMENT DERIVATIVES ARE BASED ON TWICE THE AREA-MOMENT OF THE CONTROL ABOUT ITS HINGE LINE
```

```
 0            --------- INDUCED DRAG COEFFICIENT INCREMENT , D(CDI) , DUE TO DEFLECTION ---------
 0       DELTA = -25.0      -20.0      -15.0      -10.0       -5.0        0.0        5.0       10.0       15.0
    ALPHA
 0
     -2.0        7.17E-03  6.65E-03  6.10E-03  3.69E-03  1.49E-03 -2.28E-06 -7.91E-04 -8.79E-04 -4.04E-04
     -1.0        6.83E-03  6.33E-03  5.80E-03  3.48E-03  1.39E-03 -2.07E-06 -6.84E-04 -6.67E-04 -1.01E-04
      0.0        6.49E-03  6.01E-03  5.49E-03  3.26E-03  1.28E-03 -1.86E-06 -5.77E-04 -4.52E-04  2.04E-04
      1.0        6.15E-03  5.68E-03  5.19E-03  3.05E-03  1.17E-03 -1.64E-06 -4.71E-04 -2.39E-04  5.08E-04
      2.0        5.81E-03  5.36E-03  4.89E-03  2.84E-03  1.07E-03 -1.43E-06 -3.64E-04 -2.66E-05  8.10E-04
      3.0        5.47E-03  5.04E-03  4.58E-03  2.62E-03  9.60E-04 -1.22E-06 -2.58E-04  1.86E-04  1.11E-03
      4.0        5.14E-03  4.72E-03  4.28E-03  2.41E-03  8.54E-04 -1.00E-06 -1.51E-04  3.99E-04  1.42E-03
      5.0        4.80E-03  4.40E-03  3.98E-03  2.20E-03  7.47E-04 -7.90E-07 -4.45E-05  6.13E-04  1.72E-03
      6.0        4.45E-03  4.07E-03  3.67E-03  1.98E-03  6.39E-04 -5.74E-07  6.32E-05  8.29E-04  2.03E-03
      7.0        4.11E-03  3.74E-03  3.36E-03  1.76E-03  5.30E-04 -3.57E-07  1.72E-04  1.05E-03  2.34E-03
      8.0        3.75E-03  3.40E-03  3.03E-03  1.53E-03  4.16E-04 -1.29E-07  2.86E-04  1.27E-03  2.66E-03
      9.0        3.37E-03  3.05E-03  2.70E-03  1.30E-03  2.99E-04  1.05E-07  4.03E-04  1.51E-03  3.00E-03
     10.0        2.93E-03  2.62E-03  2.30E-03  1.02E-03  1.59E-04  3.87E-07  5.44E-04  1.79E-03  3.40E-03
     11.0        2.47E-03  2.19E-03  1.89E-03  7.33E-04  1.52E-05  6.73E-07  6.87E-04  2.08E-03  3.80E-03
     12.0        2.00E-03  1.73E-03  1.46E-03  4.32E-04 -1.35E-04  9.73E-07  8.37E-04  2.38E-03  4.23E-03
     13.0        1.50E-03  1.26E-03  1.02E-03  1.20E-04 -2.91E-04  1.29E-06  9.93E-04  2.69E-03  4.68E-03
 0***NDM PRINTED WHEN NO DATCOM METHODS EXIST
  Return to main program from M57071
 1           THE FOLLOWING IS A LIST OF ALL INPUT CARDS FOR THIS CASE.
 0
  CASEID ----- Cessna Skymaster: Body, Wing, Htail, Twin Vpanel, aileron -----
   $ASYFLP
    STYPE=4.0,
    NDELTA=9.0,
    DELTAL=14.5,12.0,8.0,4.0,0.0,-5.8,-11.6,-17.4,-21.0,
    DELTAR=-21.0,-17.4,-11.6,-5.8,0.0,4.0,8.0,12.0,14.5,
    CHRDFI=0.38,
    CHRDFO=0.38,
    SPANFI=4.11,
    SPANFO=5.56$
  DAMP
 0 INPUT DIMENSIONS ARE IN M , SCALE FACTOR IS 1.0000

  Return to main program from M01001
 1                             AUTOMATED STABILITY AND CONTROL METHODS PER APRIL 1976 VERSION OF DATCOM
                                                        WING SECTION DEFINITION
 0                                  IDEAL ANGLE OF ATTACK =   0.25757 DEG.

                                   ZERO LIFT ANGLE OF ATTACK =  -1.87965 DEG.

                                      IDEAL LIFT COEFFICIENT =   0.25602

                        ZERO LIFT PITCHING MOMENT COEFFICIENT =  -0.05087

                                  MACH ZERO LIFT-CURVE-SLOPE =   0.09617 /DEG.

                                         LEADING EDGE RADIUS =   0.01587 FRACTION CHORD

                                  MAXIMUM AIRFOIL THICKNESS =   0.12000 FRACTION CHORD

                                                 DELTA-Y =   3.16898 PERCENT CHORD


 0                            MACH= 0.1370 LIFT-CURVE-SLOPE =   0.09689 /DEG.      XAC =   0.25820
 1                                AUTOMATED STABILITY AND CONTROL METHODS PER APRIL 1976 VERSION OF DATCOM
                                                     HORIZONTAL TAIL SECTION DEFINITION
 0                                  IDEAL ANGLE OF ATTACK =   0.00000 DEG.

                                   ZERO LIFT ANGLE OF ATTACK =   0.00000 DEG.

                                      IDEAL LIFT COEFFICIENT =   0.00000

                        ZERO LIFT PITCHING MOMENT COEFFICIENT =   0.00000

                                  MACH ZERO LIFT-CURVE-SLOPE =   0.09830 /DEG.

                                         LEADING EDGE RADIUS =   0.00893 FRACTION CHORD

                                  MAXIMUM AIRFOIL THICKNESS =   0.09000 FRACTION CHORD

                                                 DELTA-Y =   2.37673 PERCENT CHORD


 0                            MACH= 0.1370 LIFT-CURVE-SLOPE =   0.09912 /DEG.      XAC =   0.25657
  Return to main program from M50062
  Return to main program from M02002
  Return to main program from M51063
 1                               AUTOMATED STABILITY AND CONTROL METHODS PER APRIL 1976 VERSION OF DATCOM
                                       CHARACTERISTICS AT ANGLE OF ATTACK AND IN SIDESLIP
                                  WING-BODY-HORIZONTAL TAIL-TWIN VERTICAL PANEL CONFIGURATION
                                  ----- Cessna Skymaster: Body, Wing, Htail, Twin Vpanel, aileron -----

  ----------------------  FLIGHT CONDITIONS  ------------------------           --------------  REFERENCE DIMENSIONS  ------------
    MACH    ALTITUDE   VELOCITY    PRESSURE    TEMPERATURE     REYNOLDS              REF.      REFERENCE LENGTH    MOMENT REF. CENTER
  NUMBER                                                       NUMBER              AREA       LONG.     LAT.      HORIZ       VERT
                 M         M/SEC      N/ M**2       DEG K          1/ M              M**2         M         M         M           M
 0 0.137    1130.00      46.02   8.8469E+04     280.806      2.8670E+06            18.700      1.680    11.680     3.530      0.420
 0                                                                    -------------------DERIVATIVE (PER RADIAN)-------------------
 0 ALPHA      CD        CL        CM        CN        CA        XCP         CLA           CMA           CYB           CNB           CLB
 0
    -2.0     0.022     0.197     0.0594    0.196     0.029     0.303     5.626E+00    -6.441E-01    -7.223E-01     1.188E-01    -9.152E-02
    -1.0     0.024     0.295     0.0480    0.295     0.030     0.163     5.685E+00    -6.616E-01                                -9.311E-02
     0.0     0.027     0.395     0.0363    0.395     0.027     0.092     5.767E+00    -6.800E-01                                -9.474E-02
     1.0     0.031     0.497     0.0243    0.497     0.023     0.049     5.880E+00    -7.345E-01                                -9.644E-02
     2.0     0.037     0.600     0.0107    0.601     0.016     0.018     5.994E+00    -8.208E-01                                -9.820E-02
     3.0     0.043     0.706    -0.0044    0.707     0.006    -0.006     6.076E+00    -8.597E-01                                -1.000E-01
     4.0     0.050     0.812    -0.0194    0.814    -0.007    -0.024     6.134E+00    -8.292E-01                                -1.019E-01
     5.0     0.059     0.920    -0.0333    0.922    -0.022    -0.036     6.182E+00    -7.638E-01                                -1.038E-01
     6.0     0.068     1.028    -0.0460    1.030    -0.039    -0.045     6.224E+00    -7.072E-01                                -1.058E-01
     7.0     0.079     1.137    -0.0580    1.138    -0.060    -0.051     6.272E+00    -7.022E-01                                -1.078E-01
     8.0     0.092     1.247    -0.0705    1.248    -0.083    -0.057     6.024E+00    -7.174E-01                                -1.098E-01
     9.0     0.103     1.348    -0.0830    1.347    -0.110    -0.062     5.398E+00    -8.049E-01                                -1.115E-01
    10.0     0.114     1.436    -0.0986    1.434    -0.137    -0.069     4.851E+00    -9.101E-01                                -1.126E-01
    11.0     0.125     1.517    -0.1148    1.513    -0.167    -0.076     4.456E+00    -9.395E-01                                -1.134E-01
    12.0     0.135     1.591    -0.1314    1.585    -0.198    -0.083     4.038E+00    -9.613E-01                                -1.139E-01
    13.0     0.146     1.658    -0.1484    1.648    -0.231    -0.090     3.597E+00    -9.797E-01                                -1.140E-01
 0                                      ALPHA     Q/QINF     EPSLON   D(EPSLON)/D(ALPHA)
```

```
0
                                    -2.0      1.000      1.893        0.549
                                    -1.0      1.000      2.441        0.547
                                     0.0      1.000      2.987        0.547
                                     1.0      1.000      3.535        0.548
                                     2.0      0.985      4.084        0.549
                                     3.0      0.953      4.633        0.548
                                     4.0      0.918      5.181        0.547
                                     5.0      0.892      5.727        0.545
                                     6.0      0.885      6.270        0.541
                                     7.0      0.900      6.810        0.528
                                     8.0      0.930      7.326        0.510
                                     9.0      0.970      7.829        0.453
                                    10.0      0.997      8.232        0.398
                                    11.0      1.000      8.624        0.378
                                    12.0      1.000      8.988        0.350
                                    13.0      1.000      9.325        0.337
1                             AUTOMATED STABILITY AND CONTROL METHODS PER APRIL 1976 VERSION OF DATCOM
                                                DYNAMIC DERIVATIVES
                                        WING-BODY-HORIZONTAL TAIL-TWIN VERTICAL PANEL CONFIGURATION
                                    ----- Cessna Skymaster: Body, Wing, Htail, Twin Vpanel, aileron -----

 ----------------------  FLIGHT CONDITIONS  -------------------------           --------------  REFERENCE DIMENSIONS  ------------
  MACH    ALTITUDE   VELOCITY    PRESSURE    TEMPERATURE     REYNOLDS              REF.      REFERENCE LENGTH    MOMENT REF. CENTER
 NUMBER                                                      NUMBER               AREA       LONG.     LAT.      HORIZ       VERT
               M         M/SEC      N/ M**2       DEG K          1/ M               M**2         M         M         M          M
0 0.137    1130.00      46.02   8.8469E+04     280.806     2.8670E+06            18.700      1.680    11.680     3.530      0.420
                                                    DYNAMIC DERIVATIVES (PER RADIAN)
0           -------PITCHING-------     -----ACCELERATION------    --------------ROLLING--------------    --------YAWING--------
0   ALPHA        CLQ           CMQ           CLAD          CMAD          CLP           CYP           CNP           CNR           CLR
0
    -2.00    5.480E+00   -7.229E+00     1.431E+00   -3.526E+00       NDM           NDM           NDM           NDM           NDM
    -1.00                               1.427E+00   -3.516E+00       NDM           NDM           NDM           NDM           NDM
     0.00                               1.425E+00   -3.512E+00       NDM           NDM           NDM           NDM           NDM
     1.00                               1.429E+00   -3.522E+00       NDM           NDM           NDM           NDM           NDM
     2.00                               1.409E+00   -3.473E+00       NDM           NDM           NDM           NDM           NDM
     3.00                               1.363E+00   -3.359E+00       NDM           NDM           NDM           NDM           NDM
     4.00                               1.309E+00   -3.225E+00       NDM           NDM           NDM           NDM           NDM
     5.00                               1.266E+00   -3.120E+00       NDM           NDM           NDM           NDM           NDM
     6.00                               1.248E+00   -3.076E+00       NDM           NDM           NDM           NDM           NDM
     7.00                               1.238E+00   -3.050E+00       NDM           NDM           NDM           NDM           NDM
     8.00                               1.236E+00   -3.046E+00       NDM           NDM           NDM           NDM           NDM
     9.00                               1.146E+00   -2.824E+00       NDM           NDM           NDM           NDM           NDM
    10.00                               1.034E+00   -2.548E+00       NDM           NDM           NDM           NDM           NDM
    11.00                               9.847E-01   -2.427E+00       NDM           NDM           NDM           NDM           NDM
    12.00                               9.130E-01   -2.250E+00       NDM           NDM           NDM           NDM           NDM
    13.00                               8.792E-01   -2.167E+00       NDM           NDM           NDM           NDM           NDM
0*** NDM PRINTED WHEN NO DATCOM METHODS EXIST
0*** VEHICLE WEIGHT =  20012.00 N.
0*** LEVEL FLIGHT LIFT COEFFICIENT = 4.09551
1                             AUTOMATED STABILITY AND CONTROL METHODS PER APRIL 1976 VERSION OF DATCOM
                                      CHARACTERISTICS OF HIGH LIFT AND CONTROL DEVICES
                                         WING PLAIN TRAILING-EDGE FLAP CONFIGURATION
                                    ----- Cessna Skymaster: Body, Wing, Htail, Twin Vpanel, aileron -----
 ----------------------  FLIGHT CONDITIONS  -------------------------           --------------  REFERENCE DIMENSIONS  ------------
  MACH    ALTITUDE   VELOCITY    PRESSURE    TEMPERATURE     REYNOLDS              REF.      REFERENCE LENGTH    MOMENT REF. CENTER
 NUMBER                                                      NUMBER               AREA       LONG.     LAT.      HORIZ       VERT
               M         M/SEC      N/ M**2       DEG K          1/ M               M**2         M         M         M          M
0 0.137    1130.00      46.02   3.8590E+01     909.812     2.6635E+05            18.700      1.680    11.680     3.530      0.420
0                          ----------YAWING MOMENT COEFFICIENT,CN,DUE TO CONTROL DEFLECTION----------
0(DELTAL-DELTAR)= 35.5        29.4        19.6         9.8         0.0        -9.8       -19.6       -29.4       -35.5
0ALPHA
0
  -2.0        -1.793E-03  -1.595E-03  -1.098E-03  -5.508E-04   0.000E+00   5.508E-04   1.098E-03   1.595E-03   1.793E-03
  -1.0        -2.328E-03  -2.071E-03  -1.426E-03  -7.153E-04   0.000E+00   7.153E-04   1.426E-03   2.071E-03   2.328E-03
   0.0        -2.875E-03  -2.558E-03  -1.761E-03  -8.832E-04   0.000E+00   8.832E-04   1.761E-03   2.558E-03   2.875E-03
   1.0        -3.431E-03  -3.053E-03  -2.102E-03  -1.054E-03   0.000E+00   1.054E-03   2.102E-03   3.053E-03   3.431E-03
   2.0        -3.997E-03  -3.556E-03  -2.449E-03  -1.228E-03   0.000E+00   1.228E-03   2.449E-03   3.556E-03   3.997E-03
   3.0        -4.569E-03  -4.065E-03  -2.799E-03  -1.404E-03   0.000E+00   1.404E-03   2.799E-03   4.065E-03   4.569E-03
   4.0        -5.148E-03  -4.580E-03  -3.154E-03  -1.581E-03   0.000E+00   1.581E-03   3.154E-03   4.580E-03   5.148E-03
   5.0        -5.731E-03  -5.099E-03  -3.512E-03  -1.761E-03   0.000E+00   1.761E-03   3.512E-03   5.099E-03   5.731E-03
   6.0        -6.318E-03  -5.621E-03  -3.871E-03  -1.941E-03   0.000E+00   1.941E-03   3.871E-03   5.621E-03   6.318E-03
   7.0        -6.907E-03  -6.145E-03  -4.232E-03  -2.122E-03   0.000E+00   2.122E-03   4.232E-03   6.145E-03   6.907E-03
   8.0        -7.497E-03  -6.670E-03  -4.593E-03  -2.303E-03   0.000E+00   2.303E-03   4.593E-03   6.670E-03   7.497E-03
   9.0        -7.968E-03  -7.089E-03  -4.882E-03  -2.448E-03   0.000E+00   2.448E-03   4.882E-03   7.089E-03   7.968E-03
  10.0        -8.390E-03  -7.464E-03  -5.140E-03  -2.578E-03   0.000E+00   2.578E-03   5.140E-03   7.464E-03   8.390E-03
  11.0        -8.770E-03  -7.802E-03  -5.373E-03  -2.694E-03   0.000E+00   2.694E-03   5.373E-03   7.802E-03   8.770E-03
  12.0        -9.103E-03  -8.098E-03  -5.577E-03  -2.796E-03   0.000E+00   2.796E-03   5.577E-03   8.098E-03   9.103E-03
  13.0        -9.384E-03  -8.348E-03  -5.749E-03  -2.883E-03   0.000E+00   2.883E-03   5.749E-03   8.348E-03   9.384E-03
0
0                                              DELTAL          DELTAR          (CL)ROLL
0
                                                14.5           -21.0            3.9175E-02
                                                12.0           -17.4            3.4852E-02
                                                 8.0           -11.6            2.4001E-02
                                                 4.0            -5.8            1.2035E-02
                                                 0.0             0.0            0.0000E+00
                                                -5.8             4.0           -1.2035E-02
                                               -11.6             8.0           -2.4001E-02
                                               -17.4            12.0           -3.4852E-02
                                               -21.0            14.5           -3.9175E-02
 Return to main program from M57071
1 END OF JOB.
```

F

Aircraft data

This chapter elaborates on the performance characteristics, airframe dimensions and propulsion system of the Cessna Skymaster in section F.1, section F.2 and section F.3, respectively, extending the information provided in section 2.1. In addition, section F.3 includes a brief description of the working principle of a constant speed propeller.

F.1. Performance

Table F.1 provides an overview of the aircraft weights and fuel capacity, whereas Table F.2 lists the key airspeed values and performance parameters such as range, rate of climb and service ceiling of the Cessna 337. The information on the aircraft performance is taken from the Pilot's Operating Handbook [12], Jane's World's Aircraft [66] and the aircraft Service Manual [61].

Table F.1: Aircraft weights overview [12] [66] [61]

Symbol	Parameter	Value [Imperial units]	Value [SI units]
EW	Empty Weight	2,695 [lbs]	1,222 [kg]
LEW	Licenced Empty Weight	2,794 [lbs]	1,267 [kg]
OEW	Operational Empty Weight [1]	3,047 [lbs]	1,382 [kg]
$MTOW$	Maximum Take-Off Weight	4,630 [lbs]	2,100 [kg]
MLW	Maximum Landing Weight	4,400 [lbs]	1,996 [kg]
UL	Useful Load	1,935 [lbs]	878 [kg]
FW	Fuel weight	822 [lbs], 131 [gal]	373 [kg], 496 [l]
FW_{main}	Main tank fuel capacity	584 [lbs], 93 [gal]	265 [kg], 352 [l]
FW_{aux}	Auxiliary tank fuel capacity	239 [lbs], 38 [gal]	108 [kg], 144 [l]
$FW_{trapped}$	Trapped fuel weight	19 [lbs], 3 [gal]	8 [kg], 11 [l]

Table F.2: Aircraft airspeed and other performance parameters overview [12] [66] [61]

Symbol	Parameter	Value [Imperial units]	Value [SI units]
V_C	Cruising airspeed [2]	165 [kt]	85 [m/s]
V_A	Design maneuvring airspeed	135 [kt]	69 [m/s]
V_H	Maximum airspeed at MCP	174 [kt]	90 [m/s]
V_{min}	Stall speed [3]	70 [kt]	36 [m/s]
V_{NE}	Never exceed airspeed	198 [kt]	102 [m/s]
R	Range [4]	1,060 [mi], 5.6 [h]	1,700 [km], 5.6 [h]
h_{max}	Service ceiling	19,500 [ft]	5,900 [m]
ROC	Rate of Climb	1,200 [ft/min]	6.1 [m/s]
d_{TO}	Take-Off distance to 50 ft	1,555 [ft]	474 [m]
d_L	Landing distance from 50 ft	1,650 [ft]	503 [m]

[1] From Mass and Balance supplement for the N4207X, 17.05.2022 FAA A&P 3289471
[2] Cruise at 75% power at 5,500 ft
[3] Stall speed with flaps up, power off
[4] Range for normal lean mixture, cruise at 5,500 ft, 75% power, full main and auxiliary tanks, no reserve
[5] Mass of fuel computed assuming AVGAS density of 6.28 lbs/gal or 0.75 kg/l

F.2. Airframe

Figure F.1 outlines the shape of the C337 on a three view drawing [12], while Table F.3 provides an overview of the airframe characteristics of aircraft.

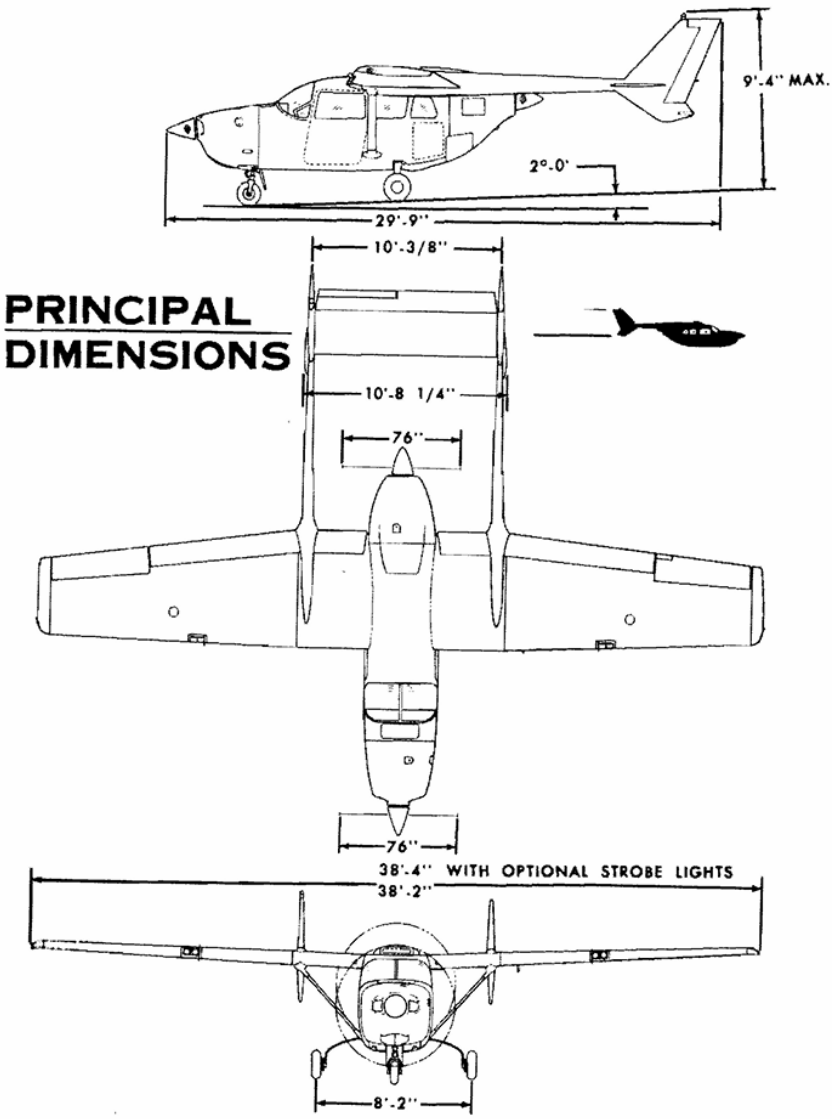

Figure F.1: Cessna 337F Super Skymaster principal dimensions [12]

Table F.3: Airframe characteristics overview [12] [66] [58] [2]

Symbol	Parameter	Value [Imperial units]	Value [SI units]
l	Length	29 [ft] 9 [in]	9.07 [m]
b	Wingspan	38 [ft] 4 [in]	11.68 [m]
$c_{b=0}$	Root Chord Length	6 [ft] 2 [in]	1.88 [m]
$h_{a/c}$	Height	9 [ft] 4 [in]	2.84 [m]
W/S	Wing Loading	22.9 [lbs/ft^2]	111.8 [kg/m^2]
S	Wing area	201 [ft^2]	18.7 [m^2]
S_v	Vertical tail area (both)	32.5 [ft^2]	3.02 [m^2]
S_h	Horizontal tail area	32.8 [ft^2]	3.05 [m^2]
t_{skin}	Skin thickness	0.016 [in]	0.41 [mm]
-	Wing airfoil	root: NACA 2412, tip: NACA 2409	
-	Empennage airfoil	NACA 0009	
AOI	Angle of incidence	root: 2°, tip: 0°	
AR	Aspect ratio	7.18 [-]	
Γ	Dihedrala ngle	3°	
λ	Taper ratio	0.67 [-]	
$\Lambda_{c/4}$	Quarter-chord sweep angle	0°	
-	Structural material	Aluminum 2024	

F.3. Powerplant

The Cessna Skymaster aircraft is powered by two Continental IO-360 engines, specifically the CB version in the front and C version in the rear. The motor is a fuel injected air cooled horizontally opposed piston engine which generates thrust by means of MTV-12 constant speed propellers mounted on the engine crankshaft. Table F.4 provides the propulsion system (engine and propeller) characteristics of the Skymaster in the current configuration.

Table F.4: Engine and propeller parameter overview [14] [44]

Symbol	Parameter	Value [Imperial Units]	Value [SI Units]
P_{MCP}	Maximum continuous engine power [1]	210 [BHP]	156.6 [kW]
P_c	Cruise engine power	157 [BHP]	117.1 [kW]
N_{max}	Maximum rated crankshaft speed	2800 [RPM]	293.2 [rad/s]
N_{min}	Engine idle speed	600 [RPM]	62.8 [rad/s]
N_c	Cruise engine speed	2600 [RPM]	272.3 [rad/s]
$l_{e,b}$	Bore	4.44 [in]	11.28 [cm]
$l_{e,s}$	Stroke	3.88 [in]	9.86 [cm]
V_e	Piston displacement	360 [in^3]	5.90 [l]
V_o	Oil capacity	5 [gal]	18.9 [l]
$m_{e,dry}$	Engine dry weight	277.8 [lbs]	126.0 [kg]
m_p	Propeller weight	55.1 [lbs]	25 [kg]
D_p	Propeller diameter	75.6 [in]	1.92 [m]
$D_{spinner}$	Spinner diameter	13.4 [in]	0.34 [m]
h_e, w_e, l_e	Engine height, width, length	22.4, 33.0, 35.3 [in]	570, 839, 898 [mm]
I_{gen}	Generator current	30 [A]	
V_{gen}	Generator voltage	28 DC [V]	
$\eta_{p,max}$	Propeller maximum efficiency	0.90 [-]	
p_3/p_0	Compression ratio	8.5 [-]	
n_{cyl}	Number of cylinders	6 [-]	
n_p	Number of propeller blades	3 [-]	

A constant speed propeller engine, such as the Continental IO-360, coupled with the MTV-12 three

[1] Reported at maximum rated crankshaft speed

blade propeller has three control inputs:

- The **throttle** controls the air mass flow into the engine cylinders (and thus the manifold pressure p_z). The Fuel Metering Unit (FMU) adjusts the fuel mass flow $\dot{m}_f$ accordingly to obtain a desired air-to-fuel ratio, the throttle controls the engine power P.
- The **engine speed** N defines the rotational speed of the engine crankshaft and the propeller installed on it. Because of the variable propeller blade pitch, a change in torque, airspeed or altitude does not imply a necessity to adjust the speed, which can be set independently.
- The **mixture** control allows to set adjust air to fuel ratio A/F. Increasing A/F (leaning) might be desired to adjust for the decrease in pressure with altitude.

Propellers are designed for a desired airspeed for which the efficiency η_p is maximised. With a change of propeller loading caused by a climb or descent, a fixed pitch propeller tends to decelerate or accelerate, respectively, if the power setting is kept the constant. This shifts the propeller to a lower efficiency zone, resulting in an increase of drag and fuel consumption. The constant speed propeller solves this problem of off-peak performance deviation by keeping the propeller loading, and thus N, constant by automatically adjusting the blade pitch angle β_p. The optimum η_p is therefore kept over a range of airspeed values.

For the installed MTV-12 propeller, the adjustment of β_p is performed by a mechanical Constant Speed Unit (CSU) also called governor. With the use of flyweights, whose position is dependent on N, connected to the throttle setting, a built up oil pressure acts against a spring, balancing the β_p. In case of a pitch down motion, N has the tendency to increase. The implies an increase in airspeed and results in the governor increasing β_p to match the propeller loading and N [28, pp. 594–595], and vice versa for a pitch up motion.